Breakup Process of Plane Liquid Sheets and Prediction of Initial Droplet Size and Velocity Distributions in Sprays

by

Sushanta Kumar Mitra

A thesis
presented to the University of Waterloo
in fulfillment of the
thesis requirement for the degree of
Doctor of Philosophy
in
Mechanical Engineering

Waterloo, Ontario, September 2001

I hereby declare that I am the sole author of this thesis. This is a true copy of the thesis, including any required final revisions, as accepted by my examiners.
I understand that my thesis may be made electronically available to the public.


Sushanta K. Mitra

Abstract

Spray models are increasingly becoming the principal tools in the design and development of gas turbine combustors. Spray modeling requires a knowledge of the liquid atomization process, and the sizes and velocities of subsequently formed droplets as initial conditions. In order to have a better understanding of the liquid atomization process, the breakup characteristics of plane liquid sheets in co-flowing gas streams are investigated by means of linear and nonlinear hydrodynamic instability analyses. The liquid sheet breakup process is studied for initial sinuous and varicose modes of disturbance. It is observed that the sheet breakup occurs at half-wavelength intervals for an initial sinuous disturbance and at full-wavelength intervals for an initial varicose disturbance. It is also found that under certain operating conditions, the breakup process is dictated by the initial varicose disturbance compare to its sinuous counterpart. Further, the breakup process is studied for the combined mode and it is found that the sheet breakup occurs at half- or full-wavelength intervals depending on the proportion of the individual sinuous and varicose disturbances. In general, the breakup length decreases with the increase in the Weber number, gas-to-liquid velocity and density ratios.

A predictive model of the initial droplet size and velocity distributions for the subsequently formed spray is also formulated here. The present model incorporates the deterministic aspect of spray formation by calculating the breakup length and the mass-mean diameter and the stochastic aspect by statistical means through the maximum entropy principle based on Bayesian entropy. The two sub-models are coupled together by the various source terms signifying the liquid-gas interaction and a prior distribution based on instability analysis, which provides information regarding the unstable wave elements on the two liquid-gas interfaces.

Experimental investigation of the breakup characteristics of the liquid sheet is performed by a high speed CCD camera and the measurement of the initial droplet size and distributions is conducted by phase-Doppler interferometry. Good agreement of the theoretical breakup length with the experiment is obtained for a planar, an annular and a gas turbine nozzle. The predicted initial droplet size and velocity distributions show reasonably satisfactory agreement with experimental data for all the three types of nozzles. Hence this spray model can be utilized to predict the initial droplet size and velocity distributions in sprays, which can then be implemented as a front-end subroutine to the existing computer codes.

Acknowledgements

I like to thank my supervisors, Dr. Xianguo Li and Dr. Metin Renksizbulut, for their help and encouragement during the entire course of my Ph.D. study. I also like to thank Mr. Carlos Salvador, Mr. Jaewan Park, and Mr. Al Hodgson for their kind help in my experimental work. The timely help from Mr. Colin Campbell regarding Matlab and MAPLE is really appreciated.

I like to mention that my stay in University of Waterloo was very enjoyable due to the support and friendship that I received from numerous friends and colleagues. Special thanks to our departmental secretaries, Susan Spaetzel, Marlene Dolson and Anita Fonn, for their kind help in various administrative matters. I also like to thank my wife for her kind patience while writing this thesis.

The financial supports from Natural Science and Engineering Research Council, Pratt & Whitney Canada, Ministry of Training and Education Ontario, and University of Waterloo are gratefully acknowledged.

To my parents and my wife Jayeeta

Contents

List of Tables

List of Figures

Nomenclature

A^*	Sheet cross-section	
a^*	Half-sheet thickness	
b^*	Sheet width	
C	Nozzle constant	
C_f	Drag coefficient	
D_{30}	Mass-mean diameter	
$\bar{D}_{cr}$	Critical droplet diameter	D^*_{cr}/D_{30}
$\bar{D}$	Nondimensional droplet diameter	D_i/D_{30}
D_i	Droplet diameter	
d^*_h	Hydraulic diameter	
d^*_{lg}	Ligament diameter	
F	Drag force	
f_0	Prior distribution	
I	Bayesian entropy	
$\mathcal{K}$	Boltzmann constant	

k	Wavenumber	$k^* a^*$
k_b	Wavenumber corresponding to λ_b	$k_b^* a^*$
k_c	Cut-off wavenumber	$k_c^* a^*$
L_b	Nondimensional breakup length	L_b^*/a^*
$\dot{m}_\ell$	Liquid mass flow rate	
N	Normalized cumulative droplet number	
$\dot{n}$	Number of droplets per unit time	
p	Probability	
Re_d	Reynolds number based on hydraulic diameter	$\rho_\ell U_\ell d_h^*/\mu_\ell$
Re_g	Gas phase Reynolds number	$\rho_g \lvert U_g - U_\ell \rvert L_b a^*/\mu_g$
S	Shannon entropy	
$\bar{S}_e$	Nondimensional energy source term	$S_e/(\dot{m}_\ell U_\ell^2)$
$\bar{S}_m$	Nondimensional mass source term	$S_m/\dot{m}_\ell$
$\bar{S}_{mv}$	Nondimensional momentum source term	$S_{mv}/(\dot{m}_\ell U_\ell)$
t	Time	$t^* U_\ell/a^*$
$\bar{U}$	Nondimensional droplet velocity	U_j/U_ℓ
U	Velocity ratio	U_ℓ/U_g
U_g	Gas phase velocity	
U_j	Droplet velocity	
U_ℓ	Liquid sheet velocity	

W	Work done by drag force	
We	Weber number	$\rho_\ell U_\ell^2 a^*/\sigma$
We_c	critical breakup Weber number	$\rho_g \lvert U_j - U_g \rvert^2 D_i/\sigma$
We_{30}	Weber number based on D_{30}	$\rho_\ell U_\ell^2 D_{30}/\sigma$
x	Spatial distance along x-axis	x^*/a^*
y	Spatial distance along y-axis	y^*/a^*
α	Angular frequency	
ϵ	Proportion of the disturbance mode	
η	Dimensionless surface deformation	η^*/a^*
η_0	Initial disturbance amplitude	η_0^*/a^*
Λ	Lagrange multiplier	
λ	Wavelength	λ^*/a^*
λ_b	Breakup wavelength	λ_b^*/a^*
λ_r^*	Rayleigh wavelength	
μ	Dynamic viscosity	
ω	Growth rate	
ϕ	Velocity potential	$\phi^*/(U_\ell a^*)$
ρ	Density ratio	ρ_g/ρ_ℓ
ρ_g	Gas density	
ρ_ℓ	Liquid density	

σ Surface tension

θ Phase angle between the disturbance modes

Super-Script

$*$ Dimensional quantity

Sub-Scripts

c Combined mode

g Gas phase

j Interface location (1 = upper, 2 = lower)

ℓ Liquid phase

max Maximum value

min Minimum value

s Sinuous mode

t Partial derivative with time

v Varicose mode

x Partial derivative with x

y Partial derivative with y

Chapter 1

Introduction

In recent years, Computational Fluid Dynamics (CFD) codes for turbulent two-phase flows have been widely used in the design and development of gas turbine combustors employing spray nozzles. For the successful operation of these CFD codes, it is required to specify the droplet size and velocity distributions in the vicinity of the nozzle as important boundary conditions. However, due to the lack of the predictive capability of the existing spray models, one has to rely on experimental data as an input or some judicious guesses for the required boundary conditions. Therefore, there is a pressing need in the spray community to develop a suitable atomization model that will predict the initial droplet size and velocity distributions in sprays. Such distributions can then be implemented as a "front-end" to the existing CFD codes.

A typical air-blast nozzle employed in a gas turbine combustor, shown in Fig. 1.1, causes the fuel to form a thin annular sheet. A number of previous studies [1, 2] indicate that the curvature effect is negligible due to the relatively small thickness of the liquid sheet compared to the radius of curvature. As a result, the fuel to be atomized may be modeled in a first approximation as a plane liquid sheet. Figure 1.2 illustrates the model of a plane liquid sheet emerging from a two-dimensional nozzle. The unstable waves are formed at the liquid-gas interfaces which eventually grow and cause the liquid sheet to break up into ligaments. The ligaments then contract to form droplets of different sizes and velocities. Therefore, the early stage of the atomization process is clearly deterministic with distinct wave motion, whereas the final stage of spray formation is random and stochastic.

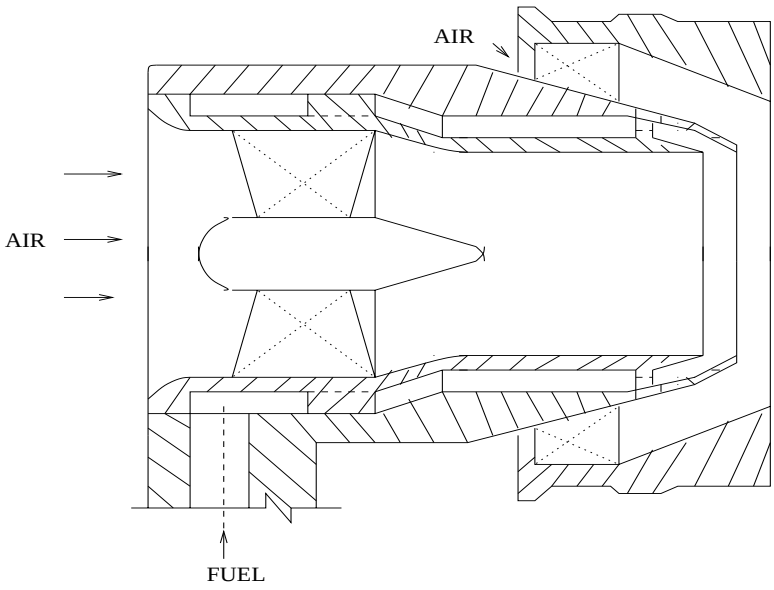

Figure 1.1: A typical air-blast nozzle for gas turbine application.

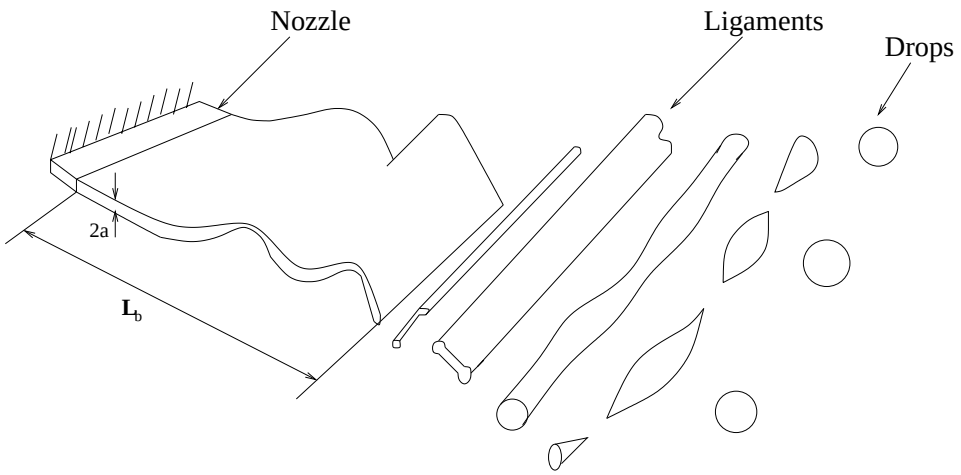

Figure 1.2: Schematic of a plane liquid sheet breakup leading to spray formation.

In order to understand the entire atomization process leading to spray formation, attention is focused on two distinct regions of the spray formation processes. The first region deals with the breakup of the liquid sheet to form ligaments and the analysis is carried out by using linear and nonlinear hydrodynamic instability theories. The second region deals with the stochastic aspect of droplet size and velocity distributions and is dealt with by using the Maximum Entropy Principle (MEP) which is based on information theory. These two regions are then coupled together through source terms, which represent the interaction between the liquid and the surrounding gas medium and a prior distribution, which contains the information about the unstable wave elements on the two liquid-gas interfaces.

1.1 Objective and Methodology

The main purpose of the study carried out in this thesis is to formulate a predictive model for the initial droplet size and velocity distributions in sprays by taking into account both the deterministic and the stochastic aspects of droplet formation processes. The deterministic aspect deals with the liquid sheet breakup process whereas the stochastic aspect deals with the formation of droplets of different diameters and velocities.

The deterministic sub-model adopts linear and nonlinear hydrodynamic instability theories. The linear instability theory yields the dominant wavelength of unstable wave development, and the nonlinear instability theory gives information on the breakup length and the breakup characteristics of the liquid sheet. The stochastic sub-model is formulated by the application of the MEP, along with the conservation of liquid mass, momentum and energy, which must be satisfied during the liquid atomization process. The two sub-models are coupled together through source terms and a prior distribution. The source terms are obtained by performing a boundary-layer type of analysis for the relative liquid-gas motion over the liquid breakup length. The prior distribution is based on the linear instability analysis of plane liquid sheets.

An experimental investigation is conducted for the verification of the theoretical model. The experiments provide two important pieces of information: the breakup length and the associated breakup features of the liquid sheet in co-flowing gas streams, which are

needed for the validation and development of the deterministic sub-model; and the size and velocity distributions of the resulting spray droplets required for the verification of the stochastic sub-model. A high speed CCD camera is used to obtain the breakup length and breakup characteristics of the liquid sheet, and a laser-based, non-intrusive technique (Phase-Doppler Particle Analyzer, PDPA) is used to measure the droplet size and velocity distributions in the immediate vicinity of the sheet breakup region.

After verification, this model is capable of providing, from first principles, the required initial conditions for CFD simulation related to combustor design and development. Although many different types of spray exist, the present physical model can be applied for each case. However, for the purpose of illustration of the present model, the sprays formed from the breakup of plane liquid sheets will be used as an example.

1.2 Scope and Outline of Thesis

The present thesis has both theoretical and experimental components. Under theoretical study, a nonlinear instability analysis is carried out to investigate the breakup process of a plane liquid sheet. As a first step, the liquid sheet breakup process is analyzed by applying a sinuous mode of disturbance (disturbance that causes the two liquid-gas interfaces to move parallel to each other) at its interfaces. As the next step, breakup process is investigated for a varicose mode of disturbance (disturbance that causes the two interfaces to move in symmetry) applied at the liquid-gas interfaces. Subsequently, a nonlinear instability analysis is performed to analyze the breakup process of the liquid sheet subjected to the combined effect of both the sinuous and the varicose modes of disturbance. The next portion of the theoretical study involves a formulation for determining the droplet size and velocity distributions, which is based on the MEP. Under experimental study, photographic investigations of spray formation from a two-dimensional planar nozzle and a gas turbine nozzle have been conducted; and the droplet size and velocity distributions of sprays produced by these nozzles are measured in order to verify the distributions obtained from the theoretical model.

The background literature on instability analysis of liquid sheets, drop size and velocity distributions and experimental works related to liquid sheets and subsequent formed

droplets are discussed in Chapter 2 of this thesis. The formulation for the nonlinear instability analysis is provided in Chapter 3. Chapters 4–6 deal with the breakup characteristics of the liquid sheet subjected to a sinuous mode, a varicose mode, and a combined mode of disturbance, respectively, which collectively form the deterministic sub-model of the present study. Chapter 7 deals with the stochastic sub-model which includes a detailed derivation of the joint probability density function (pdf) for droplet size and velocity distributions, the evaluation of various source terms and the numerical technique adopted for obtaining the pdf. The experimental set-up, the instrumentation and the nozzles used for generating sprays are discussed in Chapter 8. This is followed by Chapter 9, which shows a comparison between theoretical predictions of the breakup length and the droplet size and velocity distributions with experimental measurements. The thesis ends with Chapter 10 which presents a summary of conclusions drawn from both the theoretical and the experimental studies along with recommendations for future research.

Chapter 2

Literature Review

2.1 Instability Studies

The theoretical prediction of the droplet size and velocity distributions in sprays is difficult because the mechanism of atomization is still not well understood and differs drastically from one situation to another, according to the velocities and the physical properties of the liquid and the surrounding gas medium, the geometrical shape of the disintegrating liquid bulk, the liquid supply system and the atomizer used. However, preceding liquid bulk breakup, distinct unstable waves develop and grow with a distinct wavelength. As a result, earlier investigations of liquid atomization process are based on the instability analysis of liquid-gas interfaces. Most of these have been reviewed and a summary of state-of-art knowledge until late 1980s can be found in two books by Lefebvre [3, 4]. The earlier theoretical works are focused on linear instability of two-dimensional plane liquid sheets in a stationary gas medium, as presented by York et al. [5] and Squire [6]. Hagerty & Shea [7] showed in their work that for inviscid and incompressible liquid and gas phases, only two modes of instability exist on the two liquid-gas interfaces: sinuous (antisymmetric about the centerline) and varicose (symmetric about the centerline) modes. They were also able to successfully match the theoretical wave growth and wavelength for liquid sheets with experimental measurements under different operating conditions.

The effects of liquid viscosity were investigated by Dombrowski & Johns [8] in a one-dimensional approximation, Lin [9] for a liquid curtain with ambient gas phase neglected,

and Li & Tankin [10] for plane liquid sheets in a stationary ambient gas medium. The liquid viscosity plays a dual role by increasing the amplitude of the disturbance for sinuous mode at low Weber numbers ($\rho_\ell U_\ell^2 a^*/\sigma$) as well as damping the growth rate for the sinuous mode at large Weber numbers and for the varicose mode at any Weber number. Li [11] also performed an instability analysis of viscous liquid sheets in two gas streams of unequal velocities. Li showed that there exists two independent unstable modes, termed as para-sinuous and para-varicose modes, which depend on the relative velocities of the liquid and gas streams at large Weber numbers and on the absolute velocities of both streams at small Weber numbers. The effect of gas compressibility, investigated by Cao & Li [12], for viscous liquid sheets in two gas streams of unequal velocities shows that the gas compressibility always increases the liquid instability. This finding is especially of practical importance for gas turbine applications because the air stream velocity is very large in the air-blast atomization, often approaching the sonic velocity.

The spatial instability of plane liquid sheets has also been instigated extensively by Li [13, 14] and it is found that spatial instability differ qualitatively and quantitatively from temporal instability [11] at low Weber numbers, but produces identical results through the Gaster transformation [15] at large Weber numbers (greater than one). The study by Lin et al. [16] shows that the sinuous mode is pseudo-absolutely unstable for Weber number less than a critical value (approximately one) but it is convectively (spatially) unstable for Weber numbers greater than one and non-zero density ratios. The varicose mode is always convectively unstable unless the density ratio is zero. However, low Weber numbers are not encountered in typical atomization applications and therefore absolute instability is not present for the liquid sheets under study here.

Instability analysis is also carried out for attenuating sheets [17], *i.e.*, liquid sheets whose thickness changes with the distance from the nozzle exit, by Dombrowski & Johns [8] with one-dimensional approximation and Weihs [18] for a radial sheet. It is found that in addition to the existing Kelvin-Helmholtz type of instability, there may exist other types of instability depending on the distance from the nozzle. However, stability mechanism of attenuating sheets is not yet fully understood due to the difficulty in the solution process involving hypergeometric functions, even though such sheet geometry is very important for practical sprays.

The linear instability analyses, discussed so far, do not produce the breakup of the liquid sheet subjected to the sinuous mode of disturbance as the two interfaces remain at a constant distant apart. As pointed by Crapper et al. [19], linear instability fails to match experimental data at the later stages of the sheet development which has large amplitude waves on its interfaces. Also the liquid sheet breakup processes are inherently nonlinear as observed by Mansour & Chigier [20] and Hashimoto & Suzuki [21] in their experimental works. Therefore, a nonlinear instability analysis is required in order to understand the later stages of the breakup process of the liquid sheet. Clark & Dombrowski [22] studied the nonlinear disintegration of inviscid liquid sheets by means of perturbation expansion techniques with the initial disturbance amplitude as the perturbation parameter (up to second-order). This study shows that the sheet thinning is due to the harmonic wave appearing in the second-order solution and the breakup of the sheet occurs at half-wavelengths and at locations close to the maximum deflection region of the sheet. A similar observation was made by Rangel & Sirignano [23, 24] using the discrete-vortex method. Jazayeri & Li [25] extended the work of Clark & Dombrowski [22] up to the third-order of the initial disturbance amplitude and also concluded that the sheet ruptures at the half-wavelength for the fundamental sinuous mode. They observed that the breakup of the liquid sheet is due to the nonlinear effects with the generation of higher harmonics (varicose first harmonic and sinuous second harmonic) as well as a feedback into the fundamental sinuous mode. They argued, through the work by Bogy [26] for circular liquid jet, that perturbation solution up to third-order is adequate for the description of the breakup process in liquid sheets. Their study also shows that the breakup length decreases with the increase in the initial disturbance amplitude, the Weber number and the gas-to-liquid density ratio, and it becomes asymptotically insensitive to the variations of the Weber number and the density ratio when the respective values of Weber number and density ratio are large.

Modulational instability of weakly nonlinear capillary waves on planar liquid sheets without the interaction of an ambient gas is studied by Matsuuchi [27, 28]. It is observed that the instability of the varicose mode may lead to the breakup of the sheet rather than that of the sinuous mode, which is contrary to Squire's instability [6] of a moving liquid sheet. This work is further extended by Mehring & Sirignano [29] for infinite and semi-infinite planar liquid sheets in a void. Their numerical simulations show that in case of

the varicose mode, the sheet is unstable to superimposed sub-harmonic disturbances with sufficient strengths.

The nonlinear instability analyses discussed so far for two-dimensional liquid sheets are conducted either in a void or in a stationary gas medium. However, in actual atomization applications, the liquid sheet is blasted on both sides by air streams and hence it is very important to consider a moving gas stream in the nonlinear instability analysis leading to the breakup of liquid sheets.

Limited studies are conducted for three-dimensional wave distortion on liquid sheets. Experimental works by Mansour & Chigier [20, 30] and Lozano et al. [31] show that at low relative air/liquid velocity ratio, the ligaments produced after the sheet rapture are in the spanwise direction (parallel to the nozzle slit). With the increase in the velocity ratio, streamwise vorticity becomes equal to or greater than the spanwise component, causing cellular structure and the ligaments being oriented in parallel to the flow direction. Such observations have also been indicated in the numerical simulations by Lozano et al. [32] using a three-dimensional Lagrangian model based on vortex dynamics methods and also through a weak three-dimensional analysis for sinuous and varicose wave propagations on infinite and semi-infinite planar liquid sheets by Kim & Sirignano [33]. Such other quasi-three dimensional analyses are also cited in a review article by Sirignano & Mehring [34].

2.2 Droplet Size and Velocity Distributions

The final stage of the liquid sheet breakup process preceding the droplet formation is highly nonlinear, and theoretically requires nonlinear analysis accurate up to very large orders. This is extremely difficult to achieve, if possible at all. Further, the final breakup details depend sensitively on the history of the wave motion, the interaction among various wave elements which are not known in practice. As a result, droplet formation process appears to be random and chaotic in practical sprays. This stochastic nature of droplet formation process, coupled with a large quantity of droplets of various sizes formed per unit time in a practical spray, has called for statistical description of spray droplets. Hence, droplet size in sprays has been typically described by probability density function (pdf) and many empirical pdfs have been proposed for this purpose [35, 36, 37]. However, all proposed

empirical pdfs lack universal predictive capability.

As an alternative to the empirical approach, primarily two analytical methods for obtaining pdfs have been developed in the past two decades: the maximum entropy principle (MEP) and the discrete probability function (DPF). The DPF method, first applied to model the drop size distributions in sprays by Sovani et al. [38], divides the entire spray formation into deterministic and non-deterministic portions and produces pdfs which are dependent on initial conditions related to the fluctuations of flow conditions at the nozzle exit. These fluctuations are difficult and in some practical cases impossible to measure for real sprays. On the other hand, the MEP was developed by Jaynes [39] based on Shannon's [40] concept of information entropy, which is a measure of uncertainty of a probability distribution. The application of MEP to spray modeling was pioneered by Sellens & Brzustowski [41, 42, 43, 44] and Li & Tankin [45, 46, 47, 48, 49], which is able to predict the least biased pdf that duly satisfies a set of constraints expressing the available information related to the distribution sought. The set of constraints for the liquid atomization process contains the conservation of liquid mass, momentum and energy during the atomization process, and the interaction between the atomizing liquid and the surrounding gas is represented by mass, momentum and energy source terms. The two approaches differ in the way the constraints related to energy are dealt with. Li & Tankin used a single constraint combining together both the surface energy and kinetic energy of the system, whereas Sellens & Brzustowski used separate constraint for each kind of energy. In practical sprays such as diesel and pressure-swirl sprays, the surface energy of the liquid always increases. Therefore, separate conservation of liquid kinetic energy and surface energy not only violates the physics involved, but also requires knowledge of the total surface energy of spray droplets. However, the MEP applied for droplets produced from cylindrical liquid jets in Rayleigh breakup regime by Chin et al. [50] uses a separate constraint for surface energy. This is physically realistic because in the Rayleigh breakup regime surface tension plays a predominant role, and the effects of liquid kinetic energy as well as the surrounding gas medium are negligible.

The MEP approach has also been used by other researchers to obtain drop size distributions. Van der Geld & Vermeer[51] have obtained a size distribution function by considering primary and satellite droplet formation separately with an assumed Gaussian

distribution which is not substantiated by experiments. Instead of maximizing the continuous form of the Shannon entropy, Cousin et al. [52] derived the drop size distributions for pressure-swirl atomization by maximizing a more general expression of the Shannon entropy, which is equivalent to Bayes entropy [53]. They used a single constraint based on the definition of one mean droplet diameter instead of using conservation laws adopted in the earlier studies. This approach is semi-empirical as it needs *a priori* knowledge about the mean droplet diameter in a particular spray, which cannot be known without experimental measurements. This work is further extended by Dumouchel et al. [54, 55] to obtain the parameters needed to fit their results for practical sprays. They also proposed a three-parameter volume-based drop size distribution to overcomes some limitations in their earlier works.

In recent years, Mitra & Li [56] were able to use the MEP to obtain droplet size distributions in a completely predictive manner for the atomization of liquid sheets in a stationary gaseous medium. In their approach, the deterministic and the stochastic submodels for spray formation are coupled together by the mass-mean diameter and various source terms signifying the liquid-gas interactions.

The models based on the MEP discussed so far fail to create a direct link between the unstable wave elements present prior to the sheet breakup process and the droplets produced after the breakup process. However, it is physically intuitive that the unstable wave growth at the interfaces of the liquid sheet must somehow dictate the final drop formation in sprays.

Apart from obtaining pdf, a few theoretical models have been developed to obtain the droplet size with little success [57, 58]. These models need information regarding mass-mean and volume-mean diameters of a spray and therefore lack predictive capability to obtain drop size distributions.

2.3 Experimental Studies

Over the past decades, numerous researchers have been involved in the experimental investigation of a liquid sheet due to its simple geometry. One of the earliest studies on liquid sheets was carried out by Dombrowski et al. [17]. They were interested in finding the tra-

jectory of the boundaries of the sheet produced from a rectangular-orifice fan spray nozzle. A photographic study of Kelvin-Helmholtz waves on thin liquid sheets was performed by Crapper et al. [19] in which sinuous waves of controlled frequency and amplitude were imposed on a water sheet to obtain the maximum growth rate. Asare et al. [59] studied the wave growth on planar water sheets ejected from nozzles which were subjected to transverse forced harmonic excitation. It was observed that the linear instability theory is able to predict the onset of the unstable regime and the wave growth rate quite well for small amplitude nozzle vibrations. Similar studies of forced vibration on the liquid sheet and its effect on the resulting drop size have been carried out by Crapper & Dombrowski [60], Dressler [61], and Chung et al. [62].

In order to obtain a two-dimensional liquid sheet, Mansour & Chigier [20] used a variable geometry air-blast atomizer with a high aspect ratio and studied the detailed breakup features of water sheets by using high-speed photography. As an extension to this work, they further studied the aerodynamic instability of the liquid sheet issuing from the same two-dimensional nozzle [30]. Three distinct modes of breakup were identified from the frequency of oscillation of the liquid sheet. In a recent work by Jazayeri & Li [63], spray formation from a liquid sheet has been investigated by using a similar two-dimensional nozzle but of constant geometry. The mechanism of sheet instabilities and spray formation have also been studied by Lavergne et al. [64] for different air-blast geometries. A microphone and a frequency analyzer were used in conjunction with a high-speed video camera to track the disintegration frequency. A similar arrangement was also used by Berthoumieu et al. [65] to observe the breakup characteristics of the liquid sheet produced by a planar and an annular nozzle.

The interfacial waves that are generated on the surface of the liquid sheet have been studied by Hashimoto & Suzuki [21]. They observed that these waves greatly affect the disintegration process of the liquid sheet. A study of stationary waves on liquid sheets due to an obstacle placed normal to the sheet flow has been conducted by Luca & Costa [66]. By applying the same technique, Luca [67] further studied the onset of global instability of the liquid sheet as opposed to the local absolute and convective instabilities.

Experiments were also conducted to study the tulip-shaped and cone-shaped liquid sheets [68] formed in swirl nozzles and a critical Weber number of 150 was identified at

which the transition from the tulip-shape to the cone-shape occurs. The effects of liquid properties on the breakup of a liquid sheet have been studied by Stapper et al. [69] for a twin-fluid, two-dimensional nozzle by means of pulsed laser imaging. Using dynamic similarities and order of magnitude estimates, Hespel et al. [70] were able to obtain high speed photographs related to the mechanism of breakup of film and sheet atomization for liquid metal sprays.

A considerable amount of studies have been performed to obtain the droplet size and velocity distributions in sprays. The phase-Doppler particle analyzer (PDPA) is primarily used for obtaining such distributions. The PDPA is an advanced, laser-based, non-intrusive diagnostic instrument that can be used for simultaneous measurement of size and velocity of individual droplets by measuring the phase difference and the frequency of light scattered when a droplet passes through the intersection of two laser beams (the Doppler burst). It was first introduced by Bachalo & Houser [71], and is an extension to the well-known technique of laser-Doppler velocimetry (LDV) that was developed by Yeh & Cummins [72]. The theory behind the operation of PDPA,which is based on Lorenz-Mie scattering [73], is well established and the details of which are summarized by Bachalo & Sankar [74]. Research is still being conducted to explore the various errors involved in PDPA [75, 76] and also to increase the sensitivity of the system to small particles which are of great importance in atomization application where the spray contains large and small droplets at the same time [77].

Mansour & Chigier [30] conducted detailed measurements of mean droplet size and velocity for a two-dimensional air-assisted nozzle by using the PDPA. More recently, spray characteristics and their spatial distribution have been investigated experimentally by Jazayeri & Li [63] for sprays generated by the breakup of thin liquid sheets in co-flowing air streams. Their phase Doppler measurements show that at a given spray cross section, the droplet axial mean velocity has a maximum value at the spray center, and decreases towards the periphery of the spray; whereas the Sauter mean diameter (drop diameter whose ratio of volume to surface area is same as that of the entire spray) has a minimum value at the center and increases monotonically towards the spray edge. They also found that, sufficiently downstream of the nozzle exit, the mean velocity attains a jet-like self-similar distribution, but the Sauter mean diameter varies in a complex manner due to the sec-

ondary atomization and droplet entrainment and coalescence at downstream of the spray. However, such dynamic behavior of the spray at the downstream section can be resolved by calculating the distance and the velocity difference between consecutive droplets in sprays, as well as the number of droplets in close proximity (grouplets) and the frequency of grouplet formation [78].

Both photographic and light scattering techniques are often used to measure drop sizes. Rizk & Lefebvre [79] used such techniques to study the influence of air velocity and liquid properties on drop size distribution for an air-blast atomizer. Digital image and signal processing techniques coupled with optics have also been used to obtain the drop size, as in case of liquid jet by Moses et al. [80] and for gas-assisted liquid atomization by Snyder & Reitz [81].

However, it is often difficult to reproduce the drop size measurements obtained by a different researcher or even to obtain the same data set for a given nozzle at different locations. As pointed out by Tate [82] and Lefebvre [83], certain problems arise due to the inaccurate or incomplete information about the test atomizer and operating conditions. Therefore, care should be taken while comparing experimental data obtained from different sources.

2.4 Summary

It is evident that limited studies have been performed on the nonlinear breakup of liquid sheet, although plenty of studies exist on the linear instability of liquid sheets. However, the breakup process is highly nonlinear. So far, the nonlinear instability studies are either performed for a liquid sheet in a stationary gas medium or in a void. For air-blast applications, it is extremely important to consider the breakup process of liquid sheets in co-flowing gas media. The current literature show that the application of the MEP is successful in obtaining the droplet size and velocity distributions in sprays. However, the present stochastic models fail to address the direct connection between the unstable wave elements present at the liquid-gas interfaces with the droplet formation process. Significant works are reported by different researchers in using the PDPA system for droplet size and velocity measurements. However, limited studies exist on the experimental investigation of the breakup process of plane liquid sheet. In the foregoing chapters, attempts will be made to address the unresolved issues, which are discussed here.

Chapter 3

Nonlinear Instability Formulation

The liquid sheet breakup process is a key part in the deterministic sub-model of the present study. The formulation for the breakup of the liquid sheet by means of hydrodynamic instability analysis is discussed here. A two-dimensional liquid sheet of constant thickness $2a^*$ is considered, as shown schematically in Fig. 3.1. The liquid sheet moves at a uniform axial velocity of U_ℓ in a surrounding gas medium, which is moving with a uniform velocity of U_g. The densities of the liquid and the gas phases are ρ_ℓ and ρ_g respectively. The effect of gravity is neglected because the Froude number (defined as the ratio of liquid inertia to gravity) is typically very large for practical sprays. Both phases are assumed to be inviscid and incompressible. Even though the liquid viscosity introduces additional instability modes [10], the viscosity tends to decrease the amplification rate of any disturbance at large Weber number, such as in air-blast atomization. A similar argument is also valid for gas viscosity, as observed by Teng et al. [84]. Therefore, with no loss of generality, both the liquid and the gas viscosities are neglected here. Unequal gas stream velocity on either side of the liquid sheet does not introduce additional modes of instability, although it does modify the instability characteristics according to the degree of the gas velocity differential [11]. For the sake of simplicity, the gas stream velocities are assumed to be equal in this study.

In the present formulation, liquid and gas flows are assumed to be initially irrotational (zero vorticity) so that by Lagrange's theorem along with the inviscid assumption, the flows are irrotational for all subsequent times [85]. Therefore, the entire flow field can

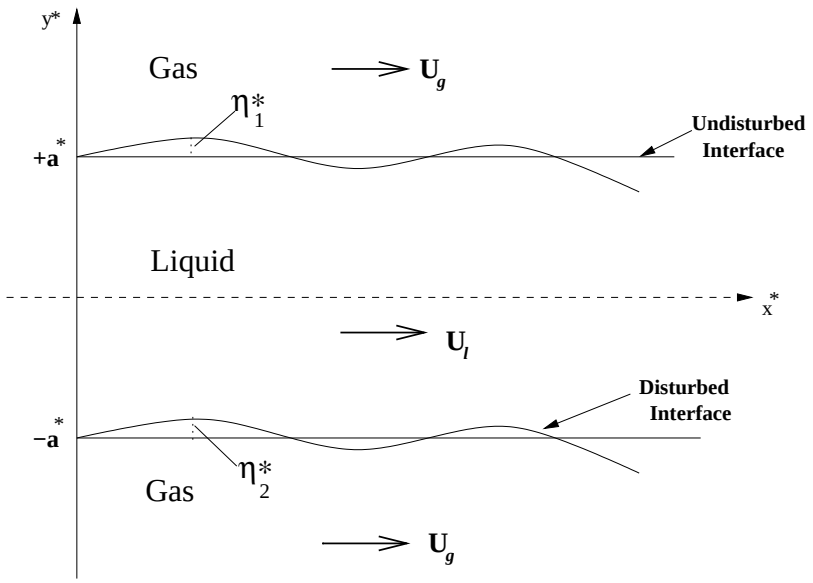

Figure 3.1: Schematic of a plane liquid sheet and imposed disturbance.

be treated as a potential flow. The uniform velocity assumption makes the pressure field constant within each phase and the difference of pressure at the interfaces is balanced by the surface tension, denoted by σ.

When the base flow, described above, is perturbed by a small disturbance, the two liquid-gas interfaces are displaced to new locations denoted by $y^* = (-1)^{j+1}a^* + \eta_j^*(x,t)$ where $j = 1$ represents the upper interface and $j = 2$ represents the lower interface. For the convenience of analysis, all the physical parameters are non-dimensionalized such that length, time and density are scaled with half-sheet thickness a^*, the convection time a^*/U_ℓ, and the liquid density ρ_ℓ. The dimensionless surface deformation η_j and the velocity potential ϕ for the liquid and the gas phases must satisfy the following governing equations:

$$\phi_{l,xx} + \phi_{l,yy} = 0 \quad \text{for } -1 + \eta_2 \leqslant y \leqslant 1 + \eta_1, \tag{3.1}$$

$$\phi_{g,xx} + \phi_{g,yy} = 0 \quad \text{for } 1 + \eta_1 \leqslant y < +\infty,\ -\infty < y \leqslant -1 + \eta_2; \tag{3.2}$$

where Eqs. (3.1)-(3.2) are mass conservation applied to liquid and gas phases, respectively and the subscripts, x and y, refer to the partial derivatives with respect to the spatial

coordinates. The conservation of momentum yields the unsteady Bernoulli equation, which provides the relationship between the pressure fields for the liquid and the gas phase flow.

Since the governing equations in this case are elliptic, they can be solved by specifying the boundary conditions on a complete contour enclosing the flow field. The boundary conditions in y can be expressed in terms of interface locations, which is described later, for both phases. The boundary conditions in x are not specified because we are seeking a wave form solution. Therefore, instead of solving the elliptic equation which needs boundary conditions for the x domain, we are seeking hyperbolic solutions to the governing equations. By implementing such a strategy, we are dealing with temporal instability analysis rather than the spatial one, which is mathematically much more involved to solve. However, the results of temporal instability are very close to those of spatial instability for the present problem because both the wave velocity and the group velocity are almost identical to the base flow velocity. For the gas phase, the boundary conditions at $y = \pm\infty$ require that the velocity potential is finite or bounded.

The boundary conditions applied to the perturbed interfaces, $y = (-1)^{j+1} + \eta_j$, are of two types: one is the kinematic boundary condition which states that the interfaces are material surfaces and the fluid particles initially on the interface will remain there subsequently; the other is the dynamic boundary condition which states that the difference in the normal stresses across the interface is balanced by the surface tension force. The interface boundary conditions are listed here:
kinematic

$$\phi_{l,y} - \eta_{j,t} - \phi_{l,x}\eta_{j,x} = 0 \tag{3.3}$$

$$\phi_{g,y} - \eta_{j,t} - \phi_{g,x}\eta_{j,x} = 0 \tag{3.4}$$

dynamic

$$\frac{1}{2} - \frac{1}{2}\rho U^2 + \rho\phi_{g,t} - \phi_{l,t} + \frac{1}{2}\rho(\phi_{g,x}^2 + \phi_{g,y}^2) - \frac{1}{2}(\phi_{l,x}^2 + \phi_{l,y}^2) = \frac{(-1)^j \eta_{j,xx}}{We(1+\eta_{j,x}^2)^{3/2}} \tag{3.5}$$

In the above equations, the dimensionless Weber number (We), velocity ratio (U), and

density ratio (ρ) are defined as:

$$We = \frac{\rho_\ell U_\ell^2 a^*}{\sigma}; \quad U = \frac{U_g}{U_\ell}; \quad \rho = \frac{\rho_g}{\rho_\ell} \tag{3.6}$$

and the subscript t refers to the partial derivative with respect to time. Since the governing equations are second-order in both x and y, four constants (unknowns) need to be evaluated. The two kinematic boundary conditions will be sufficient to evaluate the two constants. But the boundary conditions in x are not specified explicitly, but are given in terms of two unknowns: one in terms of wavenumber, denoted by k which is related to wavelength by $k = 2\pi/\lambda$; and the other as wave growth rate, denoted by ω, are introduced in the solution process, as discussed later. Therefore, one of the constants is replaced by k and the value of ω is obtained from the coupling effect of the two phases given in the dynamic boundary condition.

The surface deformations η_j must satisfy the governing equations and the associated boundary conditions given above. In order to obtain a solution for η_j, regular perturbation theory is utilized with the initial disturbance amplitude η_0 as the perturbation parameter. By means of series expansion method under the perturbation scheme, the surface deformations or the location of the two liquid-gas interfaces are expanded in power series of η_0 as:

$$\eta_j(x,t) = \sum_{n=1}^{\infty} \eta_0^n \eta_{j,n}(x,t) \tag{3.7}$$

The term η_0^0 is neglected from the expansion since it corresponds to the unperturbed interfaces, which are known. Assuming that $\eta_{j,n}$ and all its derivatives are of the same order of magnitude, the forms of the kinematic boundary conditions suggest that the velocity potentials for the liquid and the gas phases can also be expanded in power series of η_0 as:

$$\phi_l(x,y,t) = \sum_{n=0}^{\infty} \eta_0^n \phi_{l,n}(x,y,t) \tag{3.8}$$

$$\phi_g(x,y,t) = \sum_{n=0}^{\infty} \eta_0^n \phi_{g,n}(x,y,t) \tag{3.9}$$

where $\phi_{l,0} = x$ and $\phi_{g,0} = Ux$ represent the base flow field. Since the governing equations, Eqs (3.1) and (3.2), are linear, by applying the principle of superposition, each of the $\phi_{l,n}$ and $\phi_{g,n}$ must satisfy the governing equations independently. The corresponding boundary conditions are obtained by substituting Eqs. (3.7)-(3.9) into Eqs. (3.3)-(3.5), and equating to zero the successive coefficients of the same power of η_0^n. Under such a scheme, the velocity potentials need to be evaluated at the disturbed interfaces which are part of the solution and not known *a priori*. In order to overcome this difficulty, $\phi_{l,n}$ and $\phi_{g,n}$ are approximated by a Taylor series expansion around the unperturbed interfaces, $y = -1, 1$, as:

$$\begin{aligned}\phi|_{y=(-1)^{j+1}+\eta_j} &= \phi|_{y=(-1)^{j+1}} + \eta_j \phi_y|_{y=(-1)^{j+1}} + \frac{\eta_j^2}{2!}\phi_{yy}|_{y=(-1)^{j+1}} \\ &\quad + \frac{\eta_j^3}{3!}\phi_{yyy}|_{y=(-1)^{j+1}} + \cdots \end{aligned} \tag{3.10}$$

where η_j is given in Eq. (3.7). Thus the governing equations and the corresponding boundary conditions, which are evaluated at $y = -1, 1$, for the first three orders are obtained and are given below:

η_0 (or the first-order) :

$$\phi_{l,1,xx} + \phi_{l,1,yy} = 0 \quad \text{for } -1 \leqslant y \leqslant +1 \tag{3.11}$$

$$\phi_{g,1,xx} + \phi_{g,1,yy} = 0 \quad \text{for } +1 \leqslant y < +\infty,\ -\infty < y \leqslant -1 \tag{3.12}$$

$$\phi_{l,1,y} - \eta_{j,1,t} - \eta_{j,1,x} = 0 \tag{3.13}$$

$$\phi_{g,1,y} - \eta_{j,1,t} - U\eta_{j,1,x} = 0 \tag{3.14}$$

$$\rho\phi_{g,1,t} - \phi_{l,1,t} + \rho U\phi_{g,1,x} - \phi_{l,1,x} - \frac{(-1)^j}{We}\eta_{j,1,xx} = 0 \tag{3.15}$$

η_0^2 (or the second-order):

$$\phi_{l,2,xx} + \phi_{l,2,yy} = 0 \quad \text{for } -1 \leqslant y \leqslant +1 \tag{3.16}$$

$$\phi_{g,2,xx} + \phi_{g,2,yy} = 0 \quad \text{for } +1 \leqslant y < +\infty,\ -\infty < y \leqslant -1 \tag{3.17}$$

$$\phi_{l,2,y} - \eta_{j,2,t} - \eta_{j,2,x} = \eta_{j,1,x}\phi_{l,1,x} - \eta_{j,1}\phi_{l,1,yy} \tag{3.18}$$

$$\phi_{g,2,y} - \eta_{j,2,t} - U\eta_{j,2,x} = \eta_{j,1,x}\phi_{g,1,x} - \eta_{j,1}\phi_{g,1,yy} \tag{3.19}$$

$$\begin{aligned}&\rho\phi_{g,2,t} - \phi_{l,2,t} + \rho U\phi_{g,2,x} - \phi_{l,2,x} - (-1)^j\frac{\eta_{j,2,xx}}{We} = -\rho[\eta_{j,1,t}\phi_{g,1,y}\\ &+\eta_{j,1}\phi_{g,1,yt}] + [\eta_{j,1,t}\phi_{l,1,y} + \eta_{j,1}\phi_{l,1,yt}] - \frac{1}{2}\rho[\phi_{g,1,x}^2 + \phi_{g,1,y}^2\\ &+2U(\eta_{j,1,x}\phi_{g,1,y} + \eta_{j,1}\phi_{g,1,xy})] + \frac{1}{2}[\phi_{l,1,x}^2 + \phi_{l,1,y}^2\\ &+2(\eta_{j,1,x}\phi_{l,1,y} + \eta_{j,1}\phi_{l,1,yx})]\end{aligned} \tag{3.20}$$

η_0^3 (or the third-order):

$$\phi_{l,3,xx} + \phi_{l,3,yy} = 0 \quad \text{for } -1 \leqslant y \leqslant +1 \tag{3.21}$$

$$\phi_{g,3,xx} + \phi_{g,3,yy} = 0 \quad \text{for } +1 \leqslant y < +\infty,\ -\infty < y \leqslant -1 \tag{3.22}$$

$$\begin{aligned}&\phi_{l,3,y} - \eta_{j,3,t} - \eta_{j,3,x} = -\eta_{j,1}\phi_{l,2,yy} - \eta_{j,2}\phi_{l,1,yy} - \frac{1}{2}\eta_{j,1}^2\phi_{l,1,yyy}\\ &+\eta_{j,1,x}\phi_{l,2,x} + \eta_{j,2,x}\phi_{l,1,x} + \eta_{j,1,x}\eta_{j,1}\phi_{l,1,xy}\end{aligned} \tag{3.23}$$

$$\begin{aligned}&\phi_{g,3,y} - \eta_{j,3,t} - U\eta_{j,3,x} = -\eta_{j,1}\phi_{g,2,yy} - \eta_{j,2}\phi_{g,1,yy} - \frac{1}{2}\eta_{j,1}^2\phi_{g,1,yyy}\\ &+\eta_{j,1,x}\phi_{g,2,x} + \eta_{j,2,x}\phi_{g,1,x} + \eta_{j,1,x}\eta_{j,1}\phi_{g,1,xy}\end{aligned} \tag{3.24}$$

$$\begin{aligned}&\rho\phi_{g,3,t} - \phi_{l,3,t} + \rho U\phi_{g,3,x} - \phi_{l,3,x} - (-1)^j\frac{\eta_{j,3,xx}}{We} = -\rho[\eta_{j,1,t}\phi_{g,2,y}\\ &+\eta_{j,1}\phi_{g,2,yt} + \eta_{j,2,t}\phi_{g,1,y} + \eta_{j,2}\phi_{g,1,yt} + \eta_{j,1}\eta_{j,1,t}\phi_{g,1,yy} + \frac{1}{2}\eta_{j,1}^2\phi_{g,1,yyt}]\\ &+[\eta_{j,1,t}\phi_{l,2,y} + \eta_{j,1}\phi_{l,2,y,t} + \eta_{j,2,t}\phi_{l,1,y} + \eta_{j,2}\phi_{l,1,yt} + \eta_{j,1}\eta_{j,1,t}\phi_{l,1,yy}\\ &+\frac{1}{2}\eta_{j,1}^2\phi_{l,1,yyt}] - \frac{1}{2}\rho[2U(\eta_{j,1,x}\phi_{g,2,y} + \eta_{j,1}\phi_{g,2,xy} + \eta_{j,2,x}\phi_{g,1,y}\\ &+\eta_{j,2}\phi_{g,1,xy} + \eta_{j,1}\eta_{j,1,x}\phi_{g,1,yy} + \frac{1}{2}\eta_{j,1}^2\phi_{g,1,xyy}) + 2\phi_{g,1,x}(\phi_{g,2,x}\\ &+\eta_{j,1,x}\phi_{g,1,y} + \eta_{j,1}\phi_{g,1,xy}) + 2\phi_{g,1,y}(\phi_{g,2,y} + \eta_{j,1,y}\phi_{g,1,y} + \eta_{j,1}\phi_{g,1,yy})]\\ &+\frac{1}{2}[2\phi_{l,1,x}(\phi_{l,2,x} + \eta_{j,1,x}\phi_{l,1,y} + \eta_{j,1}\phi_{l,1,yx}) + 2(\eta_{j,1,x}\phi_{l,2,y} + \eta_{j,1}\phi_{l,2,yx}\\ &+\eta_{j,2,x}\phi_{l,1,y} + \eta_{j,2}\phi_{l,1,yx} + \eta_{j,1}\eta_{j,1,x}\phi_{l,1,yy} + \frac{1}{2}\eta_{j,1}^2\phi_{l,1,yyx})\\ &+2\phi_{1,y}(\phi_{l,2,y} + \eta_{j,1,y}\phi_{l,1,y} + \eta_{j,1}\phi_{l,1,yy})] - \frac{3(-1)^j}{2We}\eta_{j,1,xx}\eta_{j,1,x}^2\end{aligned} \tag{3.25}$$

The boundary conditions become linear for each order of the approximation, and the nonlinear terms present from the second-order onward are known as part of solutions from

the previous order. Therefore, successively higher orders of solutions can be obtained, which provide successively more accurate solution to the nonlinear problem. In principle, a nonlinear analysis can be carried out up to the infinite order, however, as pointed out earlier, solutions up to the first three orders are sufficiently accurate to quantify the breakup characteristics of the liquid sheet. Consequently, the present study will focus on the first three-order solutions and the subsequent chapters provide solutions for the surface deformation under different imposed disturbances at the two liquid-gas interfaces.

Chapter 4

Nonlinear Analysis for Sinuous Mode

In order to solve for the perturbed interfaces at each order satisfying the governing equations and the associated boundary conditions, an initial condition needs to be specified as the interfaces are evolving with time. The initial condition can be in terms of surface deformation, initial velocity, pressure or some combinations of the two. However, for the sake of simplicity, in this study the initial condition is based on the surface deformation at the interfaces. Again, the surface deformation can be in form a sinuous mode or a varicose mode or some combinations of these two modes. As discussed earlier, both the sinuous and the varicose modes have important effects on the liquid sheet instability [27, 29]. Therefore, as a first step, the surface deformation due to an initial sinuous disturbance is considered here. Once the nonlinear breakup characteristics of the liquid sheet subjected to an initial sinuous disturbance are fully understood, further liquid sheet breakup process for other modes will be considered.

4.1 Solution

The surface deformation is assumed to be due to an initial sinusoidal surface wave with the constant amplitude η_0 and wavenumber k. Figure 3.1 shows such imposed disturbance at the two liquid-gas interfaces. Any disturbance can be decomposed into sine and cosine functions by Fourier series, therefore, the first-order surface deformation can be written in

the following form:

$$\eta_{j,1}(x,t) = A_{1,s}\cosh(\omega_{1,s}t)\cos(\alpha_{1,s}t + kx) \tag{4.1}$$

where $\omega_{1,s}$ and $\alpha_{1,s}$ are the growth rate and the angular frequency, and $A_{1,s}$ is the amplitude of the sinuous disturbance, normalized by the initial disturbance amplitude η_0 as shown in Eq. (3.7). The surface deformation is subjected to the following initial conditions:

$$\eta_{j,1}(x,0) = \cos(kx); \quad \text{and} \quad \eta_{j,1,t}(x,0) = -\alpha_{1,s}\sin(kx) \tag{4.2}$$

Substitution of the surface deformation, given in Eq. (4.1), into Eqs. (3.13)-(3.15) and subject to Eq. (4.2) yields the following results:

$$\alpha_{1,s} = -\frac{\rho U k + k\tanh(k)}{\rho + \tanh(k)} \tag{4.3}$$

$$\omega_{1,s} = \frac{k[\rho(1-U)^2\tanh(k) - \frac{k}{We}\{\rho + \tanh(k)\}]^{1/2}}{\rho + \tanh(k)} \tag{4.4}$$

$$\eta_{1,1} = \eta_{2,1} \tag{4.5}$$

$$A_{1,s} = 1 \tag{4.6}$$

$$\begin{aligned}\phi_{l,1} = {} & \frac{\sinh(ky)}{k\cosh(k)}\big[\omega_{1,s}\sinh(\omega_{1,s}t)\cos(\alpha_{1,s}t + kx) \\ & -(\alpha_{1,s}t + kx)\cosh(\omega_{1,s}t)\sin(\alpha_{1,s}t + kx)\big]\end{aligned} \tag{4.7}$$

$$\begin{aligned}\phi_{g,1} = {} & \frac{(-1)^j}{k}\big[\omega_{1,s}\sinh(\omega_{1,s}t)\cos(\alpha_{1,s}t + kx) \\ & -(\alpha_{1,s} + Uk)\cosh(\omega_{1,s}t)\sin(\alpha_{1,s}t + kx)\big]\, e^{\{k+(-1)^j ky\}}\end{aligned} \tag{4.8}$$

The solution obtained for the first-order is similar to the result obtained from the linear instability theory [11]. This is due to the fact that at the first order, we are solving for the linearized form of the governing equations and the associated boundary conditions which in essence is the linear instability analysis. Eq. (4.5) shows that the two interfaces, upper ($j = 1$) and lower ($j = 2$), move parallel to each other and hence it represents a sinuous mode.

Some important observations can be made in relation to Eq. (4.4). For a given value of U, ρ and We, if the wavenumber k is such that it makes $\rho(1-U)^2\tanh(k) - [\rho +$

$\tanh(k)]k/We > 0$, then such surface waves will grow. On the other hand, for $\rho(1 - U)^2 \tanh(k) - [\rho + \tanh(k)]k/We < 0$, the surface waves will oscillate without decay. Such oscillation of the surface wave without decay occurs due to the inviscid assumption, the viscous effects tend to stabilize short-wavelength (large wavenumber) disturbances resulting in the decay of the amplitude of oscillation [10]. Therefore, there exists a cut-off wavenumber k_c which divides the wide spectrum of available disturbance wavenumbers into two distinct region of stable ($k > k_c$) and unstable ($k < k_c$) waves. For a given flow condition, the value of k_c is obtained by setting $\omega_{1,s} = 0$ in Eq. (4.4). Within the unstable region, the wavenumber for which the growth rate ($\omega_{1,s}$) is maximum is referred to as the dominant wavenumber. Therefore, for any disturbance, typically consisting of a wide range of wavenumbers, one can assume that the characteristic wavenumber which has the maximum potential for growth is the dominant wavenumber.

Since the first-order solution is now known, we can proceed further to solve the second-order surface deformation satisfying the governing equations, Eqs. (3.16)-(3.17), and the associated boundary conditions, Eqs. (3.18)-(3.20). Careful observation of the equations for the boundary conditions suggests that the nonlinear terms present in the left hand side of the equations are already known as a part of the solution from the first-order. Therefore, only the second-order terms need to be solved in order to obtain the desired second-order surface deformation. As mentioned earlier, the second-order surface deformation can also be resolved into sine and cosine terms, and hence can be written in the following form:

$$\eta_{j,2}(x,t) = P_{2,s}(t)\cos(2kx) - Q_{2,s}(t)\sin(2kx) \tag{4.9}$$

where $P_{2,s}$ and $Q_{2,s}$ are time dependent terms which are obtained by solving the second-order governing equations and the associated boundary conditions. For the first-order, a more compact and easily predictable form of the surface deformation was assumed. Due to the presence of the nonlinear terms in the boundary conditions for the second-order, it is difficult to assume a precise form of the surface deformation, and this makes the solution procedure for subsequent higher orders more difficult. It is also assumed that there are no initial displacement and velocity for the second-order surface deformation, which can be written as,

$$\eta_{j,2}(x,0) = 0; \quad \text{and} \quad \eta_{j,2,t}(x,0) = 0 \tag{4.10}$$

Substitution of Eq. (4.9) into the kinematic boundary conditions, Eqs. (3.18)-(3.19), along with the known first-order solutions, suggests the following form for the liquid and the gas velocity potentials:

$$\begin{aligned}
\phi_{l,2} &= f_{l2,s}(y)\big[\big\{P_{2,s,t} - 2kQ_{2,s} + K_{l2,s}(t)\big\}\cos(2kx) \\
&\quad + \big\{-Q_{2,s,t} - 2kP_{2,s} + L_{l2,s}(t)\big\}\sin(2kx)\big] + A_{l2,s}(t) \qquad (4.11)\\
\phi_{g,2} &= f_{g2,s}(y)\big[\big\{P_{2,s,t} - 2kUQ_{2,s} + K_{g2,s}(t)\big\}\cos(2kx) \\
&\quad + \big\{-Q_{2,s,t} - 2kUP_{2,s} + L_{g2,s}(t)\big\}\sin(2kx)\big] + A_{g2,s}(t) \qquad (4.12)
\end{aligned}$$

The unknown functions of y are obtained by substituting the above velocity potentials into the governing equations, Eqs. (3.16)-(3.17), and the velocity potentials take the following form:

$$\begin{aligned}
\phi_{l,2} &= \frac{\cosh(2ky)}{2k\sinh(2k)}\big[\big\{P_{2,s,t} - 2kQ_{2,s} + K_{l2,s}(t)\big\}\cos(2kx) \\
&\quad + \big\{-Q_{2,s,t} - 2kP_{2,s} + L_{l2,s}(t)\big\}\sin(2kx)\big] + A_{l2,s}(t) \qquad (4.13)\\
\phi_{g,2} &= -\frac{e^{-2ky}}{2ke^{-2k}}\big[\big\{P_{2,s,t} - 2kUQ_{2,s} + K_{g2,s}(t)\big\}\cos(2kx) \\
&\quad + \big\{-Q_{2,s,t} - 2kUP_{2,s} + L_{g2,s}(t)\big\}\sin(2kx)\big] + A_{g2,s}(t) \quad \text{for } y \geqslant 1 \qquad (4.14)\\
&= \frac{e^{2ky}}{2ke^{-2k}}\big[\big\{P_{2,s,t} - 2kUQ_{2,s} - K_{g2,s}(t)\big\}\cos(2kx) \\
&\quad + \big\{-Q_{2,s,t} - 2kUP_{2,s} - L_{g2,s}(t)\big\}\sin(2kx)\big] + A_{g2,s}(t) \quad \text{for } y \leqslant -1 \qquad (4.15)
\end{aligned}$$

Substitution of the velocity potentials into the dynamic boundary condition, Eq. (3.20), and the initial conditions, Eq. (4.10), and then collecting terms with suffixes cos(2kx) and sin(2kx), yields the above time dependent terms. After considerable amount of simplification, the following solutions for the second-order are obtained :

$$\begin{aligned}
\alpha_{2,s} &= -\frac{\rho U(2k) + (2k)\coth(2k)}{\rho + \coth(2k)} \qquad (4.16)\\
\omega_{2,s} &= \frac{(2k)[\rho(1-U)^2\coth(2k) - \frac{2k}{We}\{\rho + \coth(2k)\}]^{1/2}}{\rho + \coth(2k)} \qquad (4.17)\\
\eta_{j,2}(x,t) &= (-1)^{j+1}\big[A_{2,s}\cosh(\omega_{2,s}t)\cos(\alpha_{2,s}t + 2kx) + B_{2,s}\cosh(2\omega_{1,s}t) \\
&\quad \times \cos(2\alpha_{1,s}t + 2kx) + C_{2,s}\cos(2\alpha_{1,s}t + 2kx)\big] \qquad (4.18)
\end{aligned}$$

where $\omega_{2,s}$ is the growth rate and $\alpha_{2,s}$ is the corresponding angular frequency for the second-order; and the constants, $A_{2,s}, B_{2,s}$ and $C_{2,s}$, are provided in Appendix A.1. Important observations that can be made regarding the second-order solutions are as follows:

(1) The second-order surface deformation, $\eta_{j,2}$ given in Eq. (4.18), has the same magnitude for the upper ($j = 1$) and the lower ($j = 2$) interfaces, but opposite in sign. This, along with the forms of Eqs. (4.16)-(4.17), suggest that the second-order surface deformation is varicose in nature.

(2) The second-order surface deformation is due to two components of instability: the feed-back from the fundamental represented by $2\omega_{1,s}$ and the inherent instability from the first harmonic represented by $\omega_{2,s}$ when the dimensionless wavenumber $2k$ is such that $\rho(1-U)^2\coth(2k) - [\rho + \coth(2k)](2k)/We > 0$.

However, it should be pointed out that the nonlinear breakup of circular jets in the Rayleigh breakup regime [86] shows that both the fundamental and the first harmonic are varicose in nature and also the liquid mass is not conserved, which is not the case for the breakup of plane liquid sheets, as shown by Jazayeri & Li [25].

Following the same path as the second-order solution, the third-order surface deformation can be written as:

$$\eta_{j,3}(x,t) = P_{3,s}(t)\cos(3kx) - Q_{3,s}(t)\sin(3kx) \tag{4.19}$$

where $P_{3,s}$ and $Q_{3,s}$ are time dependent terms obtained from the third-order governing equations, Eqs. (3.21)-(3.22), and the associated boundary conditions, Eqs. (3.23)-(3.25). The initial conditions remain same as before, which can be written as:

$$\eta_{j,3}(x,0) = 0; \quad \text{and} \quad \eta_{j,3,t}(x,0) = 0 \tag{4.20}$$

Substitution of Eq. (4.19) into the kinematic boundary conditions indicates that the velocity potentials for the liquid and the gas phases can be written as:

$$\begin{aligned}\phi_{l,3} &= f_{l33}(y)\big[\big\{P_{3,s,t} - 3kQ_{3,s} + K_{l3,s}(t)\big\}\cos(3kx) + \big\{-Q_{3,s,t} - 3kP_{3,s} + L_{l3,s}(t)\big\} \\ &\quad \times \sin(3kx)\big] + f_{l31}\big[G_{l1,s}(t)\cos(kx) + H_{l1,s}(t)\sin(kx)\big] + B_{l3,s}(t) \qquad (4.21)\\ \phi_{g,3} &= f_{g33}(y)\big[\big\{P_{3,s,t} - 3kUQ_{3,s} + K_{g3,s}(t)\big\}\cos(3kx) + \big\{-Q_{3,s,t} - 3kUP_{3,s} + L_{g3,s}(t)\big\} \\ &\quad \times \sin(3kx)\big] + f_{g31}\big[G_{g1,s}(t)\cos(kx) + H_{g1,s}(t)\sin(kx)\big] + B_{g3,s}(t) \qquad (4.22)\end{aligned}$$

By substituting the above velocity potentials into the governing equations, Eqs. (3.21)-(3.22), the y dependence of the potentials can be obtained as:

$$\begin{aligned}
\phi_{l,3} &= \frac{\sinh(3ky)}{3k\cosh(3k)}\big[\big\{P_{3,s,t} - 3kQ_{3,s} + K_{l3,s}(t)\big\}\cos(3kx) + \big\{-Q_{3,s,t} - 3kP_{3,s} + L_{l3,s}(t)\big\} \\
&\quad \times \sin(3kx)\big] + \frac{\sinh(ky)}{k\cosh(k)}\big[G_{l1,s}(t)\cos(kx) + H_{l1,s}(t)\sin(kx)\big] + B_{l3,s}(t) \qquad (4.23) \\
\phi_{g,3} &= -\frac{e^{-3ky}}{3ke^{-3k}}\big[\big\{P_{3,s,t} - 3kUQ_{3,s} + K_{g3,s}(t)\big\}\cos(3kx) + \big\{-Q_{3,s,t} - 3kUP_{3,s} + L_{g3,s}(t)\big\} \\
&\quad \times \sin(3kx)\big] - \frac{e^{-ky}}{ke^{-k}}\big[G_{g1,s}(t)\cos(kx) + H_{g1,s}(t)\sin(kx)\big] + B_{g3,s}(t) \quad \text{for } y \geqslant 1 \qquad (4.24) \\
&= \frac{e^{3ky}}{3ke^{-3k}}\big[\big\{P_{3,s,t} - 3kUQ_{3,s} - K_{g3,s}(t)\big\}\cos(3kx) + \big\{-Q_{3,s,t} - 3kUP_{3,s} - L_{g3,s}(t)\big\} \\
&\quad \sin(3kx)\big] + \frac{e^{-ky}}{ke^{-k}}\big[G_{g1,s}(t)\cos(kx) + H_{g1,s}(t)\sin(kx)\big] + B_{g3,s}(t) \quad \text{for } y \leqslant -1 \qquad (4.25)
\end{aligned}$$

Finally, by substituting the velocity potentials into the dynamic boundary condition, Eq. (3.25), along with the initial conditions, Eq. (4.20), the third-order solutions are obtained, which can be written as:

$$\alpha_{3,s} = -\frac{\rho U(3k) + (3k)\tanh(3k)}{\rho + \tanh(3k)} \qquad (4.26)$$

$$\omega_{3,s} = \frac{(3k)[\rho(1-U)^2\tanh(3k) - \frac{3k}{We}\{\rho + \tanh(3k)\}]^{1/2}}{\rho + \tanh(3k)} \qquad (4.27)$$

$$\begin{aligned}
\eta_{j,3}(x,t) &= A_{3,s}\cosh(\omega_{3,s}t)\cos(\alpha_{3,s}t + 3kx) + B_{3,s}\cosh(\omega_{1,s}t + \omega_{2,s}t) \\
&\quad \times \cos(\alpha_{1,s}t + \alpha_{2,s}t + 3kx) + C_{3,s}\cosh(\omega_{2,s}t - \omega_{1,s}t) \\
&\quad \times \cos(\alpha_{1,s}t + \alpha_{2,s}t + 3kx) + D_{3,s}\cosh(3\omega_{1,s}t)\cos(3\alpha_{1,s}t + 3kx) \\
&\quad + E_{3,s}\cosh(\omega_{1,s}t)\cos(3\alpha_{1,s}t + 3kx) \qquad (4.28)
\end{aligned}$$

where $\omega_{3,s}$ is the growth rate and $\alpha_{3,s}$ is the corresponding angular frequency for the third-order; and the constants, $A_{3,s}, \cdots E_{3,s}$, are provided in the Appendix A.2.

The third-order solutions also provide important information which is listed below:

(1) The third-order surface deformation $\eta_{j,3}$, given in Eq. (4.28), is same for both the interfaces and hence it is sinuous in nature, compared to the second-order varicose surface-deformation.

(2) Similar to the second-order deformation, the growth of the interfaces is due to the energy feedback from the fundamental, represented by the terms involving $\omega_{1,s}$, and the first harmonic, $\omega_{2,s}$; and due to the inherent instability of the second harmonic for wavenumbers $3k$ satisfying the relation: $\rho(1-U)^2 \tanh(3k)-[\rho+\tanh(3k)](3k)/We > 0$.

(3) The energy transfer mechanism from the first harmonic and the fundamental is quite complicated for the third-order due to the presence of coupling terms involving $\omega_{1,s}$ and $\omega_{2,s}$.

Hence, the location of the two liquid-gas interfaces for an imposed sinuous disturbance, up to the third-order, can be written as:

$$\eta_j(x,t) = \eta_0\eta_{j,1}(x,t) + \eta_0^2\eta_{j,2}(x,t) + \eta_0^3\eta_{j,3}(x,t) \tag{4.29}$$

where the expressions for $\eta_{j,1}, \eta_{j,2}$ and $\eta_{j,3}$ are provided in Eqs. (4.1), (4.18) and (4.28), respectively. The final form of the surface deformation appears to be quite complex. However, it becomes comprehensive when the evolution of the two liquid-gas interfaces are studied for different flow conditions, as discussed in the next section.

4.2 Results and Discussions

As mentioned earlier, the surface deformation involves the growth rate terms and the unstable wavenumber k, which is an unknown parameter. Therefore, it is worthwhile to investigate the growth rates at different orders and the value of k to be used in the present analysis. A typical first-order wave growth curve is shown in Fig. 4.1 for a range of wavenumbers. The physical parameters used are $We = 40, \rho = 0.001$ and $U = 4$ which corresponds to a water spray in air at room temperature. The dominant wavenumber is 0.181, which corresponds to the maximum value of $\omega_{1,s}$. The cut-off wavenumber (k_c) is 0.359 and therefore, the wavenumbers in the range $0 < k < 0.359$ are unstable so far as the first-order wave growth is concerned. Figure 4.2 shows the growth rate curve corresponding to each order. It is observed that the range of unstable wavenumber decreases progressively as the order increases. It is also found that at the dominant wavenumber for the first-order,

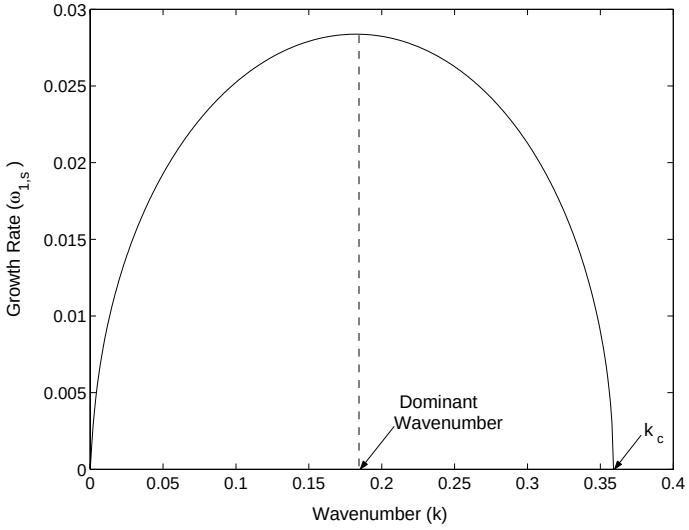

Figure 4.1: First-order wave growth $\omega_{1,s}$ as a function of wavenumber k for $We = 40, \rho = 0.001$ and $U = 4$.

i.e., $k = 0.181$, the wave growth is maximum. Therefore the dominant wavenumber for the first-order is taken as the characteristic value for k in this study.

In order to study the breakup process of the liquid sheet, the evolution of the two liquid-gas interfaces at different times is shown in Fig. 4.3. An initial disturbance amplitude of 0.1 is considered, while keeping other physical parameters same as before. It is found that at the initial time instant, the two interfaces are moving parallel to each other. However, at a later instant, for *e.g.*, at $t = 120$, waviness appears at the interfaces due to the nonlinear interaction between the three orders. This waviness eventually leads to the breakup of the liquid sheet when the two interfaces touch each other, as observed for $t = 135$. The breakup occurs at half-wavelength interval, which is consistent with the breakup observed for a liquid sheet imposed with a sinuous disturbance [22, 25]. The result of this analysis also matches with the work of Jazayeri & Li [25], where the gas phase motion is neglected. Figure 4.4 shows such surface evolutions for $U = 0$. It is observed that in the absence of gas phase motion, the breakup of the liquid sheet occurs at much later time. Therefore, the inertia of the surrounding gas medium plays an important role in the breakup process of the liquid sheet. The effect of gas phase velocity on the breakup process will be discussed

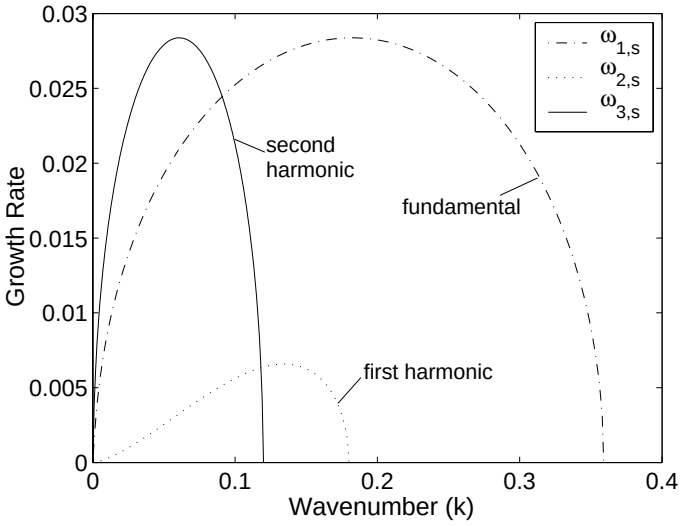

Figure 4.2: Growth rate curves for different values of wavenumber k due to an initial sinuous disturbance. $We = 40, \rho = 0.001$ and $U = 4$.

in more detail later on. Hence it is important to realize that the gas phase velocity can not be neglected in the air-blast atomization models.

As discussed earlier, the growth rate at each order is related to the fundamental, the first and the second harmonics, respectively. The effect of these on the evolution of the interfaces at the breakup time is shown in Fig. 4.5, which also reveals that each order progressively contributes towards the entire breakup process of the liquid sheet. Figure 4.5a shows the surface deformation due to the first-order (fundamental) solution only, and as expected, the two interfaces move parallel to each other without any sign of a sheet breakup. When the second-order (first harmonic) is added with the fundamental, as in the case of Fig. 4.5b, it is observed that the two interfaces are pulled close to each other and the locations where the sheet might pinch-off become distinct. With the addition of the third-order (second harmonic), as shown in Fig. 4.5c, the breakup of the liquid sheet occurs at half-wavelength intervals. Therefore, it becomes obvious that the first harmonic, which is varicose in nature, contributes significantly towards the breakup mechanism.

So far, only surface evolutions at different time instants are considered, since they can be obtained from Eq. (4.29) as outcome of this temporal instability analysis. However, as

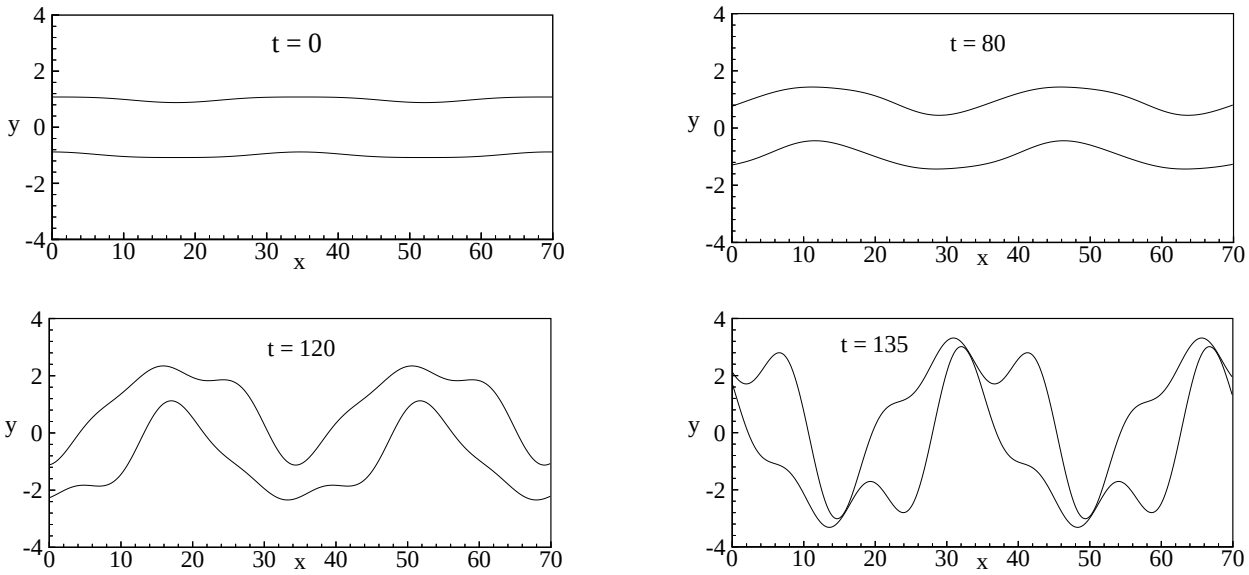

Figure 4.3: Evolution of surface deformation for $We = 40, \rho = 0.001, U = 4, k = 0.181$ and $\eta_0 = 0.1$ due to an initial sinuous disturbance.

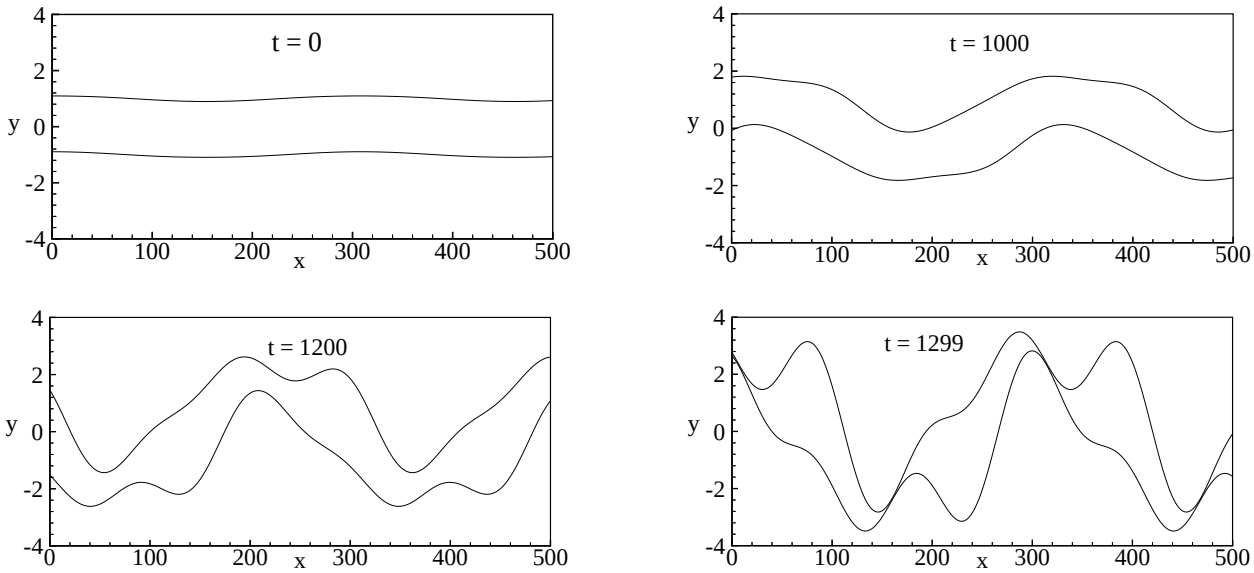

Figure 4.4: Evolution of surface deformation for $We = 40, \rho = 0.001, k = 0.021, \eta_0 = 0.1$ and zero gas phase velocity ($U = 0$) due to an initial sinuous disturbance.

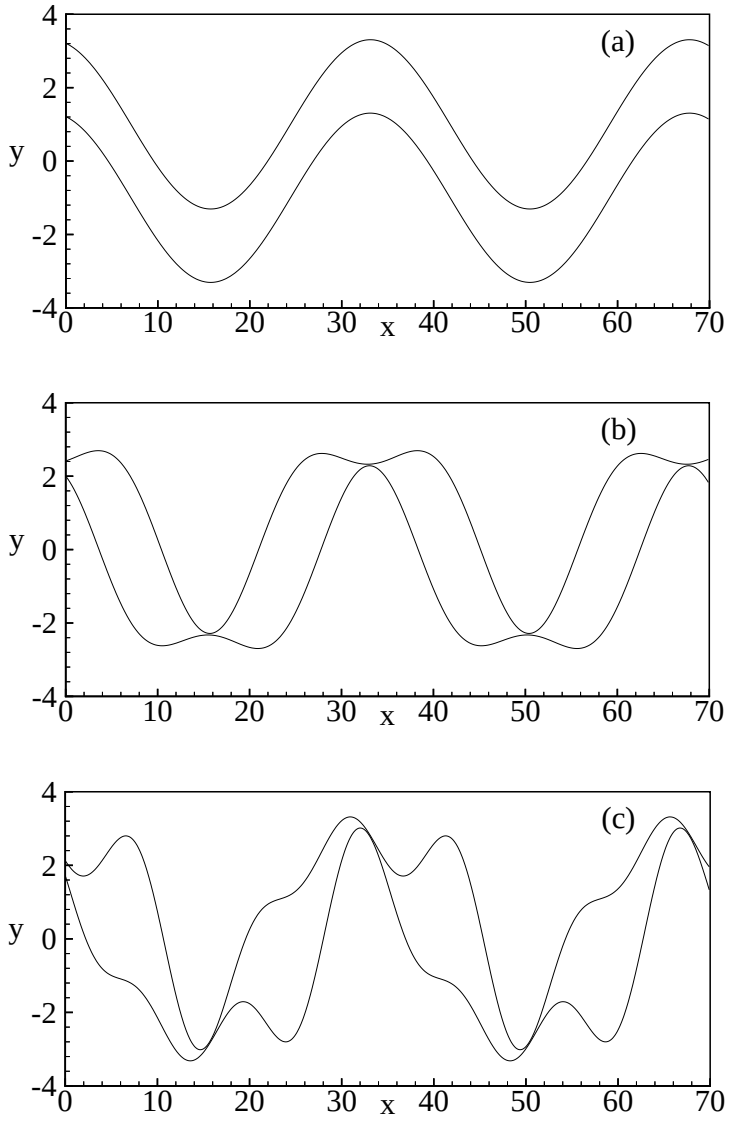

Figure 4.5: The effect of the fundamental, the first and the second harmonic on surface deformation at the breakup time $t = 135$ for $We = 40, \rho = 0.001, U = 4, k = 0.181$ and $\eta_0 = 0.1$ due to an initial sinuous disturbance

mentioned earlier, the temporal instability results can be readily transformed into spatial instability results, which give more physical understanding to the problem. Under such transformation, dimensionless time t is equivalent to the dimensionless spatial distance x. Figure 4.6 shows such spatial development of the liquid sheet as it is flows past the nozzle exit for the same set of physical parameters, while varying initial disturbance amplitude η_0 from 0.001 to 0.1. It is observed that as the liquid sheet emerges from the nozzle, the two interfaces move parallel to each other and at sufficient distance downstream of the nozzle, the nonlinear effects appear which result in the breakup of the liquid sheet. It is also found that the breakup length decreases as the strength of the initial disturbance amplitude is increased.

It is important to observe the effects of various operating parameters on the breakup process of the liquid sheet. Figure 4.7 shows the effect of velocity ratio U for $We = 40, \rho = 0.001$ and $\eta_0 = 0.1$. The wavenumber used is the dominant wavenumber for each case. With the increase in gas-to-liquid velocity ratio, the breakup time (or length) decreases substantially from $t = 48.8$ at $U = 6$ to $t = 13$ at $U = 10$. At much higher velocity ratio ($U = 10$), the two interfaces tend to move parallel with each other and the sheet amplitude at the breakup locations is quite large compared to the lower gas velocity case, as shown in Fig. 4.3 for $U = 4$. However, the breakup locations still remain at half-wavelength intervals.

The effect of the gas-to-liquid density ratio is almost similar to that of gas-to-liquid velocity ratio. Figure 4.8 shows surface evolution for $We = 40, U = 4$, $\eta_0 = 0.1$ and the wavenumber corresponds to the dominant wavenumber for each value of ρ. The breakup time decreases with the increase in the density ratio along with the increase in the sheet amplitude at the breakup points. The short breakup length causes less amount of liquid bulk available for drop formation which eventually leads to the formation of smaller droplets. Therefore at high pressure (high density ratio), more effective atomization is possible.

It is to be noted that for all cases discussed so far, the wavenumber corresponds to the dominant wavenumber is used. However, it may so happen that due to the presence of an external excitation, the imposed frequency on the liquid sheet does not corresponds to the dominant wavenumber. Under such circumstances, it is important to observe the

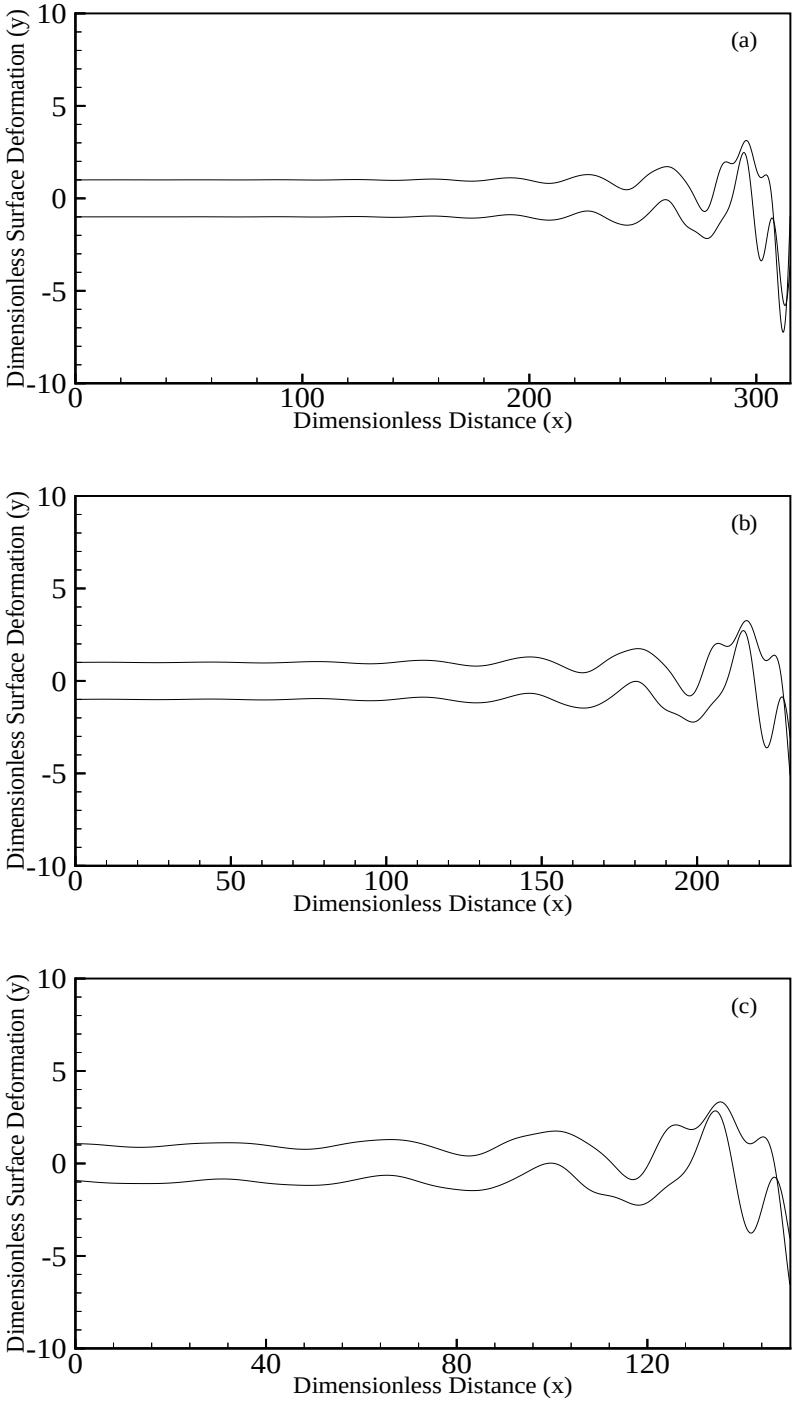

Figure 4.6: Spatial surface deformation for $We = 40, \rho = 0.001, U = 4$ and $k = 0.181$ due to an initial sinuous disturbance. (a) $\eta_0 = 0.001$, (b) 0.01 and (c) 0.1.

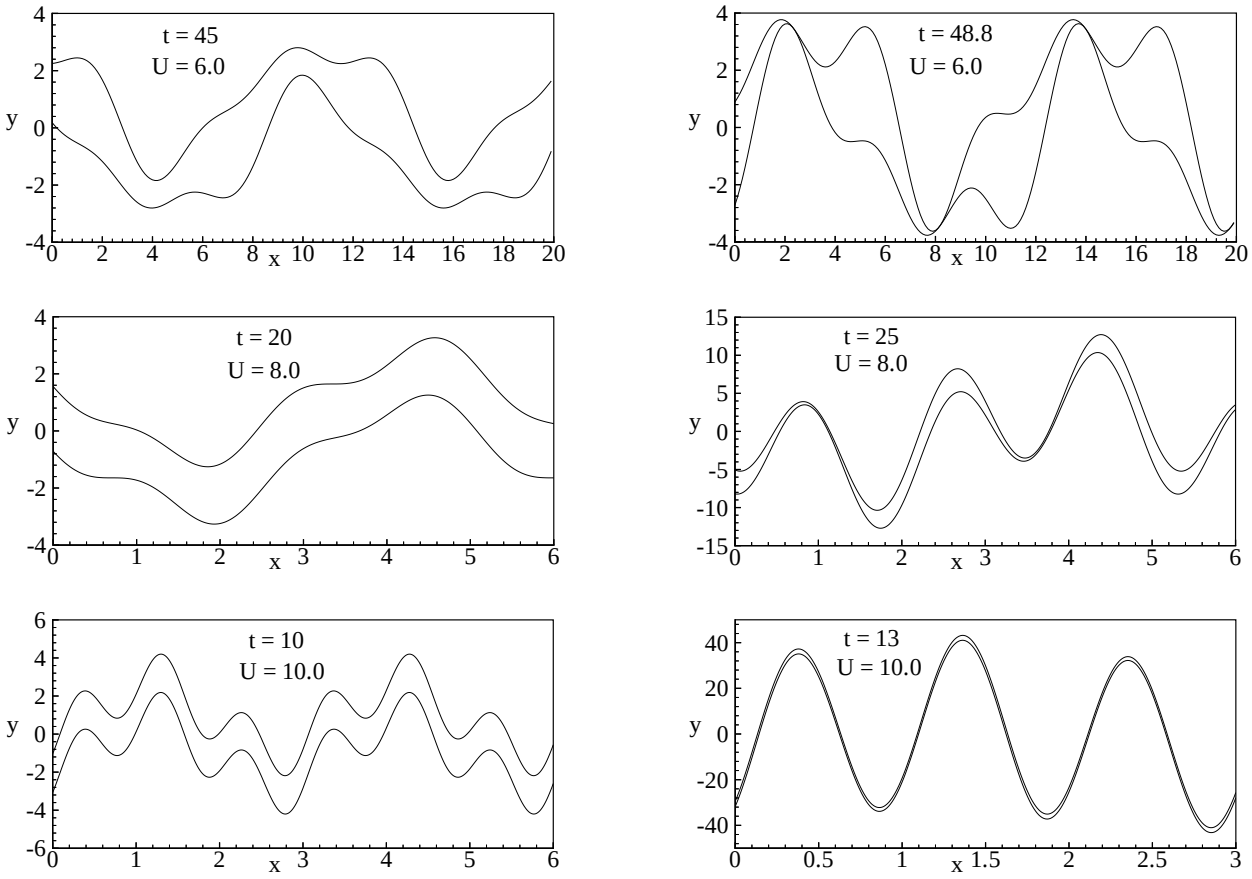

Figure 4.7: Evolution of surface deformation at different gas-to-liquid velocity ratios U for $We = 40, \rho = 0.001$ and $\eta_0 = 0.1$ due to an initial sinuous disturbance.

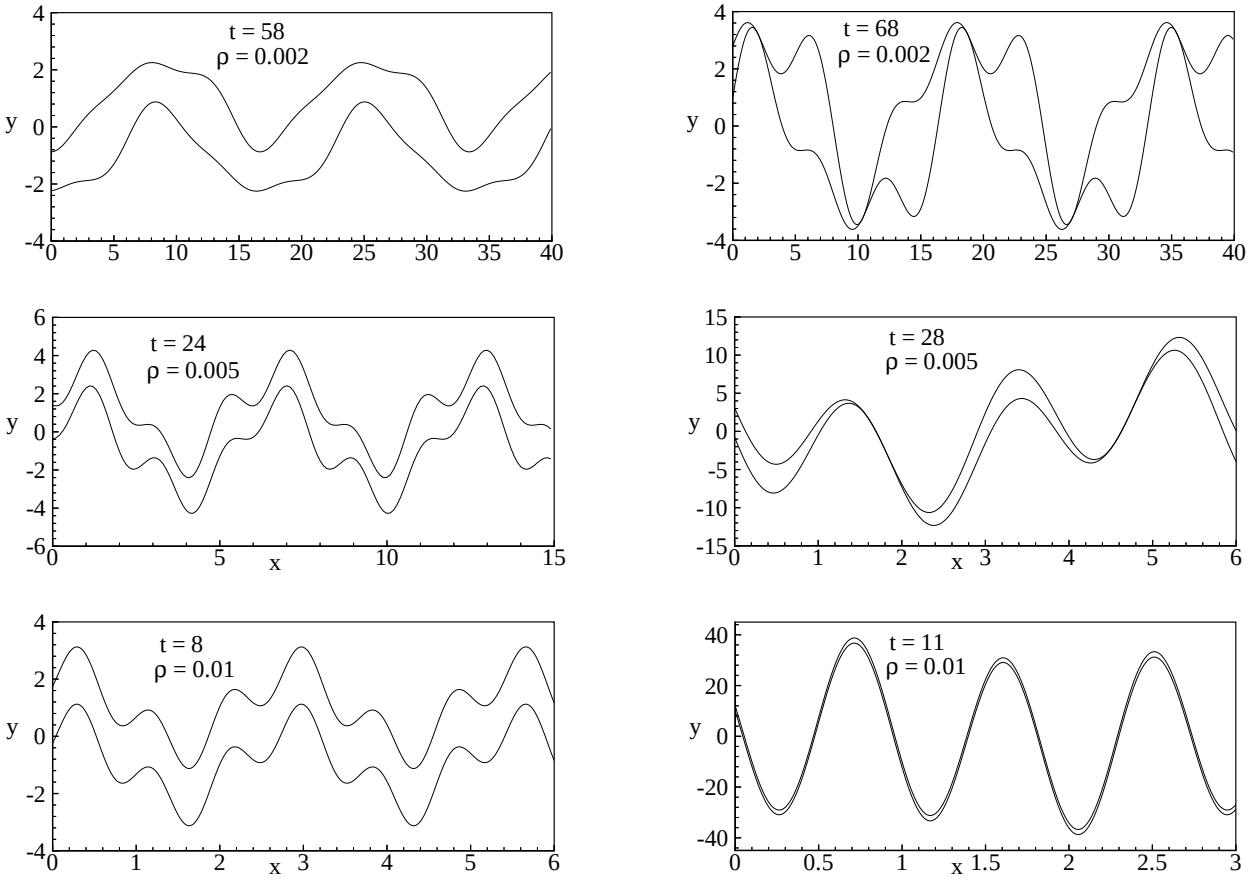

Figure 4.8: Evolution of surface deformation at different gas-to-liquid density ratios ρ for $We = 40, U = 4$ and $\eta_0 = 0.1$ due to an initial sinuous disturbance.

breakup characteristics for wavenumbers other than the dominant one. Figure 4.9 shows the surface evolution for three different wavenumbers. When $k = 0.1$, the disturbance is unstable for all the three orders, as observed from Fig. 4.2. For $k = 0.15$, the disturbance is stable for the second harmonic, but unstable for the first harmonic and the fundamental. When $k = 0.3$, the imposed disturbance is stable for both the first and the second harmonics, but unstable for the fundamental. The characteristics of the breakup process also change depending upon the wavenumber; and the breakup time increases for short wavelength (large wavenumber) disturbances. Even though the dominant wavenumber of 0.181 corresponds to the stable first and second harmonics and an unstable fundamental, the breakup characteristics, shown in Fig. 4.3, are different from those observed for $k = 0.3$ in Fig. 4.9. This is because the wave growth at $k = 0.3$ is smaller compared to that at $k = 0.181$.

4.3 Summary

The breakup process of the liquid sheet subjected to an initial sinuous mode of disturbance is studied here. Solutions for the surface deformation up to the first three orders are provided. It is found that the first-order solution (fundamental) is sinuous, the second-order (first harmonic) is varicose, and the third-order (second harmonic) is again sinuous; and also each order progressively contributes towards the breakup process of the liquid sheet. It is observed that the breakup time (or length) decreases with the increase in the gas-to-liquid velocity ratio, density ratio and the initial disturbance amplitude. It is also found that the varicose mode appearing in the second-order solution (first harmonic) is mainly responsible for the breakup of the liquid sheet subjected to a sinuous disturbance (fundamental mode). Therefore, it is imperative to investigate the behavior of the liquid sheet subject to a fundamental varicose mode of disturbance.

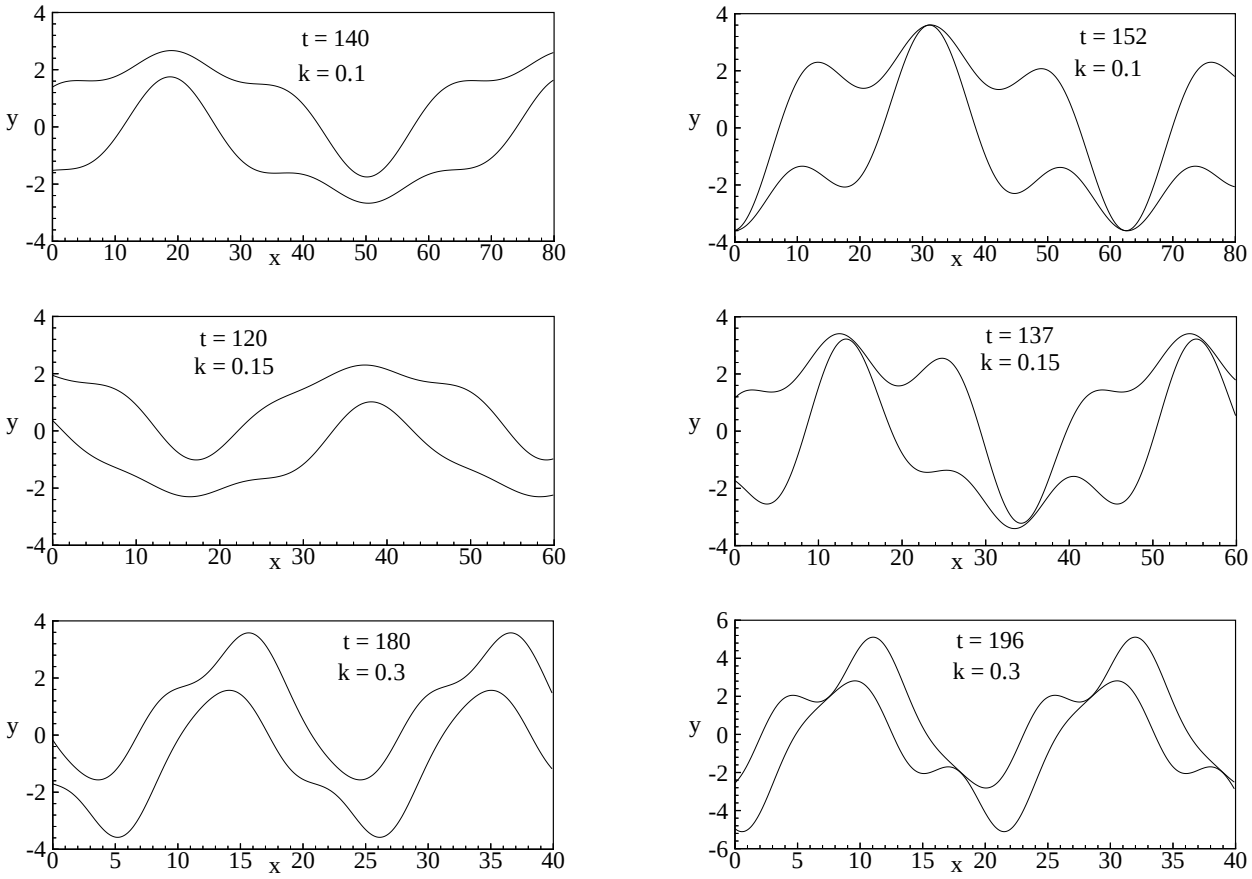

Figure 4.9: Evolution of surface deformation at different wavenumbers for $We = 40, U = 4, \rho = 0.001$ and $\eta_0 = 0.1$ due to an initial sinuous disturbance.

Chapter 5

Nonlinear Analysis for Varicose Mode

The nonlinear analysis of the liquid sheet subjected to a sinuous mode of disturbance shows that the second-order solution is varicose in nature and is responsible for the breakup of the liquid sheet. Previous nonlinear studies of liquid sheet in a void, by Matsucchi [27] and Mehring & Sirignano [29], also revealed that the varicose mode plays a significant role in the breakup process of the liquid sheet. Therefore, in this chapter, attention is focussed on the study of nonlinear breakup characteristics of the liquid sheet due to an initial varicose mode of disturbance applied at the two liquid-gas interfaces, which is shown schematically in Fig. 5.1.

5.1 Solution

The varicose mode in the present analysis has an initial disturbance amplitude of η_0 and the wavenumber k, which is same as that of the sinuous mode used in the previous chapter. Since the governing equations and the associated boundary conditions for each order remain the same, the solution procedure is similar to that used for the initial sinuous mode of disturbance.

Figure 5.1 shows that the behavior of the liquid sheet is identical about the central x axis, *i.e.*, $y = 0$. Therefore, only the solution of the upper interface ($j = 1$) is required, the

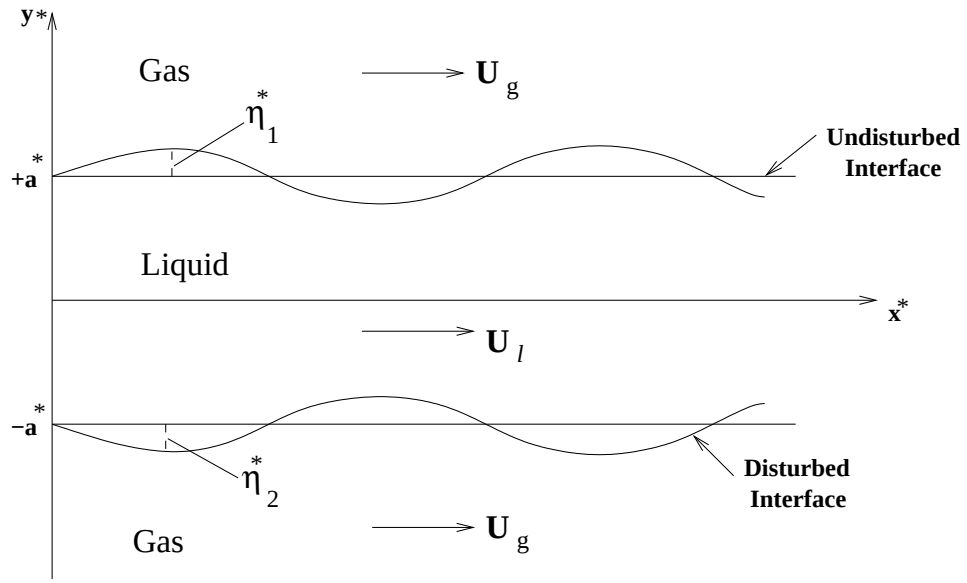

Figure 5.1: Schematic of a plane liquid sheet subjected to a varicose disturbance

lower interface ($j = 2$) solution follows automatically. In order to implement such strategy, additional boundary condition in the form of symmetry needs to be imposed at $y = 0$, which can be written in terms of the liquid velocity potential as:

$$\phi_{l,1,xy} = 0; \qquad \phi_{l,1,y} = 0 \tag{5.1}$$

$$\phi_{l,2,xy} = 0; \qquad \phi_{l,2,y} = 0 \tag{5.2}$$

$$\phi_{l,3,xy} = 0; \qquad \phi_{l,3,y} = 0 \tag{5.3}$$

Eqs. (5.1)-(5.3) are restating the fact that for each order of approximation, at $y = 0$, the normal component of the liquid velocity is zero and the axial component of the velocity is symmetric.

In order to obtain a solution for the first-order, which is the linear instability case, the surface deformation can be written as:

$$\eta_{1,1}(x,t) = A_{1,v}\cosh(\omega_{1,v}t)\cos(\alpha_{1,v}t + kx) \tag{5.4}$$

and the initial conditions as:

$$\eta_{1,1}(x,0) = \cos(kx); \quad \text{and} \quad \eta_{1,1,t}(x,0) = -\alpha_{1,v}\sin(kx) \tag{5.5}$$

Substitution of Eq. (5.4) into the governing equations and the associated boundary conditions, Eqs. (3.11)-(3.15), along with the initial conditions and the symmetry condition, provides the solutions for the first-order varicose growth rate, $\omega_{1,v}$, the corresponding angular frequency, $\alpha_{1,v}$, and the amplitude $A_{1,v}$, which can be written as:

$$\alpha_{1,v} = -\frac{\rho U k + k\coth(k)}{\rho + \coth(k)} \tag{5.6}$$

$$\omega_{1,v} = \frac{k[\rho(1-U)^2\coth(k) - \frac{k}{We}\{\rho + \coth(k)\}]^{1/2}}{\rho + \coth(k)} \tag{5.7}$$

$$A_{1,v} = 1 \tag{5.8}$$

$$\begin{aligned}\phi_{l,1} = &-\frac{\cosh(ky)}{k\sinh(k)}\big[\omega_{1,v}\sinh(\omega_{1,v}t)\cos(\alpha_{1,v}t+kx)\\ &-(\alpha_{1,v}t+kx)\cosh(\omega_{1,v}t)\sin(\alpha_{1,v}t+kx)\big]\end{aligned} \tag{5.9}$$

$$\begin{aligned}\phi_{g,1} = &\frac{(-1)^{j+1}}{k}\big[\omega_{1,v}\sinh(\omega_{1,v}t)\cos(\alpha_{1,v}t+kx)\\ &-(\alpha_{1,v}+Uk)\cosh(\omega_{1,v}t)\sin(\alpha_{1,v}t+kx)\big]e^{\{k+(-1)^j ky\}}\end{aligned} \tag{5.10}$$

Due to the symmetry condition, given in Eq. (5.1), the surface deformation for both the interfaces is of same magnitude, but opposite in sign, *i.e.*, $\eta_{2,1} = -\eta_{1,1}$. Hence the first-order solution (fundamental) is varicose in nature, which is different from the first-order solution for an initial sinuous mode of disturbance. These results are consistent with the outcomes of the linear instability, discussed earlier [13].

The second-order surface deformation can be written in terms of sine and cosine functions as,

$$\eta_{1,2}(x,t) = P_{2,v}(t)\cos(2kx) - Q_{2,v}(t)\sin(2kx) \tag{5.11}$$

where $P_{2,v}$ and $Q_{2,v}$ are time dependent terms and the initial conditions are given as,

$$\eta_{1,2}(x,0) = 0; \quad \text{and} \quad \eta_{1,2,t}(x,0) = 0 \tag{5.12}$$

Substitution of Eq. (5.11) into the kinematic boundary conditions, Eqs. (3.18) -(3.19), suggests the form of the velocity potentials for the liquid and the gas phases, similar to those given in Eqs. (4.11)-(4.12). These velocity potentials need to satisfy the governing

equations, Eqs. (3.16)-(3.17), and the symmetry condition, Eq. (5.2), and hence these can be written in terms of $P_{2,v}$ and $Q_{2,v}$, and their time derivatives in the following form:

$$\begin{aligned}\phi_{l,2} &= \frac{\cosh(2ky)}{2k\sinh(2k)}\big[\big\{P_{2,v,t} - 2kQ_{2,v} + K_{l2,v}(t)\big\}\cos(2kx) \\ &\quad + \big\{-Q_{2,v,t} - 2kP_{2,v} + L_{l2,v}(t)\big\}\sin(2kx)\big] + A_{l2,v}(t) \qquad (5.13)\\ \phi_{g,2} &= -\frac{e^{-2ky}}{2ke^{-2k}}\big[\big\{P_{2,v,t} - 2kUQ_{2,v} + K_{g2,v}(t)\big\}\cos(2kx) \\ &\quad + \big\{-Q_{2,v,t} - 2kUP_{2,v} + L_{g2,v}(t)\big\}\sin(2kx)\big] + A_{g2,v}(t) \quad \text{for } y \geqslant 1 \qquad (5.14)\end{aligned}$$

The velocity potentials are then substituted back into the dynamic boundary condition, Eq. (3.20), and the initial conditions, Eq. (5.12), to obtain the unknown time functions. After considerable amount of mathematical simplifications, the surface deformation for the upper interface can be written as:

$$\begin{aligned}\eta_{1,2}(x,t) &= A_{2,v}\cosh(\omega_{2,v}t)\cos(\alpha_{2,v}t + 2kx) + B_{2,v}\cosh(2\omega_{1,v}t)\cos(2\alpha_{1,v}t + 2kx) \\ &\quad + C_{2,v}\sinh(2\omega_{1,v}t)\sin(2\alpha_{1,v}t - 2kx) + D_{2,v}\cos(2\alpha_{1,v}t + 2kx) \qquad (5.15)\end{aligned}$$

where the constants, $A_{2,v}, \cdots D_{2,v}$, are provided in Appendix B.1; and the second-order growth rate, $\omega_{2,v}$, and its angular frequency, $\alpha_{2,v}$, are of the following form:

$$\omega_{2,v} = \frac{(2k)[\rho(1-U)^2\coth(2k) - \frac{2k}{We}\{\rho + \coth(2k)\}]^{1/2}}{\rho + \coth(2k)} = \omega_{2,s} \qquad (5.16)$$

$$\alpha_{2,v} = -\frac{\rho U(2k) + (2k)\coth(2k)}{\rho + \coth(2k)} = \alpha_{2,s} \qquad (5.17)$$

As before, the surface deformation for the lower interface is $\eta_{2,2} = -\eta_{1,2}$. Therefore, the second-order solution (first harmonic) is varicose in nature, which is same as the first harmonic obtained for the breakup of the liquid sheet subjected to an initial sinuous mode of disturbance. It is also observed that the growth of the first harmonic is due to two effects: one is the feedback of energy from the fundamental, and the other is the inherent instability of the first harmonic itself.

Finally, for the third-order solution, the surface deformation for the upper interface can be written as:

$$\eta_{1,3}(x,t) = P_{3,v}(t)\cos(3kx) - Q_{3,v}(t)\sin(3kx) \qquad (5.18)$$

along with the initial conditions:

$$\eta_{1,3}(x,0)=0; \quad \text{and} \quad \eta_{1,3,t}(x,0)=0 \tag{5.19}$$

where $P_{3,v}$ and $Q_{3,v}$ are the time dependent terms need to be solved. The upper interface, given in Eq. (5.18), is substituted back into the kinematic boundary conditions, Eq. (3.23)-(3.24), which suggests the form for the velocity potentials, similar to those given in Eqs. (4.21)-(4.22). The velocity potentials for both the phases need to satisfy the governing equations, Eqs. (3.21)- (3.22), and the symmetry condition, Eq. (5.3), and therefore can be written in the following form:

$$\begin{aligned}\phi_{l,3} &= \frac{\cosh(3ky)}{3k\sinh(3k)}\big[\big\{P_{3,v,t}-3kQ_{3,v}+K_{l3,v}(t)\big\}\cos(3kx)+\big\{-Q_{3,v,t}-3kP_{3,v}+L_{l3,v}(t)\big\}\\ &\quad\times\sin(3kx)\big]+\frac{\cosh(ky)}{k\sinh(k)}\big[G_{l1,v}(t)\cos(kx)+H_{l1,v}(t)\sin(kx)\big]+B_{l3,v}(t) \qquad (5.20)\\ \phi_{g,3} &= -\frac{e^{-3ky}}{3ke^{-3k}}\big[\big\{P_{3,v,t}-3kUQ_{3,v}+K_{g3,v}(t)\big\}\cos(3kx)+\big\{-Q_{3,v,t}-3kUP_{3,v}+L_{g3,v}(t)\big\}\\ &\quad\times\sin(3kx)\big]-\frac{e^{-ky}}{ke^{-k}}\big[G_{g1,v}(t)\cos(kx)+H_{g1,v}(t)\sin(kx)\big]+B_{g3,v}(t) \quad \text{for } y\geqslant 1 \qquad (5.21)\end{aligned}$$

The velocity potentials are then substituted back into the dynamic boundary condition, Eq. (3.25), and the initial conditions, Eq. (5.19), to obtain the unknowns $P_{3,v}$ and $Q_{3,v}$. After a considerable amount of tedious mathematical simplification, the final form of the third-order surface deformation for the upper interface can be written as:

$$\begin{aligned}\eta_{1,3} &= A_{3,v}\cosh(\omega_{3,v}t)\cos(\alpha_{3,v}t+3kx)+B_{3,v}\cosh(\omega_{1,v}t+\omega_{2,v}t)\cos(\alpha_{1,v}t+\alpha_{2,v}t+3kx)\\ &\quad+C_{3,v}\sinh(\omega_{1,v}t+\omega_{2,v}t)\sin(\alpha_{1,v}t+\alpha_{2,v}t-3kx)+D_{3,v}\cosh(3\omega_{1,v}t)\\ &\quad\times\cos(\alpha_{1,v}t+3kx)+E_{3,v}\sinh(3\omega_{1,v}t)\sin(\alpha_{1,v}t-3kx)\\ &\quad+F_{3,v}\cosh(\omega_{1,v}t)\cos(3\alpha_{1,v}t+3kx)+G_{3,v}\sinh(\omega_{1,v}t)\sin(3\alpha_{1,v}t-3kx) \qquad (5.22)\end{aligned}$$

where the constants, $A_{3,v},\cdots G_{3,v}$, are given in Appendix B.2; and the third-order growth rate, $\omega_{3,v}$, and the corresponding angular frequency, $\alpha_{3,v}$, can be written as:

$$\omega_{3,v} = \frac{(3k)[\rho(1-U)^2\coth(3k)-\frac{3k}{We}\{\rho+\coth(3k)\}]^{1/2}}{\rho+\coth(3k)} \tag{5.23}$$

$$\alpha_{3,v} = -\frac{\rho U(3k)+(3k)\coth(3k)}{\rho+\coth(3k)} \tag{5.24}$$

The surface deformation for the lower interface, ($j = 2$), is same as the upper interface, ($j = 1$), but opposite in sign, *i.e.*, $\eta_{2,3} = -\eta_{1,3}$. The third-order solution (second harmonic) is varicose in nature, as shown in Eq. (5.23), which is a direct outcome of the symmetry boundary condition. This second harmonic is different from that obtained for the fundamental sinuous mode, which is sinuous in nature, as shown in Eq. (4.27). Therefore, depending upon the initial disturbance mode, the nature of the higher harmonics will be different and its influence on the entire breakup process of the liquid sheet will be significant. It is also observed that the growth of the second harmonic is due to the complex mechanism of energy feedback from the fundamental and the first harmonic, as suggested by the terms involving $\omega_{1,v}$ and $\omega_{2,v}$ in Eq. (5.22), and also due to the inherent instability of the second harmonic itself.

Hence the final form of the surface deformation up to the first three orders for an initial varicose mode of disturbance can be obtained by using Eq. (4.29), for a given value of the initial disturbance amplitude η_0. The next section shows typical surface evolutions following Eq. (4.29).

5.2 Results and Discussions

The liquid sheet is subjected to an initial varicose mode of disturbance with a wavenumber k, which is not known and will be different from that used for the initial sinuous mode. However, as mentioned earlier, the typical value of k to be used is the dominant wavenumber for which the growth rate is maximum. Therefore it is important to observe the growth rate curves for the three different orders, as shown in Fig. 5.2, with $We = 40, \rho = 0.001$ and $U = 4$. It is found that the dominant wavenumber is 0.269 which corresponds to the maximum growth rate of the fundamental. Even though the three growth curves appear to have the same maximum growth rate, the fundamental has slightly higher growth rate compared to the first and the second harmonics. Therefore, the value of k corresponding to the maximum wave growth of the first-order (fundamental) will be used in this analysis.

Figure 5.3 shows the surface evolution at different time instants for Weber number of 40, gas-to-liquid density ratio of 0.001, gas-to-liquid velocity ratio of 4, wavenumber of 0.269 and the initial disturbance amplitude of 0.1. It is observed that the two interfaces

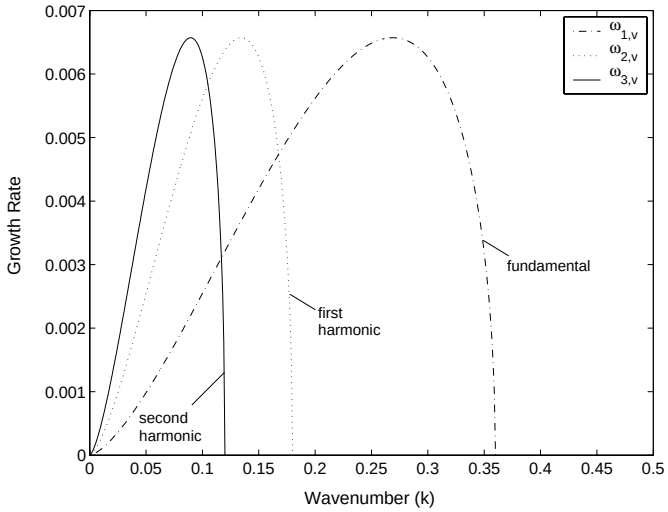

Figure 5.2: Growth rate curves as a function of wavenumber k due to an initial varicose disturbance for $We = 40, \rho = 0.001$ and $U = 4$.

grow with time, but retain the varicose nature for most of their growth time, for *e.g.*, up to $t = 300$ in this case. Nonlinear effects slowly show up at later times and eventually the sheet breaks up at full-wavelength intervals at $t = 417$, which is the typical breakup feature for an initial varicose disturbance [27, 29]. Further, in between the pinch-off points within the liquid sheet, possible 'satellite' ligament formation is observed, which is not present in the sheet breakup process for an initial sinuous mode of disturbance. Interesting enough, the wavy structures within each full-wavelength intervals correspond to the growth rate of the three orders. The possible bigger ligament formation corresponds to the fundamental whereas the other two 'satellite' ligaments belong to the first and the second harmonics. Therefore, the liquid sheet subjected to a fundamental varicose mode of disturbance shows breakup characteristics which are quite different from those observed earlier in case of a fundamental sinuous disturbance.

The effect of the fundamental, the first and the second harmonics on the surface deformation at the breakup time is shown in Fig. 5.4 for the same set of physical parameters used earlier. In the presence of the fundamental, as in Fig. 5.4a, the two liquid-gas interfaces move in symmetric manner. With addition of the first harmonic, the nonlinear

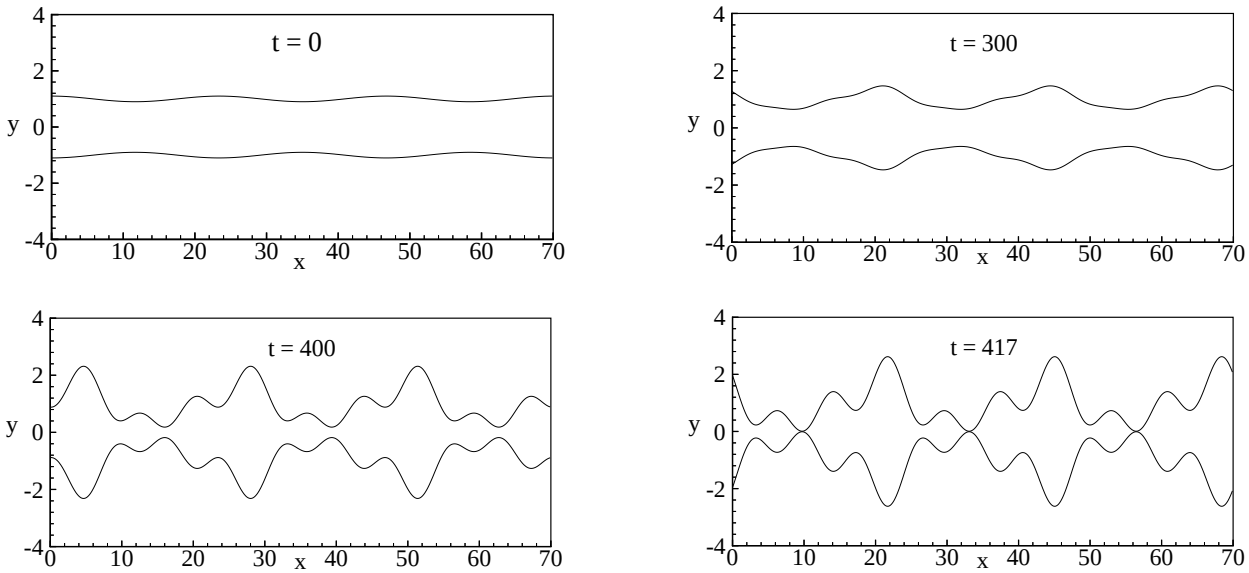

Figure 5.3: Evolution of surface deformation for $We = 40, \rho = 0.001, U = 4, k = 0.269$ and $\eta_0 = 0.1$ due to an initial varicose disturbance.

interaction between the first harmonic and the fundamental causes the two interfaces to come close to each other with the appearance of some waviness, as shown in Fig. 5.4b. When all the three orders are superimposed, as in Fig. 5.4c, the sheet breakup occurs with the formation of 'satellite' ligaments in between the breakup points. It is also important to note that the breakup time is increased compared to an initial sinuous disturbance for the same set of physical parameters, as shown in Fig. 4.3.

As mentioned earlier, one of the key parameter for modeling air-blast atomization is the relative velocity between the gas and the liquid phases. Figure 5.5 shows the effect of the velocity ratio U on the surface evolution of the two interfaces. At $U = 0$, *i.e.*, with no gas phase velocity, the breakup time is substantially long and also the 'satellite' ligaments in between the full-wavelength intervals are of comparable sizes. However, when the gas velocity on either side of the sheet is three times the liquid velocity, the breakup time decreases and the breakup characteristics also changes. The possible ligament formation

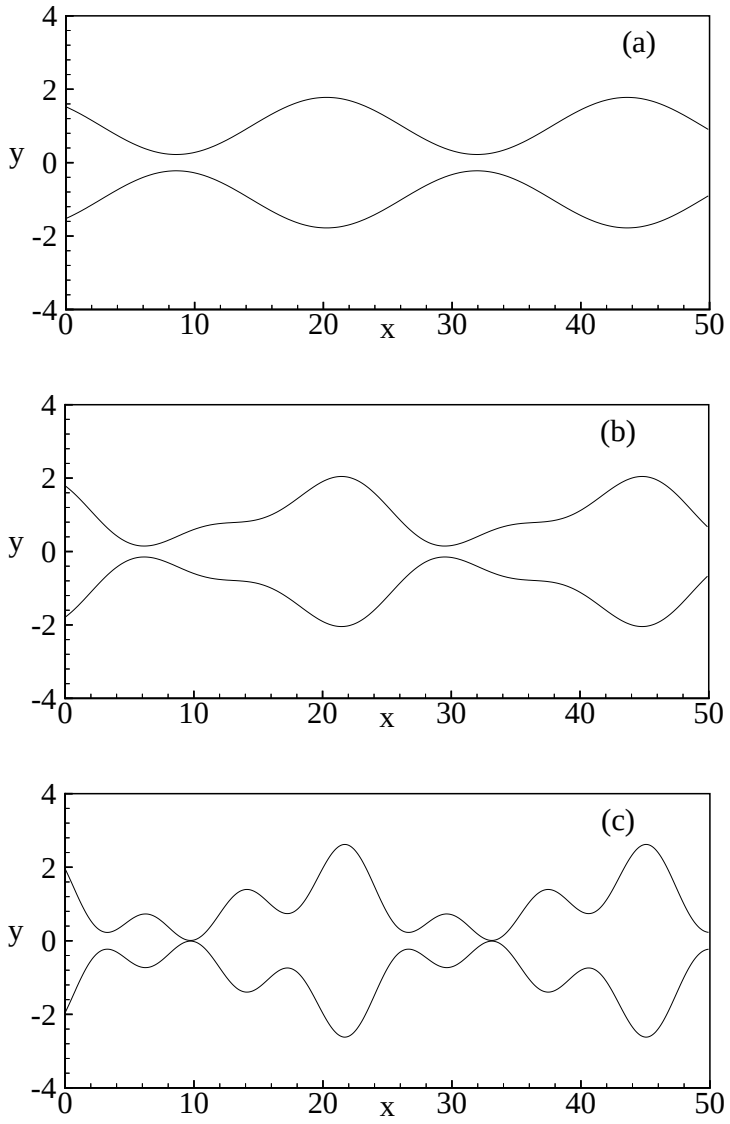

Figure 5.4: The effect of the fundamental, the first and the second harmonic on surface deformation at the breakup time $t = 417$ for $We = 40, \rho = 0.001, U = 4, k = 0.269$ and $\eta_0 = 0.1$ due to an initial varicose disturbance

due to the fundamental is bigger than that produced by the first and the second harmonics, which again switches position within the full-wavelength interval for $U = 4$, as shown earlier in Fig. 5.4. When $U = 6$, the high momentum of the gas phase tends to decrease the breakup time substantially and also the 'satellite' ligament formation tends to disappear. At the same time, with the increase in the gas velocity, the wavelength between the breakup points decreases, which intuitively tends to produce small droplets.

The effect of gas-to-liquid density ratio on the breakup characteristics of the liquid sheet is shown in Fig. 5.6. The wavenumber corresponding to the dominant wavenumber is used for each value of ρ. It is observed that as the density ratio is increased, the breakup time decreases substantially from $t = 197$ for $\rho = 0.0015$ to $t = 6.9$ for $\rho = 0.01$. It is also found that the breakup features at density ratios of 0.005 and 0.01 are similar. However, the breakup locations are still at full-wavelength intervals, which is the breakup characteristics of the varicose mode.

Instead of using the dominant wavenumber, breakup characteristics of the liquid sheet are observed for wavenumbers $k = 0.1, 0.15$ and 0.3, as shown in Fig. 5.7. It is found that for $k = 0.1$, which is unstable for all the three orders, the sizes of the possible 'satellite' ligaments are equal. Similar observation is obtained for $k = 0.15$, which is stable for the second harmonic but unstable for the first harmonic and the fundamental. The formation of 'satellite' ligaments tends to disappear for higher wavenumber, for *e.g.*, at $k = 0.3$. The breakup time also increases for the short wavelength (large wavenumber) disturbances. However, the breakup of the liquid sheet still occurs at full-wavelength intervals.

As discussed earlier, the temporal instability results presented so far can be converted into their spatial instability counterpart. Under such transformation, the breakup time is equivalent to the breakup length. Figure 5.8 shows the spatial growth of the liquid sheet for $We = 40, U = 4, \rho = 0.001, k = 0.269$ and different values of initial disturbance amplitude η_0. As expected, the breakup length decreases with the increase in the value of η_0. For small values of η_0, the surface waviness is observed only at further downstream section, whereas the large value of η_0 causes the two interfaces to show the varicose mode at much earlier part of the sheet development.

In practical applications, it is important to know the variation of the breakup length with different flow parameters and also the effect of the type of initial disturbance modes

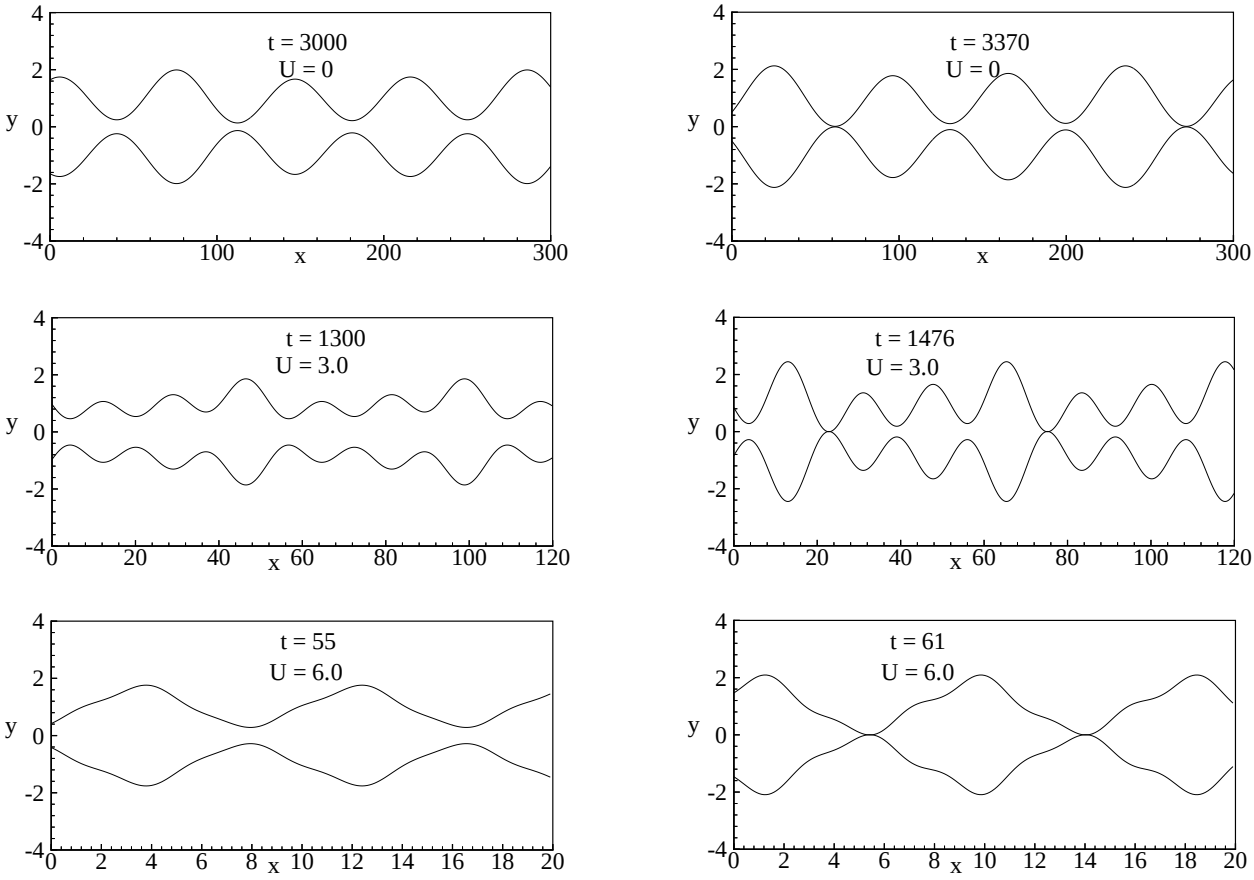

Figure 5.5: Evolution of surface deformation at different gas-to-liquid velocity ratios U for $We = 40, \rho = 0.001$ and $\eta_0 = 0.1$ due to an initial varicose disturbance.

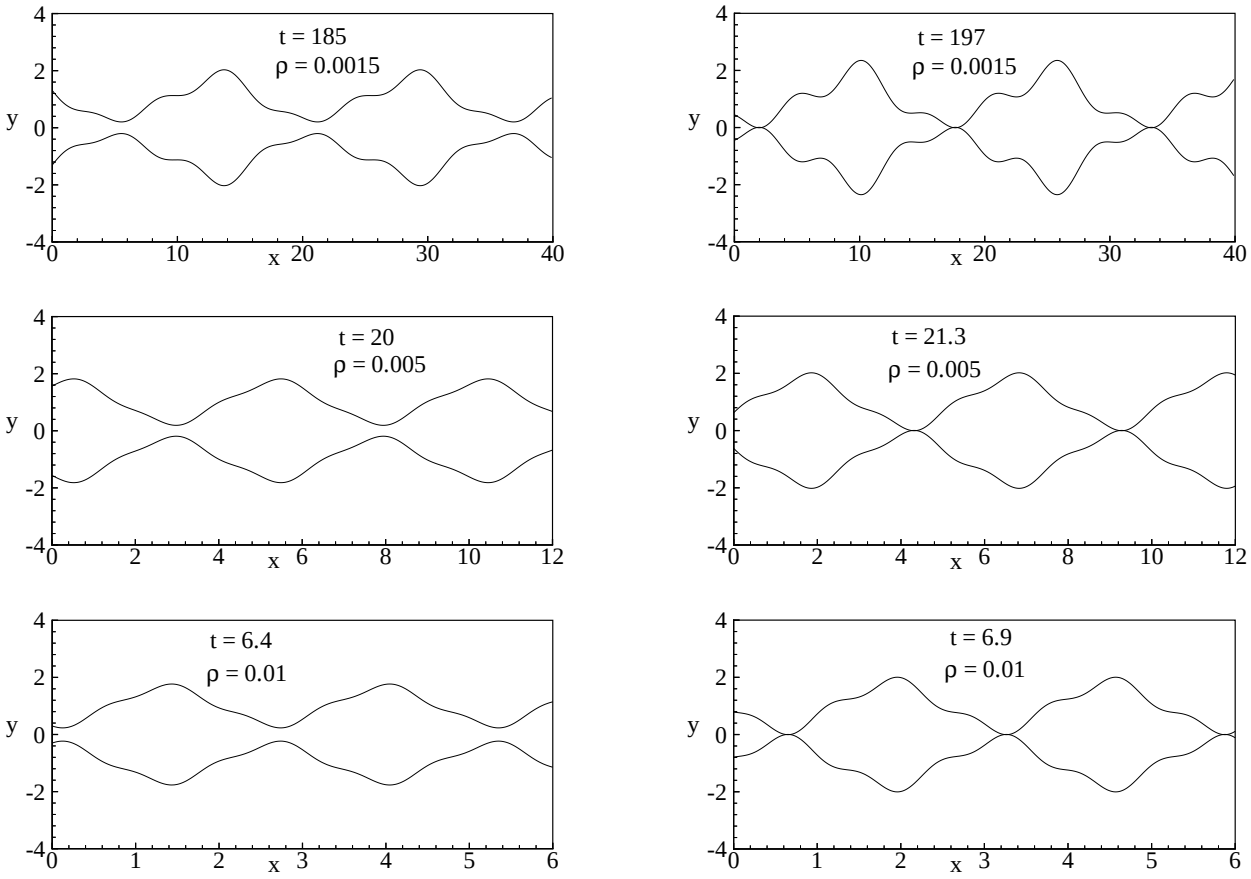

Figure 5.6: Evolution of surface deformation at different gas-to-liquid density ratios ρ for $We = 40, U = 4$ and $\eta_0 = 0.1$ due to an initial varicose disturbance.

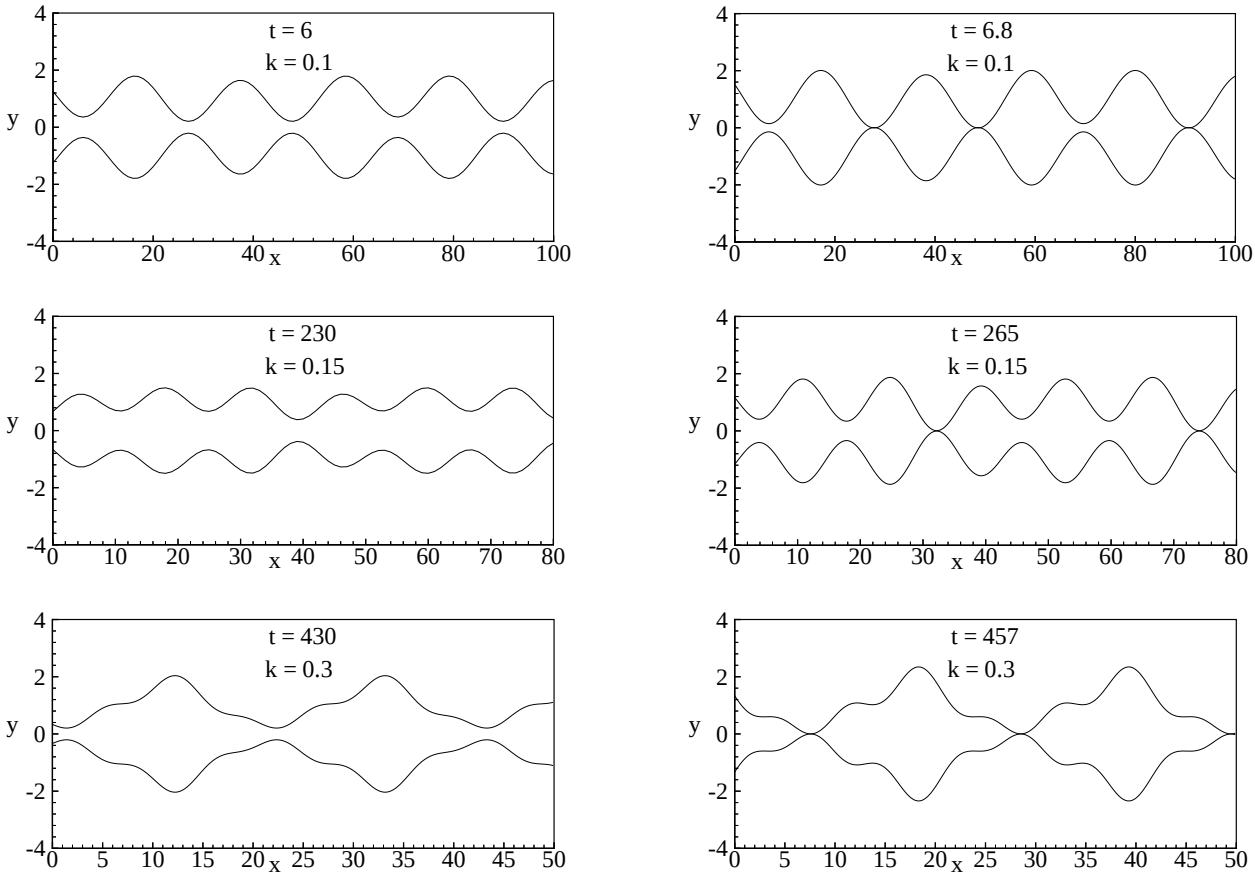

Figure 5.7: Evolution of surface deformation at different wavenumbers for $We = 40, U = 4, \rho = 0.001$ and $\eta_0 = 0.1$ due to an initial varicose disturbance.

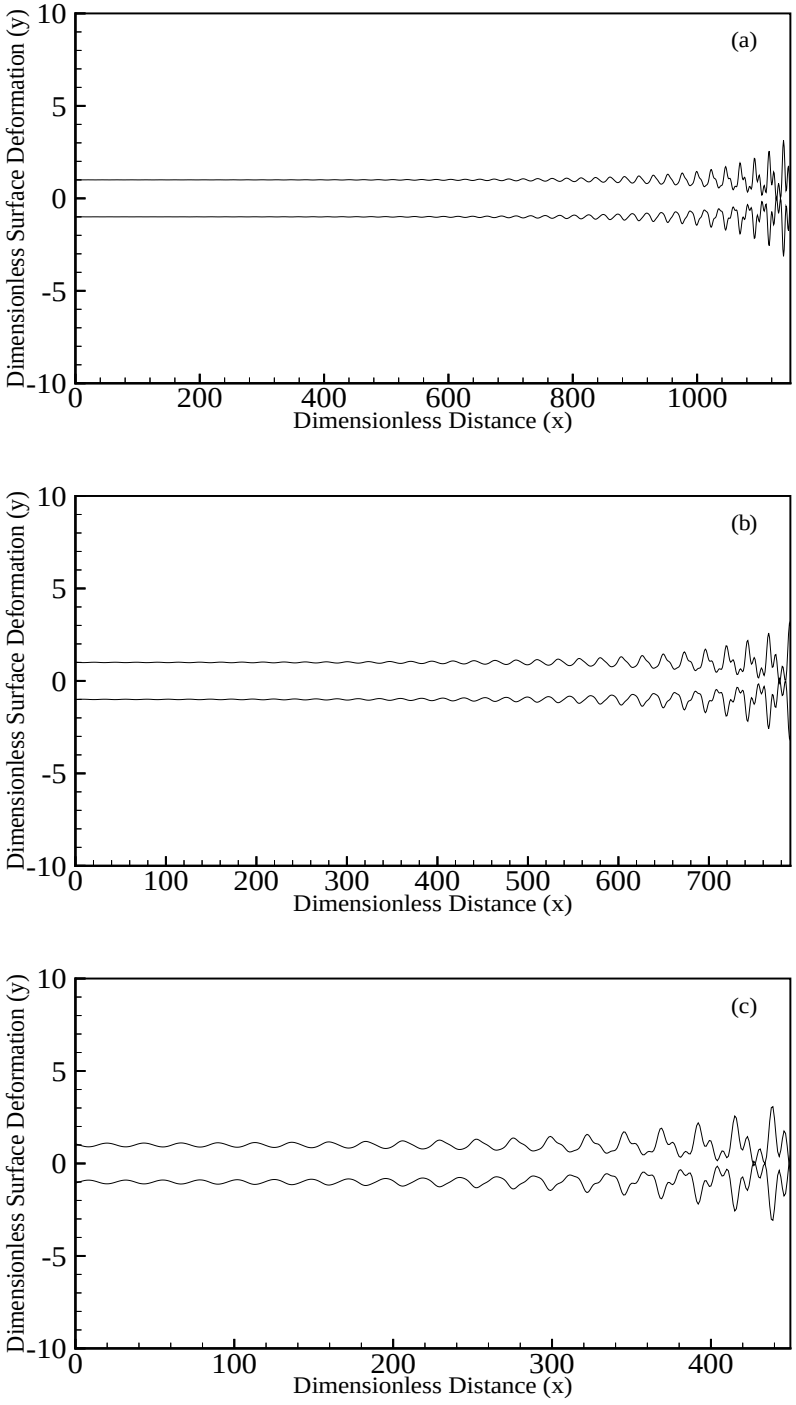

Figure 5.8: Spatial surface deformation for $We = 40, \rho = 0.001, U = 4$ and $k = 0.269$ due to an initial varicose disturbance. (a) $\eta_0 = 0.001$, (b) 0.01 and (c) 0.1.

on the breakup length of the liquid sheet. Figure 5.9 illustrates the variation of breakup length due to the initial sinuous and varicose modes as a function of Weber number at different initial disturbance amplitudes for $U = 4$ and $\rho = 0.001$. For both the modes, the breakup length first decreases rapidly with the increase in We and then it reaches an asymptotic value for large Weber numbers. This is expected as with the increase in Weber number, the aerodynamic instability of the liquid sheet increases and therefore, it results into earlier sheet breakup. It is also observed that for a particular value of η_0, there exist a critical value of Weber number at which the fundamental varicose mode takes over the breakup process from the fundamental sinuous mode. For *e.g.*, at $\eta_0 = 0.1$, the liquid sheet is found to be unstable for the fundamental sinuous mode up to $We = 142$. Thereafter, the breakup process is dominated by the fundamental varicose mode, as it causes the liquid sheet to breakup earlier than the imposed fundamental sinuous mode. However, the results of the linear instability (first-order) predict that the growth rate of the sinuous mode of disturbance increases with the increase in Weber number and it is greater than the growth rate corresponding to the varicose mode of disturbance, as shown in Fig 5.10 for $We = 100$ and 200. Therefore, it is believed that the sinuous mode, having a higher growth rate than the varicose mode, is responsible for the breakup of the liquid sheet. But the present nonlinear instability analysis shows that under certain operating conditions, the fundamental varicose mode can dictate the breakup process of the liquid sheet, even though it has a smaller growth rate than the fundamental sinuous mode. This is an important outcome of the present nonlinear analysis.

The variation of the breakup length with density ratio is shown in Figure 5.11 for different values of η_0 and for both the initial sinuous and varicose modes. It is observed that for both the modes, at first the breakup length decreases significantly with the increase in density ratio, but at higher density ratios, the change in the breakup length is very small. It is also observed that for a given value of η_0, there exists a critical value of ρ beyond which the breakup is dictated by the fundamental varicose mode rather than the sinuous counterpart. This is similar to the observation made earlier regarding Weber number and therefore it shows that the nonlinear effect due to an imposed fundamental varicose mode plays an important role in the breakup mechanism of the liquid sheet and by no means it can be ignored from the analysis.

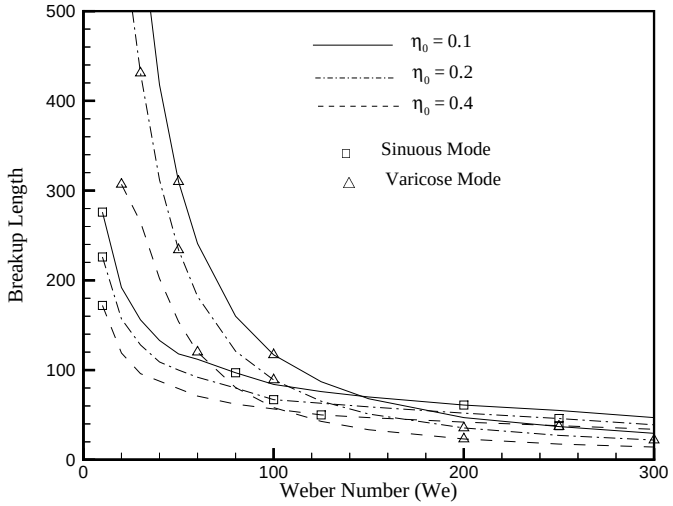

Figure 5.9: Variation of breakup length with Weber number for $U = 4, \rho = 0.001$ and different values of η_0.

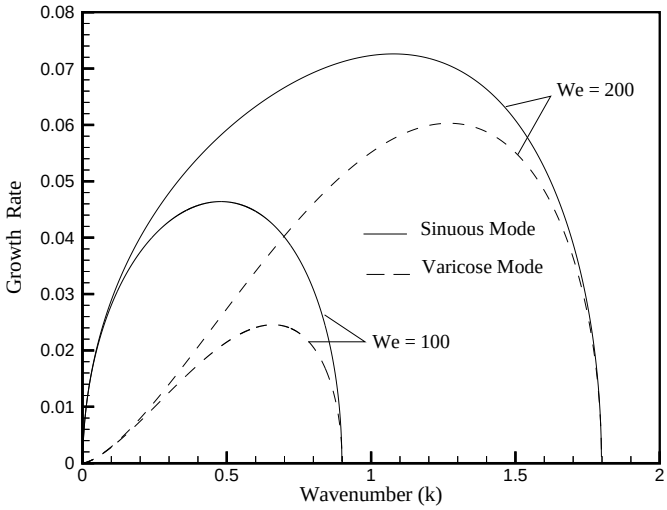

Figure 5.10: Growth rate curves of sinuous and varicose modes for $U = 4, \rho = 0.001$ and $We = 100$ and 200, respectively.

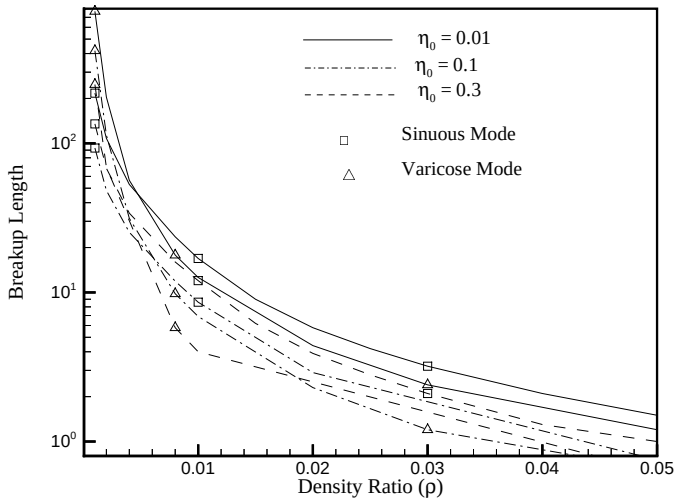

Figure 5.11: Variation of breakup length with gas-to-liquid density ratio for $We = 40, U = 4$ and different values of η_0.

As observed earlier, the gas phase velocity plays an important role in the breakup process of the liquid sheet. Figure 5.12 shows the variation of the breakup length with the gas-to-liquid velocity ratio for both the sinuous and the varicose modes and different values of initial disturbance amplitude. It is found that for both the modes, at first the breakup length decreases rapidly with the increase in the velocity ratio and later it reaches an asymptotic value for higher gas phase velocity. However, when the breakup length is plotted as a function of velocity ratio for different values of density ratio, as shown in Fig. 5.13, it is also observed that there exists a critical value of U beyond which the breakup time due to the fundamental varicose mode is shorter than the fundamental sinuous mode. This again emphasize the fact that the fundamental varicose mode indeed plays an important role in the breakup of plane liquid sheets.

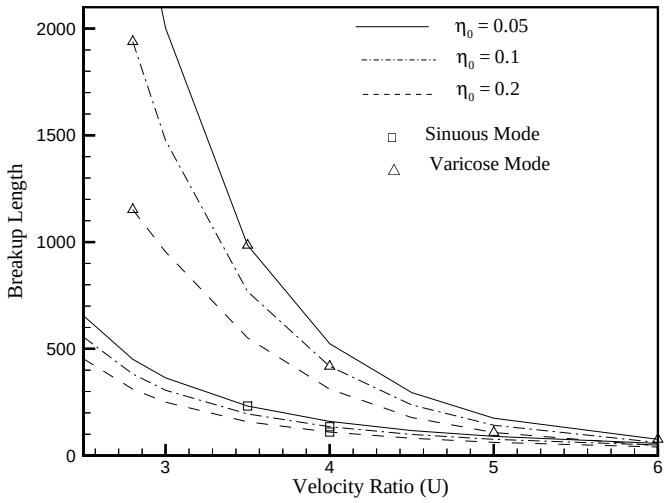

Figure 5.12: Variation of breakup length with gas-to-liquid velocity ratio for $We = 40, \rho = 0.001$ and different values of η_0.

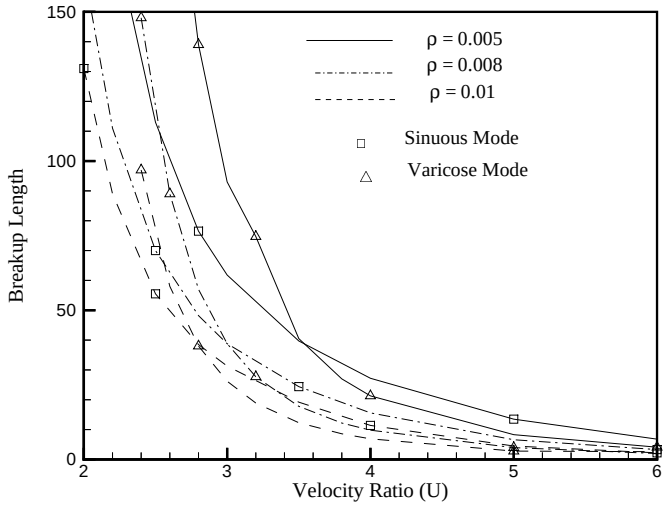

Figure 5.13: Variation of breakup length with gas-to-liquid velocity ratio for $We = 40, \eta_0 = 0.1$ and different values of ρ.

5.3 Summary

The breakup process of a plane liquid sheet subjected to an initial varicose mode of disturbance is studied here. It is found that the sheet breakup occurs at full-wavelength intervals compared to the half-wavelength intervals for an initial sinuous mode of disturbance and the possible formation of 'satellite' ligaments appears between the breakup points. In general, the breakup length (or time) decreases with the increase in Weber number, velocity and density ratios, and initial disturbance amplitude. This nonlinear analysis also shows that under certain flow conditions, the breakup process of the liquid sheet can be dictated by the fundamental varicose mode instead of the fundamental sinuous mode. This is contrary to the outcome of linear instability analysis which predicts that the sinuous mode, having a higher growth rate, always dominates the varicose mode. Therefore, both the sinuous and the varicose modes produce different characteristics during the breakup process of the liquid sheet. Hence, it is important to consider the combined effect of both the modes of disturbance in order to understand the entire breakup mechanism of the liquid sheet.

Chapter 6

Nonlinear Analysis for Combined Mode

The previous analysis of the liquid sheet subjected to an initial varicose mode of disturbance indicates that the liquid sheet breaks up at full-wavelength interval in contrast to the half-wavelength interval for an initial sinuous disturbance. Also, under certain operating conditions, the breakup process is dictated by the fundamental varicose mode rather than its sinuous counterpart. In reality, both the fundamental sinuous and varicose modes are unstable, and they grow simultaneously. Hence it is worthwhile to investigate the breakup process of plane liquid sheets under the combined influence of both the sinuous and the varicose modes (combined mode).

6.1 Solution

Figure 6.1 shows a schematic diagram of a plane liquid sheet subjected to the combined sinuous and varicose modes of disturbance with a phase angle θ between the two modes. The governing equations and the associated boundary conditions remain the same, as discussed in Chapter 3.

The initial condition for the first-order surface deformation takes into account that the two liquid-gas interfaces are initially under the combined influence of the sinuous and the

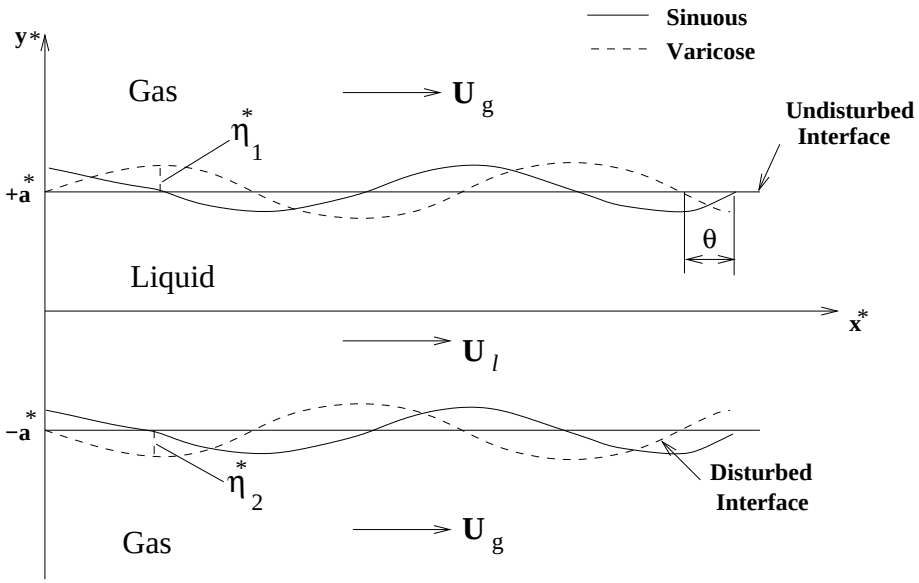

Figure 6.1: Schematic of plane liquid sheet subjected to a combined mode of disturbance.

varicose modes of disturbance. Therefore, the initial condition can be expressed as:

$$\eta_{j,1}(x,0) \;=\; \epsilon_s \cos(kx) + (-1)^{j+1}\epsilon_v \cos(kx+\theta) \tag{6.1}$$

where ϵ_s and ϵ_v are the weighting factors denoting an initial sinuous mode for $\epsilon_s = 1$ and $\epsilon_v = 0$, and an initial varicose mode for $\epsilon_s = 0$ and $\epsilon_v = 1$; k is the wavenumber of the combined mode. Seeking a wave form solution for the governing equations, Eqs. (3.11)-(3.12), the boundary conditions, Eqs. (3.13)-(3.15), and the initial condition stated in Eq. (6.1), the first-order solutions are as follows:

$$\begin{aligned}
\eta_{j,1}(x,t) \;=\;& \epsilon_s \cosh(\omega_{1,s}t)\cos(\alpha_{1,s}t+kx) + (-1)^{j+1}\epsilon_v \cosh(\omega_{1,v}t) \\
& \times \cos(\alpha_{1,v}t+kx+\theta) \qquad (6.2) \\
\phi_{l,1} \;=\;& \frac{\sinh(ky)}{k\cosh(k)}\big[\epsilon_s\omega_{1,s}\sinh(\omega_{1,s}t)\cos(\alpha_{1,s}t+kx) - \epsilon_s(\alpha_{1,s}+k)\cosh(\omega_{1,s}t) \\
& \times \sin(\alpha_{1,s}t+kx)\big] - \frac{\cosh(ky)}{k\sinh(k)}\big[\epsilon_v\omega_{1,v}\sinh(\omega_{1,v}t)\cos(\alpha_{1,v}t+kx) \\
& -\epsilon_v(\alpha_{1,v}+k)\cosh(\omega_{1,v}t)\sin(\alpha_{1,v}t+kx+\theta)\big] \qquad (6.3)
\end{aligned}$$

$$\begin{aligned}\phi_{g,1} &= (-1)^j \frac{e^{(-1)^j ky}}{ke^{-k}}\big[\big\{\epsilon_s\omega_{1,s}\sinh(\omega_{1,s}t)\cos(\alpha_{1,s}t+kx)-\epsilon_s(\alpha_{1,s}+Uk)\cosh(\omega_{1,s}t)\\ &\quad\times\sin(\alpha_{1,s}t+kx)\big\}-\big\{\epsilon_v\omega_{1,v}\sinh(\omega_{1,v}t)\cos(\alpha_{1,v}t+kx)-\epsilon_v(\alpha_{1,v}+Uk)\\ &\quad\times\cosh(\omega_{1,v}t)\sin(\alpha_{1,v}t+kx+\theta)\big\}\big] \qquad (6.4)\end{aligned}$$

Here, $\omega_{1,s}$ and $\omega_{1,v}$ represent the first-order growth rates for the sinuous and the varicose modes, respectively; and $\alpha_{1,s}$ and $\alpha_{2,s}$ are the corresponding first-order angular frequencies. The explicit forms of these parameters are already stated in Eqs. (4.3)-(4.4) and (5.6)-(5.7), respectively. It is observed that the first-order or linear instability solutions for the combined mode of disturbance are linear superposition of the solutions obtained for the individual initial sinuous and varicose modes.

To obtain the second-order solution, the surface deformation for this order can be written as:

$$\eta_{j,2}(x,t) = P_{2,c}(t)\cos(2kx) - Q_{2,c}(t)\sin(2kx) \qquad (6.5)$$

along with the initial conditions:

$$\eta_{j,2}(x,0) = 0 \quad \text{and} \quad \eta_{j,2,t}(x,0) = 0 \qquad (6.6)$$

where $P_{2,c}$ and $Q_{2,c}$ are time dependent terms to be solved. By substituting Eq. (6.5) into the kinematic boundary conditions, Eqs. (3.18)-(3.19), along with the first-order solutions, suggests the following form for the velocity potentials:

$$\begin{aligned}\phi_{l,2} &= f_{l2,c}(y)[\big\{P_{2,c,t}-2kQ_{2,s}+K_{l2,c}(t)\big\}\cos(2kx)\\ &\quad+\big\{-Q_{2,c,t}-2kP_{2,c}+L_{l2,c}(t)\big\}\sin(2kx)\big]+A_{l2,c}(t) \qquad (6.7)\\ \phi_{g,2} &= f_{g2,c}(y)\big[\big\{P_{2,c,t}-2kUQ_{2,c}+K_{g2,c}(t)\big\}\cos(2kx)\\ &\quad+\big\{-Q_{2,c,t}-2kUP_{2,c}+L_{g2,c}(t)\big\}\sin(2kx)\big]+A_{g2,c}(t) \qquad (6.8)\end{aligned}$$

where the unknown functions of y are determined by substituting the above form of the velocity potentials into the governing equations, Eqs. (3.16)-(3.17). Therefore, the liquid

and the gas velocity potentials are obtained in the following form:

$$\begin{aligned}
\phi_{l,2} &= \frac{\cosh(2ky)}{2k\sinh(2k)}\big[\big\{P_{2,c,t} - 2kQ_{2,c} + K_{l2,c}(t)\big\}\cos(2kx) \\
&\quad + \big\{-Q_{2,c,t} - 2kP_{2,c} + L_{l2,c}(t)\big\}\sin(2kx)\big] + A_{l2,c}(t) \qquad (6.9) \\
\phi_{g,2} &= -\frac{e^{-2ky}}{2ke^{-2k}}\big[\big\{P_{2,c,t} - 2kUQ_{2,c} + K_{g2,c}(t)\big\}\cos(2kx) \\
&\quad + \big\{-Q_{2,c,t} - 2kUP_{2,c} + L_{g2,c}(t)\big\}\sin(2kx)\big] + A_{g2,c}(t) \quad \text{for } y \geqslant 1 \qquad (6.10) \\
&= \frac{e^{2ky}}{2ke^{-2k}}\big[\big\{P_{2,c,t} - 2kUQ_{2,c} - K_{g2,c}(t)\big\}\cos(2kx) \\
&\quad + \big\{-Q_{2,c,t} - 2kUP_{2,c} - L_{g2,c}(t)\big\}\sin(2kx)\big] + A_{g2,c}(t) \quad \text{for } y \leqslant -1 \qquad (6.11)
\end{aligned}$$

Substitution of the above velocity potentials into the dynamic boundary condition, Eq. (3.20), and the initial conditions, Eq. (6.6), yields the time dependent terms. After a considerable amount of mathematical simplification, the following solution for the second-order surface deformation is obtained:

$$\begin{aligned}
\eta_{j,2}(x,t) &= (-1)^{j+1}\big[A_{2,c}\cosh(\omega_{2,c}t)\cos(2\alpha_{2,c}t + 2kx) + B_{2,c}\cosh[(\omega_{1,s} + \omega_{1,v})t] \\
&\quad \times \cos(\alpha_{1,s}t + \alpha_{1,v}t + \theta + 2kx) + C_{2,c}\cosh[(\omega_{1,s} - \omega_{1,v})t] \\
&\quad \times \cos(\alpha_{1,s}t + \alpha_{1,v}t + \theta + 2kx) + D_{2,c}\cosh(2\omega_{1,v}t)\cos(2\alpha_{1,v}t + 2\theta + 2kx) \\
&\quad + E_{2,c}\sinh(2\omega_{1,v}t)\sin(2\alpha_{1,v}t + 2\theta - 2kx) + F_{2,c}\cosh(2\omega_{1,s}t)\cos(2\alpha_{1,s}t + 2kx) \\
&\quad + G_{2,c}\cos(2\alpha_{1,v}t + 2\theta + 2kx) + H_{2,c}\cos(2\alpha_{1,s}t + 2kx)\big] \qquad (6.12)
\end{aligned}$$

where $\omega_{2,c} = \omega_{2,s} = \omega_{2,v}$ is the growth rate and $\alpha_{2,c} = \alpha_{2,s} = \alpha_{2,v}$ is the corresponding angular frequency for the second-order; and the constants, $A_{2,c}, \cdots H_{2,c}$, are provided in Appendix C.1. Important observations for the second-order solution are as follows:

(1) The second-order growth rate for the combined mode is varicose in nature and it is same as that obtained for an initial sinuous and varicose modes of disturbance.

(2) The constants, $B_{2,c}$ and $C_{2,c}$, involve terms containing $\epsilon_s\epsilon_v$, which suggests a coupling effect between the sinuous and the varicose modes.

(3) The growth of the second-order (first harmonic) is due to the feedback of energy from the fundamental sinuous and varicose modes, and the inherent instability of the first harmonic of the combined mode.

In order to obtain the third-order surface deformation solution for the combined mode, difficulties are encountered since the third-order growth rates for the individual sinuous and varicose modes are different, as stated in Eqs. (4.27) and (5.23). This is not the case for the second-order, as the growth rates for both the modes are varicose in nature. Therefore, in order to overcome such difficulties, the third-order surface deformation needs to be expressed in the following form:

$$\begin{aligned}\eta_{j,3}(x,t) &= P_{3,c,s}(t)\cos(3kx) - Q_{3,c,s}(t)\sin(3kx) \\ &\quad +(-1)^{j+1}\big[P_{3,c,v}(t)\cos(3kx) - Q_{3,c,v}(t)\sin(3kx)\big] \end{aligned} \tag{6.13}$$

It is to be noted that by assuming such form of the surface deformation, the sinuous and the varicose modes are not decoupled. During the process of the solution, it will be shown that the time dependent quantities, $P_{3,c,s}, Q_{3,c,s}, P_{3,c,v}$ and $Q_{3,c,v}$, involve terms containing $\epsilon_s^2\epsilon_v$ and $\epsilon_s\epsilon_v^2$ and hence, the nonlinear coupling between the two modes is always present. The initial conditions remain the same as before, and can be expressed as:

$$\eta_{j,3}(x,0) = 0 \quad \text{and} \quad \eta_{j,3,t}(x,0) = 0 \tag{6.14}$$

Substituting Eq. (6.13) into the kinematic boundary conditions, Eqs. (3.23)-(3.24), provides the form for the velocity potentials of the liquid and the gas phases in terms of unknown functions of y. The unknown functions are obtained by substituting the velocity potentials into the governing equations, Eqs. (3.21)-(3.22), and the velocity potentials for the liquid and the gas phases can be expressed as:

$$\begin{aligned}\phi_{l,3} &= \frac{\sinh(3ky)}{3k\cosh(3k)}\big[\big\{P_{3,c,s,t} - 3kQ_{3,c,s} + K_{l3,c,s}(t)\big\}\cos(3kx) + \big\{-Q_{3,c,s,t} - 3kP_{3,c,s} \\ &\quad +L_{l3,c,s}(t)\big\}\sin(3kx)\big] + \frac{\sinh(ky)}{k\cosh(k)}\big[G_{l1,c,s}(t)\cos(kx) + H_{l1,c,s}(t)\sin(kx)\big] \\ &\quad +\frac{\cosh(3ky)}{3k\sinh(3k)}\big[\big\{P_{3,c,v,t} - 3kQ_{3,c,v} + K_{l3,c,v}(t)\big\}\cos(3kx) + \big\{-Q_{3,c,v,t} - 3kP_{3,c,v} \\ &\quad +L_{l3,c,v}(t)\big\}\sin(3kx)\big] + \frac{\cosh(ky)}{k\sinh(k)}\big[G_{l1,c,v}\cos(kx) + H_{l1,c,v}\sin(kx)\big] \\ &\quad +B_{l3,c}(t) \end{aligned} \tag{6.15}$$

$$
\begin{aligned}
\phi_{g,3} &= -\frac{e^{-3ky}}{3ke^{-3k}}\big[\big\{P_{3,c,s,t} - 3kUQ_{3,c,s} + K_{g3,c,s}(t)\big\}\cos(3kx) + \big\{-Q_{3,c,s,t} - 3kUP_{3,c,s} \\
&\quad + L_{g3,c,s}(t)\big\}\sin(3kx)\big] - \frac{e^{-ky}}{ke^{-k}}\big[G_{g1,c,s}(t)\cos(kx) + H_{g1,c,s}(t)\sin(kx)\big] \\
&\quad -\frac{e^{-3ky}}{3ke^{-3k}}\big[\big\{P_{3,c,v,t} - 3kUQ_{3,c,v} + K_{g3,c,v}(t)\big\}\cos(3kx) + \big\{-Q_{3,c,v,t} - 3kUP_{3,c,v} \\
&\quad + L_{g3,c,v}(t)\big\}\sin(3kx)\big] - \frac{e^{-ky}}{ke^{-k}}\big[G_{g1,c,v}(t)\cos(kx) \\
&\quad + H_{g1,c,v}(t)\sin(kx)\big] + B_{g3,c}(t) \quad \text{for } y \geqslant 1 \qquad (6.16) \\
&= \frac{e^{3ky}}{3ke^{-3k}}\big[\big\{P_{3,c,s,t} - 3kUQ_{3,c,s} - K_{g3,c,s}(t)\big\}\cos(3kx) + \big\{-Q_{3,c,s,t} - 3kUP_{3,c,s} \\
&\quad - L_{g3,c,s}(t)\big\}\sin(3kx)\big] + \frac{e^{-ky}}{ke^{-k}}\big[G_{g1,c,s}(t)\cos(kx) + H_{g1,c,s}(t)\sin(kx)\big] \\
&\quad + \frac{e^{3ky}}{3ke^{-3k}}\big[\big\{P_{3,c,v,t} - 3kUQ_{3,c,v} - K_{g3,c,v}(t)\big\}\cos(3kx) + \big\{-Q_{3,c,v,t} - 3kUP_{3,c,v} \\
&\quad - L_{g3,c,v}(t)\big\}\sin(3kx)\big] + \frac{e^{-ky}}{ke^{-k}}\big[G_{g1,c,v}(t)\cos(kx) \\
&\quad + H_{g1,c,v}(t)\sin(kx)\big] + B_{g3,c}(t) \quad \text{for } y \leqslant -1 \qquad (6.17)
\end{aligned}
$$

Substitution of the above velocity potentials into the dynamic boundary condition, Eq. (3.25), and the initial conditions, Eq. (6.14), yields the unknown functions of time. The terms containing $\epsilon_s^2\epsilon_v$ and ϵ_s^3 are collected together to obtain the solutions for $P_{3,c,s}$ and $Q_{3,c,s}$; the terms with $\epsilon_s\epsilon_v^2$ and ϵ_v^3 are grouped together to obtain the solutions for $P_{3,c,v}$ and $Q_{3,c,v}$. After tedious mathematical simplifications, the surface deformation for the third-order takes the following form:

$$
\begin{aligned}
&\eta_{j,3}(x,t) = A_{3,c,s}\cosh(\omega_{3,s}t)\cos(\alpha_{3,s} + 3kx) + B_{3,c,s}\cosh(\omega_{1,s}t + \omega_{2,s}t) \\
&\times\cos(\alpha_{1,s}t + \alpha_{2,s}t + \theta + 3kx) + C_{3,c,s}\cosh(\omega_{1,s}t - \omega_{2,s}t)\cos(\alpha_{1,s}t + \alpha_{2,s}t + \theta + 3kx) \\
&+D_{3,c,s}\cosh(3\omega_{1,s}t)\cos(3\alpha_{1,s}t + 3kx) + E_{3,c,s}\cosh(\omega_{1,s}t)\cos(3\alpha_{1,s}t + 3kx) \\
&+F_{3,c,s}\cosh(2\omega_{1,s}t + \omega_{1,v}t)\cos(2\alpha_{1,s}t + \alpha_{1,v}t + 2\theta + 3kx) + G_{3,c,s}\cosh(2\omega_{1,s}t - \omega_{1,v}t) \\
&\times\cos(2\alpha_{1,s}t + \alpha_{1,v}t + 2\theta + 3kx) + (-1)^{j+1}[A_{3,c,v}\cosh(\omega_{3,v}t)\cos(\alpha_{3,v} + 3kx) \\
&+B_{3,c,v}\cosh(\omega_{1,v}t + \omega_{2,v}t)\cos(\alpha_{1,v}t + \alpha_2 t + \theta + 3kx) + C_{3,c,v}\sinh(\omega_{1,v}t + \omega_2 t) \\
&\times\sin(\alpha_{1,v}t + \alpha_{2,v}t + \theta - 3kx) + D_{3,c,v}\cosh(3\omega_{1,v}t)\cos(\alpha_{1,v}t + 3\theta + 3kx) \\
&+E_{3,c,v}\sinh(3\omega_{1,v}t)\sin(\alpha_{1,v}t + 3\theta - 3kx) + F_{3,c,v}\cosh(\omega_{1,v}t)\cos(3\alpha_{1,v}t + 3\theta + 3kx)
\end{aligned}
$$

$$+G_{3,c,v}\sinh(\omega_{1,v}t)\sin(3\alpha_{1,v}t+3\theta-3kx)+H_{3,c,v}\cosh(2\omega_{1,v}t+\omega_{1,s}t)$$
$$\times\cos(2\alpha_{1,v}t+\alpha_{1,s}t+2\theta+3kx)+I_{3,c,v}\cosh(2\omega_{1,v}t-\omega_{1,s}t)$$
$$\times\cos(2\alpha_{1,v}t+\alpha_{1,s}t+2\theta+3kx)] \tag{6.18}$$

where the constants, $A_{3,c,s},\cdots I_{3,c,v}$, are provided in Appendix C.2. It is observed that the growth of the two liquid-gas interfaces is due to the energy feedback from the fundamental and the first harmonic sinuous and varicose modes, and the inherent instability of the second harmonic sinuous and varicose modes. It is also found that certain terms in Eq. (6.18) involve nonlinear coupling between the two modes of disturbance.

6.2 Results and Discussions

Previous analyses show that in order to obtain the breakup of the liquid sheet, higher order solutions are needed. However, when the two liquid-gas interfaces are subjected to an initial combined mode of disturbance, the breakup of the liquid sheet can be obtained by the first-order or linear instability solution. The application of the linear theory to predict the sheet breakup, as studied by Mitra et al. [87, 88], is instructive only because the breakup phenomena are inherently nonlinear. Therefore, only results for the nonlinear analysis will be discussed here.

Figure 6.2 shows a typical interface evolution for the liquid sheet subjected to the combined mode of disturbance. The physical parameters used are $We = 50, \rho = 0.001, U = 4.0$ and $\eta_0 = 0.1$. The proportions of the initial sinuous and varicose modes are $\epsilon_s = 0.1$ and $\epsilon_v = 0.9$, respectively and it is assumed that there is no phase difference between the two modes, *i.e.*, $\theta = 0$. Since both the sinuous and the varicose modes are present at the two liquid-gas interfaces, the characteristic wavenumber can correspond to the dominant wavenumber of the either modes. As a first step, the liquid sheet breakup features are studied for the wavenumber corresponding to the dominant wavenumber for the sinuous mode of disturbance. Hence, in Fig. 6.2, $k = 0.229(\lambda = 27.4)$ corresponds to the dominant wavenumber for the sinuous mode. As the proportion of the varicose mode within the initial combined mode is large, the two liquid-gas interfaces appear to be in varicose mode for early times ($t = 10$). However, the presence of a small proportion of sinuous mode with

a higher growth rate than the varicose counterpart, slowly tends to override the varicose mode. Such phenomenon is observed at $t = 160$ when the two interfaces are moving parallel to each other and at a constant distant apart. The initial varicose mode, present in large proportion, also grows with time and makes its presence known by pulling the two interfaces close together. Eventually, at $t = 197$, the sheet breaks up at full-wavelength intervals, which is the characteristic breakup feature for the liquid sheet subjected to the varicose mode of disturbance only. It is also observed that the breakup time is significantly long for $We = 50$, which is consistent with the earlier observation shown in Fig. 5.9. Such long breakup time also provides the opportunity for both the modes to interact and produce interesting breakup features, as observed here.

The breakup features change quite significantly at large Weber numbers, for *e.g.*, at $We = 150$, as shown in Fig. 6.3. The other physical parameters remain the same with the exception of the wavenumber k, which is equal to $0.764(\lambda = 8.2)$ for $We = 150$. It is observed earlier in Fig. 5.9 that at large Weber numbers, the breakup of the liquid sheet is dictated by the varicose mode rather than the sinuous counterpart. This becomes more obvious in Fig. 6.3, where the large proportion of the varicose mode significantly reduces the breakup time to $t = 81$ compared to $t = 197$ for $We = 50$ in Fig. 6.2. It is also observed that the two interfaces appear to be in varicose mode for most of the time. The sheet breakup also occur at full-wavelength interval, which is the characteristics of the varicose mode. This suggests that for small breakup time coupled with large proportion of the varicose mode, the entire breakup process of the liquid sheet is dominated by the varicose mode.

More interesting breakup characteristics are observed in Fig. 6.4 where the proportion of the sinuous and the varicose modes are switched, keeping other parameters the same as in Fig. 6.3. Here, due to the presence of 90% sinuous mode, the two interfaces remain at constant distance apart for the majority of time. The sheet thinning starts at about $t = 70$ when the varicose mode with small proportion (10%), pulls the two interfaces close together and eventually the sheet breaks up at full-wavelength interval at $t = 76$. It is observed that the large proportion of the sinuous mode tends to cause the sheet thinning at half-wavelength intervals, which is the characteristic breakup feature due to the sinuous mode of disturbance only. It is also found that the sheet amplitude at the breakup is almost

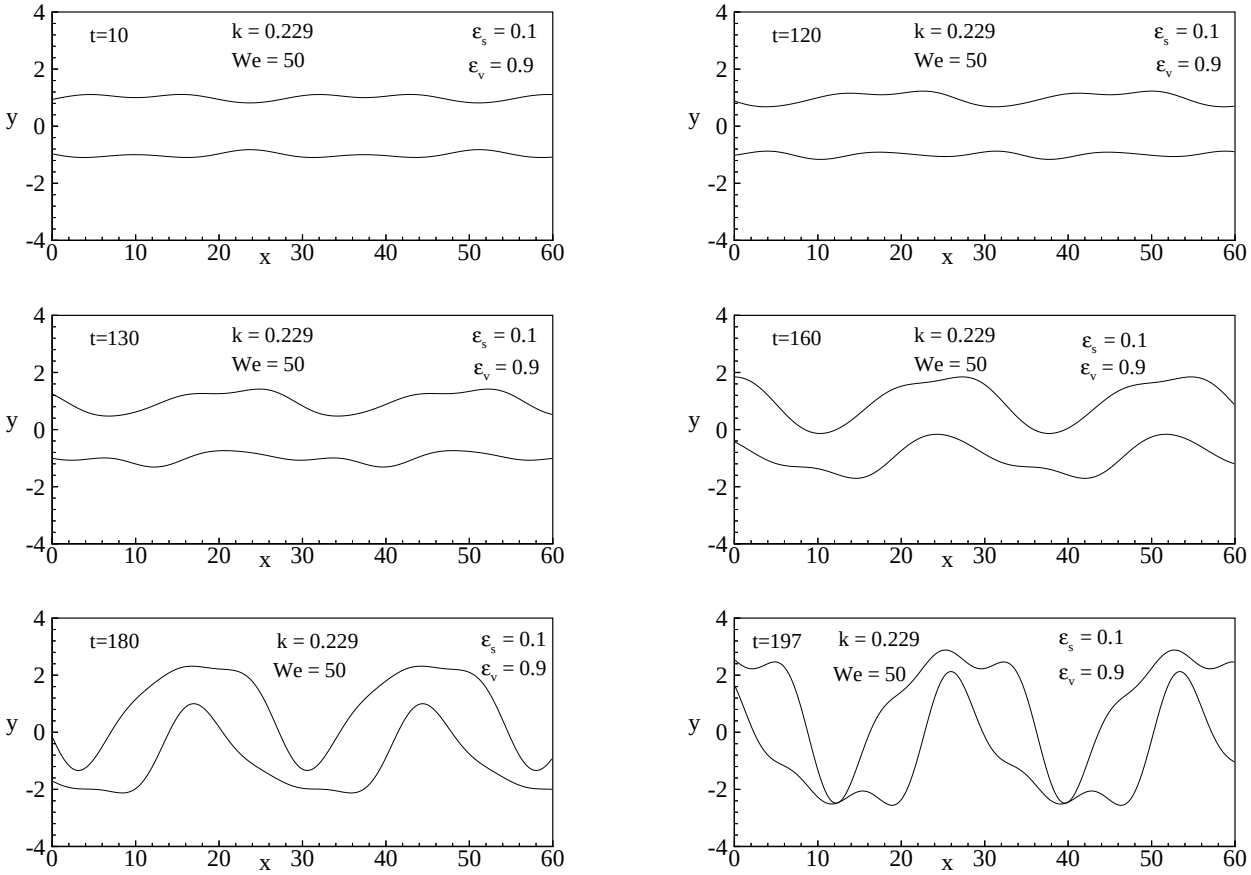

Figure 6.2: Evolution of surface deformation for $We = 50, U = 4, \rho = 0.001, k = 0.229, \theta = 0, \epsilon_s = 0.1, \epsilon_v = 0.9$ and $\eta_0 = 0.1$ due to an initial combined mode of disturbance.

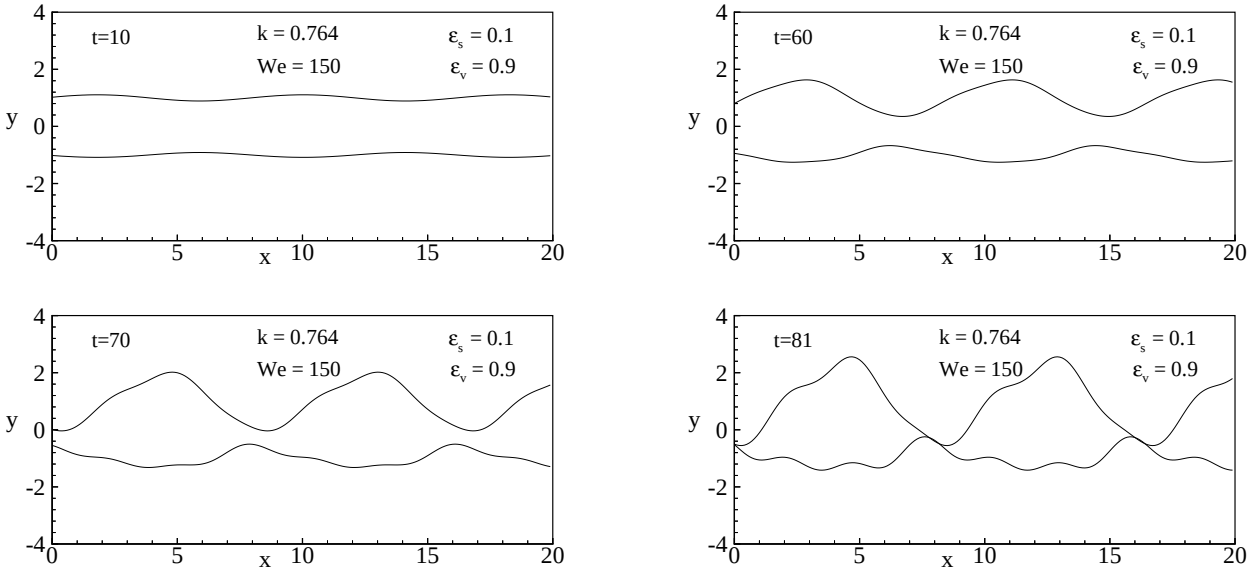

Figure 6.3: Evolution of surface deformation for $We = 150, U = 4, \rho = 0.001, k = 0.764, \theta = 0, \epsilon_s = 0.1, \epsilon_v = 0.9$ and $\eta_0 = 0.1$ due to an initial combined mode of disturbance.

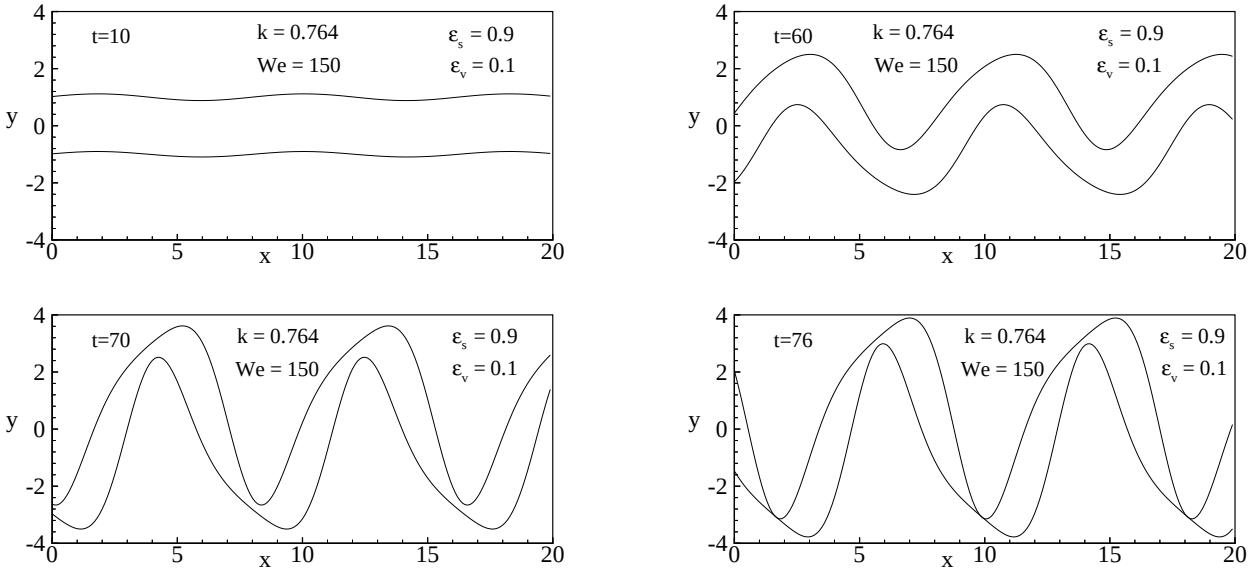

Figure 6.4: Evolution of surface deformation for $We = 150, U = 4, \rho = 0.001, k = 0.764, \theta = 0, \epsilon_s = 0.9, \epsilon_v = 0.1$ and $\eta_0 = 0.1$ due to an initial combined mode of disturbance.

double compared to that observed in Fig. 6.2, which clearly reflects the higher growth rate of the large proportion of the sinuous mode. Even though the proportion of varicose mode is much smaller than the sinuous mode, still the sheet breaks up at full-wavelength interval, demonstrating the dominance of the varicose mode at large Weber numbers.

However, for relatively small Weber numbers along with large proportion of the sinuous mode, the breakup features are quite different from that observed in Fig. 6.4. Figure 6.5 shows the surface evolution for $We = 50$, with other parameters remaining the same as before. It is observed that due to the presence of 90% sinuous mode, the two interfaces appear to move parallel to each other for most of the time and eventually the sheet breaks up at $t = 134$ due to the nonlinear interactions between the two modes. It is found that the breakup location occurs at half-wavelength interval, which is the characteristic breakup of the liquid sheet due to the sinuous mode only. This is consistent with the fact that at small Weber numbers, the breakup is dominated by the sinuous mode of disturbance. However, earlier observation of breakup locations at full-wavelength intervals in Fig. 6.2 for $We = 50$

might be due to the presence of the large proportion of the varicose mode in the initial combined mode of disturbance. Therefore, the operating Weber number along with the proportions of the two modes play significant roles in the breakup locations of the plane liquid sheet.

So far, the wavenumber used to obtain the surface evolution is the dominant wavenumber for the sinuous mode of disturbance. As mentioned earlier, the wavenumber can correspond to the dominant wavenumber for the varicose mode. Therefore, in Fig. 6.6, the breakup characteristics of the liquid sheet are observed for wavenumbers corresponding to the dominant wavenumber of the varicose mode. In Fig. 6.6a for $We = 50$, the breakup time is long ($t = 149$) and the interface deformation is different from those observed in Fig. 6.5. Here, the presence of the dominant wavenumber corresponding to the varicose mode causes the breakup to occur at full-wavelength interval as opposed to the half-wavelength interval in Fig. 6.5; the large proportion of the sinuous mode (90%) causes the sheet thinning at half-wavelength intervals. By switching the strength of the two modes, as in Fig. 6.6b, the breakup features change quite significantly and also they are different from those observed for the dominant wavenumber of the sinuous mode in Fig. 6.2. However, for $We = 150$ in Fig. 6.6c, it is observed that the interfaces at the breakup time are wavy in appearance with increased sheet amplitudes. The breakup locations are still at full-wavelength intervals with considerable amounts of sheet thinning at half-wavelength intervals. When the proportions of the two modes are switched for $We = 150$, as shown in Fig. 6.6d, the breakup features are quite similar to those observed in Fig. 6.3. These interesting characteristics of the liquid sheet clearly suggest that the disturbance wavenumber and the individual proportion of the two modes play important role in the entire breakup mechanism of the liquid sheet.

Figure 6.7 shows the effect of the initial strength of the two modes of disturbance, where the proportion of the individual sinuous and varicose modes are varied from 25% to 75% and each case is observed for the wavenumbers that correspond to the dominant wavenumbers for the sinuous and the varicose modes, respectively. It is found that for the dominant wavenumber of the sinuous mode ($k = 0.229$), the breakup time decreases with the increase in the proportion of the sinuous mode, keeping in mind that the breakup process is dominated by the sinuous mode of disturbance at relatively small Weber numbers,

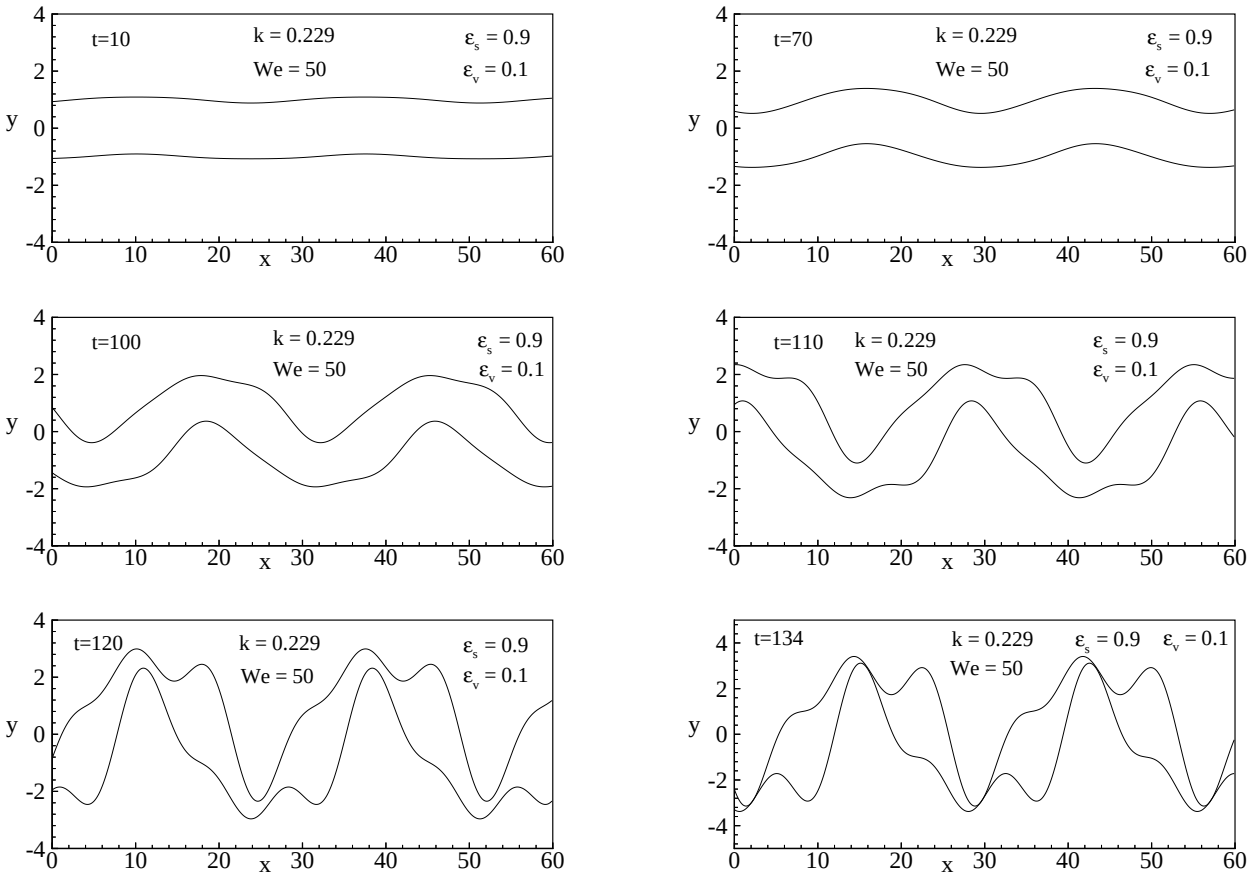

Figure 6.5: Evolution of surface deformation for $We = 50, U = 4, \rho = 0.001, k = 0.229, \theta = 0, \epsilon_s = 0.9, \epsilon_v = 0.1$ and $\eta_0 = 0.1$ due to an initial combined mode of disturbance.

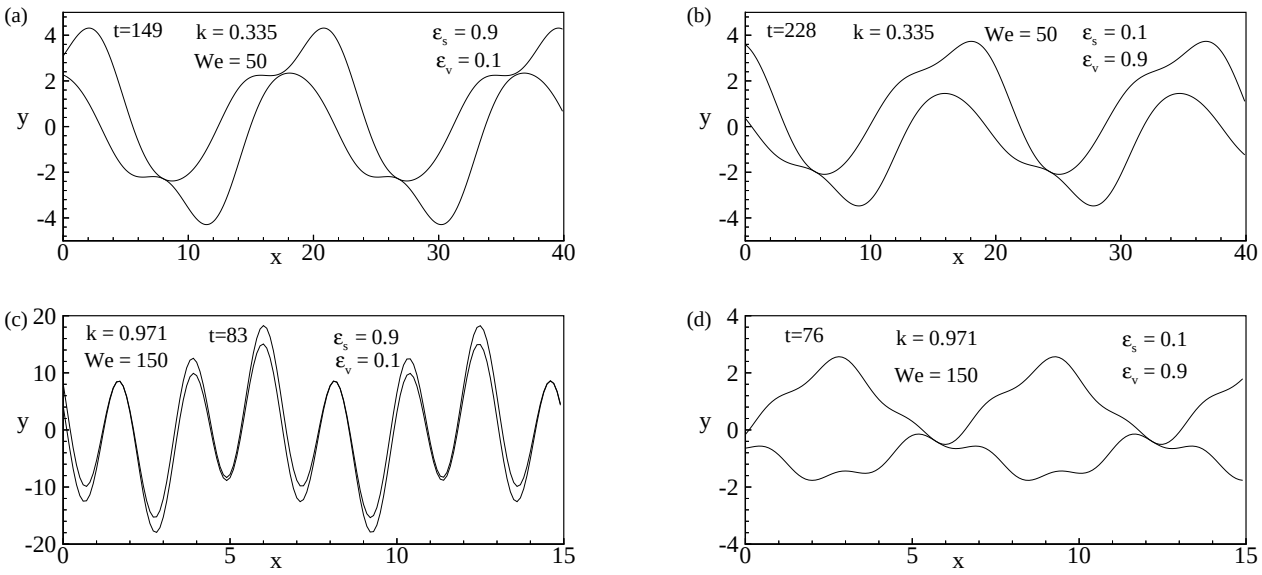

Figure 6.6: Surface deformation at breakup time for $U = 4, \rho = 0.001, \theta = 0$ and $\eta_0 = 0.1$ due to an initial combined mode of disturbance. (a) & (b) $We = 50$ and $k = 0.335$; (c) & (d) $We = 150$ and $k = 0.971$.

as in this case. The liquid sheet breaks up at full-wavelength interval for $\epsilon_s = 0.25$ and $\epsilon_v = 0.75$, but the sheet thinning at half-wavelength interval becomes more prominent with the increase in the proportion of the sinuous mode and eventually the sheet breaks up at half-wavelength interval, as shown in Fig. 6.5 for $\epsilon_s = 0.9$ and $\epsilon_v = 0.1$. For the dominant wavenumber corresponding to the varicose mode ($k = 0.335$), it is observed that the breakup time also decreases with the increase in the proportion of the sinuous mode along with visible sheet thinning at half-wavelength intervals. However, for large Weber numbers, it is found that the breakup time changes by a small magnitude when the proportion of the two modes are varied. This is evident in Figs. 6.6c and 6.6d, where the breakup time is increased by only 8% with the increase in the proportion of the sinuous mode of disturbance from 10% to 90%.

In order to obtain a more meaningful representation of the breakup process of the liquid sheet, the temporal instability results, discussed so far, can be converted to their spatial counterpart by using Gaster's transformation [15]. Under such transformation, the breakup time becomes the breakup length (L_b). Figure 6.8 shows spatial deformation of the two liquid-gas interfaces for $We = 50$ and at wavenumbers corresponding to the dominant wavenumber for the sinuous ($k = 0.229$) and the varicose ($k = 0.335$) modes. The proportions of the two modes are switched between 10% and 90%. It is observed that the profile of the interfaces is distinctly different under each specified condition and is consistent with the observations made earlier. Similar spatial developments of the interfaces are observed in Fig. 6.9 for $We = 150$ and at wavenumbers corresponding to the dominant wavenumber for the sinuous ($k = 0.764$) and the varicose ($k = 0.971$) modes.

The effect of the gas-to-liquid density ratio on the breakup characteristics of the liquid sheet is shown in Fig. 6.10. The wavenumber $k = 0.479(\lambda = 13.1)$ in Fig. 6.10a corresponds to the dominant wavenumber for the sinuous mode. At low density ratios, for *e.g.*, at $\rho = 0.002$, the two liquid-gas interfaces remain almost parallel for most of the time and the sheet breaks up at full-wavelength intervals. The breakup features are quite comparable with those observed for $\rho = 0.001$ in Fig. 6.7b, but the breakup time for $\rho = 0.002$ is substantially smaller ($t = 75$). However, at high density ratios, for *e.g.*, at $\rho = 0.006$, the growth rates of the fundamental sinuous and varicose modes are almost the same, which result in the enhancement of one interface and the attenuation of the other interface. This

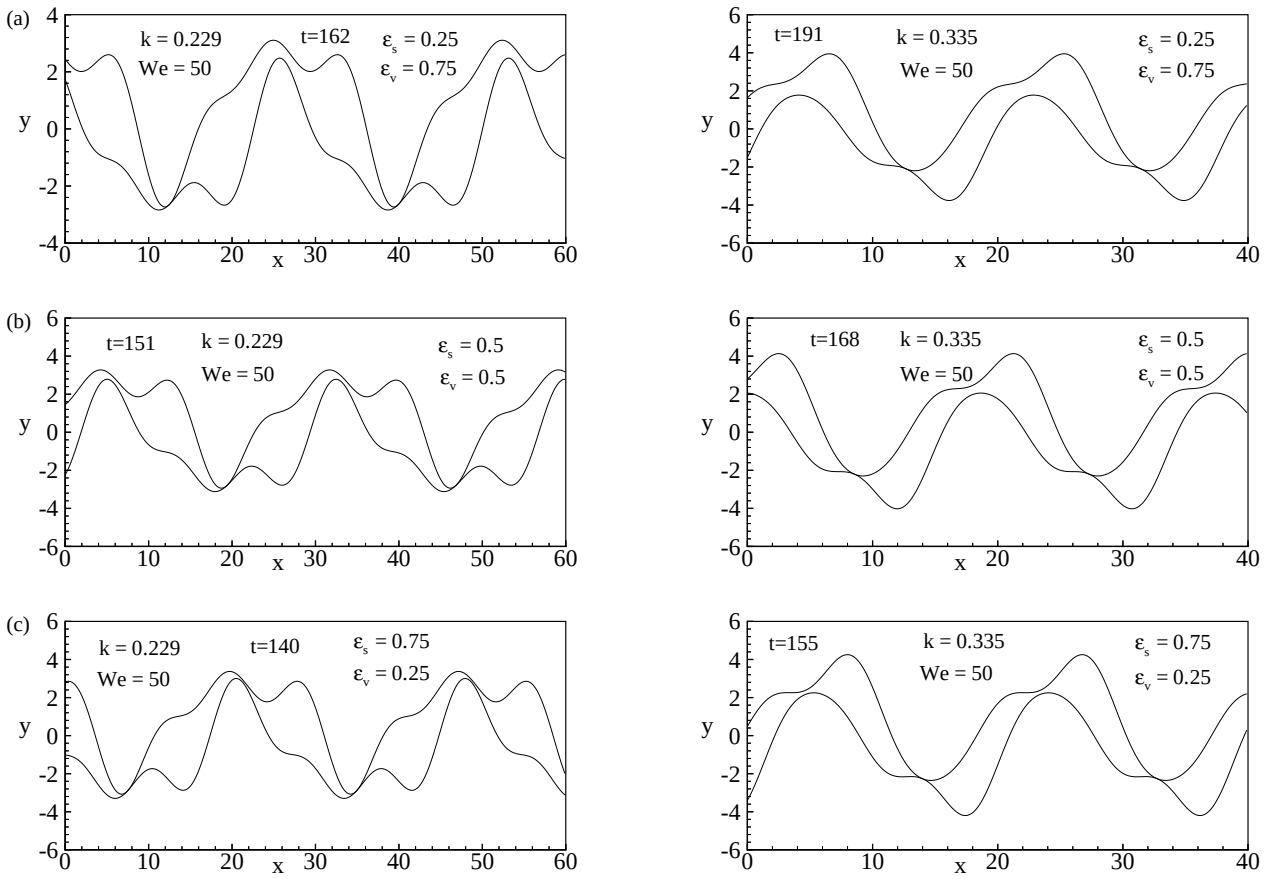

Figure 6.7: Surface deformations at breakup time for different proportions of ϵ_s and ϵ_v. $We = 50, U = 4, \rho = 0.001, \theta = 0$ and $\eta_0 = 0.1$. (a) $\epsilon_s = 0.25$ and $\epsilon_v = 0.75$; (b) $\epsilon_s = 0.5$ and $\epsilon_v = 0.5$; (c) $\epsilon_s = 0.75$ and $\epsilon_v = 0.25$.

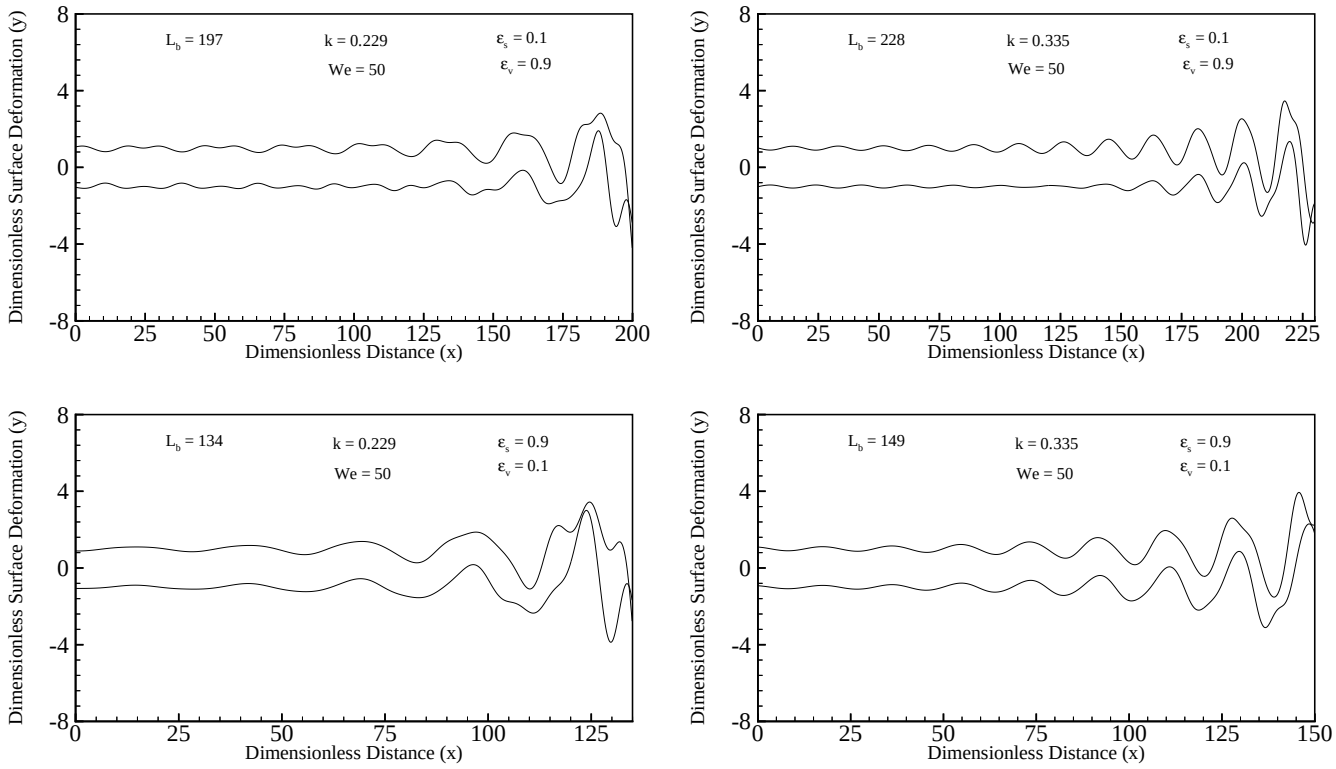

Figure 6.8: Spatial surface deformation for $We = 50, \rho = 0.001, U = 4, \theta = 0, \eta_0 = 0.1$ and different values of ϵ_s and ϵ_v.

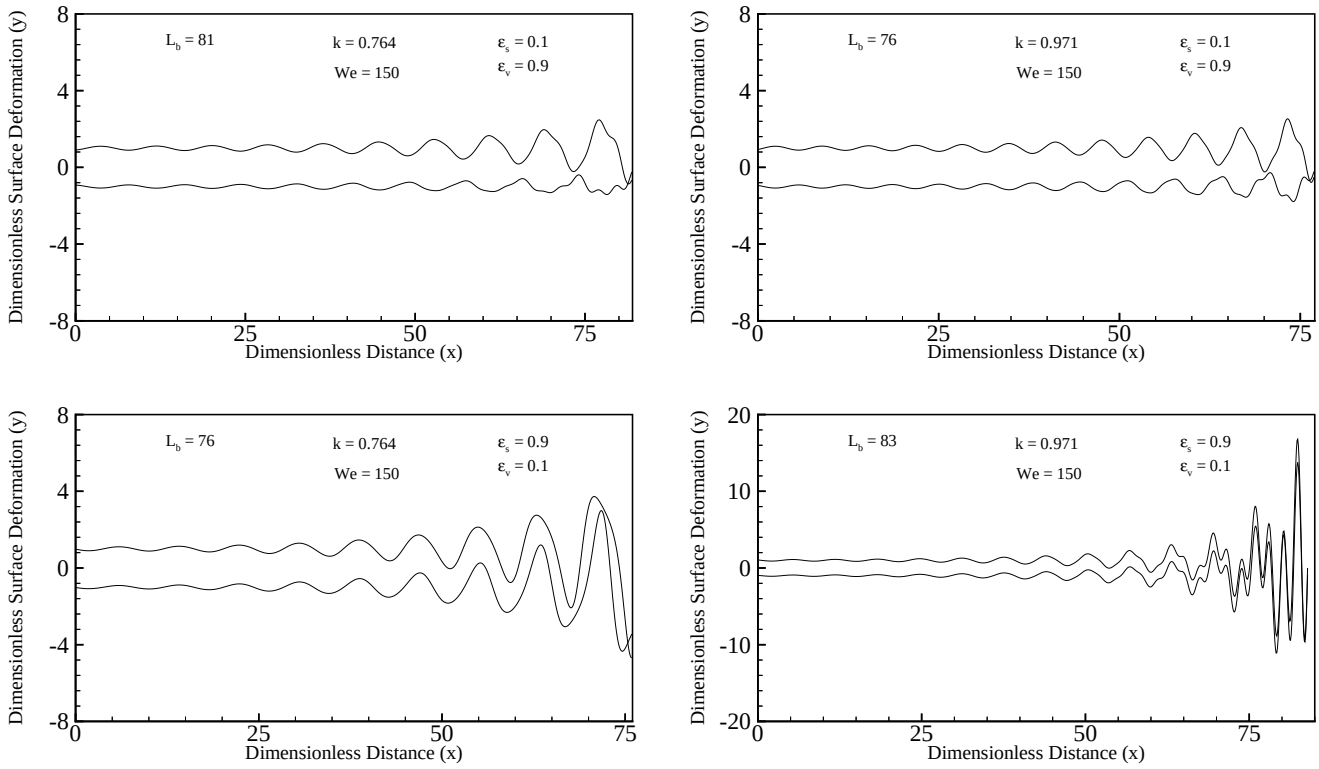

Figure 6.9: Spatial surface deformation for $We = 150, \rho = 0.001, U = 4, \theta = 0, \eta_0 = 0.1$ and different values of ϵ_s and ϵ_v.

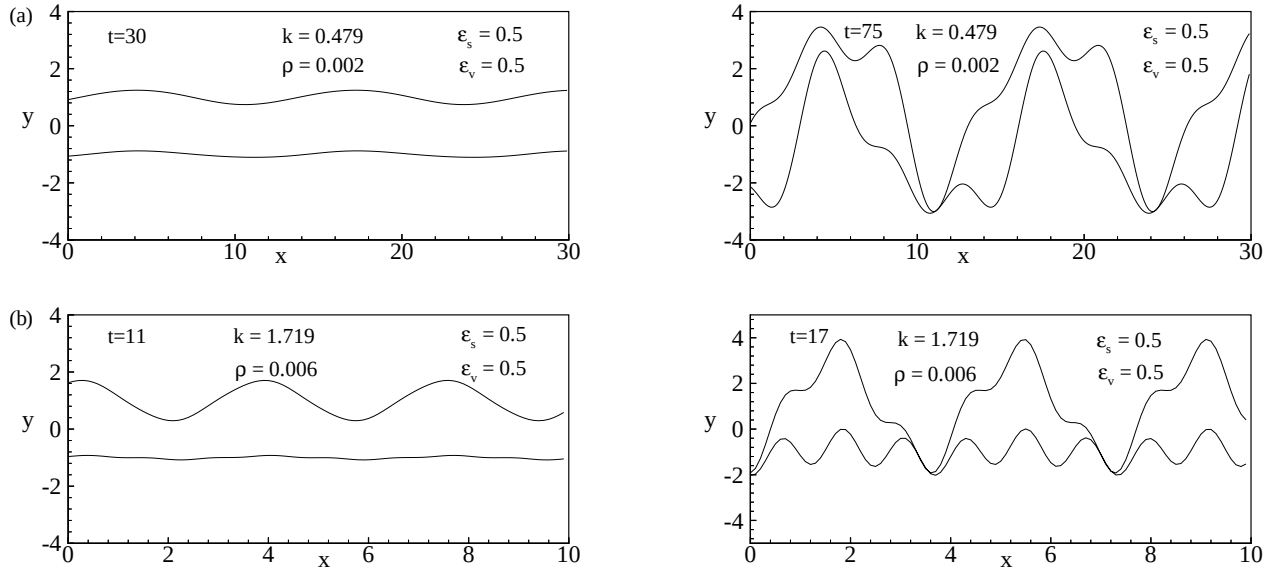

Figure 6.10: Evolution of surface deformation for $We = 50, U = 4, \theta = 0, \epsilon_s = 0.5, \epsilon_v = 0.5, \eta_0 = 0.1$ and different values of ρ. (a) $\rho = 0.002$ and $k = 0.479$; (b) $\rho = 0.006$ and $k = 1.719$.

is evident in Fig. 6.10b, where the wavenumber $k = 1.719(\lambda = 3.6)$ corresponds to the dominant wavenumber for the sinuous mode. The breakup of the liquid sheet still occurs at full-wavelength intervals with the breakup time being substantially reduced.

However, for the wavenumber corresponding to the dominant wavenumber for the varicose mode, the breakup characteristics change at low density ratios with the presence of large sheet amplitudes but remain the same at high density ratios, as shown in Fig. 6.11. This is expected as at high density ratios, the growth rates of the fundamental sinuous and varicose modes are almost same, which also causes the breakup time to remain unchanged. The spatial developments of the interfaces for $\rho = 0.002$ and 0.006 are shown in Fig. 6.12. It is found that the results agree with the qualitative observations of their temporal counterparts.

Figure 6.13 illustrates the effect of the gas-to-liquid velocity ratio on the breakup process of the liquid sheet. The wavenumbers $k = 0.697(\lambda = 9.0)$ for $U = 6$ and $k = 1.547(\lambda = 4.1)$ for $U = 8$ correspond to the dominant wavenumbers for the sinuous mode. It is observed

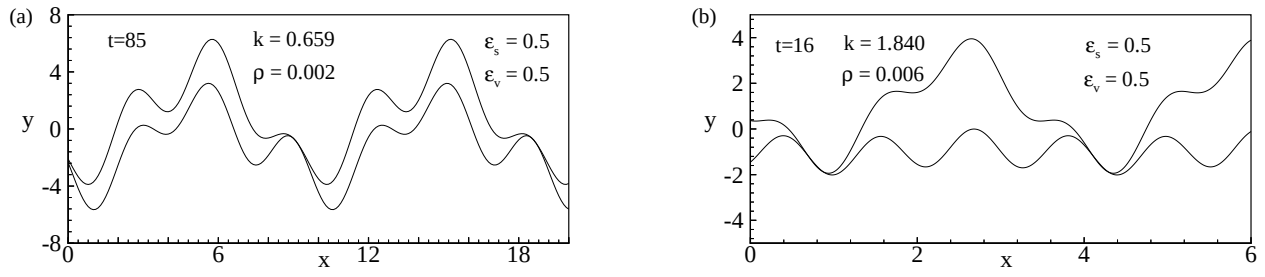

Figure 6.11: Surface deformation at breakup time for $We = 50, U = 4, \theta = 0, \epsilon_s = 0.5, \epsilon_v = 0.5, \eta_0 = 0.1$ and different values of ρ. (a) $\rho = 0.002$ and $k = 0.659$; (b) $\rho = 0.006$ and $k = 1.840$.

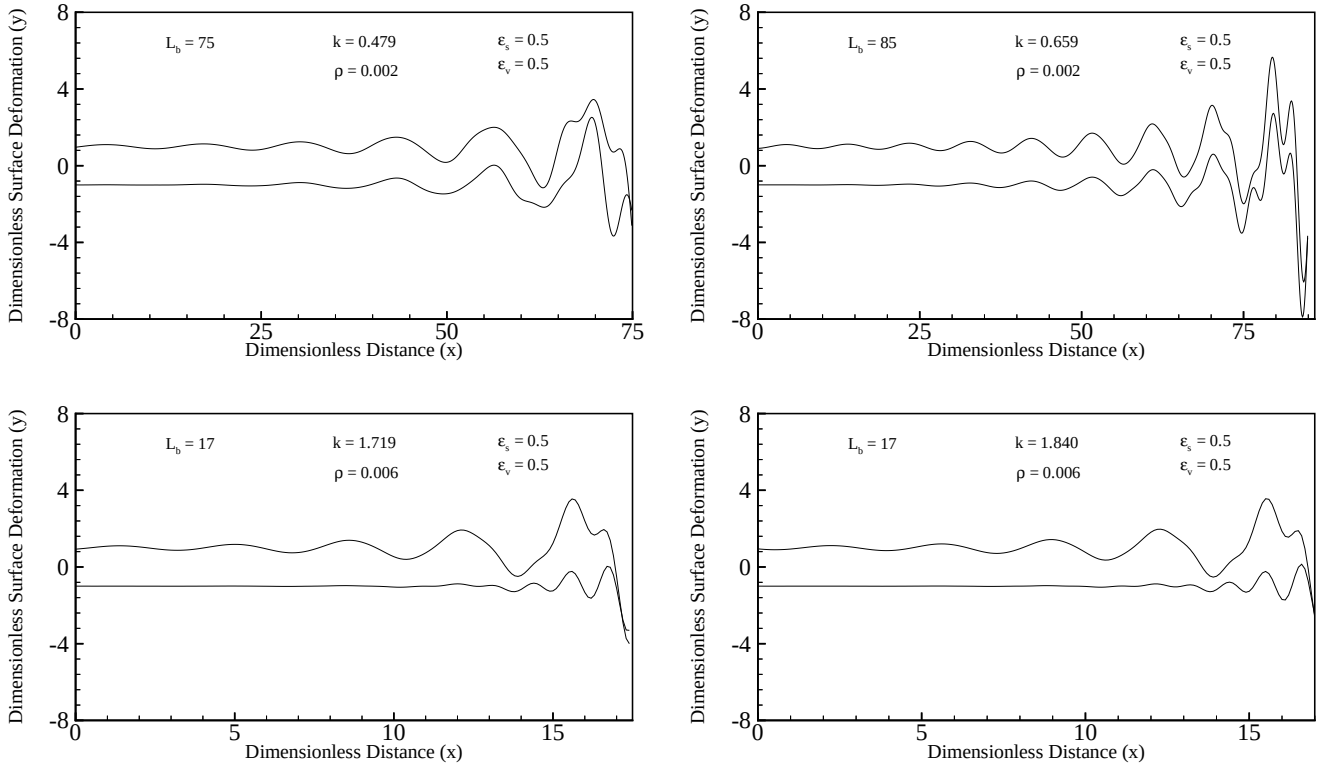

Figure 6.12: Spatial surface deformation for $We = 50, U = 4, \theta = 0, \epsilon_s = 0.5, \epsilon_v = 0.5, \eta_0 = 0.1$ and different values of ρ.

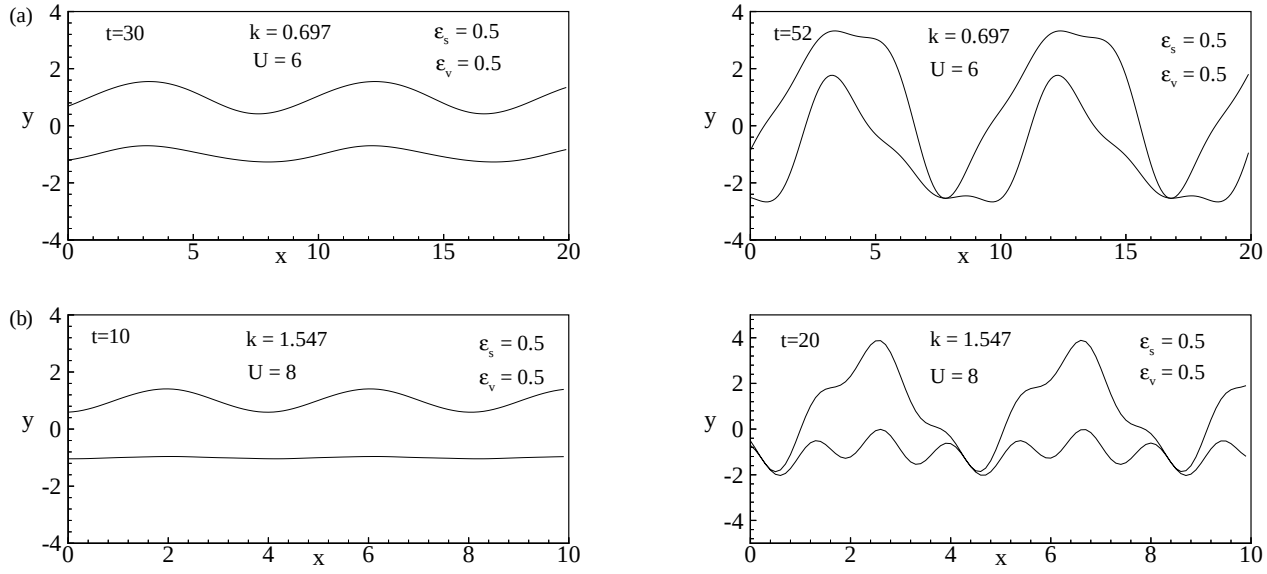

Figure 6.13: Evolution of surface deformation for $We = 50, \rho = 0.001, \theta = 0, \epsilon_s = 0.5, \epsilon_v = 0.5, \eta_0 = 0.1$ and different values of U. (a) $U = 6$ and $k = 0.697$; (b) $U = 8$ and $k = 1.547$.

that at low velocity ratios, the breakup time is long and it reduces drastically as the velocity ratio is increased, for *e.g.*, at $U = 8$, the breakup time is 20 compared with the breakup time of 151 for $U = 4$ shown in Fig. 6.7b. Similar to high density ratios, at high velocity ratios, the growth rates of the fundamental sinuous and varicose modes are almost same. This results in the strengthening of the wave growth at the upper interface and canceling at the lower interface, as shown in Fig. 6.13b. It is to be noted that the sheet breakup still occurs at full-wavelength intervals. However, at wavenumber corresponding to the dominant wavenumber for the varicose mode, as shown in Fig. 6.14a for $U = 6$, the wave amplitude at the breakup time is large and also the profile of the two interfaces are different from that shown in Fig. 6.13a. But at high velocity ratios, the breakup characteristics remain unchanged, similar to that observed for high density ratios. Figure 6.15 shows the spatial developments of the liquid sheet at different velocity ratios and they are in agreement with the temporal observations made earlier.

The effect of the phase angle between the two disturbance modes on the surface evolu-

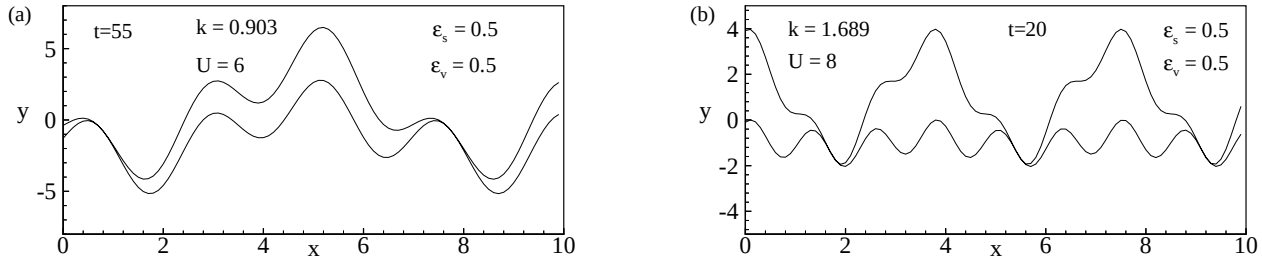

Figure 6.14: Surface deformation at breakup time for $We = 50, \rho = 0.001, \theta = 0, \epsilon_s = 0.5, \epsilon_v = 0.5, \eta_0 = 0.1$ and different values of U. (a) $U = 6$ and $k = 0.903$; (b) $U = 8$ and $k = 1.689$.

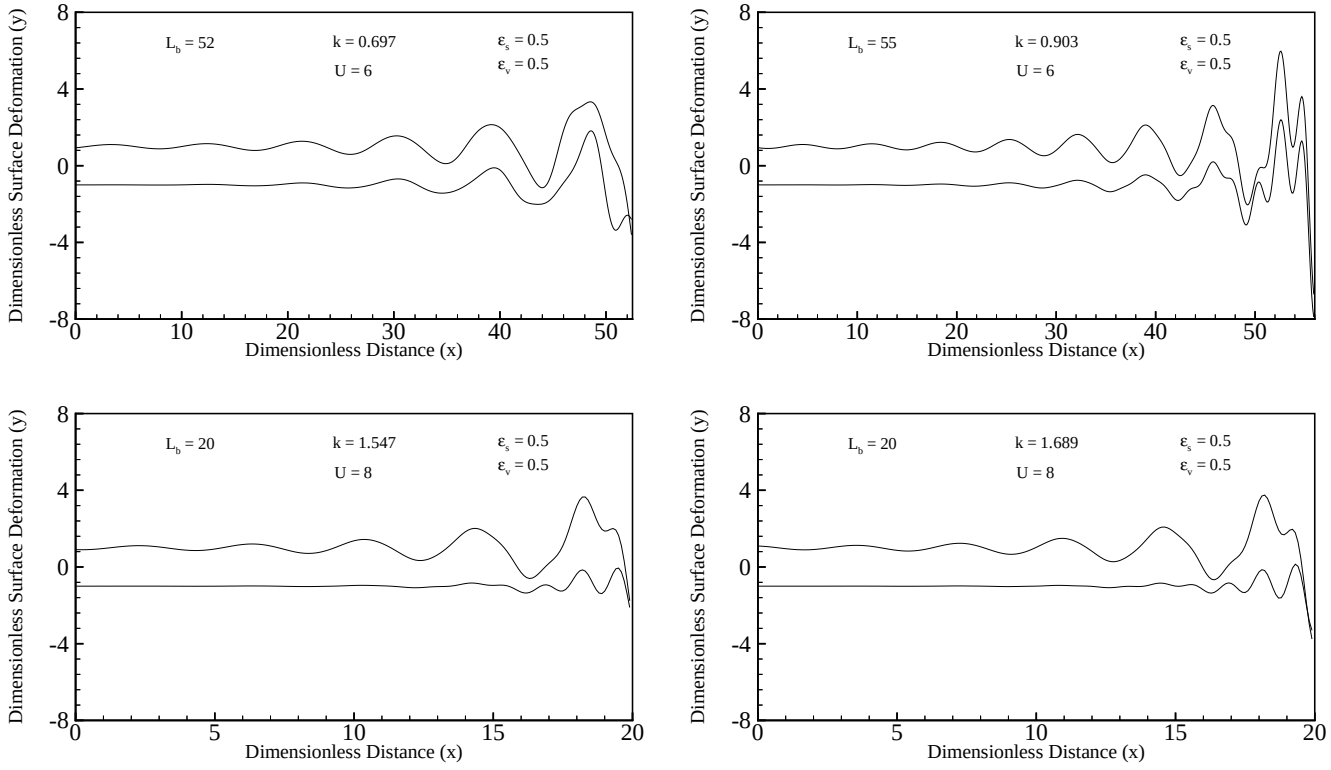

Figure 6.15: Spatial surface deformation for $We = 50, \rho = 0.001, \theta = 0, \epsilon_s = 0.5, \epsilon_v = 0.5, \eta_0 = 0.1$ and different values of U.

tion is shown in Fig. 6.16 for $We = 50, \rho = 0.001, U = 4, k = 0.229, \epsilon_s = 0.5, \epsilon_v = 0.5$ and $\eta_0 = 0.1$. It is found that even though the breakup time remains unchanged, the characteristics of the surface profile alternate at every $\pi/2$ phase angle. In order to understand more clearly the breakup characteristics at $\theta = \pi/2$, the temporal evolutions of the liquid sheet leading to the breakup is shown in Fig. 6.17. It is observed that the two interfaces remain parallel to each other for quite some time. At $t = 140$, the liquid sheet bulges out at quarter-wavelength interval and becomes thin at full-wavelength interval. Eventually the sheet breaks up at full-wavelength intervals and sheet thinning occurs at half-wavelength interval, which might be the location of further breakup of the liquid sheet.

6.3 Summary

The breakup characteristics of a plane liquid sheet in a surrounding gas stream have been investigated under the combined influence of the sinuous and the varicose modes (combined mode) with a phase angle between the two modes. It is observed that the liquid sheet breaks up at full-wavelength and half-wavelength intervals, depending on the proportions of the individual modes in the combined mode and the operating Weber numbers. It is found that at relatively large Weber numbers, the breakup process is dominated by the varicose mode, which is in accordance with the observation made for the liquid sheet subjected to the individual sinuous and varicose modes. It is also observed that the breakup characteristics depend on the dominant wavenumber corresponding to either the sinuous or the varicose modes, but its influence at high gas-to-liquid velocity and density ratios is not significant. In general, it is found that the breakup length decreases with the increase in Weber number, density and velocity ratios, but remain invariant with the change in phase angle. However, distinct breakup features are observed for complementary phase difference between the two modes.

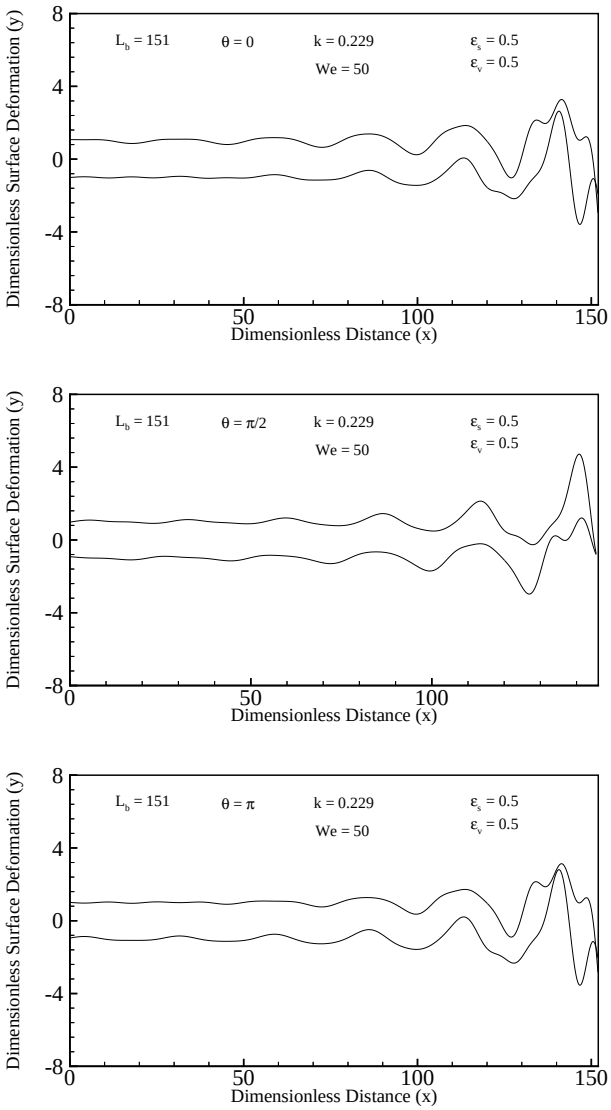

Figure 6.16: Spatial surface deformation for $We = 50, \rho = 0.001, U = 4, k = 0.229, \epsilon_s = 0.5, \epsilon_v = 0.5, \eta_0 = 0.1$ and different values of θ.

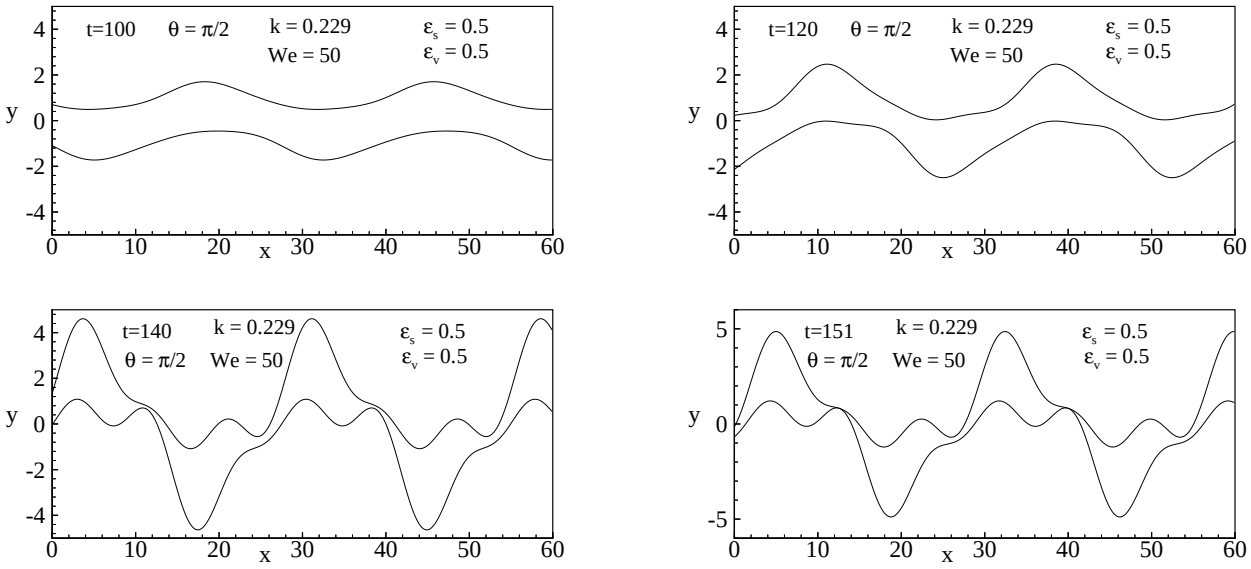

Figure 6.17: Evolution of surface deformation for $We = 50, \rho = 0.001, U = 4, k = 0.229, \theta = \pi/2, \epsilon_s = 0.5, \epsilon_v = 0.5$ and $\eta_0 = 0.1$.

Chapter 7

Droplet Size and Velocity Distributions

The deterministic sub-model, discussed so far, is valid up to the breakup of the liquid sheet. After the sheet breakup, the entire process becomes random and highly nonlinear with the formation of droplets of different diameters and velocities. However, the liquid mass, momentum, and energy must be conserved during the atomization process. For a given condition at the nozzle exit, there are infinite sets of possible droplet sizes and velocities that can satisfy the conservation requirements. Further, the enormous number of droplets with various sizes and velocities produced in a spray requires a statistical description of droplet ensembles. Therefore, the droplet formation process is dealt with the stochastic sub-model, where a probability density function (pdf) is used to describe the distribution of droplets in sprays. The most probable pdf can then be obtained by using the Maximum Entropy Principle (MEP). In this chapter, formulation of the stochastic sub-model and its coupling with the deterministic sub-model will be discussed.

7.1 Formulation

The history of the MEP goes back to 1948, when Claude Shannon [40] in his study on communication of information across channels, proposed the following definition of entropy:

$$S = -\mathcal{K} \sum_{i=1}^{n} p_i \ln p_i \tag{7.1}$$

where p_i is the probability of occurrence of the state i and $\mathcal{K}$ is the Boltzmann constant. This above definition of entropy can further be extended to a more general form, provided by Kullback & Leibler [89], as:

$$I = \mathcal{K} \sum_{i=1}^{n} p_i \ln \frac{p_i}{p_{i,0}} \tag{7.2}$$

where $p_{i,0}$ is the prior distribution of the state i and I is the measure of the nearness of the two probability distributions. This is often referred to as the Bayesian entropy [53]. Jaynes [39], starting with Shannon's information entropy, propounded a formalism - the maximization of S or minimization of I, subject to constraints which characterize macroscopically a physical system under consideration. This is referred to as the Maximum Entropy Principle, which has also been applied by Tribus [90] in a more general area like thermodynamics.

It is to be noted that the starting equation for the MEP in this study is Eq. (7.2). This is different from the stochastic sub-model used by Mitra & Li [56], where the expression for Shannon's entropy was used. By using the form given in Eq. (7.2), it is possible to couple the stochastic and the deterministic sub-models through the information about the unstable wave growth at the two liquid-gas interfaces, which play a significant role in the entire drop formation process. The details of this coupling between the two sub-models will be discussed later.

Under the MEP, many physical systems can be described by average or moment quantities which may be known for the particular system. These observations can be expressed mathematically by the following constraints:

$$\sum_{i=1}^{n} p_i g_{r,i} = < g_r > \qquad r = 1, 2, \ldots m \tag{7.3}$$

where m is the number of physical constraints for the particular system, $g_{r,i}$ is some function evaluated at state i and $< g_r >$ is the (known) expectation of average value of the function g over the entire system. The additional constraint, which arises from the definition of probability is

$$\sum_{i=1}^{n} p_i = 1 \tag{7.4}$$

where n is the number of possible states.

In the event of $m + 1 = n$, the number of equations become equal to the number of unknowns and hence the probability distribution p_i can be uniquely determined. On the other hand, if $m+1 < n$, then the system of Eqs. (7.3)-(7.4) become indeterminate and the probability distribution p_i has an infinite set of solutions. However, under such a condition, one can still obtain a reasonable prediction of p_i by minimizing I given in Eq. (7.2).

The solution of the system of equations which minimizes I can be found by using the method of Lagrange multipliers [91] $\Lambda_r, r = 1, 2, \ldots m$. Under such a scheme, Eq. (7.3) and Eq. (7.4) are multiplied by Λ_r and $(\Lambda_0 - 1)$, respectively, and then added together. The quantity I is also added with the resulting expression and finally, the derivative with respect to p_i is taken, which can be written in the following form:

$$\frac{\partial}{\partial p_i}\left[\frac{I}{\mathcal{K}} + (\Lambda_0 - 1)\sum_{i=1}^{n} p_i + \sum_{r=1}^{m}\Lambda_r \sum_{i=1}^{n} p_i g_{r,i}\right] = 0 \tag{7.5}$$

Substitution of Eq. (7.2) into the above equation, gives

$$\sum_{i=1}^{n}\Big[\ln\frac{p_i}{p_{i,0}} + 1 + (\Lambda_0 - 1) + \sum_{i=1}^{m}\Lambda_r g_{r,i}\Big]dp_i = 0 \tag{7.6}$$

To ensure that the above equation is satisfied for arbitrary dp_i, the quantity in the square bracket must be zero, which yields

$$p_i = p_{i,0}\exp\Big[-\Lambda_0 - \sum_{r=1}^{m}\Lambda_r g_{r,i}\Big] \tag{7.7}$$

where Λ_0 and Λ_r must satisfy the constraint equations. The probability distribution obtained is the solution to the problem, which maximizes the entropy under all the constraints imposed on the physical system.

The multiplier Λ_0 can be obtained by substituting Eq. (7.7) into Eq. (7.4), which gives

$$\Lambda_0 = \ln \sum_{i=1}^{n} p_{i,0} \exp\Big(- \sum_{r=1}^{m} \Lambda_r g_{r,i}\Big) \tag{7.8}$$

Eq. (7.8) allows the determination of Λ_0, once the Λ_r's are determined. In order to obtain Λ_r's, Eq. (7.7) is substituted back into the constraint equation, Eq. (7.3), which gives

$$\sum_{i=1}^{n} g_{r,i} p_{i,0} \exp\Big[- \Lambda_0 - \sum_{r=1}^{m} \Lambda_r g_{r,i}\Big] =< g_r > \tag{7.9}$$

Therefore, Eqs. (7.8)-(7.9), yield a set of $m+1$ equations with $m+1$ unknown Lagrange multipliers, Λ_0 and Λ_r, $r = 1, \ldots m$. Thus, such a probabilistic set of equations can be approached deterministically from the standpoint of their solution process.

The MEP, discussed so far, is applicable for a one dimensional system, which can be readily extended into multi-dimensions. In order to apply this principle for obtaining droplet size and velocity distributions (two dimensions), the probability p_i can be replaced by the joint probability p_{ij}, where i denotes the state of the droplet size and j denotes the corresponding state for the droplet velocity. Hence, Eqs. (7.8)-(7.9) can still be used with an additional summation over the j states.

The constraints imposed on the physical problem for determination of droplet size and velocity distributions are the conservation of mass, momentum and energy. These conservation principles are applied to the control volume enclosing the bulk liquid and extending from the atomizer exit to the plane where the droplets are produced immediately after the breakup of the liquid sheet. If $\dot{m}_\ell$ denotes the mass flow rate at which the liquid is ejected from the atomizer, $\dot{n}$ the total number of droplets being produced per unit time, then the mass conservation under steady state requires that the sum of all droplets produced per unit time be equal to the mass of the liquid sprayed per unit time, plus the mass source term (S_m), which denotes the mass transfer process between the liquid and the gas phases. Hence, the expression for the conservation of mass can be written as:

$$\sum_{i} \sum_{j} p_{ij} \frac{\pi}{6} D_i^3 \rho_\ell \dot{n} = \dot{m}_\ell + S_m \tag{7.10}$$

where the droplets are assumed to be spherical with diameter D_i.

For the conservation of liquid momentum, the total momentum of all the droplets must be equal to the momentum of the liquid at the atomizer exit, plus a momentum source term (S_{mv}), which accounts for the momentum exchange between the bulk liquid and the surrounding gas medium. Therefore, momentum conservation can be written as:

$$\sum_i \sum_j p_{ij} \frac{\pi}{6} D_i^3 \rho_\ell \dot{n} U_j = \dot{m}_\ell U_\ell + S_{mv} \tag{7.11}$$

where U_j is the velocity of the droplets with diameter D_i. The momentum source term, S_{mv}, is positive when the momentum is transfered from the gas medium into the liquid phase, as in the case for an air-blast atomizer.

Similarly, the conservation of liquid energy requires that the total energy of all the droplets formed in a spray, *i.e.*, the sum of their kinetic and surface energies, be equal to the kinetic energy of the liquid at the atomizer exit, plus a source term (S_e), which represents the exchange of energy between the two phases. Hence, the energy conservation can be written as:

$$\sum_i \sum_j p_{ij} \left[\frac{1}{2} \left(\frac{\pi}{6} D_i^3 \rho_\ell \dot{n} U_j^2 \right) + \sigma \pi D_i^2 \dot{n} \right] = \frac{1}{2} \dot{m}_\ell U_\ell^2 + S_e \tag{7.12}$$

Eqs. (7.10)-(7.12) are nondimensionalized such that the droplet diameter is scaled with the mass-mean diameter D_{30} and the droplet velocity is scaled with the liquid velocity at the atomizer exit, U_ℓ. Then, the conservation equations for the liquid mass, momentum, and energy can be written as:

$$\text{Mass:} \qquad \sum_{i,j} p_{ij} \bar{D}_i{}^3 = 1 + \bar{S}_m \tag{7.13}$$

$$\text{Momentum:} \qquad \sum_{i,j} p_{ij} \bar{D}_i{}^3 \bar{U}_j = 1 + \bar{S}_{mv} \tag{7.14}$$

$$\text{Energy:} \qquad \sum_{i,j} p_{ij} (\bar{D}_i{}^3 \bar{U}_j^2 + B \bar{D}_i{}^2) = 1 + \bar{S}_e \tag{7.15}$$

where $\bar{S}_m = S_m / \dot{m}_\ell$, $\bar{S}_{mv} = S_{mv} / (\dot{m}_\ell U_\ell)$, and $\bar{S}_e = S_e / (\dot{m}_\ell U_\ell^2)$ denote the dimensionless mass, momentum and energy source terms, respectively; $\bar{D}_i = D_i / D_{30}$ and $\bar{U}_j = U_j / U_\ell$ denote the dimensionless droplet diameter and velocity, respectively. The parameter B is

a constant and is related to the surface tension through the following relation:

$$B = \frac{12}{We_{30}}; \quad We_{30} = \frac{\rho_\ell U_\ell^2 D_{30}}{\sigma} \tag{7.16}$$

In addition to the conservation equations, there is one more constraint to be imposed on the joint probability, p_{ij}. From the definition of a probability, the sum of p_{ij} over the indices i and j should be unity, which can be expressed mathematically as:

$$\text{Normalization:} \qquad \sum_{i,j} p_{ij} = 1 \tag{7.17}$$

There are infinite sets of possible solutions of p_{ij}, which satisfy the constraints given in Eqs. (7.13)-(7.15) and Eq. (7.17). The most appropriate probability distribution is obtained by applying the MEP, as discussed earlier. Therefore, similar to Eq. (7.7), the most probable probability distribution is of the following form:

$$p_{ij} = p_{i,0} \exp\left[-\Lambda_0 - \Lambda_1 \bar{D}_i^3 - \Lambda_2 \bar{D}_i^3 \bar{U}_j - \Lambda_3 (\bar{D}_i^3 \bar{U}_j^2 + B\bar{D}_i^2)\right] \tag{7.18}$$

where $\Lambda_i (i = 0, 1, 2, 3)$ are the Lagrange multipliers to be determined by the method discussed before.

It is customary to consider the droplet size and velocity as continuous variables. Therefore, the subscripts, i and j, can be dropped, and the summations in Eqs. (7.13)-(7.15) and Eq. (7.17) can be replaced by integrals with limits from the corresponding minimum to maximum values. The discrete probability p_{ij} in Eq. (7.18) can also be replaced by the continuous joint droplet size and velocity probability density function (pdf). Thus,

$$f = f_0 \exp\left[-\Lambda_0 - \Lambda_1 \bar{D}^3 - \Lambda_2 \bar{D}^3 \bar{U} - \Lambda_3 (\bar{D}^3 \bar{U}^2 + B\bar{D}^2)\right] \tag{7.19}$$

where f_0 is the continuous prior droplet size pdf. The discrete summation form of the

conservation laws and the normalization condition can be written in their integral form as,

$$\text{Mass:} \quad \int_{\bar{D}_{min}}^{\bar{D}_{max}} \int_{\bar{U}_{min}}^{\bar{U}_{max}} f\bar{D}^3 d\bar{U} d\bar{D} = 1 + \bar{S}_m \tag{7.20}$$

$$\text{Momentum:} \quad \int_{\bar{D}_{min}}^{\bar{D}_{max}} \int_{\bar{U}_{min}}^{\bar{U}_{max}} f\bar{U}\bar{D}^3 d\bar{U} d\bar{D} = 1 + \bar{S}_{mv} \tag{7.21}$$

$$\text{Energy:} \quad \int_{\bar{D}_{min}}^{\bar{D}_{max}} \int_{\bar{U}_{min}}^{\bar{U}_{max}} f(\bar{D}^3\bar{U}^2 + B\bar{D}^2) d\bar{U} d\bar{D} = 1 + \bar{S}_e \tag{7.22}$$

$$\text{Normalization:} \quad \int_{\bar{D}_{min}}^{\bar{D}_{max}} \int_{\bar{U}_{min}}^{\bar{U}_{max}} f d\bar{U} d\bar{D} = 1 \tag{7.23}$$

As observed earlier, Eq. (7.19) represents the number-based joint pdf for the droplet size and velocity distributions in sprays. Therefore, the number-based droplet size distribution can be obtained by integrating Eq. (7.19) over the velocity space from minimum to maximum value. Hence, the number-based droplet size distribution can be expressed as:

$$\begin{aligned} \frac{dN}{d\bar{D}} &= \int_{\bar{U}_{min}}^{\bar{U}_{max}} f d\bar{U} \\ &= \frac{\sqrt{\pi}}{2} \frac{f_0 \left[\text{erf}(X_{max}) - \text{erf}(X_{min})\right]}{\sqrt{\bar{D}^3 \Lambda_3}} \exp\left[-\Lambda_0 - \Lambda_3 B\bar{D}^2 - \left(\Lambda_1 - \frac{\Lambda_2^2}{4\Lambda_3}\right)\bar{D}^3\right] \end{aligned} \tag{7.24}$$

where erf(X) denotes the error function, N the normalized cumulative droplet number, and

$$X_{max} = \left(\bar{U}_{max} + \frac{\Lambda_2}{2\Lambda_3}\right)(\Lambda_3\bar{D}^3)^{1/2}; \quad X_{min} = \left(\bar{U}_{min} + \frac{\Lambda_2}{2\Lambda_3}\right)(\Lambda_3\bar{D}^3)^{1/2} \tag{7.25}$$

Similarly, the number based droplet velocity distribution can be obtained by integrating Eq. (7.19) over the diameter space from minimum to maximum value, *i.e.*,

$$\frac{dN}{d\bar{U}} = \int_{\bar{D}_{min}}^{\bar{D}_{max}} f d\bar{D} \tag{7.26}$$

However, such integration cannot be carried out analytically, and hence needs a numerical technique.

7.2 Source Terms and D_{30}

In order to solve for the joint droplet size and velocity distributions, the source terms, $\bar{S}_m, \bar{S}_{mv}$, and $\bar{S}_e$, need to be evaluated and also the mass-mean diameter D_{30} needs to be estimated. The source terms form a link between the deterministic and the stochastic sub-models along with the prior droplet size distribution, f_0, which will be discussed later. It should be pointed out that the effect of Tollmien-Schlichting waves in the gas boundary layer is at least one order of magnitude smaller than the Kelvin-Helmholtz instability in liquid atomization [92]. As a result, the inviscid assumption for the instability analysis in the deterministic sub-model is reasonable with no loss of generality, even though Tollmien-Schlichting waves may extract kinetic energy from the mean flow and grow. This latter effect is considered in the determination of the momentum and energy source terms, as discussed here.

For the present formulation, it is assumed that the surrounding gas medium is fully saturated and therefore no mass transfer occurs. This assumption is reasonable for laboratory experiments of water sprays with air because of the large enthalpy of vaporization and low vapor pressure of water at room temperature. Therefore, the mass source term can be taken as zero, *i.e.*,

$$\bar{S}_m = 0 \tag{7.27}$$

The quantitative estimate of the degree of interaction between the liquid sheet and the co-flowing gas stream is determined from the boundary layer theory, similar to the flow over the flat plate. Even though the liquid sheet is wavy during its disintegration process, experimental observations [93] and the present nonlinear instability analysis indicate that the wave amplitude is small except very close to the breakup point. As a result, the liquid sheet may be assumed flat for the purpose of drag coefficient calculations in the boundary layer theory [94]. The method for obtaining the momentum and the energy source terms is already been discussed by Mitra & Li [56]. However, for the sake of completeness, the key steps in the derivation of the source terms are provided here.

The momentum source term is obtained by considering the drag force acting on both sides of the liquid sheet due to the relative motion of the gas phase over the nondimensional

breakup length L_b. The drag force on the liquid sheet can be written as

$$F = 2\left[\frac{1}{2}\rho_g(U_g - U_\ell)^2 A^* C_f\right]; \qquad A^* = (L_b a^*) \times b^* \tag{7.28}$$

where C_f is the drag coefficient for flow over a flat plate, which has different values for laminar and turbulent flows and b^* is the width of the nozzle. Considering the surrounding gas medium as the control volume, the rate of change of momentum is equal to the drag force. In other words, the drag force is equal to the amount of momentum transferred from the surrounding gas medium to the liquid sheet per unit time. Therefore, the momentum source term is obtained as

$$\bar{S}_{mv} = \frac{F}{\rho_\ell U_\ell^2 b^*(2a^*)} \tag{7.29}$$

Combining Eqs. (7.28) and (7.29), the momentum source term can be written as

$$\bar{S}_{mv} = \frac{1}{2} C_f \rho (U-1)^2 L_b \tag{7.30}$$

Similarly, the energy source term is calculated by considering the work done by the drag force per unit time over the length L_b, which can be expressed as:

$$W = F \times |U_g - U_\ell| \tag{7.31}$$

Combining Eqs. (7.28) and (7.31), the energy source term can be written as

$$\bar{S}_e = C_f \rho (U-1)^3 L_b \tag{7.32}$$

where ρ and U are the gas-to-liquid density and velocity ratios, respectively. Depending upon the gas phase Reynolds number, $Re_g = \rho_g |U_g - U_\ell| a^* L_b / \mu_g$, correlations are available to compute C_f [95].

The mass-mean diameter, D_{30}, is obtained by considering the mass of the liquid sheet that contracts to form ligaments, which is followed by the formation of spherical droplets. The nonlinear instability analysis discussed in Chapter 5 shows that the liquid sheet breaks up at full-wavelength or half-interval intervals depending on the proportions of the individual sinuous and varicose modes of disturbance. Figure 7.1 shows the breakup locations

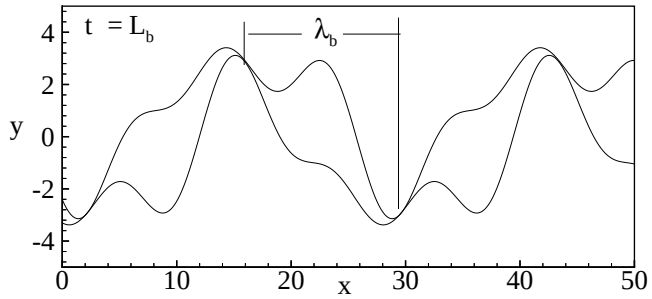

Figure 7.1: A typical interface deformation at the breakup time for a given flow condition at nozzle exit.

for a given flow condition specified at the atomizer exit, *i.e.*, at fixed $We, \rho, U, \theta, \eta_0, \epsilon_s$ and ϵ_v. The liquid mass between the two breakup points, denoted by λ_b (dimensionless) in Fig. 7.1, produces cylindrical ligaments, the diameter (d^*_{lg}) of which can be obtained from the following relation:

$$\begin{aligned} \frac{\pi}{4} d^{*2}_{lg} &= \lambda_b a^* (2a^*) \\ \Rightarrow d^*_{lg} &= 1.6 a^* \sqrt{\lambda_b} \end{aligned} \tag{7.33}$$

The ligaments so produced from the liquid sheet further break down into individual droplets by the Rayleigh instability of cylindrical liquid columns [96]. According to the Rayleigh mechanism, the droplets are formed from the ligament breakup at full-wavelength interval, with the wavelength related to the ligament diameter as

$$\lambda^*_r = 4.5 d^*_{lg} \tag{7.34}$$

Therefore, the resulting droplet diameter, which corresponds to the mass-mean diameter D_{30}, is obtained from the conservation of mass, as follows:

$$\frac{\pi}{4} d^{*2}_{lg} \lambda^*_r = \frac{\pi}{6} D^3_{30} \tag{7.35}$$

Combining Eqs. (7.33)-(7.35), the final expression for the mass-mean diameter is obtained as

$$D_{30} = 3 a^* \sqrt{\lambda_b} \tag{7.36}$$

where a^* is the half-sheet thickness. However, Eq. (7.36) is valid for an ideal spray which produces droplets according to the Rayleigh mechanism, discussed here. In an actual spray, the mass-mean diameter is most likely be expressed in the following manner:

$$D_{30} \sim a^* \sqrt{\lambda_b} \quad \Rightarrow D_{30} = C a^* \sqrt{\lambda_b} \tag{7.37}$$

where C is a nozzle constant whose value depends on the type of the nozzle and the spatial location in the spray. This technique of estimating D_{30} has also been used by Dombrowski and Hooper [93] for their fan sprays.

7.3 Prior Distribution f_0

As mentioned in Chapter 2, the models used for the MEP, so far, do not incorporate the information about the unstable wave growths at the two liquid-gas interfaces. However, as observed from the nonlinear instability analysis, the wavenumber corresponding to the maximum growth rate for the sinuous or the varicose modes of disturbance plays a significant role in the breakup mechanism of the liquid sheet. Intuitively, such behavior of the disturbance wavenumber may propagate to the droplet formation process and thereby influence the actual drop size distribution in sprays.

Traditionally, only linear instability is used to obtain the drop size in sprays [60]. However, in actual spray formation process, the initial portion of the liquid sheet formation is dictated by the linear instability while near the breakup region, the nonlinear instability plays a dominant role. But due to the complex nature of the interaction between different modes of disturbances, as discussed in Chapter 6, it is difficult to quantify the influence of the nonlinear interactions on the resultant drop formation. Therefore, in order to incorporate information about the wave elements, the prior distribution is obtained from the growth curve based on the linear instability of the plane liquid sheet. The nonlinear instability is incorporated in the droplet distribution through the breakup length L_b present in the source terms and the breakup wavelength λ_b in the mass-mean diameter.

In the present MEP formulation, based on the definition of entropy given in Eq. (7.2), the information regarding the prior droplet size distribution, f_0, can be extracted from the first-order growth rate curves, similar to those shown in Figs. 4.1 and 5.2. It is suggested

that f_0 be proportional to either $\omega_{1,s}$ or $\omega_{1,v}$, depending on the dominant wavenumber of the particular disturbance wave; and the dimensionless droplet diameter $\bar{D}$ be inversely proportional to the square root of the dimensionless wavenumber k, according to the Eq. (7.36). Therefore, in the range of the unstable wave numbers ($0 \leqslant k \leqslant k_c$), the droplet diameter varies with the wave number in the following manner:

$$\bar{D} = \sqrt{\frac{\lambda}{\lambda_b}}; \quad \lambda = \frac{2\pi}{k} \tag{7.38}$$

However, according to the linear instability theory, the wavenumbers beyond the cut-off wavenumber (k_c) are stable. Therefore, in order to accommodate the droplets corresponding to $k > k_c$, it is assumed that the prior distribution f_0 varies as the square of the droplet diameter. The smooth transition between the two regimes of the disturbance wavenumber is achieved by evaluating a critical droplet diameter, $\bar{D}_{cr}$, such that $\bar{D}_{cr}$ is the common tangent point for the two curves. This can be written mathematically as:

$$f_0 = \begin{cases} m\bar{D}^2 & \bar{D} \leqslant \bar{D}_{cr} \\ \omega_{1,s}(k_b/\bar{D}^2) \quad \text{or} \quad \omega_{1,v}(k_b/\bar{D}^2) & \bar{D} > \bar{D}_{cr} \end{cases} \tag{7.39}$$

where m denotes the slope of f_0, k_b is the breakup wavenumber corresponding to λ_b and $\omega(\cdot)$'s represent the first-order growth rates, provided in Eqs. (4.4) and (5.7), wherein k's are substituted by $k_b/\bar{D}^2$. Figure 7.2 shows such prior distribution as per Eq. (7.39), for $We = 50, \rho = 0.001, U = 4, C = 3$ and $a^* = 10\mu m$. It is observed that the distribution peaks at $\bar{D} = 1$ which corresponds to the dominant wavenumber $k = 0.228$. A smooth transition between the two portions of the curve is obtained for $\bar{D}_{cr} = 0.822$ and $m = 0.041$.

7.4 Droplet Size and Velocity Limitations

The minimum droplet velocity in a practical spray can be taken as zero, whereas the maximum value is limited for a given droplet size due to secondary droplet breakup. The maximum velocity that a droplet of size D_i can sustain depends upon the ratio of the dynamic force to surface tension force, and is governed by the following relation [97]:

$$We_c = \frac{\rho_g |U_j - U_g|^2 D_i}{\sigma} \approx 10 \tag{7.40}$$

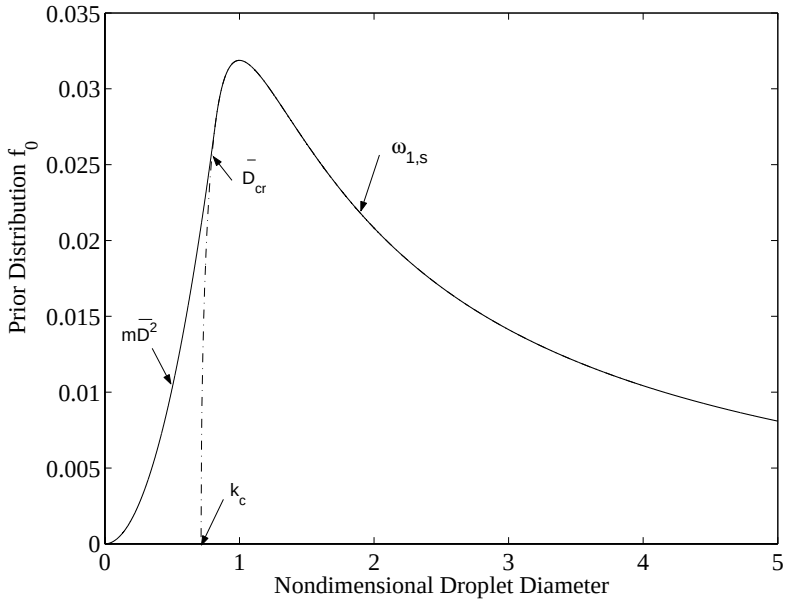

Figure 7.2: Prior droplet size distribution f_0 for $We = 50, U = 4, \rho = 0.001, C = 3$ and $a^* = 10\ \mu m$.

The above equation can be nondimensionalized to obtain the desired maximum droplet velocity for a given droplet size, which can be written as:

$$\bar{U}_{max} = U + \left(\frac{10}{\rho We_{30} \bar{D}} \right)^{1/2} \tag{7.41}$$

This is used in Eq. (7.24) for the number based droplet size distribution.

For a given droplet velocity, Eq. (7.40) yields the maximum droplet diameter

$$\bar{D}_{max} = \frac{10}{\rho We_{30} (\bar{U} - U)^2} \tag{7.42}$$

which is used in Eq. (7.26) for the number based droplet velocity distribution. The minimum droplet diameter for sprays is set to zero. It should be emphasized that the value of $\bar{U}_{max}$ only effects the smallest droplets in sprays, typically for diameters of sub-microns, which is not important for practical applications. Further, such droplets tend to lose their momentum, and hence velocities within extremely small distances, less than 1 mm. Therefore, it is physically unrealistic to have relatively large value of $\bar{U}_{max}$ for such small droplets.

7.5 Numerical Technique

The objective of the MEP formulation is to obtain the Lagrange multipliers by solving the set of equations, Eqs. (7.20)-(7.23), which are nonlinear. Therefore, a numerical technique, such as the Newton-Raphson method, is implemented to obtain the desired multipliers. Once, the Lagrange multipliers are known, Eq. (7.19), can be used to obtain the droplet size and velocity distributions in sprays.

The nonlinear set of equations, Eqs. (7.20)-(7.23), involve double integrals over velocity and diameter ranges. Since the integrals over the velocity space can be obtained analytically, as observed in Eq. (7.24), the double integrals are converted into single integrals over the diameter range to reduce the computational effort. Appendix D provides the necessary steps involve in simplifying the governing mass, momentum, energy, and normalization equations.

The integrand over the diameter range involves an exponential function, which makes the Newton-Raphson method highly sensitive to the initial guess values of the Lagrange

multipliers. However, by modifying the numerical method such that the normalization condition is enforced at each iteration step, the convergence can be improved and the strict requirement on the initial guess can also be relaxed.

Eqs. (7.20)-(7.23) can be written in a matrix form as

$$\mathbf{A}\Delta\Lambda = -\mathbf{B} \tag{7.43}$$

where $\mathbf{A}$ is the coefficient symmetric square matrix with its element, $a_{i,j}$, which is the Jacobian matrix, defined as

$$a_{i,j} = \frac{\partial B_i}{\partial \Lambda_j} \quad i,j = 0,1,2,3 \tag{7.44}$$

and $\mathbf{B} = (B_0, B_1, B_2, B_3)^T$ is a column vector, the form of which is provided in Appendix D. It is to be noted that both $\mathbf{A}$ and $\mathbf{B}$ are functions of unknown Λ_i's, $i = 1,2,3$, with Λ_0^0 being determined from the normalization condition for the initial guess values of Λ_1^0, Λ_2^0 and Λ_3^0. Therefore, for n^{th} iteration step, $\Lambda^{(n)}$ is obtained from the following relation:

$$\Lambda_i^{(n)} = \Lambda_i^{(n-1)} + \Delta\Lambda_i^{(n)} \quad i = 1,2,3 \tag{7.45}$$

where $\Delta\Lambda_i^{(n)}$'s are the solution of Eq. (7.43), and $\Lambda_0^{(n)}$ is updated from the normalization condition after $\Lambda_i^{(n)}$'s, $i = 1,2,3$, have been determined. Under such a scheme, it is ensured that $B_0 = 0$ at every iteration step, while B_i, $i = 1,2,3$, may not be equal to zero exactly. As a result of this modification, the element $a_{0,0} = -1$ for all iteration steps in the coefficient matrix $\mathbf{A}$.

It is to be noted that the values of Lagrange multipliers are very sensitive to the number of significant digits after the decimal point. Therefore, a very small tolerance value is taken as a convergence criteria for each iteration step and can be written as:

$$\max\{|B_1|, |B_2|, |B_3|\} \leq 1 \times 10^{-11} \tag{7.46}$$

Such small tolerance value ensures that an unique solution for the Lagrange multipliers, subjected to the given constraints, is obtained and hence physically realistic droplet size and velocity distributions can be predicted. A macro-flow chart for the entire numerical scheme is shown in Fig. 7.3. Generally, it is observed that the converged solution of the

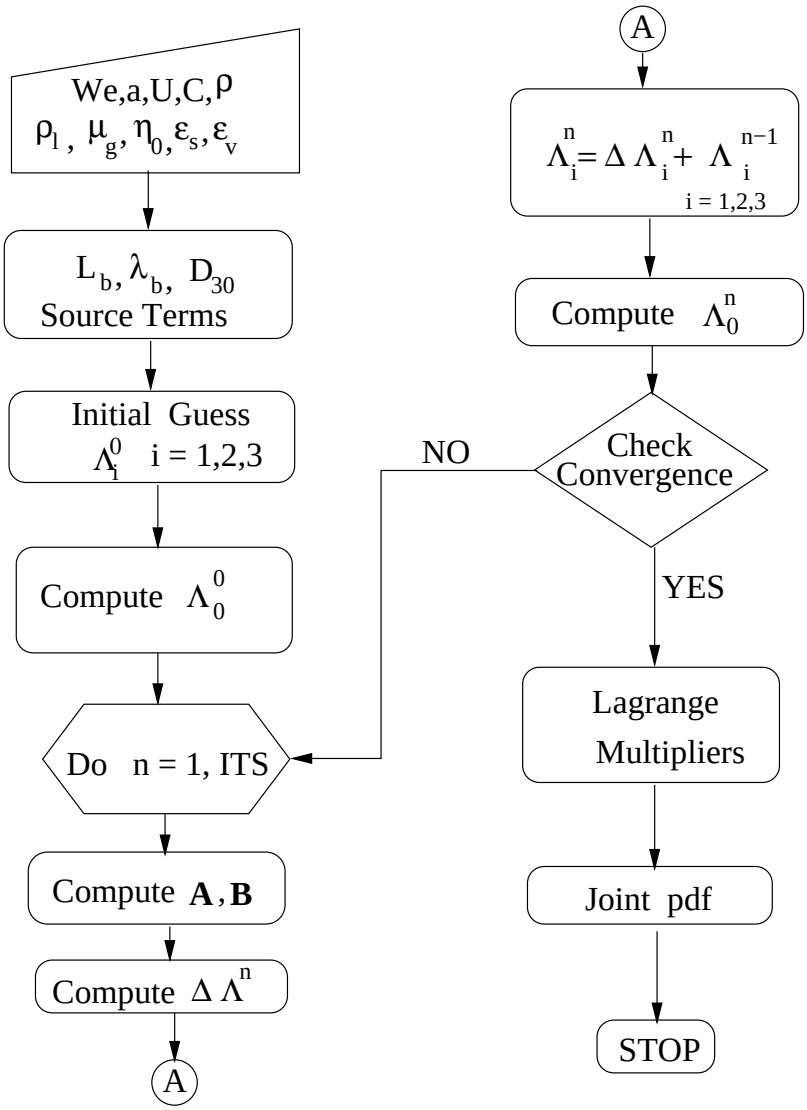

Figure 7.3: A macro-flow chart for the numerical scheme.

Lagrange multipliers for realistic droplet size distribution satisfies the following relations:

$$\Lambda_1 > 0, \quad \Lambda_3 > 0, \quad \text{and} \quad \Lambda_2 < 0$$
$$\Lambda_1 + \Lambda_3 > |\Lambda_2| \tag{7.47}$$

7.6 Results and Discussions

The MEP calculates the actual droplet size and velocity distributions for sprays when the nozzle exit conditions are specified. The nozzle exit conditions are: (a) Weber number We, (b) density ratio ρ, (c) velocity ratio U, (d) half-sheet thickness a^*, (e) initial disturbance amplitude η_0, (f) proportions of sinuous and varicose modes, ϵ_s and $\epsilon_v(\epsilon_v = 1 - \epsilon_s)$, (g) nozzle constant C, and (g) physical properties like gas phase viscosity, μ_g and liquid phase density, ρ_ℓ. Table 7.1 gives the values of the mass-mean diameter, the breakup length and the source terms for different nozzle exit conditions. Table 7.2 tabulates, for each case, the corresponding values of the Lagrange multipliers obtained by solving the nonlinear set of equations.

Figure 7.4 shows a three dimensional plot of the joint pdf for a typical spray resulting from the breakup of the liquid sheet with half-sheet thickness of $10\mu m$, Weber number of 50, density ratio of 0.001 and velocity ratio of 4. The corresponding iso-probability density curve is shown in Fig. 7.5. It is observed that there exists a global maximum for the distribution which is located at dimensionless diameter slightly less than one and dimensionless velocity close to one. It is also observed that the velocity distribution is wider for very small droplets. As discussed earlier, relative wide velocity distribution for such small droplets is practically insignificant.

The effect of Weber number on the number based droplet size distribution is shown in Fig. 7.6. It is observed that with the increase in the Weber number, We, while keeping other conditions at the nozzle exit fixed, the distribution curve shifts to smaller droplet sizes, and the population of large droplets is reduced as the liquid injection velocity is increased. It is also interesting to note that the maximum droplet diameter, as shown in Fig. 7.6, is reduced from about 350 μm at $We = 50$ to about 180 μm at $We = 500$. Figure 7.7 shows the effect of the Weber number on the number based droplet velocity distribution. It is found that the distribution peak shifts to larger droplet velocities with

Table 7.1: Estimates of mass-mean diameters and source terms for different nozzle exit conditions for $a^* = 10\mu m$, $\eta_0 = 0.1$, $\epsilon_s = \epsilon_v = 0.5$, $C = 3$, liquid density $\rho_\ell = 998kg/m^3$, gas dynamic viscosity $\mu_g = 1.8 \times 10^{-5} N.s/m^2$ and surface tension $\sigma = 0.073N/m$.

We	ρ	U	$D_{30}(\mu m)$	L_b	$\bar{S}_{mv}$	$\bar{S}_e$
50	0.001	4	157	151	2.869×10^{-2}	0.1708
		6	90	52	3.595×10^{-2}	0.3595
		8	60	20	3.693×10^{-2}	0.5170
		10	46	9	3.612×10^{-2}	0.6501
	0.002	4	108	75	2.837×10^{-2}	0.1703
	0.01	4	43	18	3.108×10^{-2}	0.1865
	0.1	4	14	0.3	1.269×10^{-2}	7.6138×10^{-2}
150	0.001	4	86	75	2.033×10^{-2}	0.1219
500	0.001	4	43	23	1.111×10^{-2}	6.6666×10^{-2}

Table 7.2: Values of Lagrange multipliers for different nozzle exit conditions for $a^* = 10\mu m$, $\eta_0 = 0.1$, $\epsilon_s = \epsilon_v = 0.5$, $C = 3$, liquid density $\rho_\ell = 998kg/m^3$, gas dynamic viscosity $\mu_g = 1.8 \times 10^{-5} N.s/m^2$ and surface tension $\sigma = 0.073N/m$.

We	ρ	U	Λ_0	Λ_1	Λ_2	Λ_3
50	0.001	4	−4.3481678748616	9.7400790999519	−19.943664831976	10.68000608991
		6	−2.5361610868733	3.6284506380845	−7.5558326062940	4.0450516935088
		8	−1.1235628222108	1.0041188370271	−2.0149310979988	1.0544634128522
		10	−0.4586785558384	1.2714337607212	−2.1569472254512	1.0058071415191
	0.002	4	−3.1484215040733	5.1110567194360	−10.563860598095	5.6623654733625
	0.01	4	−0.35343900742010	1.4902476114638	−2.1698424128921	1.0661735803751
	0.1	4	−0.276559846864092	1.0440937195022	−2.1382385844951	1.0168090551732
150	0.001	4	−3.3041352942455	5.6467781487816	−11.613666450495	6.2337659701939
500	0.001	4	−1.7724039089618	2.2356016845789	−4.6064573519788	2.4834614916249

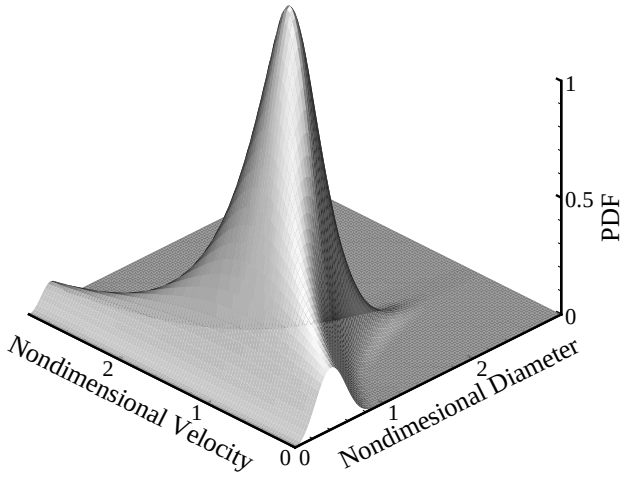

Figure 7.4: Joint droplet size and velocity distribution for $We = 50, \rho = 0.001$ and $U = 4$.

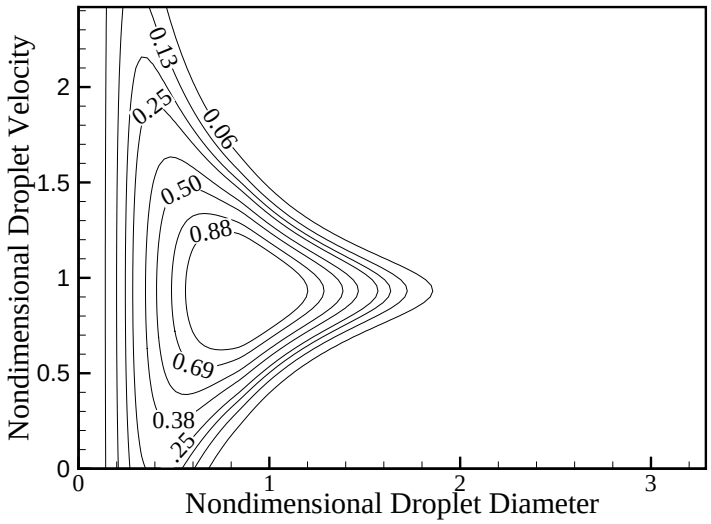

Figure 7.5: Iso-probability density curves for $We = 50, \rho = 0.001$ and $U = 4$.

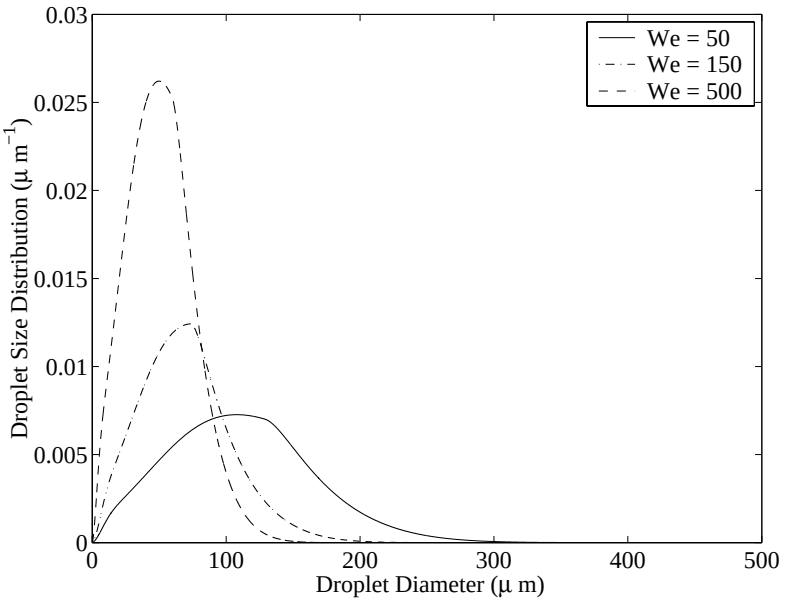

Figure 7.6: Effect of Weber number on droplet size distribution for $U = 4$ and $\rho = 0.001$.

the increase in the Weber number. However, at large droplet velocities, the distribution curves tend to collapse onto each other.

The effect of the density ratio on the number based size distribution is shown in Fig. 7.8. It is seen that the peaks of the distribution curves shift toward smaller droplet diameters as the density ratio is increased. This is due to the fact that as the density ratio is increased, or as the gas density is increased while keeping the liquid density constant, the mass-mean diameter D_{30} is decreased, which is also observed in Table 7.1. It is also interesting to note that the maximum droplet diameter is reduced from about 225 μm at $\rho = 0.002$ to about 40 μm at $\rho = 0.1$. Therefore, the quality of liquid atomization improves significantly at higher gas densities (or pressure). Figure 7.9 shows the effect of the density ratio on the number based velocity distribution. It is observed that the distribution peak shifts to the larger droplet velocities with the increase in the density ratio.

The effect of the gas-to-liquid velocity ratio on the droplet size distribution is shown in Fig. 7.10. It is observed that with the increase in the gas phase velocity, the distribution curves shift to small droplet sizes. This is due to the fact that the higher momentum of

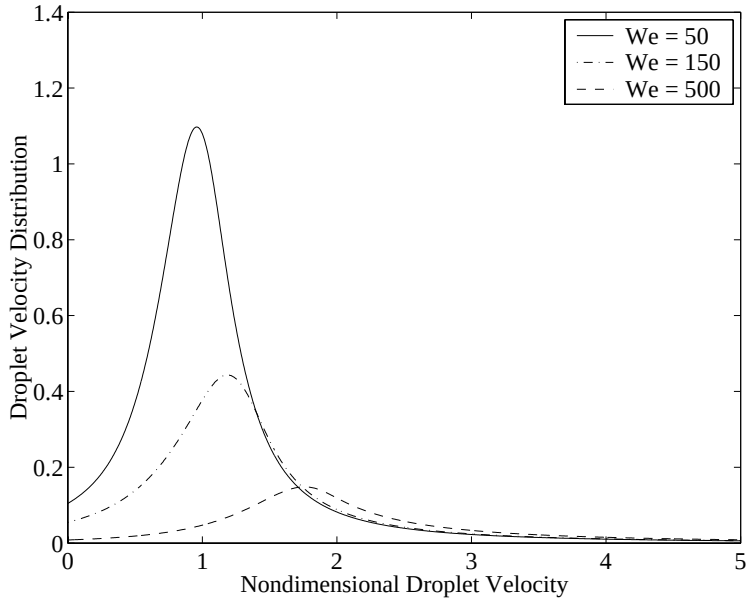

Figure 7.7: Effect of Weber number on droplet velocity distribution for $U = 4$ and $\rho = 0.001$.

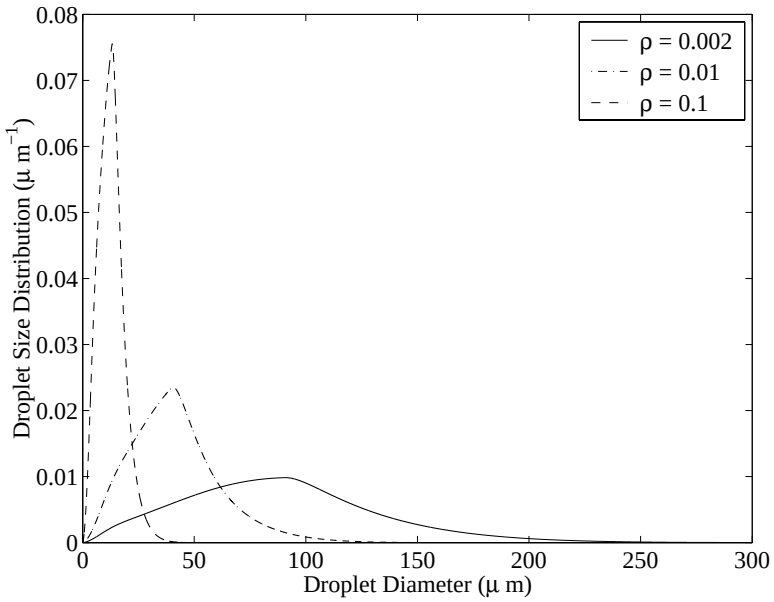

Figure 7.8: Effect of density ratio on droplet size distribution for $We = 50$ and $U = 4$.

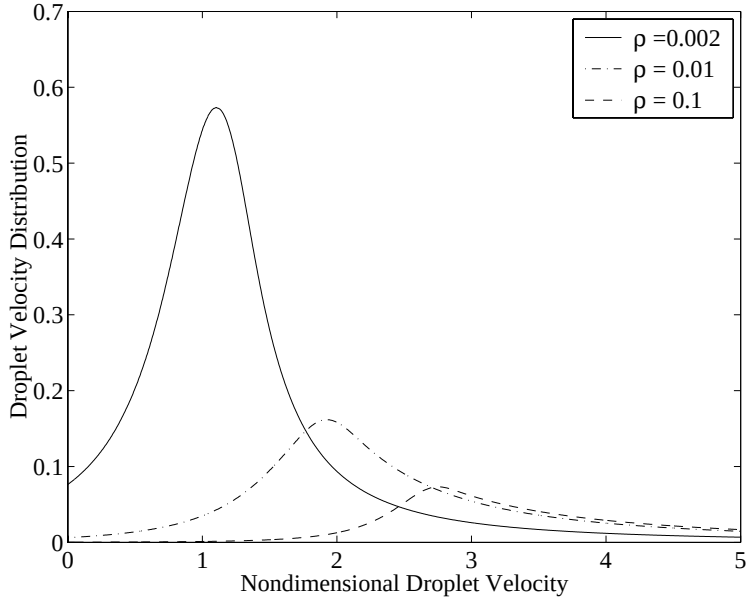

Figure 7.9: Effect of density ratio on droplet velocity distribution for $We = 50$ and $U = 4$.

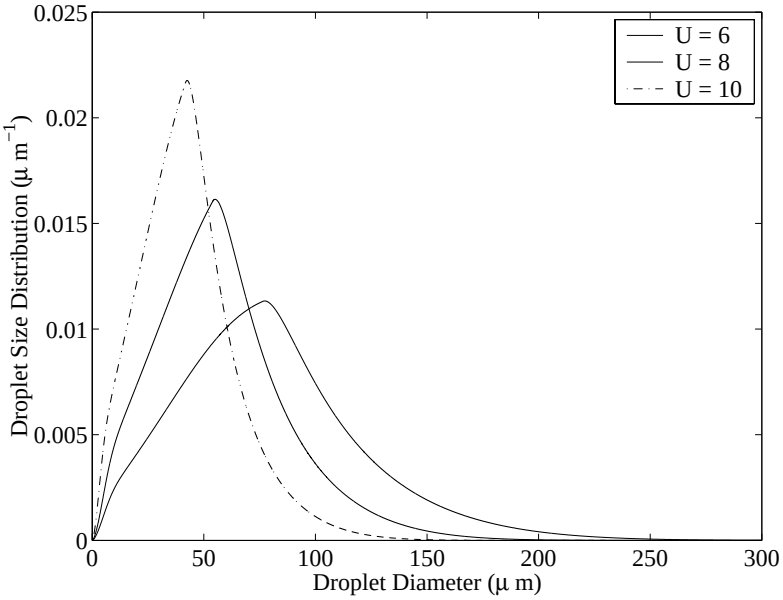

Figure 7.10: Effect of velocity ratio on droplet size distribution for $We = 50$ and $\rho = 0.001$.

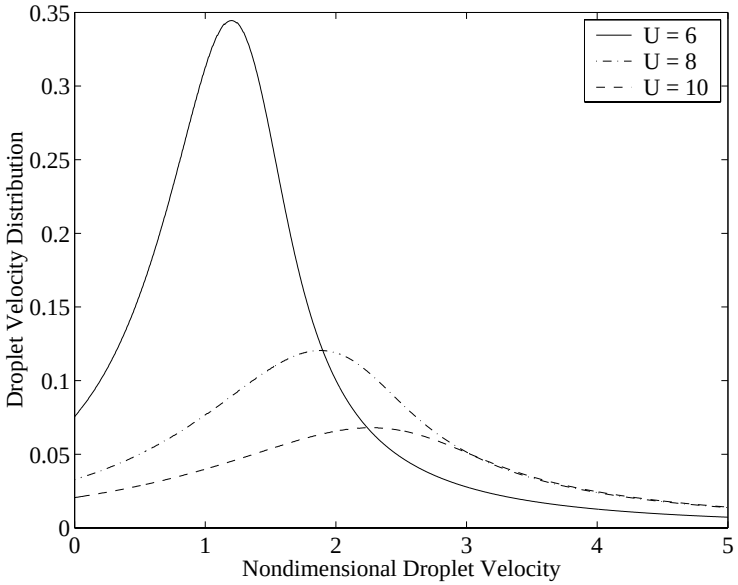

Figure 7.11: Effect of velocity ratio on droplet velocity distribution for $We = 50$ and $\rho = 0.001$.

the gas phase results in a better overall atomization and hence much smaller mass-mean diameter for the entire spray. It is observed that the maximum droplet diameter is reduced from about 250 μm at $U = 6$ to about 150 μm at $U = 10$. Figure 7.11 shows the effect of the velocity ratio on the droplet velocity distribution. It is observed that with the increase in the gas phase velocity, the peak of the distribution moves to the large droplet velocities.

7.7 Summary

A predictive model for the initial droplet size and velocity distribution in sprays has been formulated, which incorporates both the deterministic and the stochastic aspects of liquid atomization processes. The deterministic aspect is characterized by the linear and the nonlinear instability theories, and the stochastic aspect is described by statistical means through an application of the maximum entropy principle based on Bayesian entropy. The two sub-models are linked together by the various source terms that represent the interaction of the spray with its surrounding and the prior distribution which carries information about the growth of the unstable waves at the two liquid-gas interfaces. It is found that the population of large droplets is significantly reduced with the increase in Weber number, density ratio and gas-to-liquid velocity ratio. It is also found that the peaks of the velocity size distributions shift to the larger droplet velocities with the increase in the Weber number, gas-to-liquid density and velocity ratios.

Chapter 8

Experiments

Experimental investigation of the breakup process of the liquid sheet leading to the spray formation is carried out for the verification of the theoretical model discussed in the earlier chapters. The main objectives for the experimental work are to obtain the breakup length and the breakup characteristics of the liquid sheet in a co-flowing gas stream, and the initial droplet size and velocity distributions of the resulting spray. Once these quantities are measured, they can be used for the verification of the deterministic and the stochastic sub-models.

Two different nozzle configurations are used in experiments. First is a planar research nozzle which produces a plane liquid sheet blasted by a co-flowing gas stream on both sides of the liquid sheet. The geometry of the planar nozzle matches well with the theoretical model discussed earlier. Secondly, an actual gas turbine nozzle from Pratt & Whitney Canada (PWC) has been used in the experimental investigation of its spray characteristics.

In order to execute the experimental works, primarily two items of equipment have been used. A high speed CCD camera is used to obtain the breakup length and the breakup characteristics of the liquid sheet; and a two-component phase-Doppler particle analyzer (PDPA) system is used to obtain the droplet size and velocity distributions in sprays.

8.1 Apparatus

The experiments are conducted on a test rig, shown in Fig. 8.1. The test rig has a traversing unit which allows movements in three perpendicular directions. It also has a mounting plate which allows easy interchangeability of different nozzles. The table in front of the traversing unit holds the high-speed CCD camera and its associated light sources, and the transmitting and the receiving optics for the PDPA system.

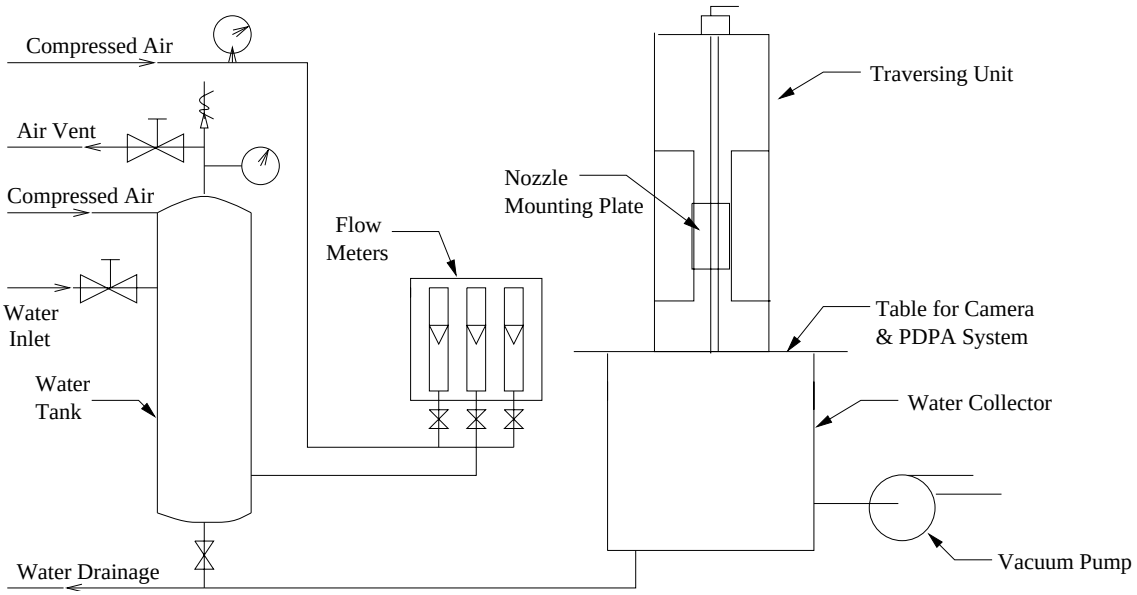

Figure 8.1: Schematic of the test rig used for experimental study.

The liquid used for the experiment is water, which is stored in a galvanized tank with a pressure rating of 125 psi (gauge). The gas phase is air which is fed into the system at a line pressure of 60 psi (gauge). In order to maintain constant pressure during the course of the experiment, the tank is pressurized by compressed air to the desired operating pressure. In general, the water pressure is maintained at 70 psi (gauge) for the entire experiment.

Flow meters are used to maintain the desired flow rates for both the liquid and gas phases. Two sets of flow meters are used for different nozzle configurations. In case of the planar nozzle, the operating ranges of the flow meters are $0. - 1.0\ gpm$ $(6.31 \times 10^{-5} m^3/s)$ and $0. - 7.0\ scfm$ $(47.14 \times 10^{-5} m^3/s)$ for water and air, respectively. However, in case of

the industrial nozzle (PWC nozzle), the flow meter for water is changed to handle a range of $106 - 388\ ml/min$, whereas the flow meter used for air remains the same. Adequate water filters are placed along the flow lines to prevent any possible clogging of the nozzles.

During the course of the experiment, the nozzles are mounted vertically downward on the traversing unit, which allows the water to be collected in the collector placed downstream. The collector has a honeycomb screen placed approximately 1 m below the nozzle exit and is connected to a vacuum pump near its bottom. These arrangements help to improve the uniformity of the flow conditions in the collector due to the proper air ventilation and prevent the mist and recirculation of large number of small droplets. This improves the overall quality of the spray measurements.

The investigation of liquid sheet breakup and the subsequent spray formation is first conducted with a two-dimensional planar nozzle as shown in Fig. 8.2, which was designed by Jazayeri & Li [63]. Within the two-dimensional nozzle, the central channel used for liquid flow has dimensions of 0.254 mm by 25.4 mm (aspect ratio 100:1) at the nozzle exit. Two air flow paths, located on either side of the liquid channel, both have the dimension of 1.397 mm by 25.4 mm. A set of honeycomb and fine screens are placed upstream of the nozzle contraction for both the flow passages to reduce the turbulence level in the flow.

The PWC nozzle, shown in Fig. 8.3, is mounted inside an air-box to provide the air flow needed for this gas turbine nozzle. For proprietary reasons, limited information is available about the geometry of the nozzle. The sheet thickness for this nozzle is also not known, which varies with the air and water flow rates. The nozzle has both inner and outer air flow passages. It is difficult to identify the proportion of the actual inner and outer air flow rates and hence, the actual gas phase velocities are not readily obtained under this situation. However, with the known air flow rate, measured from the flow meter, and the dimensions of both the inner and outer air passages, the air velocities can be estimated. Both the inner and the outer air velocities are assumed to be equal, in parallel with the present physical model. The liquid velocity is obtained by measuring the sheet velocity close to the nozzle exit by the PDPA system. The liquid sheet thickness is then calculated based on the sheet velocity and the measured liquid mass flow rate.

The PWC nozzle also produces swirl for both the liquid and gas flows. Even though the nozzle geometry does not match the present physical model, attempts will still be made

(a)

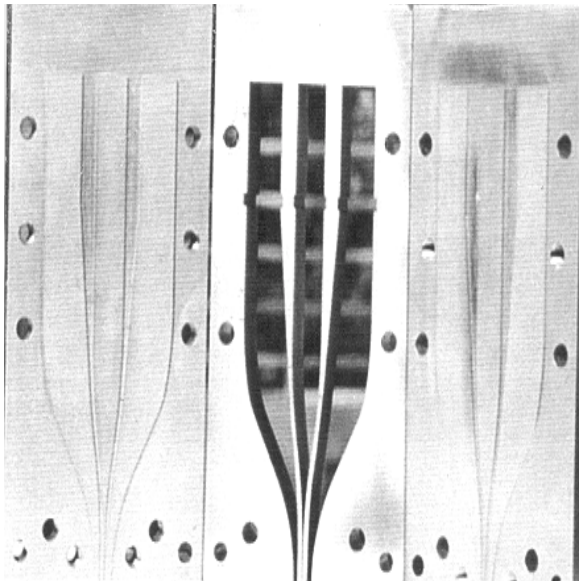

(b)

Figure 8.2: The planar nozzle used in experiment. (a) nozzle assembly; (b) cross-sectional view of nozzle exit (dimensions are in millimeters).

Figure 8.3: The PWC nozzle used for the experiment.

in the next chapter to compare the experimental results from the PWC nozzle with those from the theoretical model, which is based on a planar liquid sheet geometry.

8.2 Experimental System

In order to obtain the breakup characteristics of the liquid sheets and the size and velocity distributions for the subsequently formed droplets, primarily two systems are used. The breakup length L_b and the breakup characteristics are measured by using a high-speed CCD camera. The initial droplet size and velocity distributions are obtained by using a laser based non-intrusive measurement system called phase-Doppler particle analyzer (PDPA).

8.2.1 High-Speed CCD Camera

The flow visualization of the spray is conducted by a digital high-speed CCD camera ($SensiCam^{HS}$). The CCD camera has the capacity of taking single or multiple exposures (up to ten) on one frame. The exposure time can be varied from $100ns$ to $1000\mu s$ in steps of $1\mu s$. Delays between the exposures can also be set in the range between zero (no delay)

Pixel Size	$9.9\mu m \times 9.9\mu m$
Sensor Format	$1/2''$
Scan Area	$6.3mm \times 4.8mm$
Readout Time	$30fps$
Binning Horizontal	1 to 8
Binning Vertical	1 to 128

Table 8.1: Specifications for the $SensiCam^{HS}$ CCD camera.

Lens Attachment	WD	.5X Adapter Low-High	.67X Adapter Low-High	1X Adapter Low-High	2X Adapter Low-High
0.25X	334	120.0-12.8	95.6-9.6	64.0-6.4	32.0-3.2
0.5X	160	64.0-6.4	47.8-4.8	32.0-3.2	16.0-1.6
0.75X	107	42.7-4.3	31.8-3.2	21.3-2.1	10.7-1.1

Table 8.2: Working distance (WD) (in mm) for the standard lens and various lens adapters for TenX zoom system.

to $1000\mu s$. The camera can record images at a rate of $10,000,000$ images per second, and has resolution of $640(H) \times 480(V)$ pixels and a high ASA rating between $2,500$ and $6,400$. Additional specifications for the camera are provided in Table 8.1.

The camera is operated through software which allows different features of $SensiCam^{HS}$ to be used easily. Optical lenses are used in conjunction with the camera to get images of appropriate interrogation area on the liquid sheet. The lens system consists of a lens attachment and adapters that give a wide range of working distance (WD, *i.e.*, distance between object and the camera) and field of view. The zoom matrix for the $TenX$ lens system is provided in Table 8.2.

The digital images, once captured by the camera, are processed by using image analysis software ($ImagePro$). $ImagePro$ is versatile software which allows enhancement, noise

reduction, and spatial measurements of the images. By using *ImagePro*, quantitative estimates of the breakup characteristics of the liquid sheet can be obtained.

Figure 8.4 illustrates the arrangement used for taking pictures with the CCD camera. Proper lighting is very important to achieve a good quality image of the breakup process of the liquid sheet. Two halogen photo optic lamps (300 W rating) are used to get the desired quality of lighting.

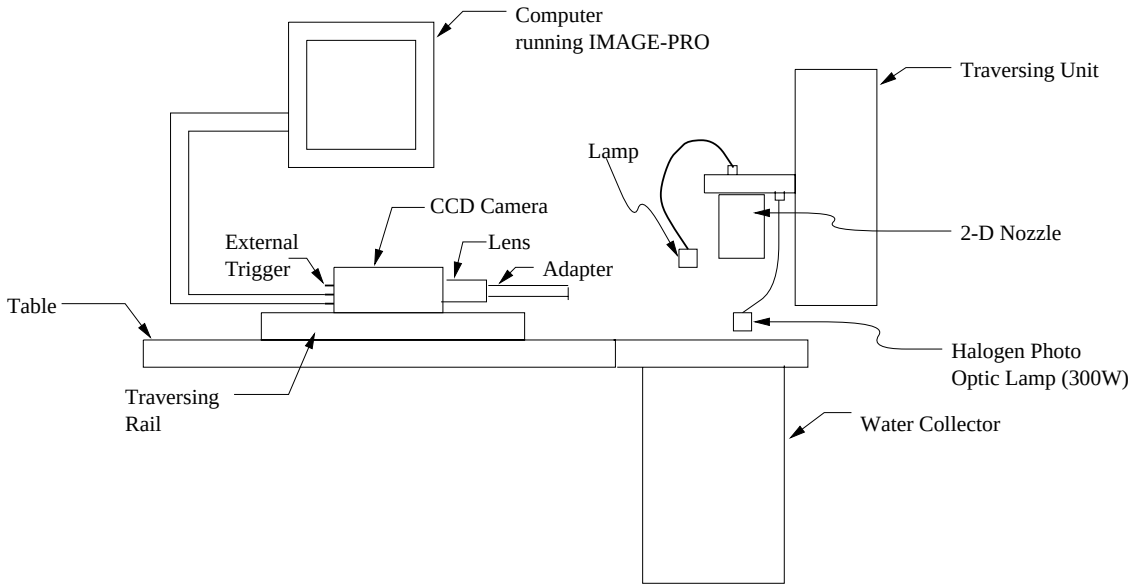

Figure 8.4: Schematic of the arrangement used for taking pictures with CCD camera.

8.2.2 Phase-Doppler Particle Analyzer (PDPA)

The Aerometrics PDPA used for the experiment is a commercial particle sizing system based on the phase-Doppler method [71]. This system is being used with confidence by a number of researchers in our laboratory to obtain droplet size and velocity distributions in sprays [98, 99]. The schematic of the entire system is shown in Fig. 8.5. This is a two component system which allows the flexibility of measuring the diameter and velocity of the droplets simultaneously. It consists of an argon ion laser, a beam separator and fibre optic module, a transmitter, a receiver and photo-multipliers, a signal analyzer, and a PC

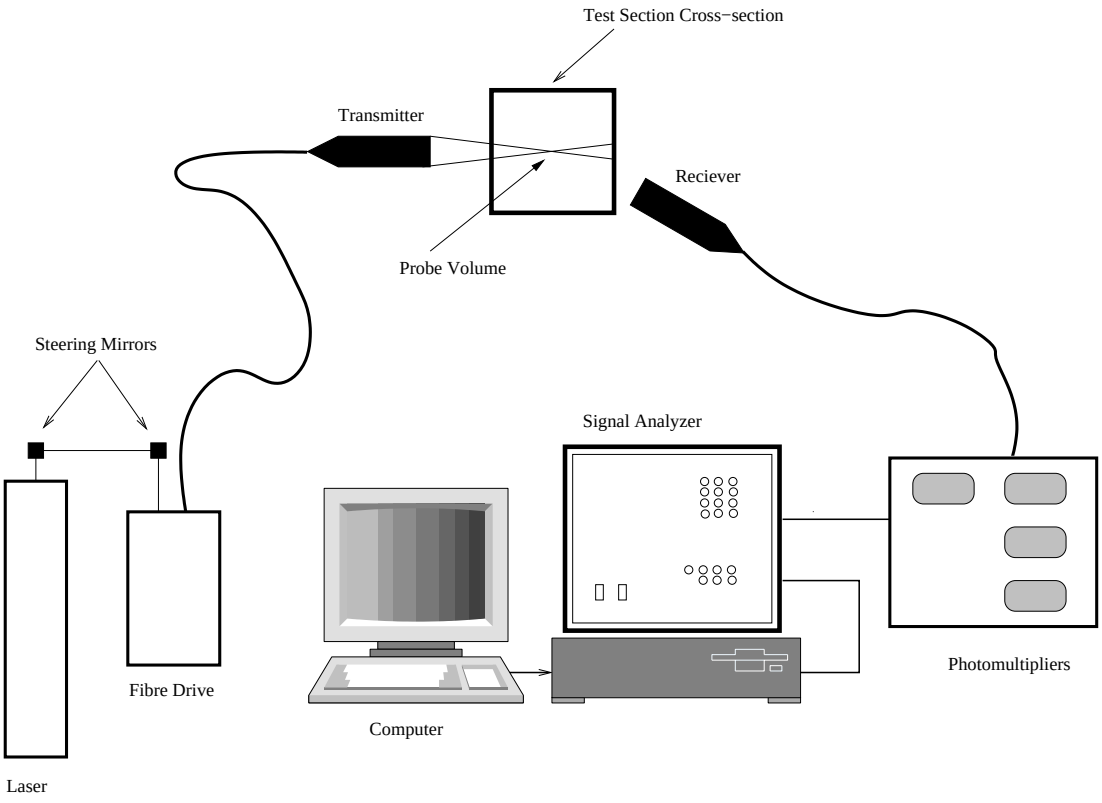

Figure 8.5: Schematic of the PDPA system [99].

computer.

A water-cooled Coherent Inova 90 argon-ion laser is used to produce the desired laser beam with an output power range of 250 mW to 2 W. Typical operating power used is $500 - 650$ mW. The polarized laser beam is guided by the two steering mirrors into the beam separator, where the beam splits into two beams. One of these beams passes through a Bragg cell which shifts the frequency of the beam by 40 MHz. After the Bragg cell, each beam splits again, which results into four beams - a pair of green (515 nm) and a blue (488 nm) with a shifted beam per pair. All four beams are then launched into mode-preserving fibres and sent into the transmitter module with coupling efficiencies varying in the range 30 % to 50 %.

The transmitter module consists of four fibre-optic terminators, collimating optics,

removable beam expanding telescope, and focusing lens. The combination of these optic devices produces the measuring or the probe volume by focusing all the four beams to a common point in space. The receiver, which is also focussed at the same point, consists of a receiving lens, a spatial filter (slit), collimating optics, and a multi-mode, multi-fibre cable termination. The image of the probe volume gets transmitted to the photo-multiplier module consisting of four photo-multipliers. The control of the photo-multipliers and the subsequent signal processing is done by the Doppler Signal Analyzer (DSA). By using fast Fourier transform, DSA evaluates the frequency and the phase of the Doppler signal. The entire system is controlled by Aerometrics software. Appendix E lists the optical parameters and some typical settings used in the experiments for the Aerometrics PDPA system.

8.3 Results and Discussions

The breakup characteristics and the breakup lengths of the liquid sheet are obtained by using the high speed CCD camera for different liquid and gas flow rates. Figure 8.6 shows the breakup process of the liquid sheet produced by the planar nozzle for two different air flow rates. It is observed that at low air flow rate, *i.e.*, at low gas-to-liquid velocity ratio, the breakup length is long. However, by increasing the air flow rate on both sides of the liquid sheet, the breakup length decreases substantially. It is to be noted that the breakup location is difficult to identify as the stretching and the shearing of the ligaments take place over a certain distance before the droplets are produced. When the water flow rate is increased, while keeping a low air flow rate, it is observed that the large momentum of the liquid sheet tends to cause the breakup location to move further downstream of the nozzle, as shown in Fig. 8.7a. The breakup region for this case is stretched over a few millimeters and the large wave distortion at the breakup location becomes more obvious. However, by increasing the gas-to-liquid velocity ratio, the momentum of the air tends to blast the liquid sheet from both sides resulting in much shorter and distinct breakup location, as observed in Fig. 8.7b.

The deformation of the liquid sheet near the breakup region can be observed by capturing the side view of the liquid sheet. Figure 8.8 shows such breakup characteristics

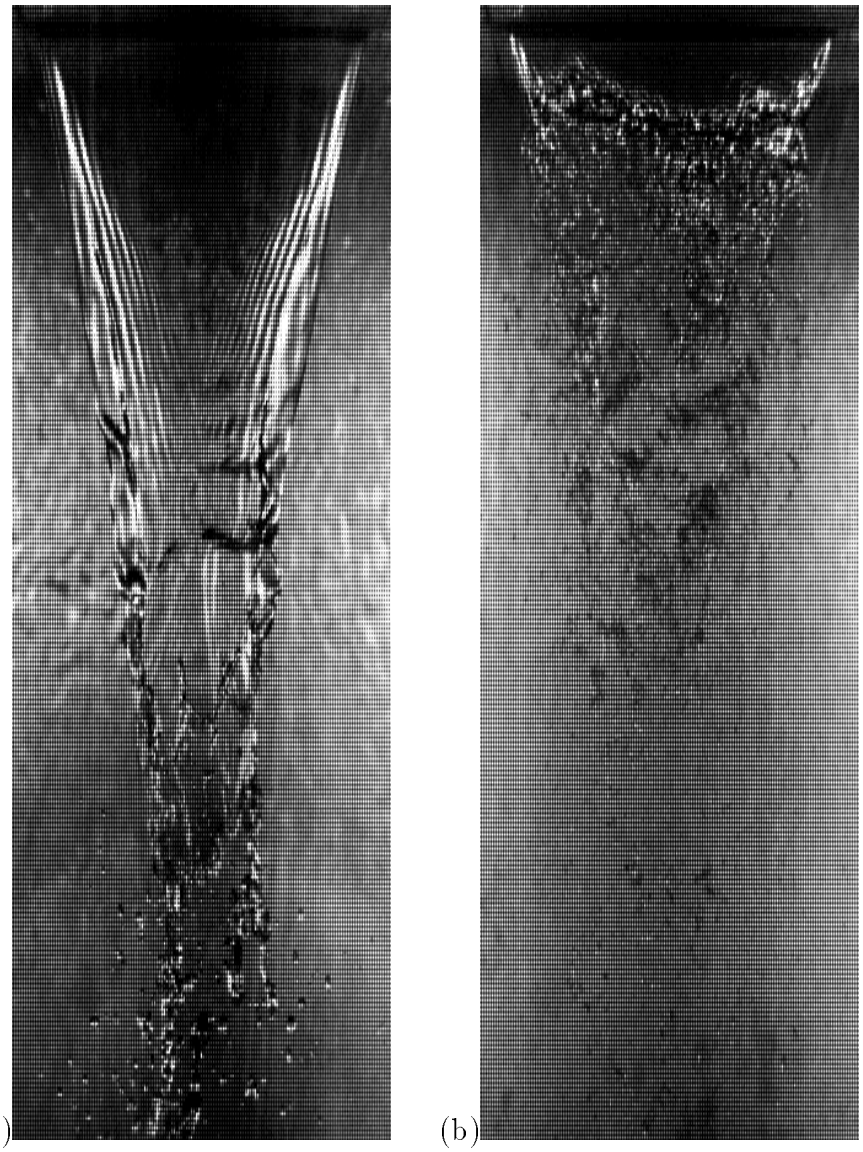

(a) (b)

Figure 8.6: Breakup of the liquid sheet from the planar nozzle with $Re_d = 981.0$ and $We = 6.7$. (a) $U_\ell = 2.0\ m/s, U_g = 27\ m/s$; (b) $U_\ell = 2.0\ m/s, U_g = 93\ m/s$.

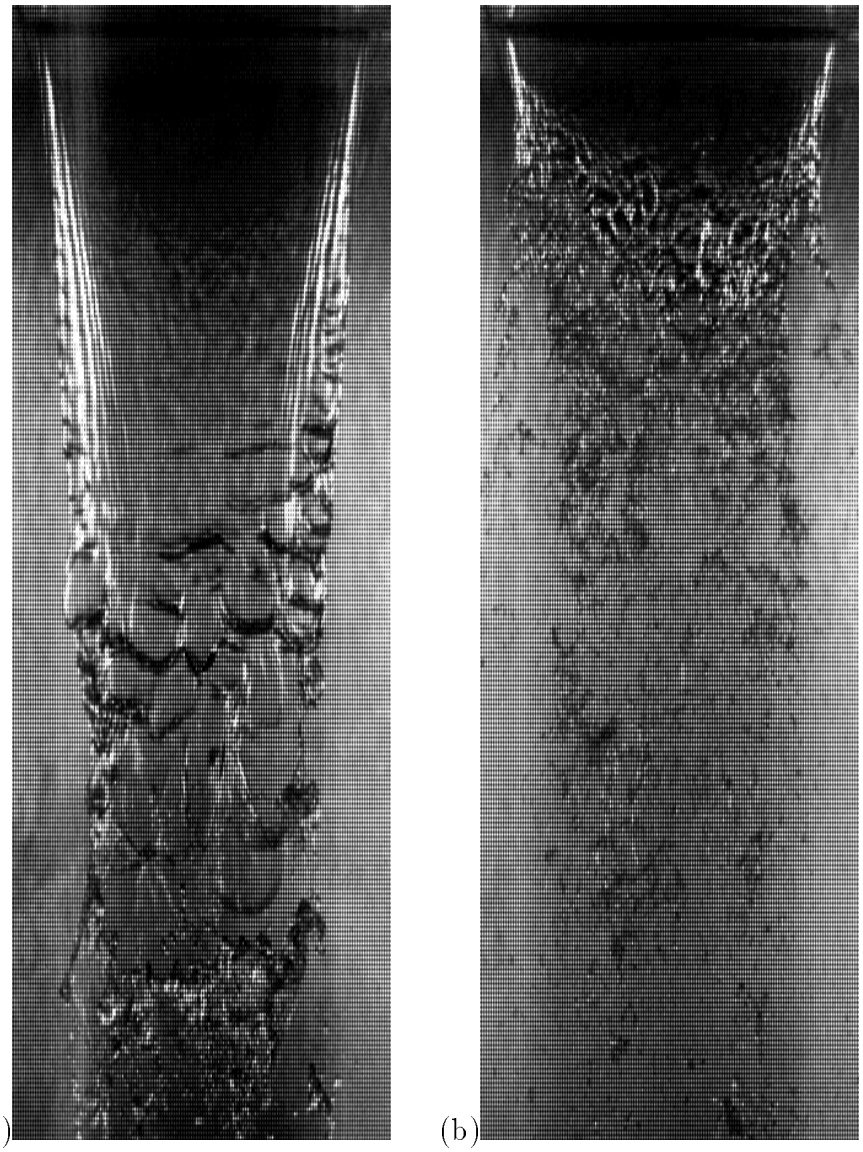

(a) (b)

Figure 8.7: Breakup of the liquid sheet from the planar nozzle with $Re_d = 1956.9$ and $We = 26.5$. (a) $U_\ell = 3.9\ m/s, U_g = 40\ m/s$; (b) $U_\ell = 3.9\ m/s, U_g = 93\ m/s$.

of the liquid sheet for two different flow conditions. It is found that initially the liquid sheet remains undisturbed for some distance from the nozzle exit. Slowly the nonlinear interaction of different modes of disturbance becomes prominent, which eventually leads to the breakup of the liquid sheet with large surface deformation near the breakup location. However, with the increase in air flow rate, as shown in Fig. 8.8b, the large deformation of the two interfaces are not prominent enough. The momentum of the increased air flow tends to breakup the bulk liquid associated with the large surface deformation and carries the liquid mass along with it to form droplets in the downstream section.

Figure 8.9 shows the quantitative variation of the breakup length with the air velocity for different values of liquid sheet velocities. It is observed that within the operating conditions, at a given water flow rate, the breakup length decreases with the increase in the atomizing air velocity. It is found that, for this planar nozzle, the difference in the breakup lengths for different liquid velocities is large at low air flow rates. It is also observed that at a given air flow rate, the breakup length tends to increase with the increase in the liquid flow rate.

Figure 8.10 shows the breakup characteristics of the liquid sheet produced by the PWC nozzle. It is observed that the breakup length decreases with the increase in the air flow rate. At high air flow rates, the breakup location is not well defined. It is to be noted that the sheet thickness also changes with different combinations of liquid and gas velocities.

In order to obtain the initial droplet size and velocity distributions, the PDPA measurements need to be carried out in the immediate vicinity of the breakup location of the liquid sheet. As observed from the images of the liquid sheet, the region near the breakup point has large irregular droplets and often some stretched ligaments. Therefore, PDPA measurements in this location often become difficult, if not impossible. Also, since the PDPA only accounts for the spherical droplets, the validation rates of the measurements are often low. Keeping these difficulties in mind, attempts have been made to obtain reasonable measurements as close as possible to the breakup location.

It is to be noted that there is an error of about 1 % in droplet velocity measurements and an error of about 4 % associated with size measurements [98], except for small droplets less than 10 μm, for which errors may be large. The PDPA system used in the experiments is already calibrated and expected to have an error even less than 4 % for larger droplet

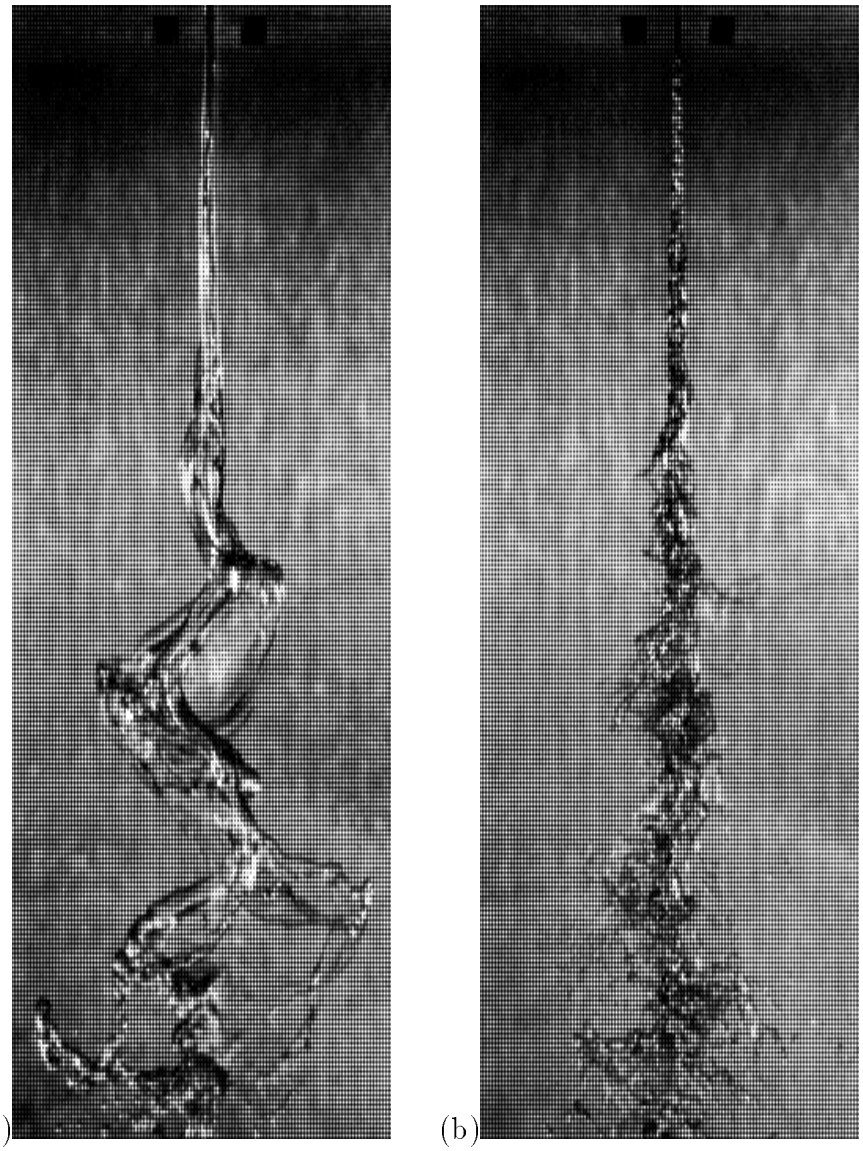

(a) (b)

Figure 8.8: Side view of the liquid sheet breakup process from the planar nozzle. (a) $U_\ell = 2.0\ m/s, U_g = 27\ m/s, Re_d = 981.0$ and $We = 6.7$; (b) $U_\ell = 6.9\ m/s, U_g = 53\ m/s, Re_d = 1956.9$ and $We = 81.5$.

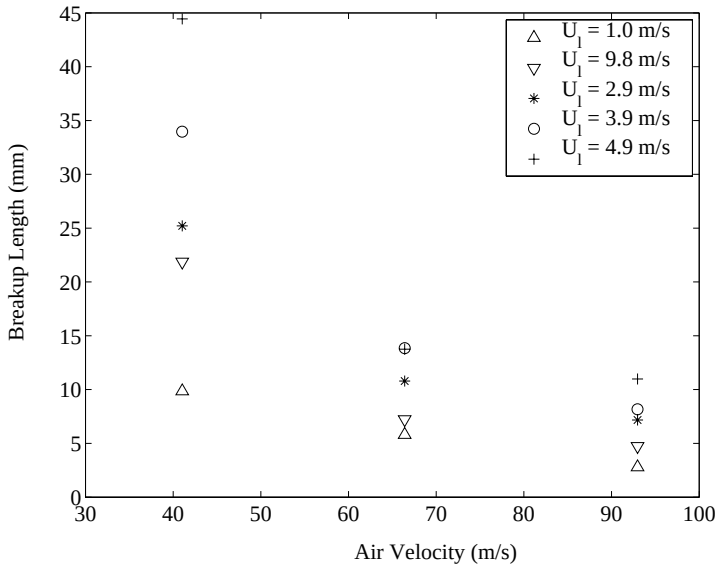

Figure 8.9: Variation of the breakup length of the planar nozzle with the air velocity for different liquid velocities.

size measurements. However, the system errors are of secondary nature in comparison to the error encountered due to the inability of the PDPA system to measure all the droplets passing through its probe volume and hence giving rise to a validation rate of only around 60 %. Therefore, it is judicious to refrain from allocating error bars with the experimental data obtained from the PDPA system.

Figure 8.11 shows the variation of the dimensional droplet size distribution of the planar nozzle with the droplet diameter for $U_g = 80\ m/s$ and at two different liquid velocities. It is observed that at lower water flow rate, the population of droplets below 100 μm is large. With the increase in the water flow rate, more large droplets are produced.

The dimensional droplet velocity distribution for the planar nozzle is shown in Fig. 8.12. It is observed that at higher liquid flow rate, the population of droplets with low velocities is large. However the number of droplets with high velocities is the same for both liquid flow rates. The maximum droplet velocity is about 45 m/s. The spray produced by this planar nozzle is usually coarse with large number of non-spherical particles. As a result, the validation rate for the droplet size and velocity measurements is around 65 %.

(a)

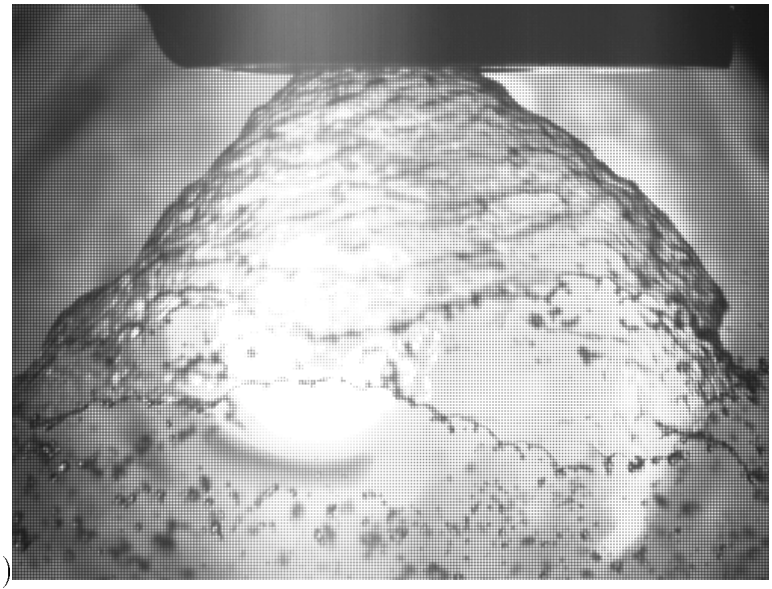

(b)

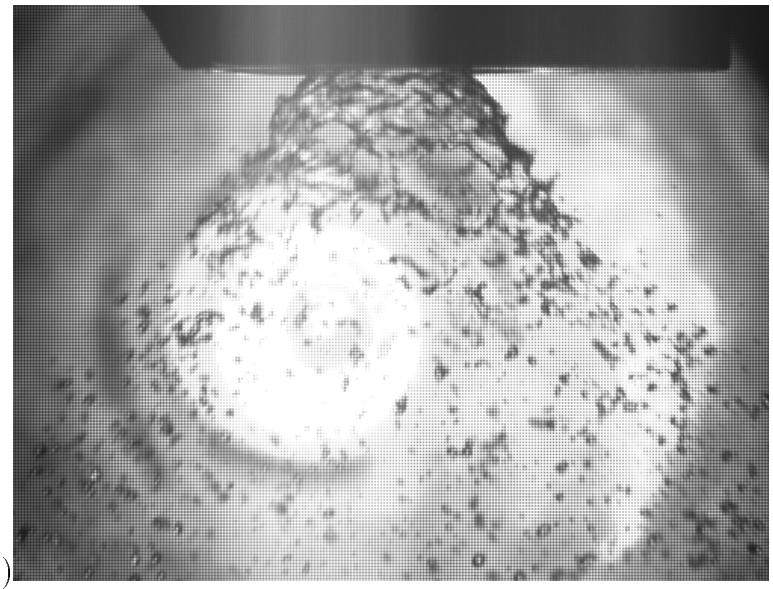

Figure 8.10: Breakup of the liquid sheet from the PWC nozzle. (a) $U_\ell = 3.9\ m/s, U_g = 28\ m/s, Re_d = 1021.8$ and $We = 21.5$; (b) $U_\ell = 4.2\ m/s, U_g = 42\ m/s, Re_d = 1023.3$ and $We = 23.3$.

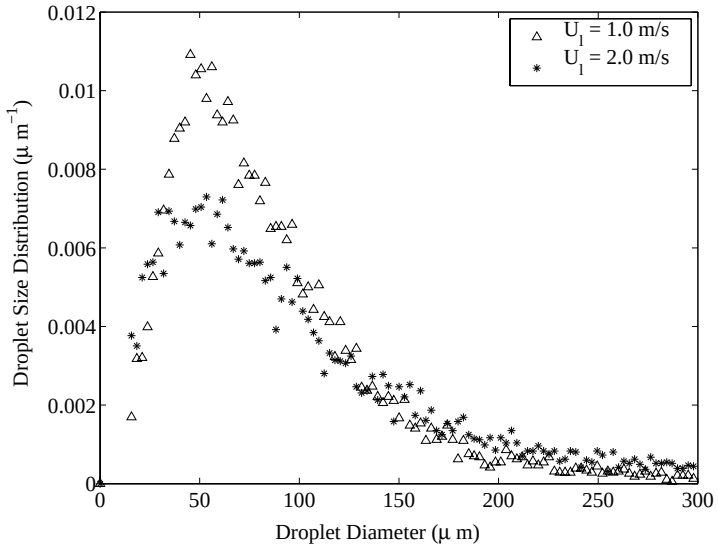

Figure 8.11: Droplet size distribution of the planar nozzle for $U_g = 80\ m/s$ and two different liquid velocities.

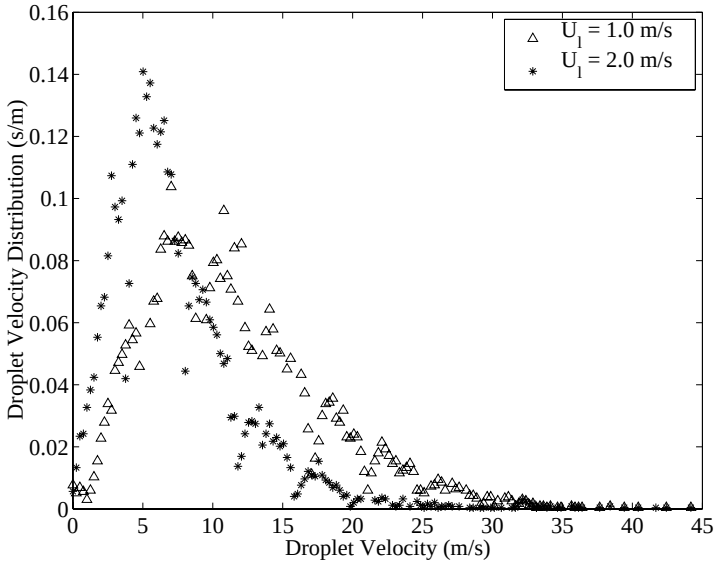

Figure 8.12: Droplet velocity distribution of the planar nozzle for $U_g = 80\ m/s$ and two different liquid velocities.

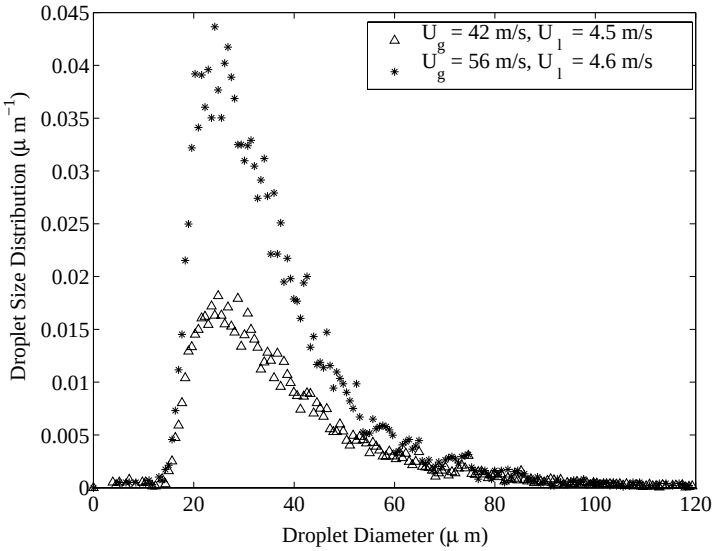

Figure 8.13: Droplet size distribution of the PWC nozzle for two different flow conditions.

In case of the PWC nozzle, measurements near the breakup location are shown in Figs. 8.13 and 8.14. The dimensional droplet size distribution in Fig. 8.13 shows that a significantly large number of small droplets are produced with the increase in the atomizing air velocity. A good quality spray is produced by this nozzle and small droplets, less than 10 μm, are present in the spray. The sheet velocity is obtained by conducting PDPA measurement close to the nozzle exit with measurement control volume near the edge of the liquid sheet.

Figure 8.14 shows the dimensional droplet velocity distribution of the spray produced by the PWC nozzle for two different flow conditions. The velocity distributions are uniform with the peak shifting towards the higher velocity for the higher gas flow rate. The maximum droplet velocities are 30 m/s for $U_g = 42\ m/s$ and 40 m/s for $U_g = 56\ m/s$, respectively. Since the spray is much uniform and fine, a high validation rate, about 82 %, can be obtained for the droplet size and velocity measurements at the vicinity of the breakup region.

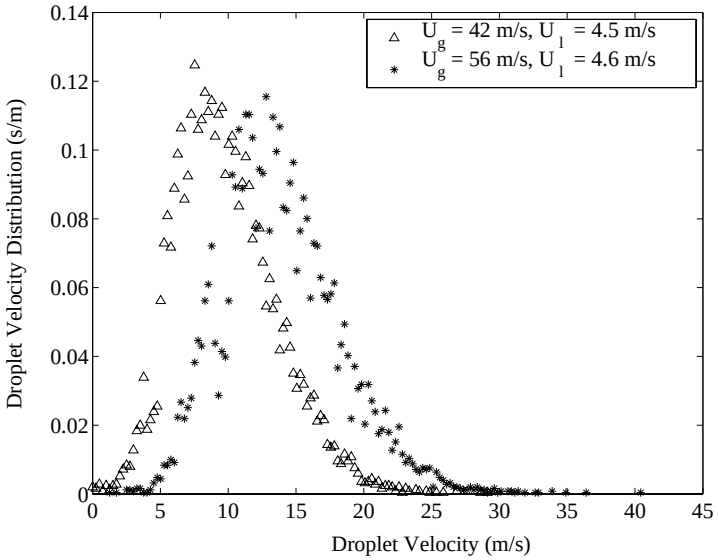

Figure 8.14: Droplet velocity distribution of the PWC nozzle for two different flow conditions.

8.4 Summary

The experiments are conducted for a planar research nozzle and an actual gas turbine nozzle to obtain the breakup length and the initial droplet size and velocity distributions. A high speed CCD camera is used to obtain the breakup characteristics of the liquid sheet. It is found that the breakup length decreases with the increase in the gas phase velocity. The droplet size and velocity distributions are obtained by using a two-component phase-Doppler particle analyzer system. It is found that conducting measurements near the breakup region of the spray is extremely difficult.

Chapter 9

Experimental Validation of the Model

In the preceding chapters, the theoretical development of the spray model that incorporates both the deterministic and the stochastic aspect of the spray has been discussed. For specified flow conditions at the nozzle exit, the spray model predicts the breakup length of the liquid sheet and also the initial droplet size and velocity distributions of the subsequent formed sprays. The experimental techniques for the model validation have been discussed in Chapter 8. In the validation process, the quantities that need to have reasonable agreement with their theoretical counterparts are the breakup length L_b and the initial droplet size and velocity distributions.

For the verification of the model, the planar research nozzle is first used, which produces a 254 μm thick liquid sheet blasted on both sides by equal velocity gas streams. The geometry of this nozzle matches well with the liquid sheet model used here. As a second step, the model is validated against an annular research nozzle, which offer a better simulation of the real air-blast gas turbine nozzles. This annular nozzle also generates a 254 μm thick liquid sheet, which is blasted by equal velocity of inner and outer gas streams. Finally, the model is tested for the actual gas turbine nozzle provided by Pratt & Whitney Canada (PWC nozzle).

9.1 Comparison of Breakup Length

The spatial evolution of the two liquid-gas interfaces up to the breakup point is theoretically obtained from the nonlinear instability analysis of the plane liquid sheet. This is verified with the experimental breakup length obtained from the CCD image of the plane liquid sheet.

Figure 9.1 shows the comparison of the liquid sheet profiles between the experiment and the theoretical prediction for the planar nozzle. The water and air velocities are 2 m/s and 27 m/s, respectively, which corresponds to a Weber number of 6.7, gas-to-liquid velocity ratio of 13.5 and gas-to-liquid density ratio of 1.202×10^{-3}. Since, the wavenumber k is needed for the model, it is assumed that the disturbance wavenumber corresponds to the dominant wavenumber for the sinuous mode. The dominant wavenumber is then calculated from Eq. (4.4) and is found to be 0.7041 for the specified flow conditions. The experimental breakup length, obtained from Fig. 9.1a, is around 20 mm. It is found that the theoretical evolution of the liquid sheet matches well with the experimental result for $\eta_0 = 0.00008$ and $\epsilon_s = \epsilon_v = 0.5$, with a breakup length $L_b = 157$ (or 20 mm). For a fixed value of ϵ_s, the breakup length is obtained by using a trial and error method over a range of η_0. As observed earlier, the breakup length decreases with the increase in the value of η_0.

It might appear from the side view of the liquid sheet that breakup occurs further downstream. However, the front view of the liquid sheet clearly suggests that indeed the liquid sheet breaks up much earlier and the ligament formation and their stretching cause the interfaces to have large deformations, which are observed in the side view of the liquid sheet. It is to be noted that the nonlinear instability analysis can predict the profiles of the two liquid gas interfaces till the breakup point. Therefore, the ligament formation and the further stretching of the liquid sheet, as shown in Fig. 9.1a, is not observed for the theoretical prediction.

Figure 9.2 shows the breakup process of the liquid sheet for a different set of flow conditions. Here, $We = 14.9, U = 13.8, \rho = 1.202 \times 10^{-3}, k = 1.829, \eta_0 = 0.0002$ and $\epsilon_s = \epsilon_v = 0.5$. The experimental breakup length is around 17 mm, and the breakup length obtained from the model is $L_b = 134$ (or 17 mm). Even though the breakup length is more or less the same as the previous case, the images of the two liquid sheets are different. This trend is also observed for the theoretical predictions, where the sheet profiles in Figs. 9.1c

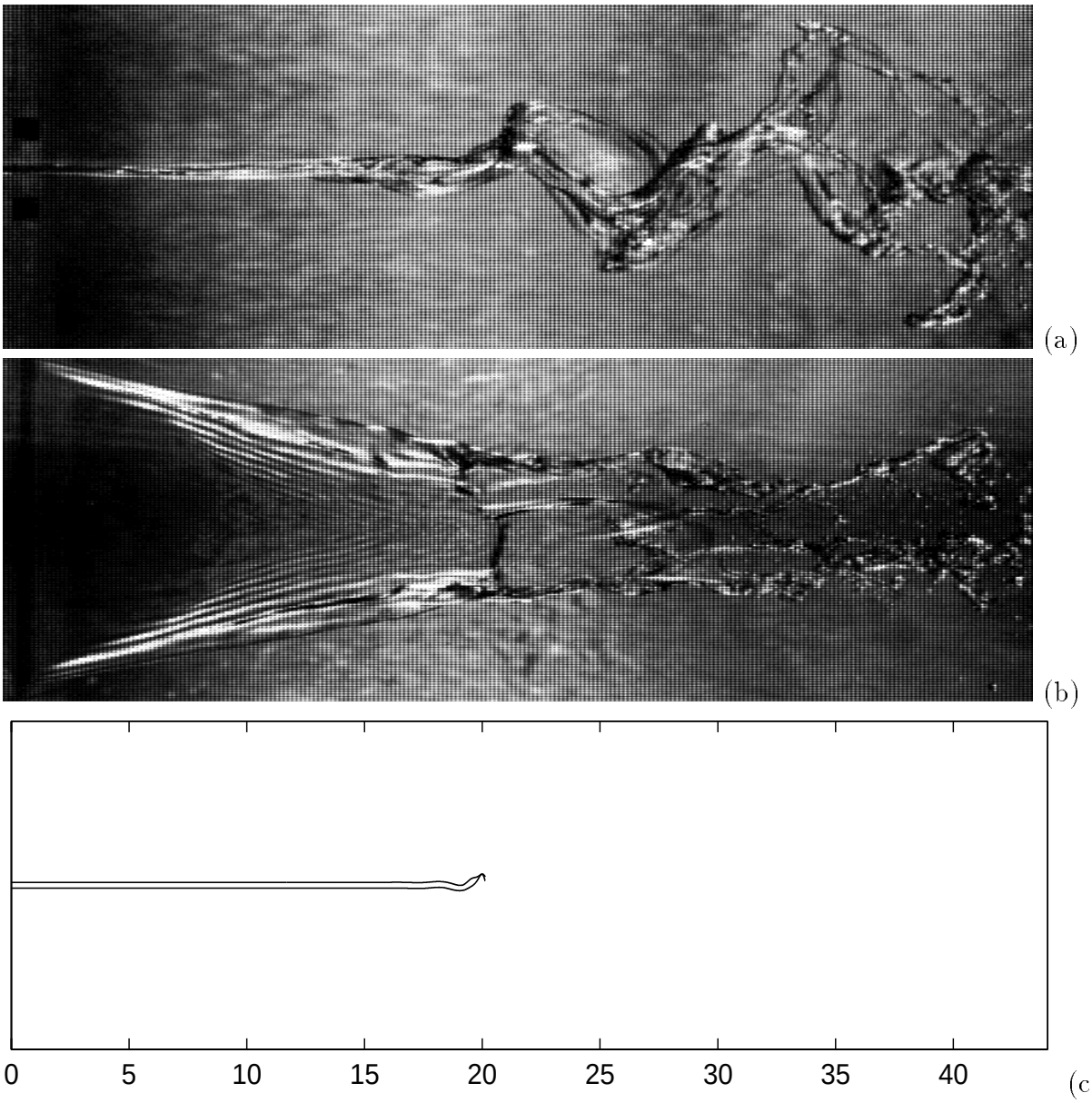

Figure 9.1: Breakup process of the liquid sheet produced by the planar nozzle for $U_\ell = 2.0\ m/s$ and $U_g = 27\ m/s$. (a) Side view; (b) Front view; (c) Prediction (scale in mm).

and 9.2c are different.

With the increase in the liquid and the air flow rates, the breakup characteristics of the liquid sheet also change, as shown in Fig. 9.3. Here $We = 26.5, U = 13.6, \rho = 1.202 \times 10^{-3}, k = 3.356, \eta_0 = 0.00009, \epsilon_s = 0.7$ and $\epsilon_v = 0.3$. For this case, the measured breakup length is around 18 mm and the predicted breakup length is $L_b = 142$ (or 18 mm). In general, it is observed that the prediction of the breakup characteristics for the planar nozzle is reasonable for the choices of the initial disturbance amplitude η_0 around $0.00008 - 0.0002$ and $\epsilon_s = 0.5 - 0.8$. The breakup length L_b can be theoretically estimated with reasonable accuracy, even though the sheet profiles may not match with the experiments. The matching of the breakup length is important, since its value is required for the estimation of the different source terms in the stochastic sub-model, which in turn effect the final size and velocity distributions of the spray.

The present model is also verified with the liquid sheet images taken by Berthoumieu et al. [65] for a planar nozzle which generates a liquid sheet of 300 μm thick. In their experiments, they used two CCD cameras, positioned perpendicular to one another, which were synchronized in such a way that simultaneous images of the liquid sheet can be obtained, as shown in Fig. 9.4a. Such images clearly shows the distinct breakup location of the liquid sheet and as well as the large sheet deformation caused by the ligaments after the breakup point, as stated earlier. The nozzle exit conditions are $We = 23.7, U = 11.8, \rho = 1.202 \times 10^{-3}, k = 2.147, \eta_0 = 0.001, \epsilon_s = 0.8$, and $\epsilon_v = 0.2$. The theoretical breakup length with these parameters is found to be 10 mm compared to the measured length of 11 mm. The deformation of the sheet close to the breakup point matches well with the experiment.

So far the comparison of the breakup length has been done assuming that the wavenumber of the disturbance on the liquid sheet interfaces corresponds to the dominant wavenumber for the sinuous mode. Mansour & Chigier [20] conducted experimental investigation of the breakup process of the plane liquid sheet where they are able to capture the frequency of disturbance wave present on the liquid sheet. Figure 9.5a shows the breakup characteristics of 254 μm thick liquid sheet obtained from a planar nozzle whose geometry is similar to that of the research planar nozzle. They observed that under the given flow conditions, the frequency of the disturbance wave on the liquid sheet is around 500 Hz and

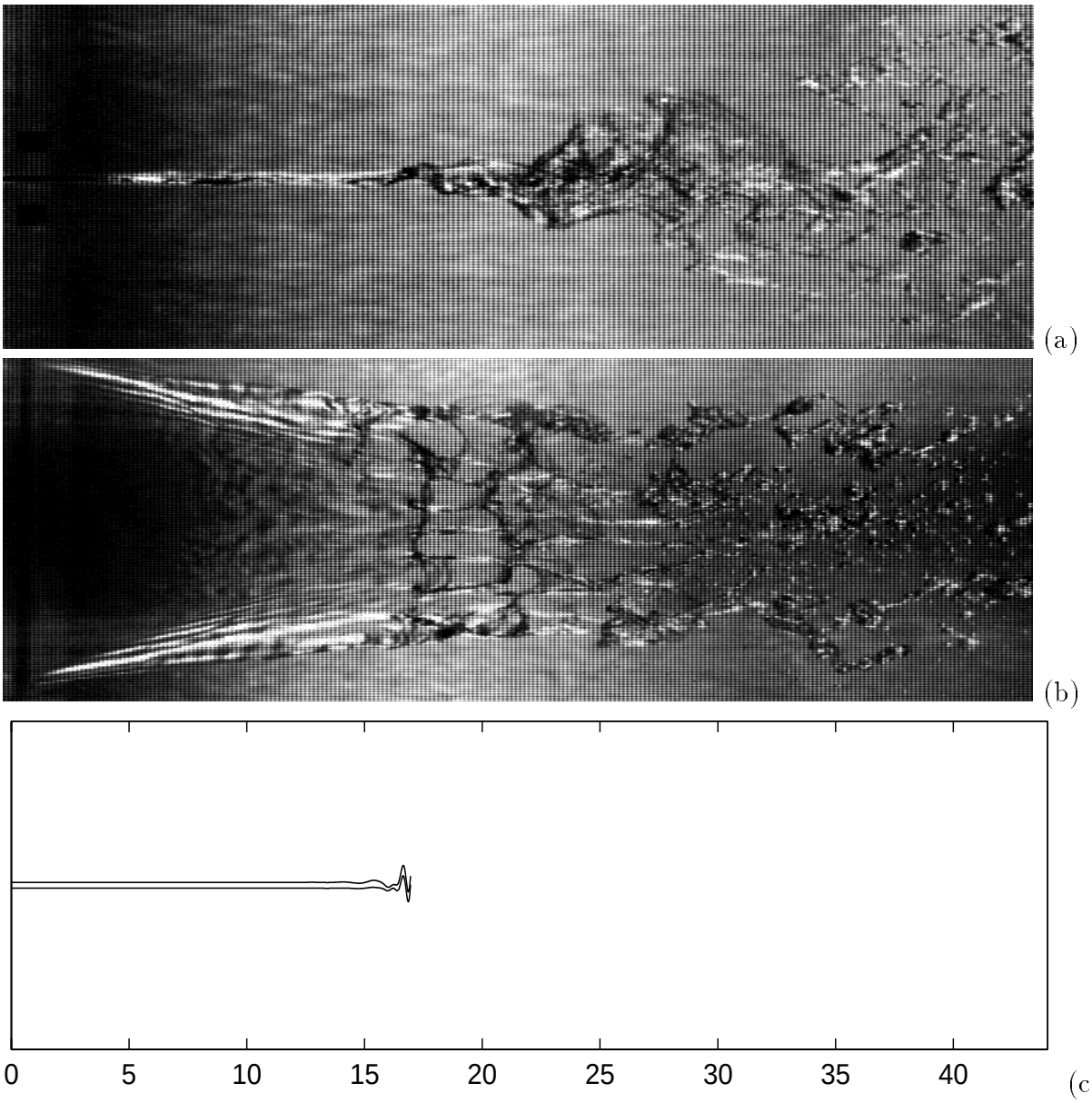

Figure 9.2: Breakup process of the liquid sheet produced by the planar nozzle for $U_\ell = 2.9\ m/s$ and $U_g = 40\ m/s$. (a) Side view; (b) Front view; (c) Prediction (scale in mm).

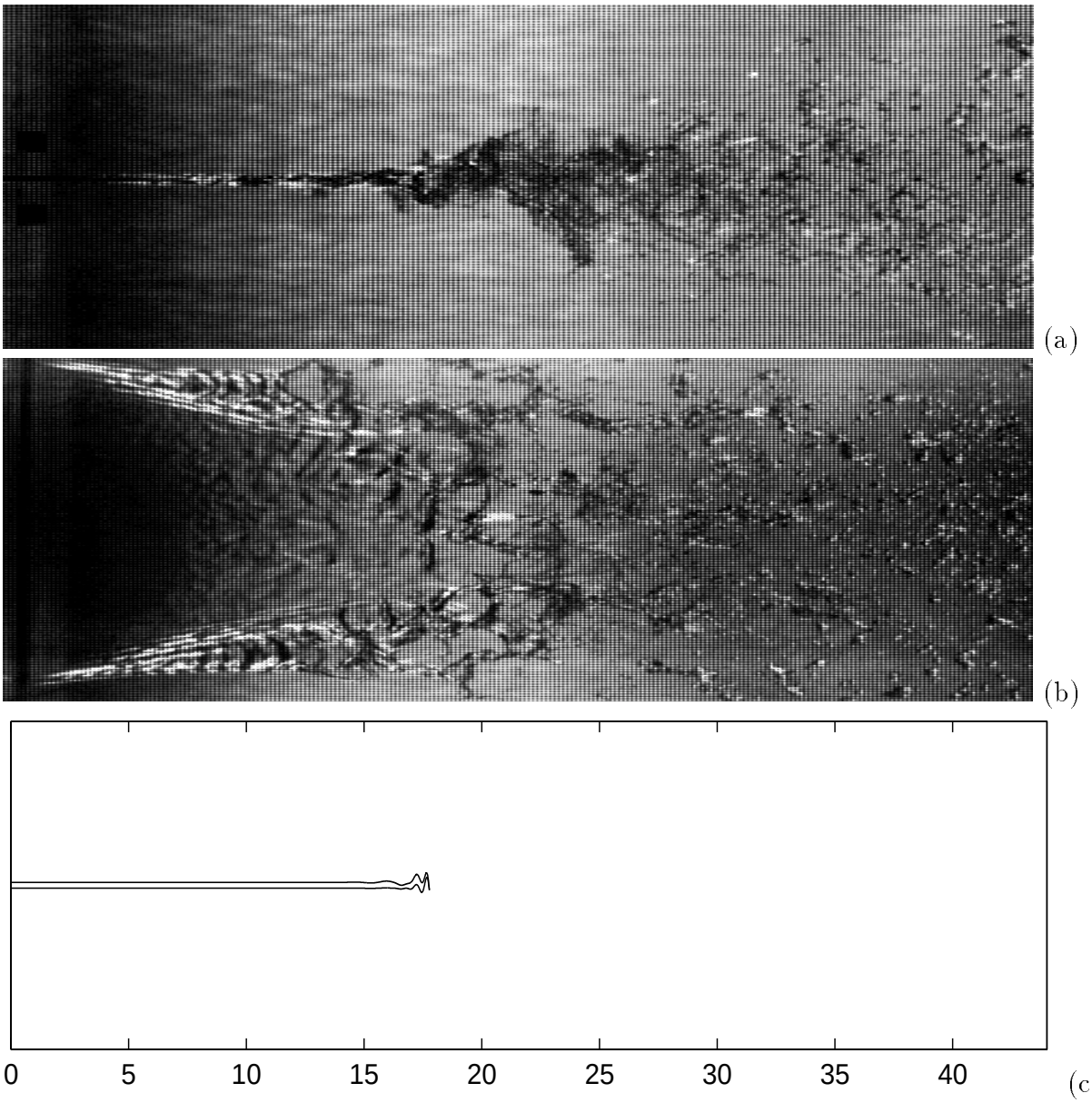

Figure 9.3: Breakup process of the liquid sheet produced by the planar nozzle for $U_\ell = 3.9\ m/s$ and $U_g = 53\ m/s$. (a) Side view; (b) Front view; (c) Prediction (scale in mm).

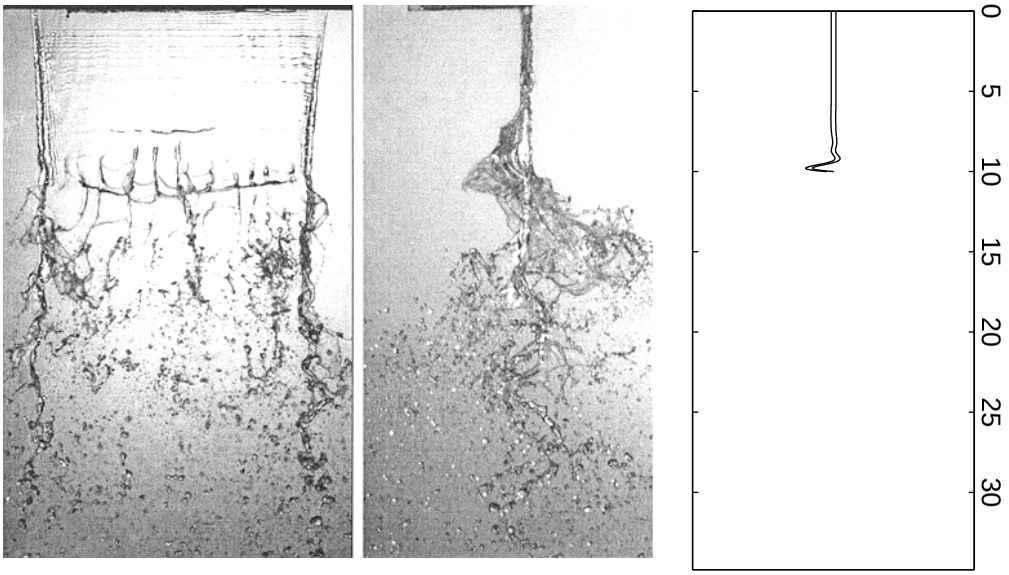

(a) (b)

Figure 9.4: Breakup process of 300 μm thick plane liquid sheet for $U_\ell = 3.4\ m/s$ and $U_g = 40\ m/s$. (a) Experiment [65, 100]; (b) Prediction (scale in mm).

(a)

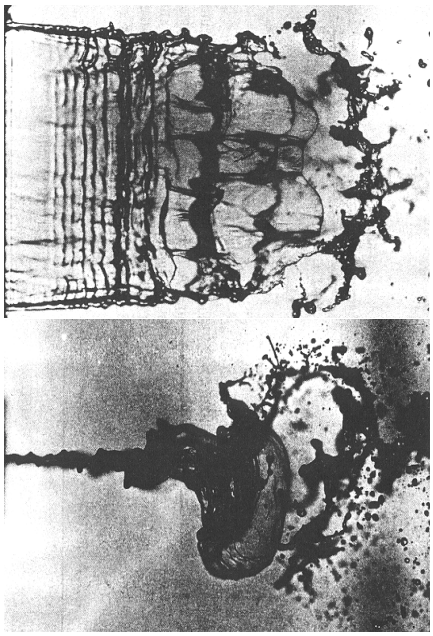

(b)

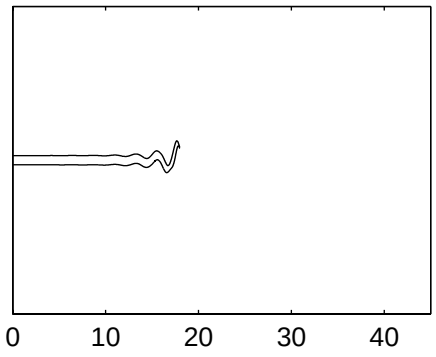

Figure 9.5: Breakup process of 274 μm thick plane liquid sheet for $U_\ell = 3.9\ m/s$ and $U_g = 31\ m/s$. (a) Experiment [30]; (b) Prediction (scale in mm).

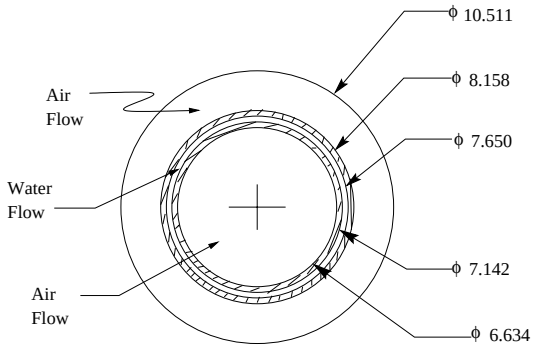

Figure 9.6: Cross-section of the annular nozzle [101] (dimension in mm).

the breakup of the liquid sheet occurs at 17 mm downstream of the nozzle exit. In order to match their results, the wavenumber corresponding to the measured frequency need to be determined. The wavenumber can be obtained by solving the dispersion relation for the growth rate, in terms of real and imaginary parts, provided by Li [11]. The imaginary part of the growth rate is related to the disturbance frequency as 2π times the measured frequency; the real part is same as that given in Eq. 4.4. Therefore, by using the dispersion relation for $We = 26.3, U = 7.9$, and $\rho = 1.202 \times 10^{-3}$, the wavenumber corresponding to 500 Hz is found to be 0.0945. With this value of k, it is found that the breakup length of 18 mm can be predicted for the choices of $\eta_0 = 0.0002, \epsilon_s = 0.8$ and $\epsilon_v = 0.2$. Hence, it is found that the theoretical model can predict the breakup characteristics of the liquid sheet with reasonable accuracy for the disturbance wavenumber different from the dominant one.

As a next step, the theoretical model for the liquid sheet breakup process is verified with an annular nozzle, the cross-section of which is shown in Fig. 9.6. This nozzle also produces a liquid sheet of 254 μm thick. Figure 9.7a shows the breakup process of the liquid sheet produced by this annular nozzle for $U_\ell = 1.1\ m/s$ and $U_g = 14\ m/s$. The breakup location is measured to be around 6 mm downstream of the nozzle exit. Similar to the planar nozzle, there are distinct ligament formation and the buckling of the sheet after the breakup location. Since, the geometry is annular, the theoretical profiles are drawn for the outer interface only with a spacing between the profiles equal to the diameter of the liquid sheet. For the theoretical prediction, following parameters are used: $We = 2.0, U = 12.7, \rho = 1.202 \times 10^{-3}, k = 0.167, \eta_0 = 0.001, \epsilon_s = 0.4$ and $\epsilon_v = 0.6$. The breakup length

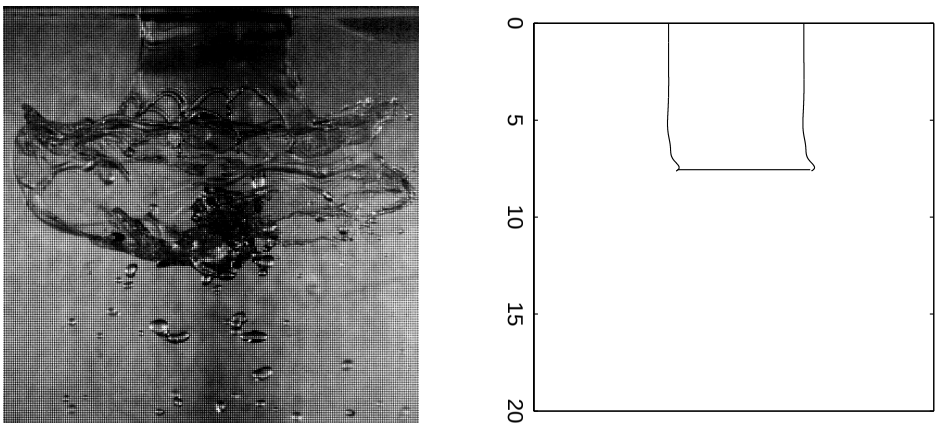

(a) (b)

Figure 9.7: Breakup process of the liquid sheet generated by the annular nozzle for $U_\ell = 1.1\ m/s$ and $U_g = 14\ m/s$. (a) Experiment [101]; (b) Prediction (scale in mm).

for these parameters is found to be 7 mm.

The prediction of the liquid sheet breakup for a different flow condition is shown in Fig. 9.8. Here $We = 8.0, U = 12.9, \rho = 1.202 \times 10^{-3}, k = 0.743, \eta_0 = 0.0009, \epsilon_s = 0.3$ and $\epsilon_v = 0.7$. The predicted breakup length is 8 mm compared to the measured length of 7 mm. It is observed that in order to match the breakup length of the annular nozzle, the initial disturbance amplitude and the proportion of the varicose mode need to be larger than the planar nozzle.

The model is also verified with the images of the liquid sheet produced from an annular nozzle by Berthoumieu et al. [65]. Their annular nozzle is also designed in such a manner that it generates a liquid sheet of 300 μm thick, same as their planar nozzle. Figure 9.9 shows the breakup process of the liquid sheet for the annular nozzle. The parameters used to match the experimental breakup length of 6 mm are as follows: $We = 12.8, U = 16.0, \rho = 1.202 \times 10^{-3}, k = 2.262, \eta_0 = 0.002, \epsilon_s = 0.7$ and $\epsilon_v = 0.3$. Therefore, it can be inferred that the plane liquid sheet model can be extended to predict the breakup length for the annular geometry.

Finally, the theoretical model is verified with the breakup length measurements ob-

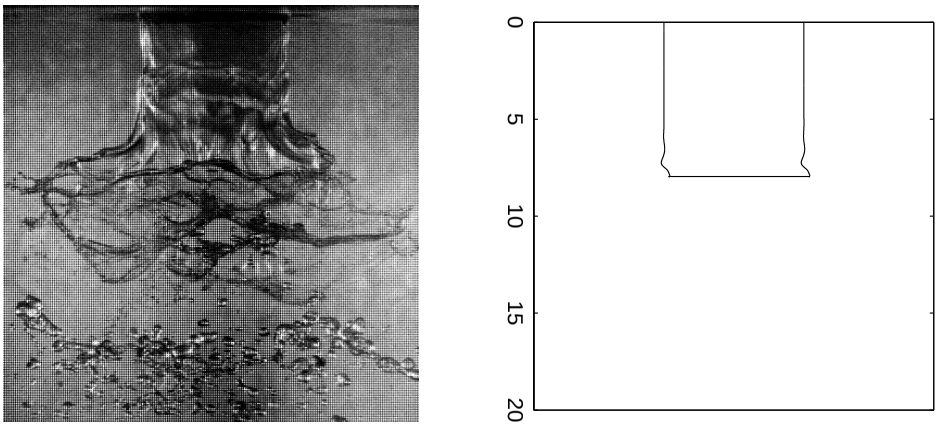

(a) (b)

Figure 9.8: Breakup process of the liquid sheet generated by the annular nozzle for $U_\ell = 2.1\ m/s$ and $U_g = 27\ m/s$. (a) Experiment [101]; (b) Prediction (scale in mm).

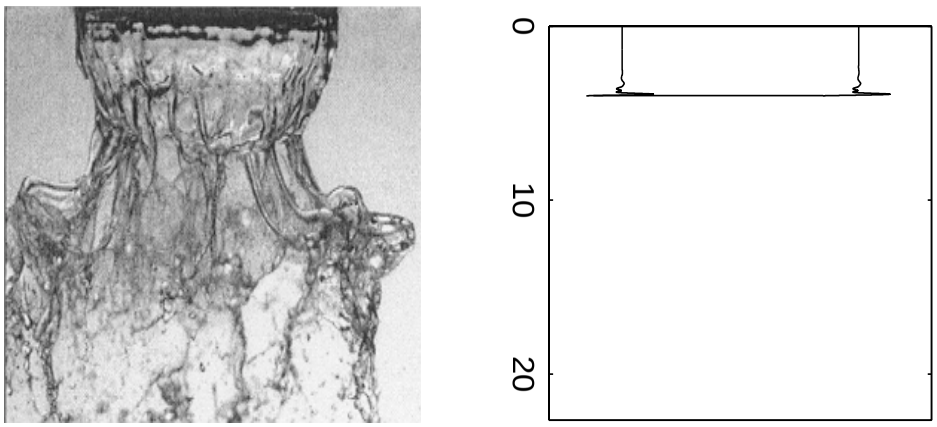

(a) (b)

Figure 9.9: Breakup process of 300 μm thick liquid sheet generated by the annular nozzle for $U_\ell = 2.5\ m/s$ and $U_g = 40\ m/s$. (a) Experiment [65]; (b) Prediction(scale in mm).

Table 9.1: Typical parameters for the breakup length of the PWC nozzle. The half-sheet thicknesses are Case I: $a^* = 93\ \mu m$, Case II: $a^* = 96\ \mu m$, Case III: $a^* = 69\ \mu m$ and Case IV: $a^* = 67\ \mu m$. The density ratio $\rho = 1.202 \times 10^{-3}$ for all cases.

Experiment				Prediction						
Case	U_ℓ (m/s)	U_g (m/s)	L_b^* (mm)	We	U	k	η_0	ϵ_s	ϵ_v	L_b^* (mm)
I	4.4	56	3	24.2	12.7	2.615	0.0003	0.6	0.4	3
II	4.2	42	7	23.3	10.0	1.360	0.0001	0.7	0.3	6
III	4.5	42	8	18.9	9.3	0.902	0.0001	0.7	0.3	8
IV	4.6	56	4	19.5	12.2	1.816	0.0003	0.6	0.4	4

tained from the PWC nozzle. However, as shown earlier in Fig. 8.10, the geometry of the liquid sheet produced by this nozzle is quite different than that of the plane liquid sheet. Therefore, attempts are made to match the breakup length of the sheet, instead of the evolution of the two interfaces of the liquid sheet. Table 9.1 shows different parameters that are used in the theoretical model to match the experimental breakup lengths. It is observed that by varying the initial disturbance amplitude between $0.0001 - 0.0003$ and the value of ϵ_s between $0.6 - 0.7$, a reasonable agreement with the experimental breakup length is obtained. It is to be noted that the liquid velocity is obtained by measuring the sheet velocity close to the nozzle exit by the PDPA system. Based on such sheet velocities, the liquid sheet thickness is obtained by using conservation of mass for the known flow rates. However, in order to validate the model more accurately, the actual sheet thickness for the PWC nozzle need to be known by some experimental means.

9.2 Comparison of Droplet Size and Velocity Distributions

The present theoretical model is able to predict the initial droplet size and velocity distributions in sprays. Such distributions can be compared with the experimental distributions

Table 9.2: Exit flow conditions for the planar nozzle with half-sheet thickness $a^* = 127\ \mu m$, liquid density $\rho_\ell = 998\ kg/m^3$, gas density $\rho_g = 1.2\ kg/m^3$, dynamic viscosity $\mu_g = 1.8 \times 10^{-5}\ kg/m.s$ and $\sigma = 0.073 N/m$.

Experiment			Prediction					
Case	U_ℓ (m/s)	U_g (m/s)	We	U	k	η_0	ϵ_s	ϵ_v
I	1.0	93	1.7	93.0	11.736	0.0001	0.7	0.3
II	2.0	80	6.7	40.0	8.373	0.0002	0.6	0.4
III	1.0	80	1.7	80.0	8.589	0.0001	0.7	0.3
IV	2.0	93	6.7	46.5	11.462	0.0001	0.7	0.3

obtained from the PDPA system. The comparison is first provided for the planar nozzle, followed by the annular nozzle and finally for the actual gas turbine nozzle (PWC nozzle).

The planar nozzle matches well with the physical model, but it produces a coarse spray and often large irregular droplets which are not suitable for measurement with a PDPA system. Therefore, the nozzle can be operated within a small range of flow conditions to obtain reasonable measurements, especially close to the breakup region, with a high validation rate for the measured droplet size and velocity. Such measurements are compared with the theoretical distributions and their corresponding flow conditions at the nozzle exit are provided in Table 9.2. For the specified flow conditions at the nozzle exit, the breakup length L_b, and the momentum and the energy source terms are obtained, with the assumption that the mass source term is zero for the spray at room temperature. Table 9.3 shows the relevant parameters needed to obtain the droplet size and velocity distributions in spray.

Figure 9.10 shows the comparison between the droplet size distribution obtained from the PDPA measurement and the theoretical prediction for the conditions corresponding to the Case I in Table 9.2. The PDPA measurement is obtained at a distance 5 mm from the nozzle exit and at the center plane of the nozzle. The validation rate for the measured data is about 65 %. It is observed that the theoretical distribution predicts more smaller droplets

Table 9.3: Estimates of breakup length, nozzle constant and source terms for different nozzle exit conditions of the planar nozzle.

Experiment			Prediction			
Case	L_b^* (mm)	D_{30} (μm)	L_b^* (mm)	C	$\bar{S}_{mv}$	$\bar{S}_e$
I	3	96	2	1.0	0.4949	92.8999
II	6	131	5	1.2	0.2148	17.0404
III	3	112	3	1.0	0.4796	77.0317
IV	5	120	5	1.3	0.2582	23.9766

compared to the PDPA measurements. This may be related to the prior distribution f_0, for which a $\bar{D}^2$ variation is assumed for smaller droplets. Also such difference in the distributions may be due to the dynamic range of the photo-multipliers used in PDPA system, which allows the detection of the large droplets by sacrificing the smaller ones. However, it is observed that the prediction matches well with the experimental data for droplet diameters greater than 50 μm and the peak of the distribution curve also shows reasonable agreement.

The velocity distribution corresponding to the Case I is shown in Fig. 9.11. It is observed that the peak of the theoretical distribution is slightly shifted towards the larger droplet velocity compared to the experimental distribution. However, there exist differences between the prediction and the experiment for very small and large droplet velocities. This is due to the fact that the maximum droplet diameter, given by Eq. (7.42), used in obtaining the velocity distribution is not accurate enough for very small and large droplet velocities. It is also to be noted that the extremely small droplet velocities corresponds to droplet diameters less than 1 μm, which are not significant so far as the entire spray is concerned.

The comparisons between the experimental and the theoretical distributions corresponding to the Case II are shown in Figs. 9.12-9.13. The PDPA measurements for this case is conducted at the center plane located 8 mm downstream of the nozzle exit with a validation rate of about 65 %. It is observed that for the droplet size distribution, the

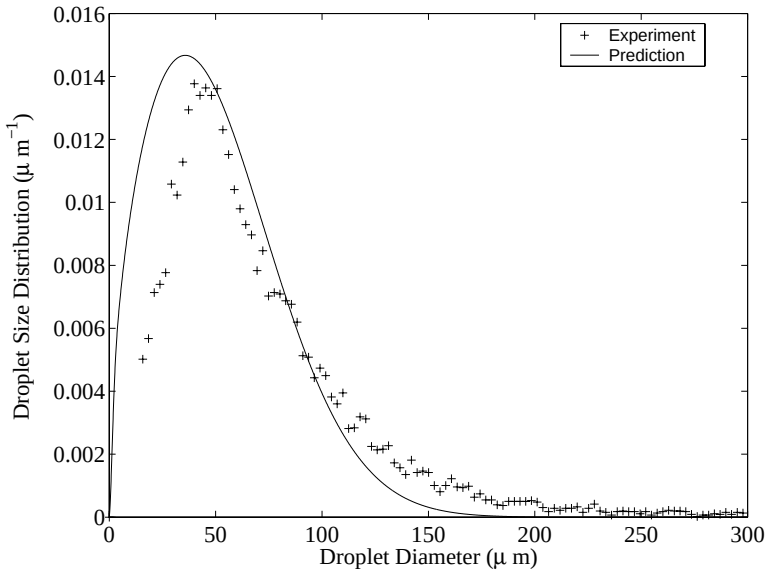

Figure 9.10: Comparison between the experimental and the theoretical droplet size distribution for the planar nozzle (Case I).

prediction matches reasonably with the experimental data, except for droplet diameters larger than 150 μm. The presence of such large number of droplets more than 200 μm is always questionable and it might be due to the presence of irregular shaped droplets near the breakup region of the liquid sheet. The velocity prediction matches well with the experimental distribution, except the distribution peak being slightly shifted towards the larger droplet velocity.

Figures 9.14-9.15 show the comparisons between the predicted droplet size and velocity distributions with the experimental distributions corresponding to Case III for the planar nozzle. The measurements are taken at the center plane located 5 mm downstream of the nozzle exit with a validation rate of about 65 %. It is observed that for droplet diameters less than 50 μm, the theoretical distribution over predicts due to the reasons discussed earlier. The distribution shows a good agreement for droplet sizes larger than 50 μm. For the droplet velocity distribution, it is observed that the distribution peak is shifted towards the larger droplet velocity. It is also found that the distribution does not match well for smaller droplet velocities, for which even the experimental data show some irregularities.

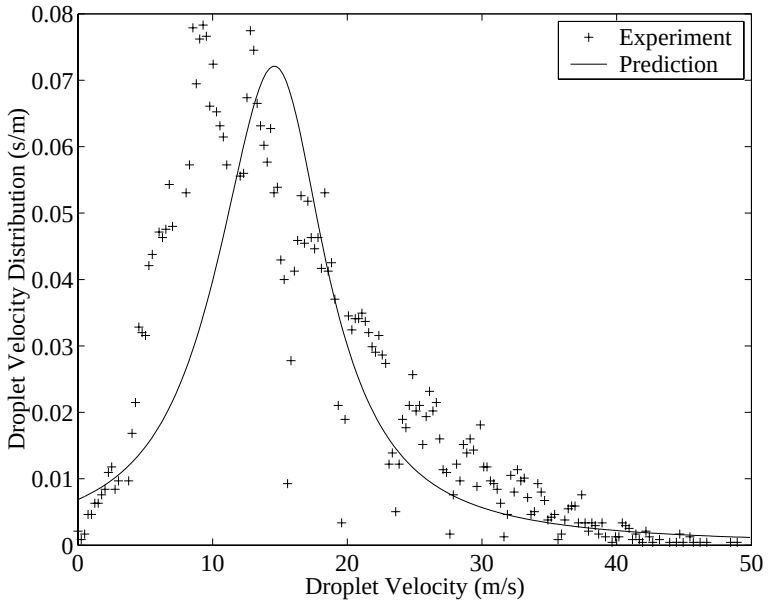

Figure 9.11: Comparison between the experimental and the theoretical droplet velocity distribution for the planar nozzle (Case I).

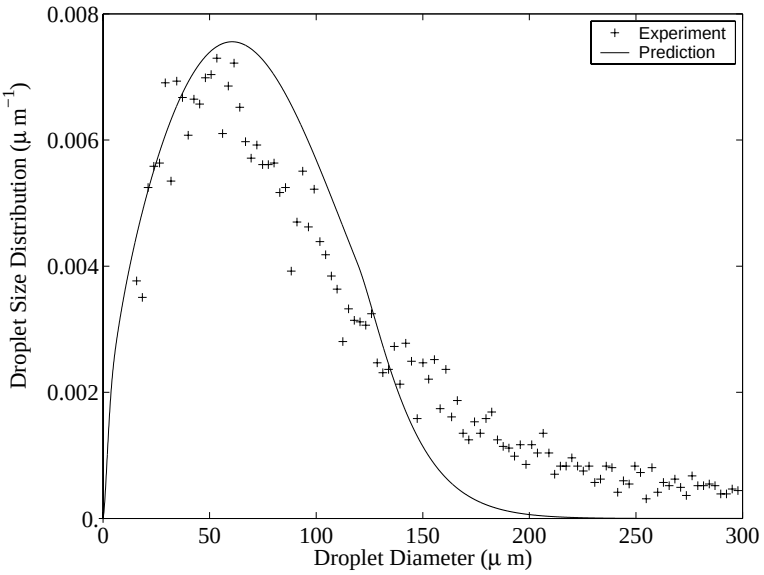

Figure 9.12: Comparison between the experimental and the theoretical droplet size distribution for the planar nozzle (Case II).

The theoretical and the experimental distributions corresponding to the Case IV for the planar nozzle is illustrated in Figs. 9.16-9.17. The PDPA measurements are conducted at the center plane located 8 mm downstream of the nozzle exit with a validation rate of about 65 %. In this case also, the presence of such large number of droplets greater than 200 μm is questionable. The distribution peak for the droplet size matches reasonably and the theoretical distribution again over predicts smaller droplet sizes. The velocity distribution matches well with the experimental data, except the peak being shifted towards the larger droplet velocity.

As a next step, the present model is compared with the initial droplet size and velocity distributions obtained for the annular research nozzle [101], which produces a liquid sheet of same thickness as that of the planar nozzle. The flow conditions at the nozzle exit for two different cases are listed in Table 9.4. For the annular nozzle also, there is a limited range of operating flow conditions such that a good quality spray can be obtained. The validation rate for the measured data is about 65 %. For the specified flow conditions at

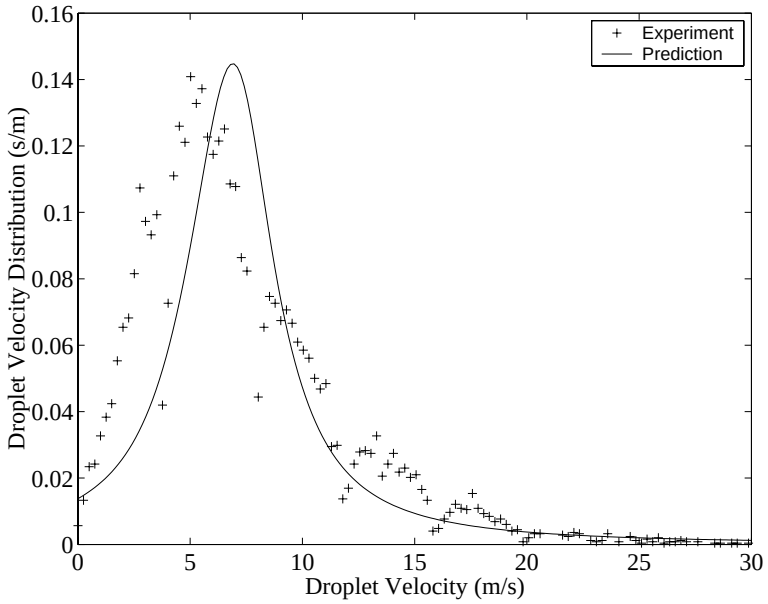

Figure 9.13: Comparison between the experimental and the theoretical droplet velocity distribution for the planar nozzle (Case II).

Table 9.4: Exit flow conditions for the annular nozzle with half-sheet thickness $a^* = 127\ \mu m$, liquid density $\rho_\ell = 998\ kg/m^3$, gas density $\rho_g = 1.2\ kg/m^3$, dynamic viscosity $\mu_g = 1.8 \times 10^{-5}\ kg/m.s$ and $\sigma = 0.073 N/m$.

Experiment			Prediction					
Case	U_ℓ (m/s)	U_g (m/s)	We	U	k	η_0	ϵ_s	ϵ_v
I	1.1	43	2.0	39.1	2.377	0.001	0.3	0.7
II	2.1	68	8.0	32.4	6.072	0.001	0.4	0.6

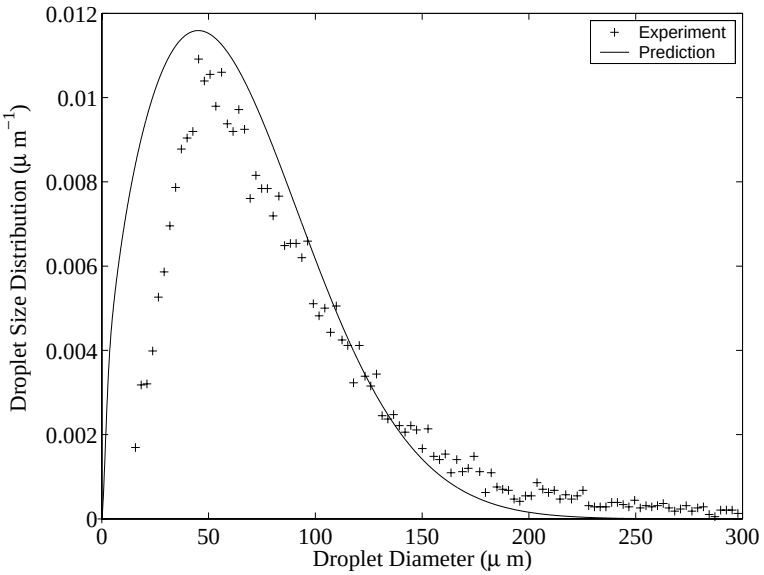

Figure 9.14: Comparison between the experimental and the theoretical droplet size distribution for the planar nozzle (Case III).

the nozzle exit, the breakup length L_b, and the momentum and the energy source terms are obtained, with the assumption that the mass source term is zero for the spray at room temperature. Table 9.5 shows the relevant parameters needed to obtain the droplet size and velocity distributions in spray for the annular nozzle.

Figures 9.18-9.19 show the comparison between the theoretical and the experimental distributions for the nozzle exit conditions corresponding to Case I. The PDPA measurements are obtained at the center plane located 5 mm downstream of the nozzle exit with a validation rate of about 65 %. It is observed that except for the smaller droplet diameters, the prediction for the droplet size matches well with the experimental distribution. The difference in the distributions for the smaller droplets can be attributed to the prior distribution f_0, which is based on the linear instability for the planar liquid sheet. The prediction for the smaller droplets may be improved by using a prior distribution based on this annular configuration. In the case the droplet velocity distribution, the theoretical distribution matches well with the experimental data, except for very small droplet velocities. It is also observed that the distribution peaks match reasonably well.

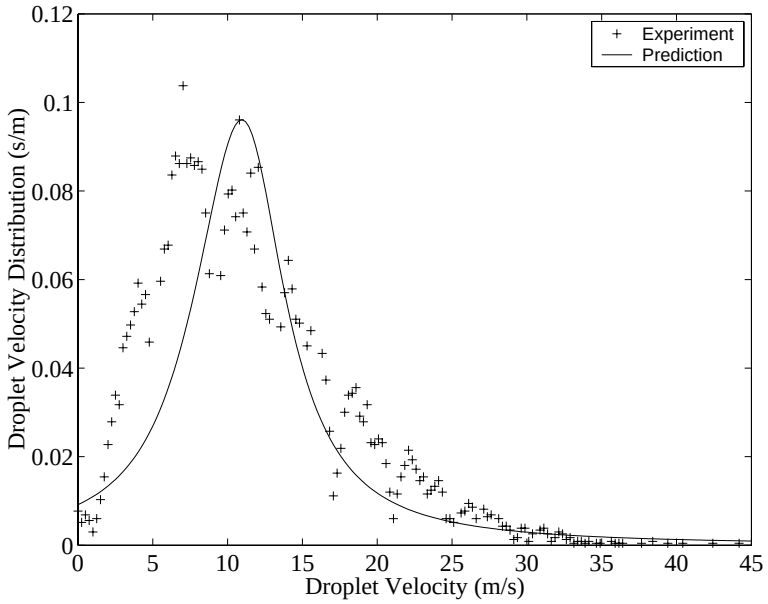

Figure 9.15: Comparison between the experimental and the theoretical droplet velocity distribution for the planar nozzle (Case III).

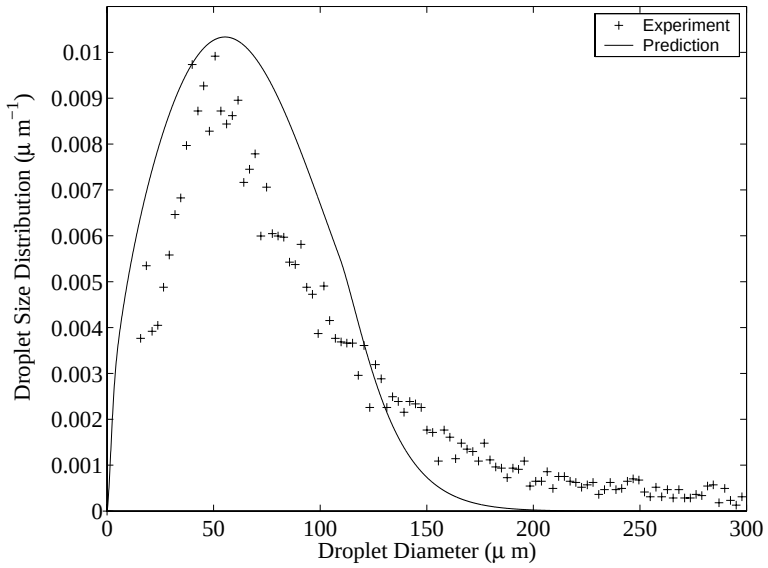

Figure 9.16: Comparison between the experimental and the theoretical droplet size distribution for the planar nozzle (Case IV).

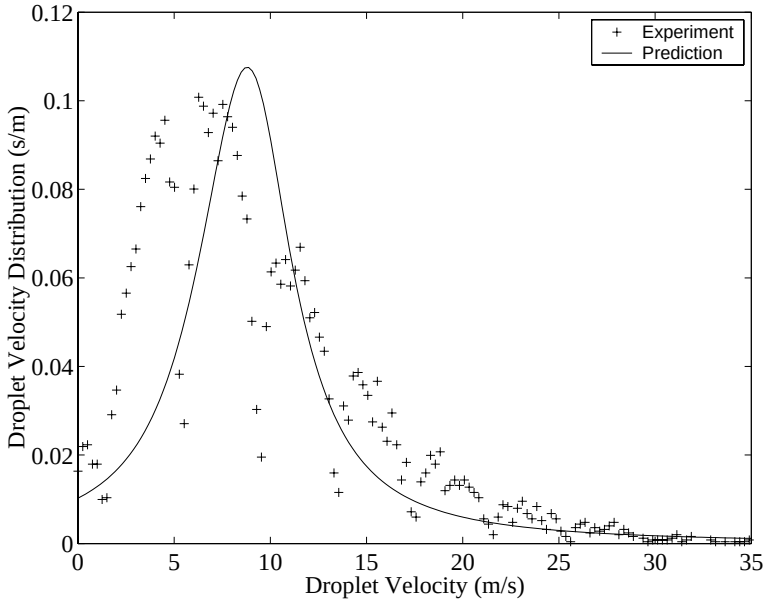

Figure 9.17: Comparison between the experimental and the theoretical droplet velocity distribution for the planar nozzle (Case IV).

Table 9.5: Estimates of breakup length, nozzle constant and source terms for different nozzle exit conditions of the annular nozzle.

Experiment			Prediction			
Case	L_b^* (mm)	D_{30} (μm)	L_b^* (mm)	C	$\bar{S}_{mv}$	$\bar{S}_e$
I	2	76	2	0.5	0.1146	8.9323
II	2	92	2	0.7	0.0936	5.7880

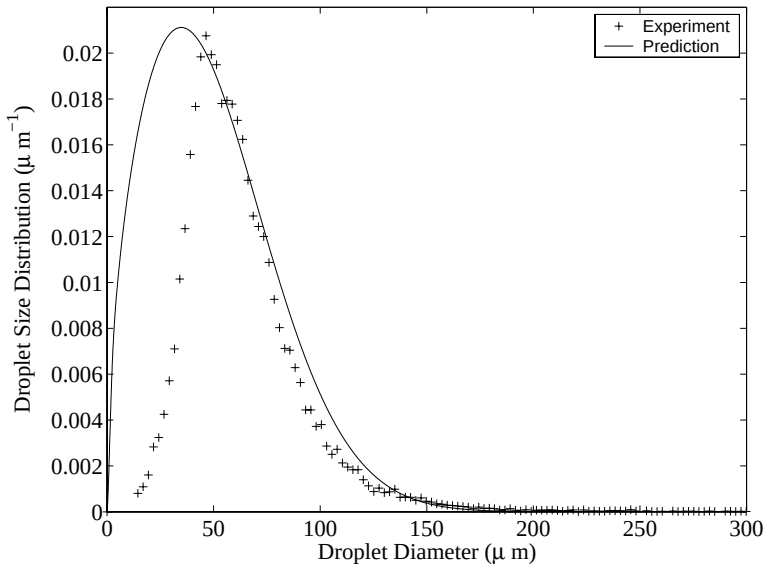

Figure 9.18: Comparison between the experimental [101] and the theoretical droplet size distribution for the annular nozzle (Case I).

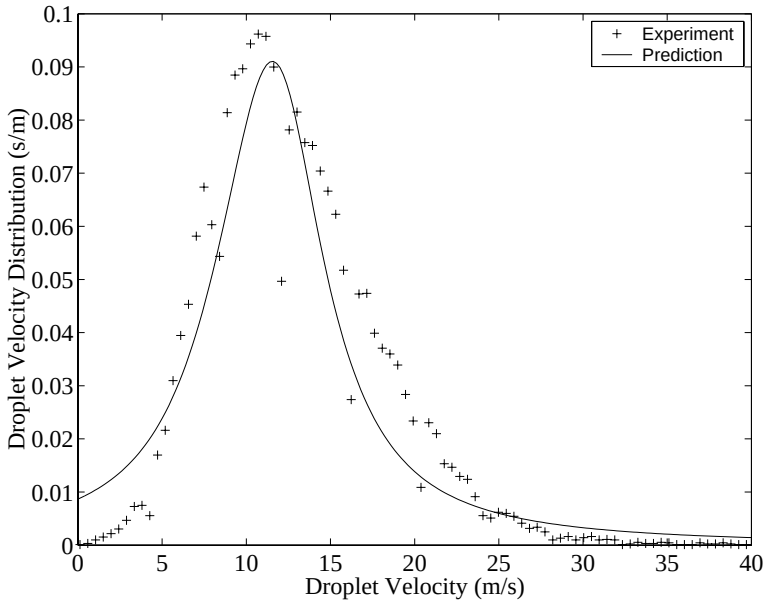

Figure 9.19: Comparison between the experimental [101] and the theoretical droplet velocity distribution for the annular nozzle (Case I).

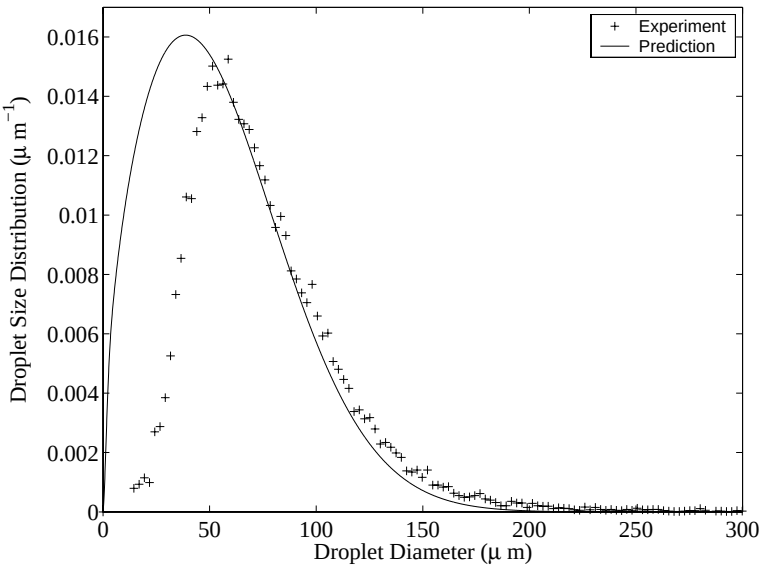

Figure 9.20: Comparison between the experimental [101] and the theoretical droplet size distribution for the annular nozzle (Case II).

The theoretical and the experimental distributions corresponding to Case II for the annular nozzle is illustrated in Figs. 9.20-9.21. It is found that for the droplet size distribution, the prediction matches well with the experimental data for diameters greater than 50 μm. The prediction deviates from the experimental distribution for smaller droplet diameters, the reasons for which are discussed earlier. However, in the case of the droplet velocity distribution, it is observed that the experimental distribution is very symmetric, which is the typical velocity distribution for annular geometry [102]. Therefore, for this case, the velocity distribution does not match well with the experimental counterpart near the small and the larger droplet velocities. Still, it is found that the distribution peaks match reasonably well. Hence, it can be concluded that even though the annular configuration is different from the planar sheet geometry, the present model shows reasonable agreement with the experimental data for the initial droplet size and velocity distributions.

Finally, the present model is compared with the actual gas turbine nozzle provided by Pratt & Whitney Canada. Since this nozzle produces a good spray, a high validation

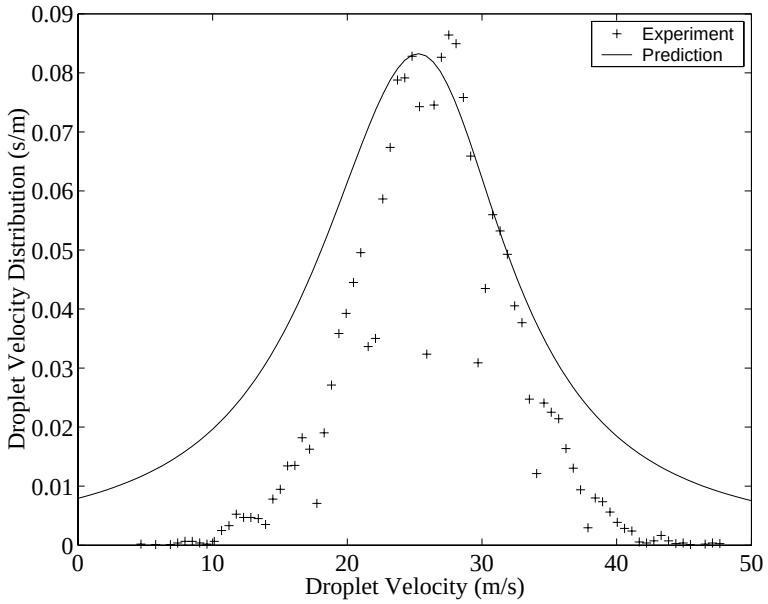

Figure 9.21: Comparison between the experimental [101] and the theoretical droplet velocity distribution for the annular nozzle (Case II).

Table 9.6: Estimates of nozzle constant and source terms for different nozzle exit conditions of the PWC nozzle.

Experiment		Prediction		
Case	D_{30} (μm)	C	$\bar{S}_{mv}$	$\bar{S}_e$
I	41	0.4	3.6630×10^{-2}	0.8571
II	47	0.3	3.2998×10^{-2}	0.5847
III	52	0.4	4.7434×10^{-2}	0.7865
IV	45	0.5	4.7434×10^{-2}	0.7865

rate of about 80 % is obtained for the measured PDPA data. The different nozzle exit conditions for the PWC nozzle is provided in Table 9.1. The nozzle constants and the source terms required for obtaining the corresponding theoretical distributions are provided in Table 9.6. Figures 9.22-9.23 show the comparison between the theoretical and the experimental distributions for the PWC nozzle corresponding to Case I. The measurements are carried out at the center plane located 5 mm downstream from the nozzle exit. It is observed that the droplet size distribution over predicts for smaller droplet diameters. This may be due to the use of an over simplified prior distribution f_0 for this complex nozzle configuration. However, for droplet diameters greater than about 20 μm, the theoretical prediction matches well with the experimental distribution. In the case of the velocity distribution, it is observed that the prediction matches well, except close to smaller droplet velocities.

The distributions corresponding to the Case II for the PWC nozzle is shown in Figs. 9.24-9.25. The measurements are obtained at the center plane located 8 mm downstream of the nozzle exit. For this case also, the droplet size distribution over predicts the small droplet sizes. It is observed that the velocity distribution matches well with the experimental data and also the distribution peaks agree well with each other.

Figures 9.26-9.27 shows the droplet size and velocity distributions, respectively, for the nozzle exit conditions stated in Case III. The measurements are obtained at the center

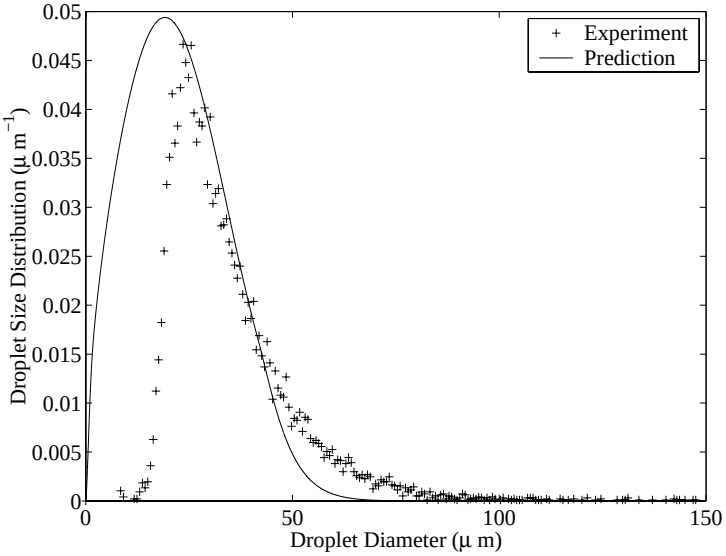

Figure 9.22: Comparison between the experimental and the theoretical droplet size distribution for the PWC nozzle (Case I).

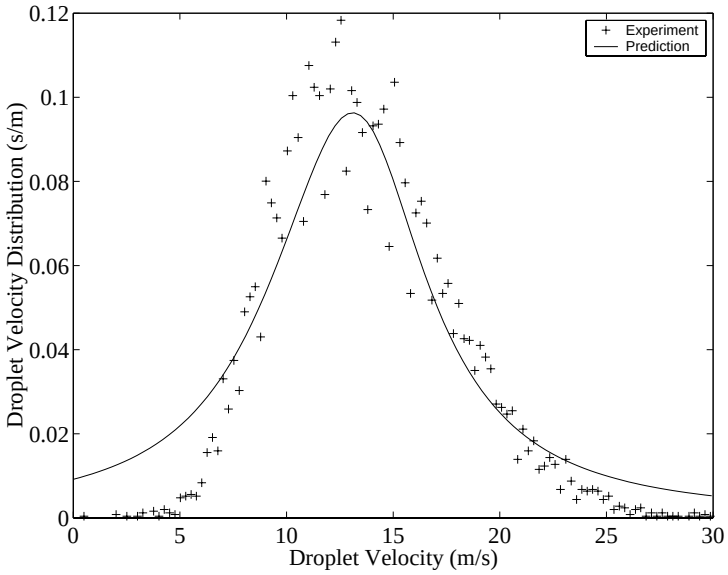

Figure 9.23: Comparison between the experimental and the theoretical droplet velocity distribution for the PWC nozzle (Case I).

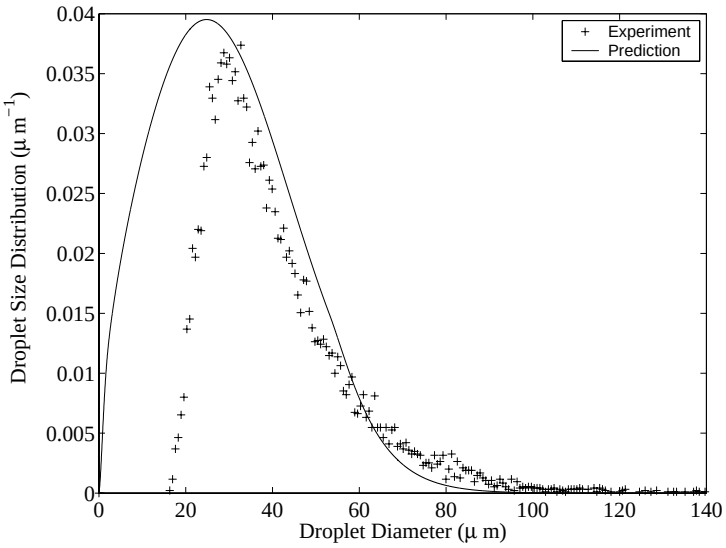

Figure 9.24: Comparison between the experimental and the theoretical droplet size distribution for the PWC nozzle (Case II).

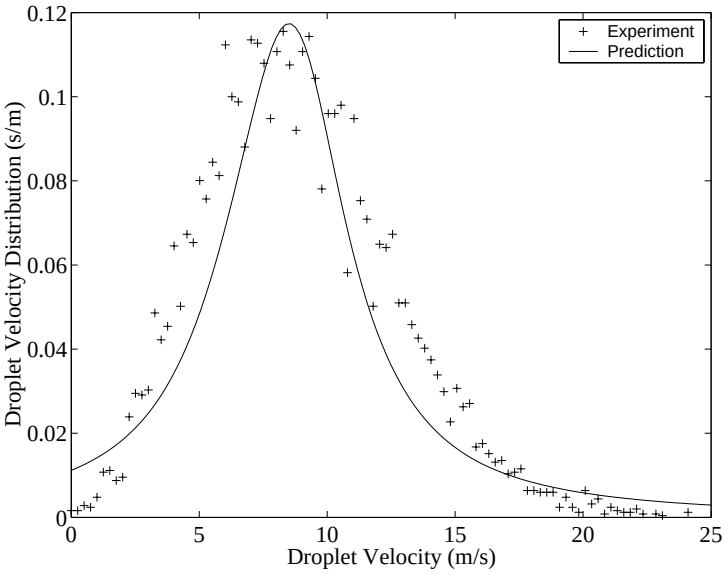

Figure 9.25: Comparison between the experimental and the theoretical droplet velocity distribution for the PWC nozzle (Case II).

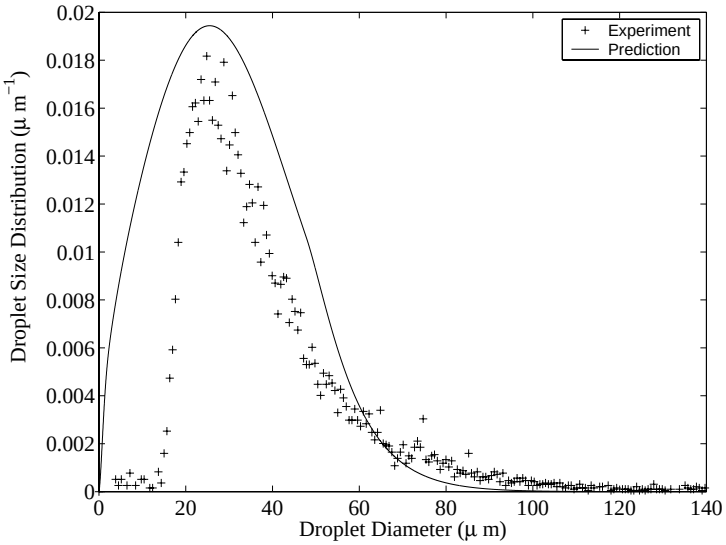

Figure 9.26: Comparison between the experimental and the theoretical droplet size distribution for the PWC nozzle (Case III).

plane located 10 *mm* downstream of the nozzle exit. It is observed that the droplet size distribution over predicts even for larger droplet diameters. However, the velocity distribution shows a good agreement with the experimental distribution.

The comparison of the theoretical and the experimental distributions corresponding to the Case IV is presented in Figs. 9.28-9.29. The PDPA measurements are collected at the center plane located 5 *mm* downstream of the nozzle exit. It is observed that the distribution peak for the droplet size matches well with the experimental data. In case of the velocity distribution, the theoretical distribution matches well with the experimental distribution, except for small droplet velocities.

In order to use the initial droplet size and velocity distributions in a computer code for CFD applications, often the cross correlation between the droplet diameter and the droplet velocity is required. With such information, along with the knowledge of the droplet trajectories, the users can specify the much needed "initial condition" for their combustion codes. Figures 9.30-9.33 show the droplet velocity-diameter cross correlation for the four cases of the PWC nozzle. A reasonably good agreement is observed between the experimental data and the prediction, except for the larger droplet diameters. It is to

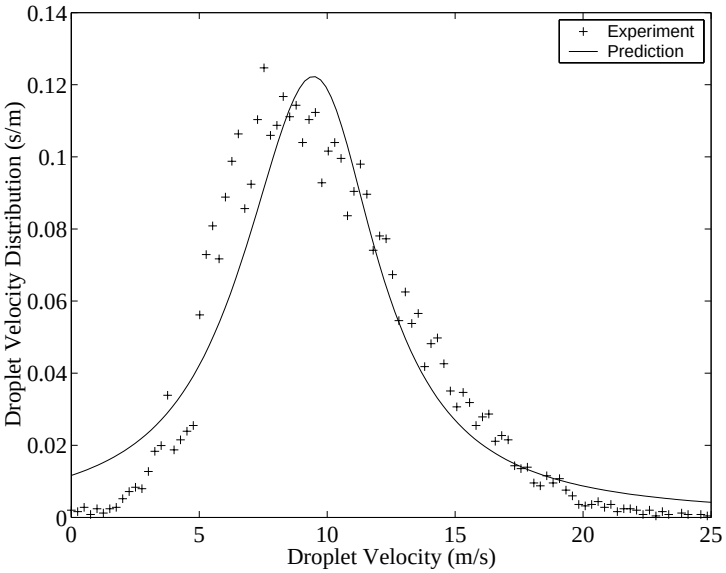

Figure 9.27: Comparison between the experimental and the theoretical droplet velocity distribution for the PWC nozzle (Case III).

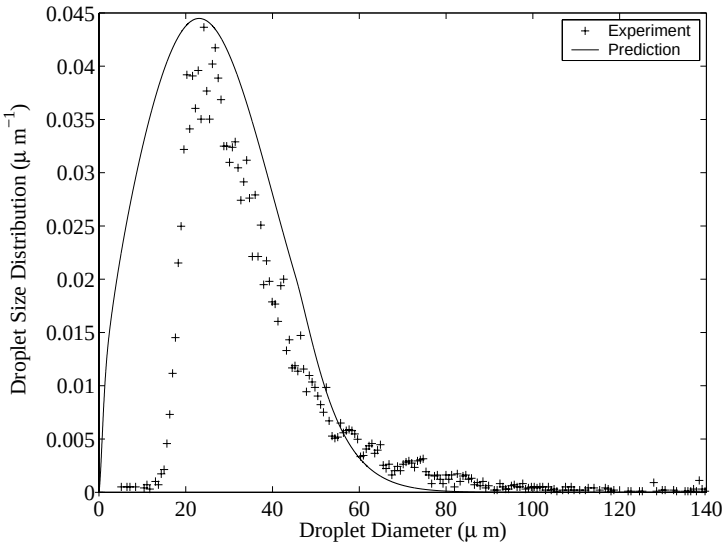

Figure 9.28: Comparison between the experimental and the theoretical droplet size distribution for the PWC nozzle (Case IV).

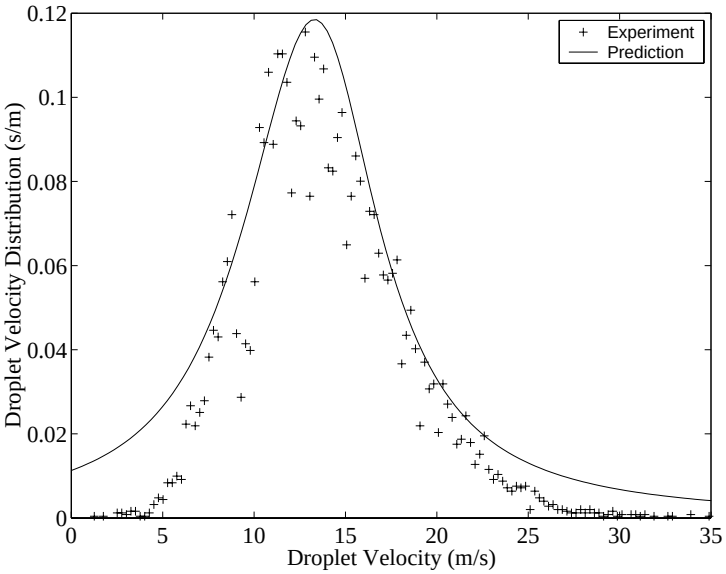

Figure 9.29: Comparison between the experimental and the theoretical droplet velocity distribution for the PWC nozzle (Case IV).

be noted that the PDPA measurements for droplet velocities are accurate, but there are errors associated in the size measurements, especially for the larger ones due to the droplet deformation. This is evident in the experimental data where a large scatter is observed for droplet diameters greater than 80 μm.

It is important to note that the critical breakup Weber number based on droplet diameter (We_c), given in Eq. (7.40), is not a constant, rather it varies over a range, depending upon the type of droplet breakup process [4]. In this thesis, the value for the critical breakup Weber number is taken as 10. Figures 9.34-9.35 show the effect of the breakup Weber number on the droplet-velocity correlation and the droplet size distribution for the PWC nozzle corresponding to the Case IV. It is observed that by changing the critical value from 5 to 20, the cross correlation changes, and appears to provide better agreement for the larger droplet diameters when the critical Weber number is less than 10. However, for the droplet size distribution, there is insignificant change in the distributions with the variation of the critical breakup Weber number.

The above comparisons show that the present model can predict initial droplet size and

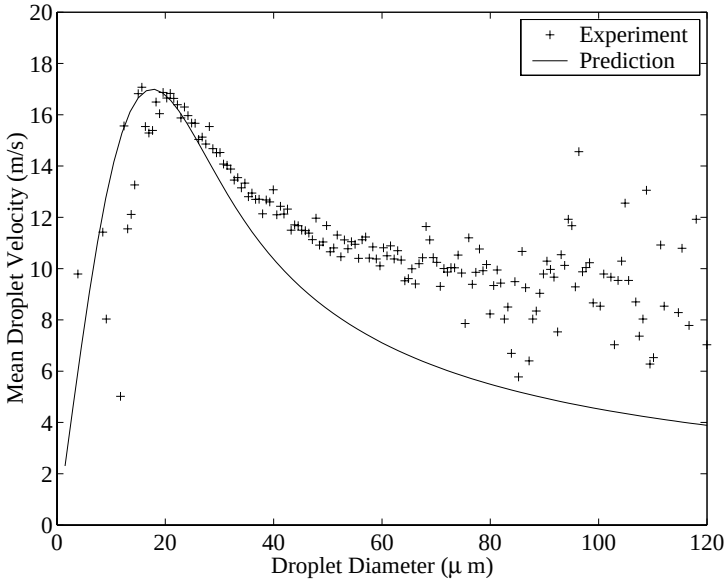

Figure 9.30: Comparison between the experimental and the theoretical droplet velocity-diameter correlation for the PWC nozzle (Case I).

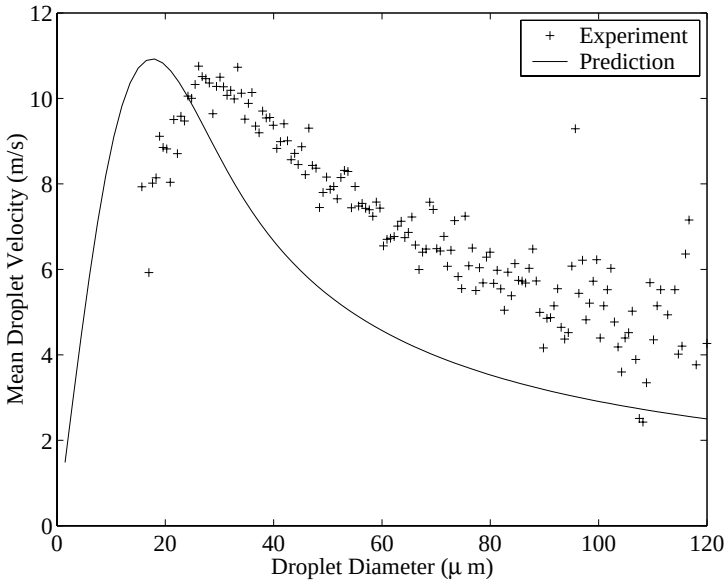

Figure 9.31: Comparison between the experimental and the theoretical droplet velocity-diameter correlation for the PWC nozzle (Case II).

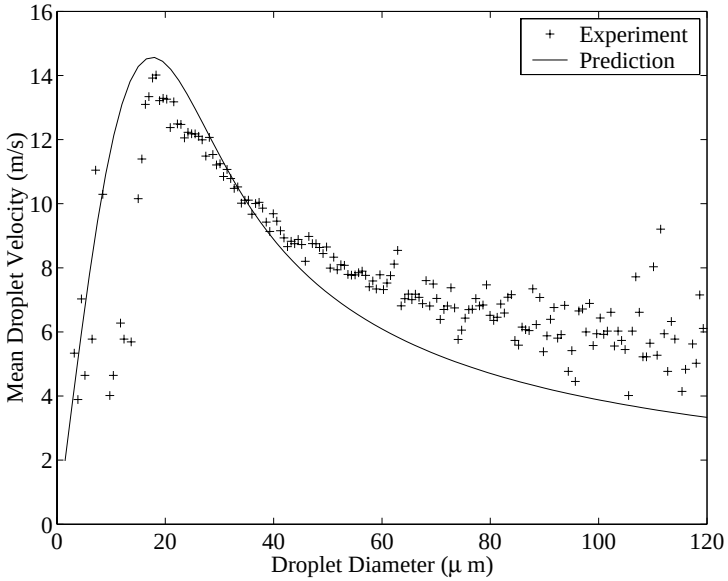

Figure 9.32: Comparison between the experimental and the theoretical droplet velocity-diameter correlation for the PWC nozzle (Case III).

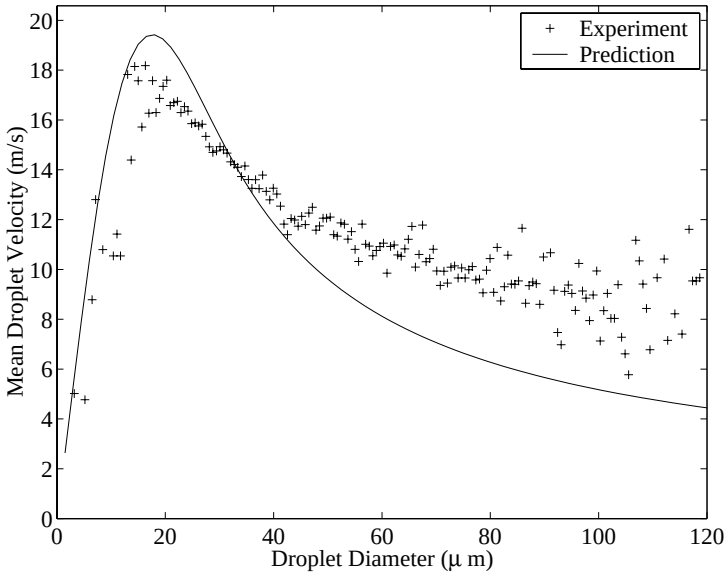

Figure 9.33: Comparison between the experimental and the theoretical droplet velocity-diameter correlation for the PWC nozzle (Case IV).

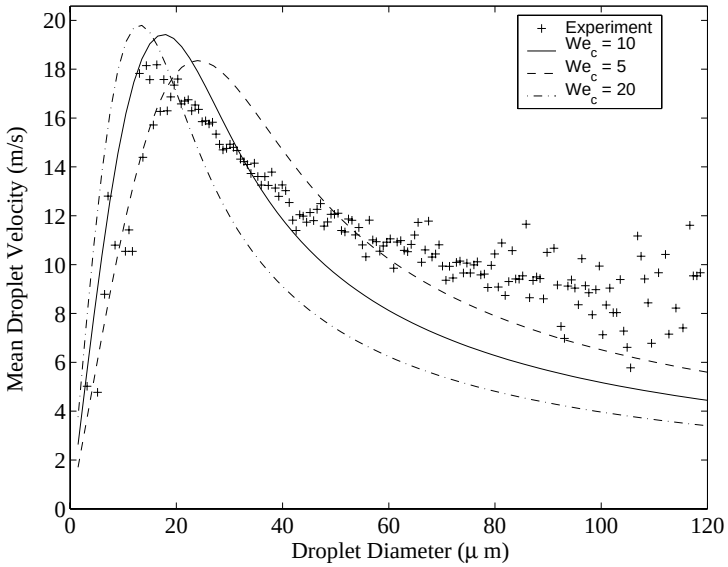

Figure 9.34: The effect of the critical breakup Weber number (We_c) on the droplet velocity-diameter correlation for the PWC nozzle (Case IV).

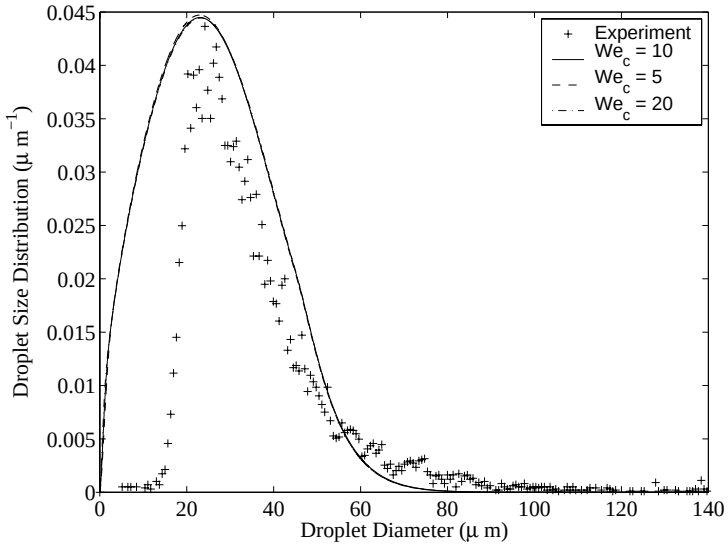

Figure 9.35: The effect of the critical breakup Weber number (We_c) on the droplet size distribution for the PWC nozzle (Case IV).

velocity distributions reasonably for the actual gas turbine nozzle. Even though the PWC nozzle geometry is quite different than the physical geometry used in the present model, yet the performance of the present model is quite satisfactory.

9.3 Critical Review

As stated earlier, in order to obtain the initial droplet size and velocity distributions in sprays, certain parameters are needed as inputs for the present theoretical model. These inputs parameters are discussed below:

- Liquid and gas velocities (U_ℓ and U_g) - In most applications, the mass flow rates for both the fuel and the atomizing gas are known from the measurements obtained by calibrated flow meters. The gas phase velocity is relatively easier to calculate since the geometries of the inner and the outer flow passages are known, as in the case of the PWC nozzle. However, for the present model, it is assumed that the gas velocities on both sides of the liquid sheet are equal, which may not necessarily be the case for the actual nozzles. In case of the liquid velocity, the flow path is not always easily determined, as in the case of the PWC nozzle. For such a complex geometry, one has to rely on the measurement of the liquid sheet velocity close to the nozzle exit. Once the velocities of both phases are known, then the gas-to-liquid velocity ratio U can be readily calculated.

- Half-sheet thickness (a^*) - The determination of half-sheet thickness is very important as it effects the value of mass-mean diameter D_{30} and the operating Weber number We. Ideally, the value of the sheet thickness should be provided as an input from another model, which does the calculation for the half-sheet thickness a^* within the nozzle. However, in the absence of such a model, one can obtain the sheet thickness by using the liquid sheet velocity and the mass flow rate, as done in the case of the PWC nozzle.

- Nozzle constant (C) - This is a weak parameter in the model and it effects D_{30} significantly. In the case of the planar nozzle it is found that typical value of C ranges between $1.0 - 1.3$, whereas for the annular and the PWC nozzle the ranges

are $0.5 - 0.7$ and $0.3 - 0.5$, respectively. Such variation of the value of C for different nozzles is expected as this parameter depends on the nozzle geometry and also on the spatial location in the spray. Therefore, an experimental value of the mass-mean diameter is needed in order to obtain the accurate value of C, which in turn will produce distributions representative of the actual spray.

- Initial disturbance amplitude (η_0) - In practical applications, natural disturbances are produced from a variety of sources. The amplitude of such disturbance can be obtained experimentally, but it is not within the mandate of the research carried out in this thesis. Current literature show that the initial disturbance amplitude for the Rayleigh breakup of a circular liquid jet has been identified. If similar experimental efforts are also directed towards the plane liquid sheets, it is possible to obtain a value for η_0, which can then be used in our present model. However, for the three nozzle geometries studied here, the value of η_0 is found to be within the range of $0.001 - 0.00008$, which is also a small parameter for the mathematical validity of the nonlinear instability analysis presented here. The value of η_0 affects the determination of breakup length L_b, which in turn affects the evaluation of the different source terms needed in the model. In an actual spray, the breakup lengths are extremely small, of the order of few millimeters, and hence its effect on the overall droplet size and velocity distribution is not dramatic.

- Proportion of the modes (ϵ_s or ϵ_v) - This parameter is difficult to obtain experimentally for practical sprays. In the present study, it is observed that for a given nozzle geometry, the value of ϵ_s or ϵ_v is more or less constant. Its value affects the breakup length and as discussed earlier, it will not have significant impact on the overall spray.

- Physical properties - The determination of the physical properties are relatively easier compared to the other input parameters discussed above. From the known physical properties, the gas-to-liquid density ratio ρ can be calculated, which is an input to the present model. However, difficulties may arise in obtaining an accurate value for the surface tension σ, whose value sensitively depends on the concentration of surface contaminants Surface contaminants may be always present for practical operation.

Despite some shortcomings, the present theoretical model predicts the initial droplet size and the velocity distributions reasonably well, even for the "real world" application such as a gas turbine nozzle. Hence, this model can be applied in more adverse situations, such as a high pressure gas turbine application, where conducting reliable spray measurements are very difficult.

Chapter 10

Conclusions and Recommendations

The breakup process of a plane liquid sheet in a co-flowing gas stream has been studied and a predictive model for the initial droplet size and velocity distributions in sprays has been formulated. The characteristics of the breakup process and the initial droplet size and velocity distributions have been experimentally investigated. Comparisons of the theoretical predictions with the experimental measurements have also been performed.

10.1 Conclusions

The liquid sheet breakup process is investigated by using linear and nonlinear hydrodynamic instability theories. The breakup characteristics of the liquid sheet are studied for the initial sinuous and the varicose modes of disturbance. It is observed that the sheet breakup occurs at half-wavelength intervals for an initial sinuous disturbance and at full-wavelength interval for an initial varicose disturbance. It is also found that under certain operating conditions, the breakup process is dictated by the initial varicose mode compare to its sinuous counterpart. Further, the breakup process is studied for the combined mode and it is found that indeed the breakup characteristics change. The breakup occurs at half- or full-wavelength intervals, depending on the proportion of the individual sinuous and varicose modes. In general, the breakup length decreases with the increase in the Weber number, gas-to-liquid velocity and density ratios.

The predictive model for the spray formation incorporates both the deterministic and

the stochastic aspects of liquid atomization process. The deterministic aspect involves the determination of the breakup length by means of hydrodynamic instability theory. The stochastic aspect is described by statistical means through an application of the maximum entropy principle based on Bayesian entropy. The two sub-models are coupled together by the various source terms signifying the liquid-gas interaction and a prior distribution which provides information regarding the unstable wave elements on the two liquid-gas interfaces.

Experimental investigation of the breakup process of the liquid sheet produced by a planar nozzle and an actual gas turbine nozzle is performed with a high speed CCD camera. The droplet size and velocity distributions for these nozzles, near the breakup region, are obtained by using a two-component phase-Doppler particle analyzer (PDPA) system. Good agreement of the breakup length is obtained for the planar nozzle, the annular nozzle, and the gas turbine nozzle. It is observed that a satisfactory agreement of the predicted initial droplet size and velocity distributions is obtained for the planar nozzle. The application of this theoretical model to different geometries, like the annular and the gas turbine nozzles, for the prediction of the droplet size and velocity distributions also shows reasonable agreement with the measurements. Despite some shortcomings, the present model can be utilized in obtaining the initial droplet size and velocity distributions for a wide range of spray applications.

10.2 Recommendations

The breakup process of the liquid sheet can be investigated, in a similar manner, for an annular geometry and further for the case with swirl in both the liquid and gas phases. Such an analysis will closely resemble the actual air-blast nozzles used in gas turbine applications. In the present nonlinear analysis, the liquid sheet thickness is assumed to be constant. However, in the actual application, the sheet thickness tends to vary with the distance from the nozzle exit. It will be interesting to study a variable thickness sheet geometry, even from the linear instability stand point.

Regarding the predictive model for the initial droplet size and velocity distributions, further attempts can be made to obtain a more accurate prior distribution for different

complex geometries based on the information from the linear and nonlinear instability analyses. Modeling effort is needed in obtaining a relation between the droplet diameter and the wavenumber greater than the cut-off wavenumber. Also, an additional prior distribution based on the droplet velocity can be coupled with the present prior distribution to obtain a better agreement with the experimental measurements. Studies can be directed towards a better formulation for the source terms for complex nozzle geometries.

The weakest parameter in the present model is the nozzle constant C. A better understanding of the droplet formation process is needed, which will provide a better modeling for the mass-mean diameter D_{30}. At present, calculation of D_{30} is based on the Rayleigh breakup mechanism, which is too idealized for real sprays.

Finally, more experimental measurements need to be carried out for different nozzle geometries and their comparisons with the theoretical predictions to be done. This might help in characterizing a particular type of nozzle for which a fixed combination of the nozzle constant C, the initial disturbance amplitude η_0 and the strength of the disturbance mode (ϵ_s or ϵ_v) will produce optimum agreement with the experiment.

Appendix A

Constants for Sinuous Mode

A.1 Second-Order Solution

$$
\begin{aligned}
B_{2,s} \;=\; & \frac{1}{8}[4\omega_{2,s}^2\omega_{1,s}^2\sinh(k)\cosh(k)\cosh(2k) - 4k^2\alpha_{2,s}^2\sinh(k)\cosh(k)\cosh(2k) \\
& -16k^2\alpha_{2,s}\alpha_{1,s}\sinh(2k)\cosh(k)^2 \; - 8k\alpha_{1,s}\omega_{2,s}^2\sinh(k)\cosh(k)\cosh(2k) \\
& +8k\alpha_{1,s}\omega_{2,s}^2\sinh(2k)\cosh(k)^2 \; + 4\omega_{2,s}^2\alpha_{2,s}^2\sinh(2k)\cosh(k)^2 \\
& +16k\omega_{1,s}^2\sinh(k)\cosh(k)\cosh(2k) \; + 32\alpha_{2,s}^2\omega_{1,s}^2\sinh(2k)\cosh(k)^2 \\
& -32\alpha_{1,s}\omega_{1,s}\sinh(k)\cosh(k)\cosh(2k) \; - 4\alpha_{2,s}\omega_{1,s}\sinh(2k)\cosh(k)^2 \\
& -16\alpha_{2,s}\alpha_{1,s}\omega_{1,s}^2\sinh(2k)\cosh(k)^2 \; + 16\alpha_{2,s}\alpha_{1,s}\omega_{1,s}^2\sinh(k)\cosh(k)\cosh(2k) \\
& -4\omega_{2,s}^2\alpha_{1,s}^2\sinh(k)\cosh(k)\cosh(2k) \; + 4\alpha_{2,s}^2\omega_{1,s}^2\sinh(k)\cosh(k)\cosh(2k) \\
& -32k\omega_{1,s}^2\alpha_{2,s}\sinh(2k)\cosh(k)^2 \; + 32k\omega_{1,s}^2\alpha_{2,s}\sinh(k)\cosh(k)\cosh(2k) \\
& -32k\omega_{1,s}^2\alpha_{1,s}\sinh(k)\cosh(k)\cosh(2k) \; - 16\omega_{1,s}^4\sinh(k)\cosh(k)\cosh(2k) \\
& -4\omega_{2,s}^2\omega_{1,s}^2\sinh(2k)\cosh(k)^2 \; + 32k\omega_{1,s}^2\alpha_{1,s}\sinh(2k)\cosh(k)^2 \\
& +16\alpha_{1,s}^4\sinh(2k)\cosh(k)^2 \; - 4k^2\omega_{1,s}^2\sinh(2k) \\
& -4\alpha_{2,s}^2\alpha_{1,s}^2\sinh(k)\cosh(k)\cosh(2k) \; - 32k\alpha_{1,s}^2\alpha_{2,s}\sinh(2k)\cosh(k)^2 \\
& +32k\alpha_{1,s}^2\alpha_{2,s}\sinh(k)\cosh(k)\cosh(2k) \; + 4\alpha_{2,s}^2\alpha_{1,s}^2\sinh(2k)\cosh(k)^2 \\
& -8k\alpha_{1,s}\alpha_{2,s}^2\sinh(k)\cosh(k)\cosh(2k) \; + 16k^2\alpha_{1,s}^2\sinh(2k)\cosh(k)^2
\end{aligned}
$$

$$
\begin{aligned}
&-16k^2\alpha_{1,s}^2\sinh(k)\cosh(k)\cosh(2k) \; -16\alpha_{2,s}\alpha_{1,s}^3\sinh(2k)\cosh(k)^2\\
&-16\alpha_{1,s}^4\sinh(k)\cosh(k)\cosh(2k) \; +16\alpha_{2,s}\alpha_{1,s}^3\sinh(k)\cosh(k)\cosh(2k)\\
&+16k^2\alpha_{1,s}\alpha_{2,s}\sinh(k)\cosh(k)\cosh(2k) \; +8k\alpha_{1,s}\omega_{2,s}^2\sinh(2k)\cosh(k)^2\\
&+32k\alpha_{1,s}^3\sinh(2k)\cosh(k)^2 \; -32k\alpha_{1,s}^3\sinh(k)\cosh(k)\cosh(2k)\\
&+4k^2\omega_{2,s}^2\sinh(2k)\cosh(k)^2 \; -4k^2\omega_{2,s}^2\sinh(k)\cosh(k)\cosh(2k)\\
&-16k^2\omega_{1,s}^2\sinh(2k)\cosh(k)^2 \; +4k^2\alpha_{2,s}^2\sinh(2k)\cosh(k)^2\\
&+4\alpha_{1,s}^4\sinh(2k)-8k\omega_{1,s}^2\alpha_{2,s}\sinh(2k)-8k\alpha_{1,s}^2\alpha_{2,s}\sinh(2k)\\
&+2k\alpha_{1,s}\omega_{2,s}^2\sinh(2k)+16\omega_{1,s}^4\sinh(2k)\cosh(k)^2 \; +8k\omega_{1,s}^2\alpha_{1,s}\sinh(2k)\\
&-\omega_{2,s}^2\omega_{1,s}^2\sinh(2k)+4\omega_{1,s}^4\sinh(2k)-4\alpha_{1,s}\alpha_{2,s}\omega_{1,s}^2\sinh(2k)\\
&+\omega_{2,s}^2\alpha_{1,s}^2\sinh(2k)+8\alpha_{1,s}^2\omega_{1,s}^2\sinh(2k)-\alpha_{2,s}^2\omega_{1,s}^2\sinh(2k)\\
&+8k\alpha_{1,s}^3\sinh(2k)+4k^2\alpha_{1,s}^2\sinh(2k)-4k^2\alpha_{2,s}\alpha_{1,s}\sinh(2k)\\
&+2k\alpha_{1,s}\alpha_{2,s}^2\sinh(2k)-4\alpha_{2,s}\alpha_{1,s}^3\sinh(2k)+k^2\alpha_{2,s}^2\sinh(2k)\\
&+\alpha_{2,s}^2\alpha_{1,s}^2\sinh(2k)+k^2\omega_{2,s}^2\sinh(2k)]/\\
&[\sinh(2k)\cosh(k)^2 \; (\alpha_{2,s}^4 \; +16\alpha_{1,s}^4 \; -32\alpha_{2,s}\alpha_{1,s}^3 \; -8\alpha_{2,s}^3\alpha_{1,s}+24\alpha_{2,s}^2\alpha_{1,s}^2\\
&-8\omega_{2,s}^2\omega_{1,s}^2 \; +8\alpha_{2,s}^2\omega_{1,s}^2 \; -32\alpha_{2,s}\omega_{1,s}^2\alpha_{1,s} \; +8\omega_{2,s}^2\alpha_{1,s}^2 \; +32\alpha_{1,s}^2\omega_{1,s}^2\\
&+16\omega_{1,s}^4-8\alpha_{1,s}\alpha_{2,s}\omega_{2,s}^2 \; +2\alpha_{2,s}^2\omega_{2,s}^2 \; +\omega_{2,s}^4 \;)] \qquad \text{(A.1)}
\end{aligned}
$$

$$
\begin{aligned}
C_{2,s} \;=\; &[-8k\alpha_{1,s}\cosh(k)^2-4\alpha_{1,s}^2\cosh(k)^2-4k^2\cosh(k)^2\\
&+\coth(2k)\tanh(k)\cosh(k)^2(4\alpha_{1,s}^2 \; +8k\alpha_{1,s} \; +4k^2)-2k\alpha_{1,s}\\
&-\omega_{1,s}^2 \; -k^2-\alpha_{1,s}^2 \;]/[\alpha_{2,s}^2 \; -4\alpha_{1,s}\alpha_{2,s} \; +\omega_{2,s}^2 \; +4\alpha_{1,s}^2 \;]\cosh(k)^2 \qquad \text{(A.2)}
\end{aligned}
$$

$$
A_{2,s} \;=\; -[B_{2,s}+C_{2,s}] \qquad \text{(A.3)}
$$

A.2 Third-Order Solution

$$S_1 = \tanh(k)\coth(2k) \tag{A.4}$$

$$S_2 = \tanh(3k)\tanh(k) \tag{A.5}$$

$$S_3 = \tanh(3k)\coth(2k) \tag{A.6}$$

$$S_4 = \tanh(3k)\coth(2k)\tanh(k) \tag{A.7}$$

$$a_{31} = \rho + \tanh(3k) \tag{A.8}$$

$$a_{32} = (3k)^2\rho U^2 + (3k)^2\tanh(3k) - \frac{(3k)^3}{We} \tag{A.9}$$

$$a_{33} = 3k[\rho + \tanh(3k)] \tag{A.10}$$

$$\begin{aligned} B_{3,s} = & -A_{2,s}[S_2(-0.75k\alpha_{1,s}\alpha_{2,s} - 2.25k^3 - 0.75k^2\alpha_{1,s}\alpha_{2,s} + 0.75k\alpha_{1,s}^2 - 0.75k\alpha_{1,s}^2 \\ & +0.75k\omega_{1,s}\omega_{2,s} + 3k^2\alpha_{1,s}) + S_1(-1.5k^3 - 0.75k^2\alpha_{2,s} - 1.5k^2\alpha_{1,s} - 0.75k\alpha_{1,s}\alpha_{2,s} \\ & +0.75k\omega_{1,s}\omega_{2,s}) + S_3(-4.5k^3 - 3.75k^2\alpha_{2,s} - 1.5k^2\alpha_{1,s} - 0.75k\alpha_{2,s}^2 \\ & +0.75k\omega_{2,s}^2 - 0.75k\alpha_{1,s}\alpha_{2,s} + 0.75k\omega_{1,s}\omega_{2,s}) + 8.25k^3 + 5.25k^2\alpha_{2,s} + 6k^2\alpha_{1,s} \\ & -0.375k\omega_{2,s}^2 + 0.375k\alpha_{2,s}^2 - 0.75k\omega_{1,s}^2 + 0.75k\alpha_{1,s}^2 - 1.5Uk^2\alpha_{2,s} \\ & +1.5\rho Uk^2\alpha_{2,s} + 0.375\rho k\alpha_{2,s}^2 - 0.375k\rho\omega_{2,s}^2 + 1.5k\alpha_{1,s}\alpha_{2,s} \\ & +0.75k\rho\alpha_{1,s}\alpha_{2,s} - 2.25k\omega_{1,s}\omega_{2,s}]/[a_{33} - a_{31}\omega_{1,s}^2 - a_{31}\omega_{2,s}^2 \\ & +a_{31}\alpha_{1,s}^2 + a_{31}\alpha_{2,s}^2 + 2a_{32}\alpha_{1,s} + 2a_{32}\alpha_{2,s} - 2a_{31}\omega_{1,s}\omega_{2,s} + 2a_{31}\alpha_{1,s}\alpha_{2,s}] \end{aligned} \tag{A.11}$$

$$\begin{aligned} C_{3,s} = & -A_{2,s}[S_2(-0.75k\alpha_{1,s}\alpha_{2,s} - 2.25k^3 - 0.75k^2\alpha_{1,s}\alpha_{2,s} - 3k^2\alpha_{1,s} + 0.75k\omega_{1,s}^2 \\ & -0.75k\alpha_{1,s}^2 - 0.75k\omega_{1,s}\omega_{2,s}) + S_1(-1.5k^3 - 0.75k^2\alpha_{2,s} - 1.5k^2\alpha_{1,s} - 0.75k\omega_{1,s}\omega_{2,s} \\ & -0.75k\alpha_{1,s}\alpha_{2,s}) + 8.25k^3 + 5.25k^2\alpha_{2,s} - 6k^2\alpha_{1,s} - 0.375k\omega_{2,s}^2 + 0.375k\alpha_{2,s}^2 \\ & -0.75k\omega_{1,s}^2 + 0.75k\alpha_{1,s}^2 - 1.5Uk^2\alpha_{2,s} + 1.5\rho Uk^2\alpha_{2,s} + 0.375\rho k\alpha_{2,s}^2 \\ & -0.375\rho k\omega_{2,s}^2 + 1.5k\alpha_{1,s}\alpha_{2,s} + 0.75\rho k\alpha_{1,s}\alpha_{2,s} + 2.25k\omega_{2,s}\omega_{1,s} \\ & +S_3(-4.5k^3 - 3.75k^2\alpha_{2,s} - 1.5k^2\alpha_{1,s} - 0.75k\alpha_{2,s}^2 + 0.75k\omega_{2,s}^2 - 0.75k\alpha_{1,s}\alpha_{2,s} \\ & -0.75k\omega_{2,s}\omega_{1,s})]/[a_{33} - a_{31}\omega_{1,s}^2 - a_{31}\omega_{2,s}^2 + a_{31}\alpha_{1,s}^2 \\ & +a_{31}\alpha_{2,s}^2 + 2a_{32}\alpha_{1,s} + 2a_{32}\alpha_{2,s} + 2a_{31}\omega_{2,s}\omega_{1,s} + 2a_{31}\alpha_{1,s}\alpha_{2,s}] \end{aligned} \tag{A.12}$$

$$
\begin{aligned}
D_{3,s} &= -[\tanh(3k)(-0.28125k^4 - 5.625k^3\alpha_{1,s} + 0.28125k^2\omega_{1,s}^2 - 0.28125k\alpha_{1,s}^2) \\
&+S_4(1.125k^4 - 0.9375k^2\omega_{1,s}^2 + 2.25k^3\alpha_{1,s} + 1.125k^2\alpha_{1,s}^2) + \tanh(k)(-1.5k^4 \\
&+0.28125k^2\omega_{1,s}^2 - 1.59375k^2\alpha_{1,s}^2 + 0.75k\omega_{1,s}^2 - 3k^3\alpha_{1,s}) + \coth(2k)(0.375k^4 \\
&+0.75k^3\alpha_{1,s} - 0.375k^2\omega_{1,s}^2 + 0.375k^2\alpha_{1,s}^2) + S_3(-4.5B_{2,s}k^3 - 9k^2B_{2,s}\alpha_{1,s} \\
&+3.75kB_{2,s}\omega_{1,s}^2 - 4.5kB_{2,s}\alpha_{1,s}^2) + S_2(-4.5B_{2,s}k^3 - 4.5B_{2,s}k^2\alpha_{1,s} + 1.5kB_{2,s}\omega_{1,s}^2 \\
&-2.25kB_{2,s}\alpha_{1,s}^2) + S_1(-1.5k^3B_{2,s} + 1.5kB_{2,s}\omega_{1,s}^2) - \frac{2.8125}{We}k^5 + 8.25k^3B_{2,s} \\
&+0.75k^2\omega_{1,s}^2 - 0.375k^2\alpha_{1,s}^2 - 0.375k^3U\alpha_{1,s} + 0.375\rho k^2\alpha_{1,s}^2 - 0.1875\rho k^2\omega_{1,s}^2 \\
&+16.5k^2B_{2,s}\alpha_{1,s} + 6.75kB_{2,s}\alpha_{1,s}^2 - 8.25kB_{2,s}\omega_{1,s}^2 + 3.75k^3\rho U\alpha_{1,s} \\
&-1.5Uk^2B_{2,s}\alpha_{1,s} + 1.5\rho Uk^2B_{2,s}\alpha_{1,s} + 1.5k\rho B_{2,s}\alpha_{1,s}^2 - 1.5\rho kB_{2,s}\omega_{1,s}^2] \\
&/[6a_{32} + a_{33} - 9a_{31}\omega_{1,s}^2 + 9a_{31}\alpha_{1,s}^2] \qquad \text{(A.13)} \\
E_{3,s} &= -[C_{2,s}(15k\alpha_{1,s}^2 + 4.5k^3 + 34.5k^2\alpha_{1,s} - 1.5k\omega_{1,s}^2 + 3k\rho\alpha_{1,s}^2 \\
&-3Uk^2\alpha_{1,s} + 3Uk^2\alpha_{1,s}\rho) + S_4(3.375k^4 - 0.5625k^2\omega_{1,s}^2 + 6.75k^3\alpha_{1,s} \\
&+3.375k^2\alpha_{1,s}^2) + S_2(-4.5k^3C_{2,s} - 4.5B_{2,s}k^3 - 9C_{2,s}k^2\alpha_{1,s} + 1.5kC_{2,s}\omega_{1,s}^2 \\
&-4.5kC_{2,s}\alpha_{1,s}^2 - 1.5kB_{2,s}\omega_{1,s}^2 - 4.5B_{2,s}k^2\alpha_{1,s} - 2.25kB_{2,s}\alpha_{1,s}^2 \\
&+S_3(-9C_{2,s}k^3 - 4.5k^3B_{2,s} - 13.5k^2C_{2,s}\alpha_{1,s} + 1.5kB_{2,s}\omega_{1,s}^2 - 9kC_{2,s}\alpha_{1,s}^2 \\
&-9k^2B_{2,s}\alpha_{1,s} - 4.5kB_{2,s}\alpha_{1,s}^2) + S_1(-3k^3C_{2,s} - 0.75k^3\alpha_{1,s} - 1.5k^3B_{2,s} \\
&-6k^2C_{2,s}\alpha_{1,s} - 3kC_{2,s}\alpha_{1,s}^2 - 1.5kB_{2,s}\omega_{1,s}^2 - 3k^2B_{2,s}\alpha_{1,s} - 1.5kB_{2,s}\alpha_{1,s}^2) \\
&+B_{2,s}(8.25k^3 + 3.75k\omega_{1,s}^2 + 16.5k^2\alpha_{1,s} + 6.75k\alpha_{1,s}^2 - 1.5Uk^2\alpha_{1,s} \\
&+1.5Uk^2\alpha_{1,s}\rho + 1.5k\rho\alpha_{1,s}^2 - 1.5k\rho\omega_{1,s}^2) + \tanh(k)(-4.5k^4 \\
&-4.78125k^2\alpha_{1,s}^2 - 9k^3\alpha_{1,s} - 1.03125k^2\omega_{1,s}^2 - 0.75kB_{2,s}\omega_{1,s}^2) \\
&+\tanh(3k)(-0.84375k^4 + 0.09375k^2\omega_{1,s}^2 - 1.6875k^3\alpha_{1,s}) \\
&+\coth(2k)(1.125k^4 + 0.375k^2\omega_{1,s}^2 + 1.5k^3\alpha_{1,s} + 1.125k^2\alpha_{1,s}^2) \\
&-1.125k^2\alpha_{1,s}^2 + 0.375k^2\omega_{1,s}^2 - 0.5625k^2\rho\omega_{1,s}^2 + 1.125k^2\rho\alpha_{1,s}^2 - 1.125k^3U\alpha_{1,s} \\
&+1.125k^3U\alpha_{1,s}\rho - \frac{0.84375}{We}k^5]/[a_{33} + 6a_{32}\alpha_{1,s} - a_{31}\omega_{1,s}^2 + 9a_{31}\alpha_{1,s}^2] \qquad \text{(A.14)} \\
A_{3,s} &= -[B_{3,s} + C_{3,s} + D_{3,s} + E_{3,s}] \qquad \text{(A.15)}
\end{aligned}
$$

Appendix B

Constants for Varicose Mode

B.1 Second-Order Solution

$$
\begin{aligned}
X1 &= -\frac{1}{\rho+\coth(2k)}k[\omega_{1,v}^2+(\alpha_{1,v}+k)^2][0.25\{\coth(k)^2-1\} \\
&\quad -\{1-\coth(k)\coth(2k)\}] && \text{(B.1)}\\
X2 &= -\frac{0.5}{\rho+\coth(2k)}k\omega_{1,v}(\alpha_{1,v}+k)[5-\coth(k)^2-4\coth(2k)\coth(k)] && \text{(B.2)}\\
A1 &= 4(\alpha_{1,v}^2\omega_{1,v}^2)+(\omega_{2,v}^2+\alpha_{2,v}^2) && \text{(B.3)}\\
A2 &= 8\alpha_{1,v}\omega_{1,v} && \text{(B.4)}\\
B_{2,v} &= \frac{4X2\alpha_{2,v}\omega_{1,v}+4X1\alpha_{1,v}\alpha_{2,v}+X1A1+X2A2}{A2^2-16\omega_{1,v}^2\alpha_{2,v}^2+A1^2-16\alpha_{1,v}^2\alpha_{2,v}^2} && \text{(B.5)}\\
C_{2,v} &= \frac{-A2X1+4\omega_{1,v}\alpha_{2,v}X1+A1X2-4\alpha_{1,v}\alpha_{2,v}X2}{A_2^2-16\omega_{1,v}^2\alpha_{2,v}^2+B_{2,v}^2-16\alpha_{1,v}^2\alpha_{2,v}^2} && \text{(B.6)}\\
B1 &= -k(\alpha_{1,v}+k)^2\{1-\coth(k)\coth(2k)\} && \text{(B.7)}\\
B2 &= 0.25k[\omega_{1,v}^2+(k+\alpha_{1,v})^2][1-\coth(k)^2] && \text{(B.8)}\\
D_{2,v} &= -\frac{B1+B2}{[4\alpha_{1,v}^2+(\omega_{2,v}^2+\alpha_{2,v}^2)-4\alpha_{1,v}\alpha_{2,v}][\rho+\coth(2k)]} && \text{(B.9)}\\
A_{2,v} &= -[B_{2,v}+C_{2,v}+D_{2,v}] && \text{(B.10)}
\end{aligned}
$$

B.2 Third-Order Solution

$$
\begin{aligned}
b_1 &= 0.75kA_{2,v}[\coth(3k)\coth(2k)\{\omega_{2,v}^2 - 2k\alpha_{2,v} - 2\alpha_{1,v}k - \alpha_{1,v}\alpha_{2,v} - \alpha_{2,v}^2 \\
&\quad -\alpha_{2,v}^2 - \omega_{1,v}\omega_{2,v}\} + \coth(k)\coth(2k)\{\omega_{1,v}^2 \\
&\quad -\alpha_{1,v}\alpha_{2,v} - \omega_{1,v}\omega_{2,v} - \alpha_{2,v}k - k\alpha_{1,v}\}] && \text{(B.11)} \\
b_2 &= A_{2,v}[1.5k\alpha_{1,v}\alpha_{2,v} + 1.5k\omega_{1,v}\omega_{2,v} + 2.25\alpha_{1,v}k^2 + 0.75k^2\alpha_{2,v} \\
&\quad -0.75k\omega_{2,v}^2 + 0.75k\alpha_{2,v}^2 - 0.75k\omega_{1,v}^2 + 0.75k\alpha_{1,v}^2] && \text{(B.12)} \\
b_3 &= -0.75k\coth(k)\coth(2k)A_{2,v}[\alpha_{1,v}\alpha_{2,v} + 2\alpha_{1,v}k + k\alpha_{2,v} + 2k^2\omega_{1,v}\omega_{2,v}] && \text{(B.13)} \\
b_4 &= 0.75kA_{2,v}[\alpha_{1,v}\alpha_{2,v} + 2\alpha_{1,v}k + k\alpha_{2,v} + 2k^2 + \omega_{1,v}\omega_{2,v}] && \text{(B.14)} \\
b_5 &= -0.75k^2A_{2,v}[\coth(3k)\coth(2k)\{2\alpha_{2,v} + 6k\} + \coth(3k)\coth(k) \\
&\quad \{3\alpha_{1,v} + 3k\} - 3\alpha_{2,v} - 8k - 2\alpha_{1,v}] && \text{(B.15)} \\
x_{3b} &= (b_1 + b_2 + b_3 + b_4 + b_5)/[\rho + \coth(3k)] && \text{(B.16)} \\
c_1 &= -0.75kA_{2,v}[\coth(3k)\coth(2k)\{\alpha_{1,v}\omega_{2,v} + 2\alpha_{2,v}\omega_{2,v} + 2\omega_{1,v}k + 2k\omega_{2,v} \\
&\quad +\alpha_{2,v}\omega_{1,v}\} + \coth(3k)\coth(k)\{\omega_{2,v}\alpha_{1,v} + \alpha_{2,v}\omega_{1,v} + \omega_{2,v}k \\
&\quad +k\omega_{1,v} + 2\alpha_{1,v}\omega_{1,v}\}] && \text{(B.17)} \\
c_2 &= A_{2,v}k[1.5\alpha_{1,v}\omega_{2,v} + \alpha_{2,v}\omega_{1,v} + k\omega_{1,v} + \omega_{2,v}\alpha_{2,v} + k\omega_{2,v} + \omega_{1,v}\alpha_{1,v}] && \text{(B.18)} \\
c_3 &= -0.75kA_{2,v}\coth(2k)\coth(k)[2\omega_{1,v}k + k\omega_{2,v} + \alpha_{1,v}\omega_{2,v} + \omega_{1,v}\alpha_{2,v}] && \text{(B.19)} \\
c_4 &= 0.75kA_{2,v}(2\omega_{1,v}k + k\omega_{2,v} + \alpha_{1,v}\omega_{2,v} + \omega_{1,v}\alpha_{2,v}] && \text{(B.20)} \\
c_5 &= -0.75k^2A_{2,v}[2\omega_{2,v}\coth(3k)\coth(k) + 3\omega_{1,v}\coth(3k)\coth(k) \\
&\quad -3\omega_{2,v} - 2\omega_{1,v}] && \text{(B.21)} \\
x_{3c} &= (c_1 + c_2 + c_3 + c_4 + c_5)/[\rho + \coth(3k)] && \text{(B.22)} \\
B_{3,v} &= \{-x_{3c}[2\omega_{1,v}\alpha_{1,v} + 2\omega_{1,v}\alpha_{3,v} + 2\alpha_{2,v}\omega_{2,v} + 2\alpha_{2,v}\omega_{1,v} + 2\alpha_{1,v}\omega_{2,v} + 2\alpha_{3,v}\omega_{2,v}] \\
&\quad -x_{3b}[-\omega_{1,v}^2 + \alpha_{1,v}^2 + \omega_{3,v}^2 + \alpha_{3,v}^2 + 2\alpha_{1,v}\alpha_{3,v} - \omega_{2,v}^2 + 2\alpha_{1,v}\alpha_{2,v} + \alpha_{2,v}^2 \\
&\quad +2\alpha_{2,v}\alpha_{3,v} - 2\omega_{1,v}\omega_{2,v}]\}/[4\alpha_{1,v}^2\omega_{1,v}\omega_{2,v} + 2\alpha_{1,v}^2\omega_{1,v}^2 - 6\omega_{1,v}^2\alpha_{3,v}^2 - 2\omega_{1,v}^2\omega_{3,v}^2 \\
&\quad +2\alpha_{1,v}^2\omega_{3,v}^2 - 2\alpha_{1,v}^2\alpha_{3,v}^2 + 2\omega_{3,v}^2\alpha_{3,v}^2 + \omega_{1,v}^4\alpha_{1,v}^4 + \omega_{3,v}^4 + \alpha_{3,v}^4 - 4\omega_{1,v}\omega_{2,v}\omega_{3,v}^2 \\
&\quad +4\alpha_{1,v}\alpha_{2,v}\omega_{3,v}^2 + 2\alpha_{1,v}^2\omega_{2,v}^2 + 2\alpha_{2,v}^2\omega_{2,v}^2 + 2\alpha_{2,v}^2\omega_{1,v}^2 - 6\alpha_{3,v}^2\omega_{2,v}^2 + 4\omega_{1,v}^3\omega_{2,v} \\
&\quad +6\omega_{1,v}^2\omega_{2,v}^2 + 4\omega_{1,v}\omega_{2,v}^3 - 2\omega_{2,v}^2\omega_{3,v}^2 + 4\alpha_{1,v}^3\alpha_{2,v} + 6\alpha_{1,v}^2\alpha_{2,v}^2 + 4\alpha_{1,v}\alpha_{2,v}^3 \\
&\quad +2\alpha_{2,v}^2\omega_{3,v}^2 - 2\alpha_{2,v}^2\alpha_{3,v}^2 + 4\alpha_{1,v}\omega_{1,v}^2\alpha_{2,v} + 4\alpha_{1,v}\omega_{2,v}^2\alpha_{2,v} + 4\alpha_{2,v}^2\omega_{1,v}\omega_{2,v}
\end{aligned}
$$

$$-12\omega_{1,v}\alpha_{3,v}^2\omega_{2,v} - 4\alpha_{1,v}\alpha_{2,v}\alpha_{3,v}^2 + \omega_{2,v}^4 + \alpha_{2,v}^4 + 8\alpha_{1,v}\omega_{1,v}\alpha_{2,v}\omega_{2,v}] \tag{B.23}$$

$$\begin{aligned} C_{3,v} &= \{-x_{3c}[\alpha_{3,v}^2 - 2\alpha_{1,v}\alpha_{3,v} - 2\alpha_{3,v}\alpha_{2,v} - \omega_{1,v}^2 - 2\omega_{2,v}\omega_{1,v} + \alpha_{1,v}^2 - \omega_{2,v}^2 \\ &\quad +2\alpha_{1,v}\alpha_{2,v} + \omega_{3,v}^2 + \alpha_{2,v}^2] - x_{3b}[2\alpha_{3,v}\omega_{1,v} + 2\alpha_{3,v}\omega_{2,v} - 2\alpha_{1,v}\omega_{1,v} - 2\alpha_{2,v}\omega_{1,v} \\ &\quad -2\alpha_{1,v}\omega_{2,v} - 2\alpha_{2,v}\omega_{2,v}]\}/[4\alpha_{1,v}^2\omega_{1,v}\omega_{2,v} + 2\alpha_{1,v}^2\omega_{1,v}^2 - 6\omega_{1,v}^2\alpha_{3,v}^2 - 2\omega_{1,v}^2\omega_{3,v}^2 \\ &\quad +2\alpha_{1,v}^2\omega_{3,v}^2 - 2\alpha_{1,v}^2\alpha_{3,v}^2 + 2\omega_{3,v}^2\alpha_{3,v}^2 + \omega_{1,v}^4 + \alpha_{1,v}^4 + \omega_{3,v}^4 + \alpha_{3,v}^4 - 4\omega_{1,v}\omega_{2,v}\omega_{3,v}^2 \\ &\quad +4\alpha_{1,v}\alpha_{2,v}\omega_{3,v}^2 + 2\alpha_{1,v}^2\omega_{2,v}^2 + 2\alpha_{2,v}^2\omega_{2,v}^2 + 2\alpha_{2,v}^2\omega_{1,v}^2 - 6\alpha_{3,v}^2\omega_{2,v}^2 + 4\omega_{1,v}^3\omega_{2,v} \\ &\quad +6\omega_{1,v}^2\omega_{2,v}^2 + 4\omega_{1,v}\omega_{2,v}^3 - 2\omega_{2,v}^2\omega_{3,v}^2 + 4\alpha_{1,v}^3\alpha_{2,v} + 6\alpha_{1,v}^2\alpha_{2,v}^2 + 4\alpha_{1,v}\alpha_{2,v}^3 \\ &\quad +2\alpha_{2,v}^2\omega_{3,v}^2 - 2\alpha_{2,v}^2\alpha_{3,v}^2 + 4\alpha_{1,v}\alpha_{2,v}\omega_{2,v}^2 + 4\alpha_{2,v}^2\omega_{1,v}\omega_{2,v} - 12\omega_{1,v}\alpha_{3,v}^2\omega_{2,v} \\ &\quad -4\alpha_{1,v}\alpha_{2,v}\alpha_{3,v}^2 + \omega_{2,v}^4 + \alpha_{2,v}^4 + 8\alpha_{1,v}\alpha_{2,v}\omega_{1,v}\omega_{2,v}] \end{aligned} \tag{B.24}$$

$$\begin{aligned} d_1 &= -0.1875k[\coth(3k)\coth(2k)\{\omega_{1,v}\alpha_{1,v}C_{2,v} + 8\omega_{1,v}kC_{2,v} - 20\alpha_{1,v}\omega_{1,v}C_{2,v} \\ &\quad +115\alpha_{1,v}^2B_{2,v}\} + \coth(3k)\coth(k)\{8C_{2,v}\omega_{1,v}\alpha_{1,v} + 4C_{2,v}\omega_{1,v}k\}] \end{aligned} \tag{B.25}$$

$$\begin{aligned} d_2 &= 0.046875k[\coth(k)\{5\omega_{1,v}^2k - 9\alpha_{1,v}k^2 - 9\alpha_{1,v}^2k\} - 32\omega_{1,v}^2B_{2,v} - 16B_{2,v}\alpha_{1,v} \\ &\quad -64C_{2,v}\alpha_{1,v}\omega_{1,v} + 48kC_{2,v}\omega_{1,v} + 16\alpha_{1,v}^2B_{2,v}] \end{aligned} \tag{B.26}$$

$$d_3 = -3\coth(2k)\coth(k)k\alpha_{1,v}\omega_{1,v}C_{2,v} \tag{B.27}$$

$$\begin{aligned} d_4 &= 0.046875k[\coth(k)\{-12\alpha_{1,v}k^2 - 6k^3 - 3\omega_{1,v}^2k - 5\alpha_{1,v}^2k\} - 16\alpha_{1,v}^2B_{2,v} \\ &\quad +64C_{2,v}\alpha_{1,v}\omega_{1,v} + 16B_{2,v}\alpha_{1,v}] \end{aligned} \tag{B.28}$$

$$\begin{aligned} d_5 &= -0.046875k^2[\coth(3k)\coth(2k)\{64C_{2,v}\omega_{1,v} - 32B_{2,v}\alpha_{1,v}\} \\ &\quad -48C_{2,v}\omega_{1,v}\coth(3k)\coth(k) - \coth(3k)\{-3\alpha_{1,v}k - 3k^2\} \\ &\quad +\coth(k)\{k\alpha_{1,v} + k^2\} - 64C_{2,v}\omega_{1,v}] \end{aligned} \tag{B.29}$$

$$d_6 = -0.0703125\frac{k^5}{We} \tag{B.30}$$

$$x_{3d} = (d_1 + d_2 + d_3 + d_4 + d_5 + d_6)/[\rho + \coth(3k)] \tag{B.31}$$

$$\begin{aligned} e_1 &= 0.375k[3k\alpha_{1,v}\omega_{1,v}\coth(3k)\coth(2k)\coth(k) + \coth(3k)\coth(2k)\{3k^2\omega_{1,v} \\ &\quad -3k\omega_{1,v}\alpha_{1,v} + 12\omega_{1,v}^2C_{2,v} + 2k\alpha_{1,v}C_{2,v}\} + \coth(3k)\coth(k)\{2C_{2,v}\alpha_{1,v}k \\ &\quad -8B_{2,v}\alpha_{1,v}\omega_{1,v} + 2C_{2,v}\alpha_{1,v}^2 + 6C_{2,v}\omega_{1,v}^2\}] \end{aligned} \tag{B.32}$$

$$e_2 = -0.1875k[\coth(k)\{-\omega_{1,v}k^2 + 8\omega_{1,v}k\alpha_{1,v}\} - 12C_{2,v}\alpha_{1,v}^2 - 4B_{2,v}\alpha_{1,v}\omega_{1,v}$$

$$+12C_{2,v}\alpha_{1,v}k + 36C_{2,v}\omega_{1,v}^2] \tag{B.33}$$

$$e_3 = \frac{0.375k\cosh(k)\coth(2k)}{\cosh(k)^2-1}[\sinh(k)\{4C_{2,v}\omega_{1,v}^2 - 4k^2C_{2,v} + 4C_{2,v}\alpha_{1,v}^2\}$$
$$+\cosh(k)\{\omega_{1,v}^2k - \omega_{1,v}k^2\}] \tag{B.34}$$

$$e_4 = -0.1875k[\coth(k)\{2\omega_{1,v}^2k - \omega_{1,v}k^2 + \omega_{1,v}k\alpha_{1,v}\}$$
$$+8C_{2,v}\omega_{1,v}^2 - 8k^2C_{2,v} + 8C_{2,v}\alpha_{1,v}^2] \tag{B.35}$$

$$e_5 = -0.046875k^2[\coth(3k)\coth(2k)\coth(k)\{24k\omega_{1,v} - 24\omega_{1,v}\}$$
$$+\coth(3k)\coth(k)\{-64C_{2,v}\alpha_{1,v} - 32B_{2,v}\omega_{1,v} + 96kC_{2,v}\}$$
$$+\coth(3k)\coth(k)\{49C_{2,v}k + 48C_{2,v}\alpha_{1,v} - B_{2,v}\omega_{1,v}\} + 12k\omega_{1,v}\coth(3k)$$
$$-4\omega_{1,v}k\coth(k) + 32B_{2,v}\omega_{1,v} + 96C_{2,v}\alpha_{1,v} - 96kC_{2,v}] \tag{B.36}$$

$$x_{3e} = (e_1+e_2+e_3+e_4+e_5)/[\rho+\coth(3k)] \tag{B.37}$$

$$D_{3,v} = \{-x_{3d}[2\alpha_{1,v}\alpha_{3,v} - 9\omega_{1,v}^2 + \alpha_{1,v}^2 + \omega_{3,v}^2 + \alpha_{3,v}^2] - x_{3e}[6\alpha_{1,v}\omega_{1,v} + 3\omega_{1,v}\alpha_{3,v}]\}$$
$$/[18\alpha_{1,v}^2\omega_{1,v}^2 - 27\omega_{1,v}^2\alpha_{3,v}^2 + 81\omega_{1,v}^4 + \alpha_{1,v}^4 + \omega_{3,v}^4 + \alpha_{3,v}^4 - 18\omega_{1,v}^2\omega_{3,v}^2$$
$$+2\alpha_{1,v}^2\omega_{3,v}^2 - 2\alpha_{1,v}^2\alpha_{3,v}^2 + 2\omega_{3,v}^2\alpha_{3,v}^2] \tag{B.38}$$

$$E_{3,v} = \{-x_{3d}[3\alpha_{3,v}\omega_{1,v} - 6\alpha_{1,v}\omega_{1,v}] - x_{3e}[\alpha_{3,v}^2 - 2\alpha_{3,v}\alpha_{1,v} + \alpha_{1,v}^2 - 9\omega_{1,v}^2 + \omega_{3,v}^2]\}$$
$$/[18\alpha_{1,v}^2\omega_{1,v}^2 - 27\omega_{1,v}^2\alpha_{3,v}^2 + 18\omega_{1,v}^4 + \alpha_{1,v}^4 + \omega_{3,v}^4 + \alpha_{3,v}^4 18\omega_{1,v}^2\omega_{3,v}^2$$
$$+2\alpha_{1,v}^2\omega_{3,v}^2 - 2\alpha_{1,v}^2\alpha_{3,v}^2 + 2\omega_{3,v}^2\alpha_{3,v}^2] \tag{B.39}$$

$$f_1 = 0.09375k[\coth(3k)\coth(2k)\{48B_{2,v}\omega_{1,v}^2 - 48kB_{2,v}\alpha_{1,v} - 48\alpha_{1,v}^2B_{2,v}$$
$$-8\alpha_{1,v}kC_{2,v}\} + \coth(3k)\coth(2k)\coth(k)\{-20k\omega_{1,v}^2 + 36k\alpha_{1,v}^2$$
$$+24\alpha_{1,v}k^2\} + \coth(3k)\coth(k)\{-24B_{2,v}\alpha_{1,v}k + 24B_{2,v}\omega_{1,v}^2 - 24B_{2,v}\alpha_{1,v}^2\}$$
$$+\coth(3k)\{5k\omega_{1,v}^2 - 9k\alpha_{1,v}^2\}] \tag{B.40}$$

$$f_2 = -0.09375k[\coth(k)\{21\alpha_{1,v}k^2 - 5k\omega_{1,v}^2 + 17k\alpha_{1,v}^2\} - 72kB_{2,v}\alpha_{1,v}$$
$$-144\alpha_{1,v}kD_{2,v} - 144\alpha_{1,v}^2D_{2,v} + 10k\alpha_{1,v}^2 + 16D_{2,v}\omega_{1,v}^2 + 2k\omega_{1,v}^2 + 6\alpha_{1,v}k^2$$
$$-72\alpha_{1,v}^2B_{2,v} + 56B_{2,v}\omega_{1,v}^2] \tag{B.41}$$

$$f_3 = -\frac{0.09375k\cosh(k)}{\cosh(k)^2-1}[-\coth(2k)\cosh(k)\{-12k^3 - 4k\omega_{1,v}^2$$
$$-12k\alpha_{1,v}^2 - 24\alpha_{1,v}k^2\} + \coth(2k)\sinh(k)\{64\alpha_{1,v}kD_{2,v} + 32\alpha_{1,v}^2D_{2,v}$$
$$+32k^2D_{2,v} + 16k^2B_{2,v} + 32k\alpha_{1,v}B_{2,v} + 16\alpha_{1,v}^2B_{2,v} - 16B_{2,v}\omega_{1,v}^2\}$$
$$+\sinh(k)\{11k^3 + 4k\omega 1,v^2 + 12k\alpha_{1,v}^2 + 24k^2\alpha_{1,v}\}] \tag{B.42}$$

$$
\begin{aligned}
f_4 &= 0.046875k[\coth(k)\{-19k^3 - 18k\alpha_{1,v}^2 - 36\alpha_{1,v}k^2 - 6k\omega_{1,v}^2\} \\
&\quad -32B_{2,v}\omega_{1,v}^2 + 64\alpha_{1,v}^2 D_{2,v} + 32k^2 B_{2,v} + 64k^2 D_{2,v} + 32\alpha_{1,v}^2 B_{2,v} \\
&\quad +128\alpha_{1,v}kD_{2,v} + 64kB_{2,v}\alpha_{1,v}] \qquad \text{(B.43)} \\
f_5 &= -0.046875k^2[\coth(3k)\coth(2k)\coth(k)\{-72k\alpha_{1,v} - 72k^2\} \\
&\quad + \coth(3k)\coth(2k)\{192kD_{2,v} + 64B_{2,v}\alpha_{1,v} + 96kB_{2,v} + 64C_{2,v}\omega_{1,v} \\
&\quad +128D_{2,v}\alpha_{1,v}\} + \coth(3k)\coth(k)\{48B_{2,v}\alpha_{1,v} + 48B_{2,v}k \\
&\quad +96D_{2,v}\alpha_{1,v} + 96D_{2,v}k\} + \coth(3k)\{15\alpha_{1,v}k + 15k^2\} + \coth(k)\{51k\alpha_{1,v} \\
&\quad +36k^2\} - 128kB_{2,v} - 256kD_{2,v} - 128B_{2,v}\alpha_{1,v} - 256D_{2,v}\alpha_{1,v}] \qquad \text{(B.44)} \\
f_6 &= 0.6328125\frac{k^5}{We} \qquad \text{(B.45)} \\
x_{3f} &= (f_1 + f_2 + f_3 + f_4 + f_5 + f_6)/[\rho + \coth(3k)] \qquad \text{(B.46)} \\
g_1 &= -0.09375k[-24k\omega_{1,v}\alpha_{1,v}\coth(3k)\coth(2k)\coth(k) \\
&\quad + \coth(3k)\coth(2k)\{32\omega_{1,v}kD_{2,v} + 16\omega_{1,v}kB_{2,v} + 32\omega_{1,v}D_{2,v}\alpha_{1,v} \\
&\quad +64B_{2,v}\omega_{1,v}\alpha_{1,v} - 8C_{2,v}\omega_{1,v}^2 - 12k^2\omega_{1,v}\} + \coth(3k)\coth(k)\{64D_{2,v}\omega_{1,v}\alpha_{1,v} \\
&\quad +8B_{2,v}\omega_{1,v}k + 16D_{2,v}k\omega_{1,v} - 16B_{2,v}\alpha_{1,v}\omega_{1,v} + 4C_{2,v}\alpha_{1,v}^2 + 8C_{2,v}\omega_{1,v}^2\} \\
&\quad + \coth(3k)\{3k^2\omega_{1,v} + 6k\omega_{1,v}\alpha_{1,v}\}] \qquad \text{(B.47)} \\
g_2 &= -0.09375k\omega_{1,v}[\coth(k)\{9k^2 + 10k\alpha_{1,v}\} + 8k\alpha_{1,v} - 32C_{2,v}\omega_{1,v} \\
&\quad -96D_{2,v}\alpha_{1,v} - 48B_{2,v}\alpha_{1,v} - 48D_{2,v}k - 24B_{2,v}k] \qquad \text{(B.48)} \\
g_3 &= \frac{0.75k\omega_{1,v}\cosh(k)}{\cosh(k)^2 - 1}[\coth(2k)\{-4D_{2,v}\alpha_{1,v} - 4D_{2,v}k\} \\
&\quad + \coth(2k)\cosh(k)\{k\alpha_{1,v} + k^2\} + \sinh(k)\{-k^2 - k\alpha_{1,v}\}] \qquad \text{(B.49)} \\
g_4 &= -0.1875k\omega_{1,v}[\coth(k)\{3k\alpha_{1,v} + 3k^2\} - 16D_{2,v}\alpha_{1,v} - 16D_{2,v}k] \qquad \text{(B.50)} \\
g_5 &= 0.001875k^2[600k\omega_{1,v}\coth(3k)\coth(2k)\coth(k) \\
&\quad + \coth(3k)\coth(2k)\{-1600B_{2,v}\omega_{1,v} - 800C_{2,v}\alpha_{1,v}\} \\
&\quad + \coth(3k)\coth(k)\{-2400D_{2,v}\omega_{1,v} + 1200B_{2,v}\omega_{1,v}\} \\
&\quad + \coth(3k)\{-125k\omega_{1,v} - 119\omega_{1,v}k\} + 1600B_{2,v}\omega_{1,v} + 1600D_{2,v}\omega_{1,v}] \qquad \text{(B.51)} \\
x_{3g} &= (g_1 + g_2 + g_3 + g_4 + g_5)/[\rho + \coth(3k)] \qquad \text{(B.52)} \\
F_{3,v} &= \{-x_{3f}[-\omega_{1,v}^2 + \omega_{3,v}^2 + 6\alpha_{1,v}\alpha_{3,v} + 9\alpha_{1,v}^2 + \alpha_{3,v}^2] - x_{3g}[6\alpha_{1,v}\omega_{1,v} + 2\omega_{1,v}\alpha_{3,v}]\} \\
&\quad /[18\alpha_{1,v}^2\omega_{1,v}^2 - 6\omega_{1,v}^2\alpha_{3,v}^2 + \omega_{1,v}^4 + 81\alpha_{1,v}^4 + \omega_{3,v}^4 + \alpha_{3,v}^4 - 2\omega_{1,v}^2\omega_{3,v}^2
\end{aligned}
$$

$$+18\alpha_{1,v}\omega_{3,v}^2 - 18\alpha_{1,v}^2\alpha_{3,v}^2 + 2\omega_{3,v}^2\alpha_{3,v}^2] \tag{B.53}$$

$$\begin{aligned} G_{3,v} &= \{-x_{3f}[2\alpha_{3,v}\omega_{1,v} - 6\alpha_{1,v}\omega_{1,v}] - x_{3g}[\alpha_{3,v}^2 - 6\alpha_{3,v}\alpha_{1,v} + \omega_{3,v}^2 - \omega_{1,v}^2 + 9\alpha_{1,v}^2]\} \\ &\quad /[18\alpha_{1,v}^2\omega_{1,v}^2 - 6\omega_{1,v}^2\alpha_{3,v}^2 + \omega_{1,v}^4 + 81\alpha_{1,v}^4 + \omega_{3,v}^4 + \alpha_{3,v}^4 - 2\omega_{1,v}^2\omega_{3,v}^2 \\ &\quad +18\alpha_{1,v}^2\omega_{3,v}^2 - 18\alpha_{1,v}^2\alpha_{3,v}^2 + 2\omega_{3,v}^2\alpha_{3,v}^2] \end{aligned} \tag{B.54}$$

$$A_{3,v} = -[B_{3,v} + C_{3,v} + D_{3,v} + E_{3,v} + F_{3,v} + G_{3,v}] \tag{B.55}$$

Appendix C

Constants for Combined Mode

C.1 Second-Order Solution

$$a_1 = \rho + \coth(2k) \tag{C.1}$$

$$b_1 = (2k)^2 U^2 \rho + (2k)^2 \coth(2k) - \frac{(2k)^3}{We} \tag{C.2}$$

$$c_1 = 2kU\rho + 2k\coth(2k) \tag{C.3}$$

$$T = \frac{1}{4} - \frac{3}{4\cosh(k)^2} + \frac{1}{2\cosh(k)^4} \tag{C.4}$$

$$\begin{aligned}
B_{2,c} = {} & 0.5k\epsilon_s\epsilon_v\rho[\omega_{1,s}^2 - \omega_{1,v}^2 - \alpha_{1,s}^2 + \alpha_{1,v}^2] - 0.5k\cosh(2k)^2\epsilon_s\epsilon_v[\omega_{1,s}^2 - \alpha_{1,s}^2 + \cosh(k)^2\alpha_{1,v}^2 \\
& + \alpha_{1,v}k\{\cosh(k)^2 - 1\} - \cosh(k)^2\omega_{1,v}^2 + \alpha_{1,s}k\{\cosh(k)^2 - 1\} + \omega_{1,s}\omega_{1,v}\{1 - \cosh(k)^2\} \\
& + \alpha_{1,s}\alpha_{1,v}\{\cosh(k)^2 - 1\}] + k\epsilon_s\epsilon_v\rho U k^2(\alpha_{1,v} - \alpha_{1,s}) - \frac{1 - 0.5\cosh(k)^2 - \frac{0.5}{\cosh(k)^2}}{1 - \cosh(k)^2} k\epsilon_s\epsilon_v[k^2 \\
& - \alpha_{1,s}\alpha_{1,v} + \omega_{1,s}\omega_{1,v}] - 0.5\epsilon_s\epsilon_v k\rho[\omega_{1,s}^2 - \omega_{1,v}^2 + \alpha_{1,v}^2 - \alpha_{1,s}^2] \\
& - \epsilon_s\epsilon_v\coth(2k)\coth(k)[k^2T(\omega_{1,s} + \omega_{1,v}) + 0.5k\omega_{1,v}(\omega_{1,s} + \omega_{1,v}) + k\alpha_{1,s}T(\alpha_{1,s} + \alpha_{1,v}) \\
& - k^2T(\alpha_{1,s} + \alpha_{1,v}) - 0.5k\alpha_{1,v}(\alpha_{1,s} + \alpha_{1,v})] - k^2\epsilon_s\epsilon_v\rho U(\alpha_{1,v} - \alpha_{1,s}) \\
& - 2k^2\coth(2k)\coth(k)\epsilon_s\epsilon_v[T\alpha_{1,s} - kT - 0.5\alpha_{1,v}] \\
& / [a_1\{(\omega_{1,s} + \omega_{1,v})^2 - (\alpha_{1,s} + \alpha_{1,v})^2\} - b_1 - 2c_1(\alpha_{1,s} + \alpha_{1,v})]
\end{aligned} \tag{C.5}$$

$$C_{2,c} = 0.5k\epsilon_s\epsilon_v\rho[\omega_{1,s}^2 - \omega_{1,v}^2 - \alpha_{1,s}^2 + \alpha_{1,v}^2] - 0.5k\cosh(2k)^2\epsilon_s\epsilon_v[\omega_{1,s}^2 - \alpha_{1,s}^2 + \cosh(k)^2\alpha_{1,v}^2$$
$$+\alpha_{1,v}k\{\cosh(k)^2 - 1\} - \cosh(k)^2\omega_{1,v}^2 + \alpha_{1,s}k\{\cosh(k)^2 - 1\} + \omega_{1,s}\omega_{1,v}\{1 - \cosh(k)^2\}$$
$$+\alpha_{1,s}\alpha_{1,v}\{\cosh(k)^2 - 1\}] + k\epsilon_s\epsilon_v\rho Uk^2(\alpha_{1,v} - \alpha_{1,s}) - \frac{1 - 0.5\cosh(k)^2 - \frac{0.5}{\cosh(k)^2}}{1 - \cosh(k)^2}k\epsilon_s\epsilon_v[k^2$$
$$-\alpha_{1,s}\alpha_{1,v} + \omega_{1,s}\omega_{1,v}] - 0.5\epsilon_s\epsilon_v k\rho[\omega_{1,s}^2 - \omega_{1,v}^2 + \alpha_{1,v}^2 - \alpha_{1,s}^2]$$
$$-\epsilon_s\epsilon_v\coth(2k)\coth(k)[k^2T(\omega_{1,s} + \omega_{1,v}) + 0.5k\omega_{1,v}(\omega_{1,s} + \omega_{1,v}) + k\alpha_{1,s}T(\alpha_{1,s} + \alpha_{1,v})$$
$$-k^2T(\alpha_{1,s} + \alpha_{1,v}) - 0.5k\alpha_{1,v}(\alpha_{1,s} + \alpha_{1,v})] - k^2\epsilon_s\epsilon_v\rho U(\alpha_{1,v} - \alpha_{1,s})$$
$$-2k^2\coth(2k)\coth(k)\epsilon_s\epsilon_v[T\alpha_{1,s} - kT - 0.5\alpha_{1,v}]$$
$$/[a_1\{(\omega_{1,s} - \omega_{1,v})^2 - (\alpha_{1,s} + \alpha_{1,v})^2\} - b_1 - 2c_1(\alpha_{1,s} + \alpha_{1,v})] \tag{C.6}$$
$$X_1 = k\epsilon_v^2\rho[-\omega_{1,v}^2 + \alpha_{1,v}^2 + \alpha_{1,v}Uk] - k\epsilon_v^2[-\omega_{1,v}^2 + \alpha_{1,v}k + \alpha_{1,v}^2]$$
$$+\epsilon_v^2k^2\rho U[Uk + \alpha_{1,v}] - \frac{k}{1 - \cosh(k)^2}\epsilon_v^2[k^2\{\frac{3}{4} - \cosh(k)^2\} + \alpha_{1,v}k\{\frac{1}{2} - \cosh(k)^2\}$$
$$-\frac{1}{4}\alpha_{1,v}^2 + \frac{1}{4}\omega_{1,v}^2] - \rho\epsilon_v^2k[\alpha_{1,v}^2 - \omega_{1,v}^2] - \coth(2k)\coth(k)\epsilon_v^2k[\omega_{1,v}^2 - \alpha_{1,v}^2]$$
$$-k^2\epsilon_v^2U\rho + k^2\coth(2k)\coth(k)(\alpha_{1,v} + k)\epsilon_v^2/[a_1\{4\omega_{1,v}^2 - 4\alpha_{1,v}^2\} - b_1 - 4\alpha_{1,v}c_1] \tag{C.7}$$
$$X_2 = 2k\rho\epsilon_v^2[\omega_{1,v}\alpha_{1,v} + 0.5\omega_{1,v}Uk] - 2k\epsilon_v^2[\omega_{1,v}\alpha_{1,v} + 0.5\omega_{1,v}k) + k\rho\epsilon_v^2\omega_{1,v}Uk$$
$$-\frac{k\epsilon_v^2}{\cosh(k)^4(1 - \cosh(k)^2)}[-k\omega_{1,v}\cosh(k)^6 - 0.5\omega_{1,v}\alpha_{1,v}\cosh(k)^4$$
$$+0.5\omega_{1,v}k\cosh(k)^4] - \rho\epsilon_v^2[k\omega_{1,v}\{\alpha_{1,v} + Uk\} + k\omega_{1,v}\alpha_{1,v}]$$
$$+\coth(2k)\coth(k)k\omega_{1,v}\epsilon_v^2(\alpha_{1,v} + k) - \rho kU\epsilon_v^2\omega_{1,v} \tag{C.8}$$
$$D_{2,c} = -\frac{a_1\alpha_{1,v}^2X_1 + a_1\omega_{1,v}\alpha_{1,v}X_2 - a_1\omega_{1,v}^2X_1 - c_1\alpha_{1,v}X_1 + b_1X_1 - c_1\omega_{1,v}X_2}{4(a_1^2\alpha_{1,v}^4 - a_1^2\alpha_{1,v}^2\omega_{1,v}^2 + a_1\alpha_{1,v}^2b_1 + a_1^2\omega_{1,v}^4 - a_1\omega_{1,v}^2b_1 + b_1^2 - c_1^2\alpha_{1,v}^2 - c_1^2\omega_{1,v}^2)} \tag{C.9}$$
$$E_{2,c} = -\frac{a_1\alpha_{1,v}^2X_2 - a_1\omega_{1,v}^2X_2 + c_1\alpha_{1,v}X_2 - \omega_{1,v}a_1\alpha_{1,v}X_1 - c_1\omega_{1,v}X_1}{4(a_1^2\alpha_{1,v}^4 - a_1^2\alpha_{1,v}^2\omega_{1,v}^2 + a_1\alpha_{1,v}^2b_1 + a_1^2\omega_{1,v}^4 - a_1\omega_{1,v}^2b_1 + b_1^2 - c_1^2\alpha_{1,v}^2 - c_1^2\omega_{1,v}^2)} \tag{C.10}$$
$$F_{2,c} = \epsilon_s^2k\rho[\omega_{1,s}^2 - \alpha_{1,s}^2 - \alpha_{1,s}Uk] - \frac{k\epsilon_s^2}{\cosh(k)^2}[\omega_{1,s}^2 - \alpha_{1,s}^2 - \alpha_{1,s}k]$$
$$-\epsilon_s^2Uk^2\rho[Uk + \alpha_{1,s}] - \frac{k}{1 - \cosh(k)^2}\epsilon_s^2[\omega_{1,s}^2\{\frac{1}{4\cosh(k)^4} + \frac{1}{2}\cosh(k)^2 - \frac{1}{2}\}$$
$$-k^2\{\frac{1}{2\cosh(k)^4} + \frac{1}{\cosh(k)^2} + \frac{1}{4}\cosh(k)^2 - \frac{3}{2}\} - \frac{1}{2}k\alpha_{1,s}\{\frac{1}{\cosh(k)^4} + \cosh(k)^2\}$$
$$+\alpha_{1,s}^2\{\frac{1}{2} - \frac{1}{4\cosh(k)^4} - \frac{1}{4}\cosh(k)^2\}] - \rho\epsilon_s^2k[\omega_{1,s}^2 - \alpha_{1,s}(\alpha_{1,s} + Uk)]$$

$$-2\coth(2k)\coth(k)\epsilon_s^2 kT[-\omega_{1,s}^2+\alpha_{1,s}^2+\alpha_{1,s}k]+k^2\epsilon_s^2\rho U(\alpha_{1,s}+Uk)$$
$$-2k^2\coth(k)\coth(2k)\epsilon_s^2 T[\alpha_{1,s}+k]/[4a_1(\omega_{1,s}^2-\alpha_{1,s}^2)-b_1-4c_1\alpha_{1,s}] \quad \text{(C.11)}$$
$$G_{2,c}=k\rho\epsilon_v^2[\alpha_{1,v}^2+\alpha_{1,v}Uk]-k\epsilon_v^2[\alpha_{1,v}k+\alpha_{1,v}^2]+Uk^2\epsilon_v^2\rho[Uk+\alpha_{1,v}]$$
$$-\frac{k}{1-\cosh(k)^2}\epsilon_v^2[-\frac{1}{4}\omega_{1,v}^2+k^2\{\frac{3}{4}-\cosh(k)^2\}-\frac{1}{4}\alpha_{1,v}^2+\alpha_{1,v}k\{\frac{1}{2}-\cosh(k)^2\}]$$
$$-k\epsilon_v^2\rho\alpha_{1,v}(\alpha_{1,v}+Uk)+\coth(2k)\coth(k)\epsilon_v^2 k\alpha_{1,v}(\alpha_{1,v}+k)-k^2U\rho\epsilon_v^2(\alpha_{1,v}+Uk)$$
$$-k^2\coth(2k)\coth(k)\epsilon_v^2(\alpha_{1,v}+k)/[-4a_1\alpha_{1,v}^2-b_1-4c_1\alpha_{1,v}] \quad \text{(C.12)}$$
$$H_{2,c}=-k\epsilon_s^2\rho[\alpha_{1,s}Uk+\alpha_{1,s}^2]+\frac{k\epsilon_s^2}{\cosh(k)^2}[\alpha_{1,s}k+\alpha_{1,s}^2]-\epsilon_s^2k^2U\rho[Uk+\alpha_{1,s}]$$
$$-\frac{k}{1-\cosh(k)^2}\epsilon_s^2[\omega_{1,s}^2\{\frac{1}{2}-\frac{1}{4\cosh(k)^4}-\frac{1}{2}\cosh(k)^2\}-k^2\{\frac{1}{2\cosh(k)^4}+\frac{1}{\cosh(k)^2}$$
$$-\frac{3}{2}+\frac{1}{4}\cosh(k)^2\}-\frac{1}{2}k\alpha_{1,s}\{\cosh(k)^2+\frac{1}{\cosh(k)^4}\}+\alpha_{1,s}^2\{\frac{1}{2}-\frac{1}{4\cosh(k)^4}-\frac{1}{4}\cosh(k)^2\}]$$
$$+k\rho\epsilon_s^2\alpha_{1,s}(\alpha_{1,s}+Uk)-2kT\coth(2k)\coth(k)\epsilon_s^2[\alpha_{1,s}^2+k\alpha_{1,s}]+k^2\rho\epsilon_s^2U(\alpha_{1,s}+Uk)$$
$$-2k^2\coth(2k)\coth(k)\epsilon_s^2T(\alpha_{1,s}+k)/[-4a_1\omega_{1,s}^2-b_1-4c_1\alpha_{1,s}] \quad \text{(C.13)}$$
$$A_{2,c}=-[B_{2,c}+C_{2,c}+D_{2,c}+E_{2,c}+F_{2,c}+G_{2,c}+H_{2,c}] \quad \text{(C.14)}$$

C.2 Third-Order Solution

$$a_2 = \rho + \tanh(3k) \tag{C.15}$$

$$b_2 = (3k)^2 U^2 \rho + (3k)^2 \tanh(3k) - \frac{(3k)^3}{We} \tag{C.16}$$

$$c_2 = 3kU\rho + 3k\tanh(3k) \tag{C.17}$$

$$a_3 = \rho + \coth(3k) \tag{C.18}$$

$$b_3 = (3k)^2 U^2 \rho + (3k)^2 \coth(3k) - \frac{(3k)^3}{We} \tag{C.19}$$

$$c_3 = 3kU\rho + 3k\coth(3k) \tag{C.20}$$

$$\begin{aligned}
B_{3,c,s} = \{&-\rho[0.25\epsilon_s\alpha_{1,s}A_{2,c}\alpha_{2,s} + 0.25\epsilon_s\alpha_{1,s}UkA_{2,c} + 0.25\epsilon_s\omega_{1,s}\omega_{2,s}A_{2,c} + \frac{1}{8}\epsilon_s\omega_{1,s}^2A_{2,c} \\
&-\frac{5}{8}\epsilon_s\alpha_{1,s}^2A_{2,c} - \frac{3}{8}\epsilon_s\alpha_{1,s}UkA_{2,c} + \frac{1}{8}\epsilon_s\alpha_{2,s}UkA_{2,c} + \frac{1}{8}\epsilon_s\omega_{2,s}^2A_{2,c} \\
&-\frac{1}{8}\epsilon_s\alpha_{2,s}^2A_{2,c}] + \frac{0.25}{\cosh(k)^3\sinh(k)}[-0.5\epsilon_s\omega_{2,s}^2A_{2,c} + \epsilon_s\omega_{2,s}kA_{2,c} + \frac{1}{2}\epsilon_s\alpha_{2,s}^2A_{2,c} \\
&-\frac{1}{2}\epsilon_sk\alpha_{2,s}A_{2,c}] - 0.25\epsilon_sk\alpha_{2,s}A_{2,c} + 0.5\epsilon_skU\alpha_{1,s}A_{2,c} + 0.5\epsilon_sU^2k^2A_{2,c} \\
&+0.25\epsilon_s\alpha_{1,s}\alpha_{2,s}A_{2,c} - 0.25\epsilon_s\omega_{1,s}\omega_{2,s}A_{2,c} + 0.25\epsilon_sUk\alpha_{2,s}A_{2,c}\} \\
&/[a_2\{(\omega_{1,s}+\omega_{2,s})^2 - (\alpha_{1,s}+\alpha_{2,s})^2\} - b_2 - 2c_2(\alpha_{1,s}+\alpha_{2,s})]
\end{aligned} \tag{C.21}$$

$$\begin{aligned}
C_{3,c,s} = \{&-\rho[0.25\epsilon_s\alpha_{1,s}A_{2,c}\alpha_{2,s} + 0.25\epsilon_s\alpha_{1,s}UkA_{2,c} - 0.25\epsilon_s\omega_{1,s}\omega_{2,s}A_{2,c} + \frac{3}{8}\epsilon_s\omega_{1,s}^2A_{2,c} \\
&-\frac{5}{8}\epsilon_s\alpha_{1,s}^2A_{2,c} + \frac{1}{8}\epsilon_s\alpha_{1,s}UkA_{2,c} + \frac{1}{8}\epsilon_s\alpha_{2,s}UkA_{2,c} - \frac{1}{8}\epsilon_s\omega_{2,s}^2A_{2,c} \\
&-\frac{1}{8}\epsilon_s\alpha_{2,s}^2A_{2,c}] + \frac{0.25}{\cosh(k)^3\sinh(k)}[-0.5\epsilon_s\omega_{2,s}^2A_{2,c} + \epsilon_s\omega_{2,s}kA_{2,c} - \frac{1}{2}\epsilon_s\alpha_{2,s}^2A_{2,c} \\
&-\frac{1}{2}\epsilon_sk\alpha_{2,s}A_{2,c}] - 2.25\epsilon_sUk^2A_{2,c} - 0.75\epsilon_sk\alpha_{2,s}A_{2,c} - 0.75\epsilon_sk\alpha_{1,s}\} \\
&/[a_2\{(\omega_{1,s}-\omega_{2,s})^2 - (\alpha_{1,s}+\alpha_{2,s})^2\} - b_2 - 2c_2(\alpha_{1,s}+\alpha_{2,s})]
\end{aligned} \tag{C.22}$$

$$\begin{aligned}
D_{3,c,s} = \{&-\rho[\frac{3}{8}\epsilon_s^3\omega_{1,s}k\alpha_{1,s} + \frac{1}{2}\epsilon_s\omega_{1,s}^2F_{2,c} + \frac{1}{2}\epsilon_s\alpha_{1,s}^2H_{2,c} - \frac{1}{16}\epsilon_s^3\alpha_{1,s}^2k - \frac{5}{8}\epsilon_s\alpha_{1,s}^2F_{2,c} \\
&+\frac{1}{8}\epsilon_s\omega_{1,s}^2H_{2,c} - \frac{2}{3}\epsilon_s\alpha_{1,s}UkH_{2,c} + \frac{1}{8}\epsilon_s\omega_{1,s}UkH_{2,c} + \frac{5}{8}\epsilon_s\omega_{1,s}UkF_{2,c} \\
&-\frac{1}{16}\epsilon_s^3\alpha_{1,s}k^2U - \frac{1}{2}\epsilon_s\alpha_{1,s}UkF_{2,c} + \frac{1}{16}\epsilon_s^3\alpha_{1,s}^2k - \frac{1}{16}\epsilon_s^3\omega_{1,s}^2k] \\
&+\frac{0.25}{\cosh(k)^3\sinh(k)}[\frac{1}{4}\epsilon_s^3\alpha_{1,s}^2k + \frac{1}{4}\epsilon_s^3\omega_{1,s}\alpha_{1,s}k + \frac{3}{8}\epsilon_s^3\omega_{1,s}k
\end{aligned}$$

$$-\epsilon_s^3 k^2 \alpha_{1,s}^2 - \frac{5}{8}\epsilon_s k\omega_{1,s} F_{2,c} + \frac{1}{8}\epsilon_s k\alpha_{1,s} H_{2,c} - \frac{1}{2}\epsilon_s k\omega_{1,s} H_{2,c}]$$
$$-\frac{1}{16}\epsilon_s^3 \alpha_{1,s} k^2 - 2.25\epsilon_s k\alpha_{1,s} F_{2,c} - \frac{1}{8}\epsilon_s^3 k^3 U\}/[9a_2(\omega_{1,s}^2 - \alpha_{1,s}^2) - b_2 - 6c_2\alpha_{1,s}] \qquad \text{(C.23)}$$

$$E_{3,c,s} = \{-\rho[-\frac{1}{2}\epsilon_s\omega_{1,s}^2 F_{2,c} + \frac{1}{2}\epsilon_s\alpha_{1,s}^2 H_{2,c} + \frac{1}{16}\epsilon_s^3\alpha_{1,s}^2 k - \frac{1}{16}\epsilon_s^3\alpha_{1,s}k^2 U - \frac{1}{2}\epsilon_s\alpha_{1,s}UkF_{2,c}$$
$$-\epsilon_s\alpha_{1,s}UkH_{2,c} - \frac{1}{8}\epsilon_s^2\alpha_{1,s}k^2 U - \epsilon_s\alpha_{1,s}^2 H_{2,c} - \frac{1}{16}\epsilon_s^3\alpha_{1,s}^2 k + \epsilon_s\alpha_{1,s}^2 H_{2,c}$$
$$-\frac{1}{8}\epsilon_s^3\omega_{1,s}k\alpha_{1,s} - \frac{1}{16}\epsilon_s^3\omega_{1,s}^2 k + \frac{1}{4}\epsilon_s\omega_{1,s}^2 H_{2,c}]$$
$$+\frac{0.25}{\cosh(k)^3\sinh(k)}[\frac{1}{4}\epsilon_s^3\alpha_{1,s}^2 k + \epsilon_s^3\omega_{1,s}\alpha_{1,s}k + \frac{3}{8}\epsilon_s^3\omega_{1,s}k - \epsilon_s^3\omega_{1,s}^2 - \epsilon_s^3 k^2\alpha_{1,s}^2]$$
$$-\frac{1}{8}\epsilon_s^3 k^2\alpha_{1,s} - 4.5\epsilon_s k\alpha_{1,s}H_{2,c} - \frac{1}{4}\epsilon_s Uk^2 H_{2,c} - \frac{1}{16}\epsilon_s^3 k^3 U - 2.25\epsilon_s Uk^2 F_{2,c}$$
$$+\frac{1}{8}\epsilon_s k\alpha_{1,s}F_{2,c} + \frac{1}{4}\epsilon_s Uk^2 F_{2,c} - \frac{3}{8}\epsilon_s k\alpha_{1,s}F_{2,c}\}$$
$$/[a_2(\omega_{1,s}^2 - 9\alpha_{1,s}^2) - b_2 - 6c_2\alpha_{1,s}] \qquad \text{(C.24)}$$

$$F_{3,c,s} = \{-\rho[\frac{1}{8}\epsilon_s^2\epsilon_v\alpha_{1,s}Uk^2 - \frac{1}{8}\epsilon_s^2\epsilon_v\alpha_{1,v}Uk^2 - \frac{1}{8}\epsilon_s^2\epsilon_v\omega_{1,s}\alpha_{1,s}k - \frac{1}{8}\epsilon_s^2\epsilon_v\omega_{1,s}\alpha_{1,s}^2$$
$$+\frac{1}{4}\epsilon_s\omega_{1,s}^2 B_{2,c} + \frac{1}{4}\epsilon_s\omega_{1,s}\omega_{1,v}B_{2,c} - \frac{1}{2}\epsilon_s\omega_{1,s}\omega_{1,v}F_{2,c} - \frac{1}{16}\epsilon_s^2\epsilon_v k\omega_{1,s}\omega_{1,v} - \frac{1}{16}\epsilon_s^2\epsilon_v\alpha_{1,s}\alpha_{1,v}k$$
$$-\frac{1}{16}\epsilon_s\alpha_{1,s}\alpha_{1,v}B_{2,c} + \frac{3}{8}\epsilon_s\alpha_{1,s}UkB_{2,c} + \frac{1}{4}\epsilon_s\alpha_{1,s}^2 B_{2,c} - \frac{1}{16}\epsilon_s^2\epsilon_v\omega_{1,s}^2 k]$$
$$+\frac{0.25}{\cosh(k)^3\sinh(k)}[-\frac{1}{4}\epsilon_s^2\epsilon_v\alpha_{1,s}^2 k + \frac{1}{4}\epsilon_s^2\epsilon_v\omega_{1,s}^2 k + \frac{1}{4}\epsilon_s^2\epsilon_v\alpha_{1,s}\alpha_{1,v}k$$
$$+\frac{1}{4}\epsilon_s^2\epsilon_v\omega_{1,s}\omega_{1,v}k + \frac{1}{4}\epsilon_s^2\epsilon_v\alpha_{1,s}\omega_{1,v}k + \frac{1}{4}\epsilon_s^2\epsilon_v\alpha_{1,v}^2 k\cosh(k)^4]$$
$$-0.25\epsilon_s\omega_{1,s}\omega_{1,v}B_{2,c} + 0.25\epsilon_s\alpha_{1,s}\alpha_{1,v}B_{2,c} - 0.25\epsilon_s\omega_{1,s}^2 B_{2,c} + 0.25\epsilon_s Uk\alpha_{1,v}B_{2,c}$$
$$-0.5625\epsilon_s^2\epsilon_v\alpha_{1,s}k^2 + 0.28125\epsilon_s^2\epsilon_v\alpha_{1,v}k^2 - 0.28125\epsilon_s^2\epsilon_v k^3 U\}$$
$$/[a_2\{(2\omega_{1,s}^2 + \omega_{1,v})\}^2 - (2\alpha_{1,s} + \alpha_{1,v})^2 - b_2 - 2c_2(2\alpha_{1,s} + \alpha_{1,v})] \qquad \text{(C.25)}$$

$$G_{3,c,s} = \{-\rho[\frac{1}{8}\epsilon_s^2\epsilon_v\alpha_{1,s}Uk^2 - \frac{1}{8}\epsilon_s^2\epsilon_v\omega_{1,s}\alpha_{1,s}^2 + \frac{1}{4}\epsilon_s\omega_{1,s}\omega_{1,v}C_{2,c}$$
$$-\frac{1}{8}\epsilon_s^2\epsilon_v\omega_{1,s}\omega_{1,v}k + \frac{1}{2}\epsilon_s\omega_{1,s}\omega_{1,v}F_{2,c} - \frac{1}{2}\epsilon_s\omega_{1,s}^2 C_{2,c} + \frac{3}{8}\epsilon_s\alpha_{1,s}UkC_{2,c} + \frac{1}{16}\epsilon_s^2\epsilon_v\alpha_{1,s}\alpha_{1,v}k$$

$$+\frac{1}{8}\epsilon_s^2\epsilon_v\alpha_{1,s}^2k-\frac{1}{4}\epsilon_s\alpha_{1,s}\alpha_{1,v}C_{2,c}-\frac{1}{4}\epsilon_s\alpha_{1,s}^2C_{2,c}-\frac{3}{8}\epsilon_s\alpha_{1,s}UkC_{2,c}+\frac{1}{4}\epsilon_s\alpha_{1,s}^2C_{2,c}$$
$$-\frac{1}{16}\epsilon_s^2\epsilon_v\omega_{1,s}\omega_{1,v}k-\frac{1}{16}\epsilon_s^2\epsilon_vk+\frac{0.25}{\cosh(k)^3\sinh(k)}[\frac{1}{4}\epsilon_s^2\epsilon_v\alpha_{1,s}^2k+\frac{1}{4}\epsilon_s^2\epsilon_v\omega_{1,s}^2k$$
$$-\frac{1}{4}\epsilon_s^2\epsilon_v\omega_{1,s}\omega_{1,v}k-\epsilon_s\alpha_{1,v}kC_{2,c}-\frac{3}{8}\epsilon_s\omega_{1,v}kC_{2,c}]-0.5625\epsilon_s^2\epsilon_v\alpha_{1,s}k^2-1.5\epsilon_s\alpha_{1,s}kC_{2,c}$$
$$+0.28125\epsilon_s^2\epsilon_v\alpha_{1,v}k^2-0.75\epsilon_s\alpha_{1,v}C_{2,c}-2.25\epsilon_sUk^2C_{2,c}-0.28125\epsilon_s^2\epsilon_vk^3U\}$$
$$/[a_2\{(2\omega_{1,s}^2-\omega_{1,v})\}^2-(2\alpha_{1,s}+\alpha_{1,v})^2-b_2-2c_2(2\alpha_{1,s}+\alpha_{1,v})] \tag{C.26}$$
$$A_{3,c,s}=-[B_{3,c,s}+C_{3,c,s}+D_{3,c,s}+E_{3,c,s}+F_{3,c,s}+G_{3,c,s}] \tag{C.27}$$
$$B_{3,c,v}=\{-\rho[-0.25\epsilon_v\alpha_{1,v}A_{2,c}\alpha_{2,v}-0.25\epsilon_v\alpha_{1,v}UkA_{2,c}+0.25\epsilon_v\omega_{1,v}\omega_{2,v}A_{2,c}+\frac{3}{8}\epsilon_v\omega_{1,v}^2A_{2,c}$$
$$-\frac{1}{8}\epsilon_v\alpha_{1,v}^2A_{2,c}+\frac{3}{8}\epsilon_v\alpha_{1,v}UkA_{2,c}+\frac{3}{8}\epsilon_v\alpha_{2,v}UkA_{2,c}-\frac{1}{8}\epsilon_v\omega_{2,v}^2A_{2,c}$$
$$-\frac{5}{8}\epsilon_v\alpha_{2,v}^2A_{2,c}]+\frac{0.25}{\cosh(k)^3\sinh(k)}[-0.5\epsilon_v\omega_{2,v}^2A_{2,c}-\epsilon_v\omega_{2,v}kA_{2,c}+\frac{1}{4}\epsilon_v\alpha_{2,v}^2A_{2,c}-\frac{1}{2}\epsilon_vk\alpha_{2,v}A_{2,c}]$$
$$+0.25\epsilon_vk\alpha_{2,v}A_{2,c}+0.25\epsilon_vkU\alpha_{1,v}A_{2,c}-0.5\epsilon_vU^2k^2A_{2,c}+0.25\epsilon_v\alpha_{1,v}\alpha_{2,v}A_{2,c}$$
$$-0.5\epsilon_v\omega_{1,v}\omega_{2,v}A_{2,c}-0.25\epsilon_vUk\alpha_{2,v}A_{2,c}\}$$
$$/[a_3\{(\omega_{1,v}+\omega_{2,v})^2-(\alpha_{1,v}+\alpha_{2,v})^2\}-b_3-2c_3(\alpha_{1,v}+\alpha_{2,v})] \tag{C.28}$$
$$C_{3,c,v}=\{-\rho[0.25\epsilon_v\alpha_{1,v}A_{2,c}\alpha_{2,v}-0.5\epsilon_v\alpha_{1,v}UkA_{2,c}+0.25\epsilon_v\omega_{1,v}\omega_{2,v}A_{2,c}-\frac{5}{8}\epsilon_v\omega_{1,v}^2A_{2,c}$$
$$+\frac{3}{8}\epsilon_v\alpha_{1,v}^2A_{2,c}-\frac{1}{8}\epsilon_v\alpha_{1,v}UkA_{2,c}-\frac{1}{8}\epsilon_v\alpha_{2,v}UkA_{2,c}+\frac{3}{8}\epsilon_v\omega_{2,v}^2A_{2,c}$$
$$-\frac{3}{8}\epsilon_v\alpha_{2,v}^2A_{2,c}]+\frac{0.25}{\cosh(k)^3\sinh(k)}[-0.5\epsilon_v\omega_{2,v}^2A_{2,c}+0.25\epsilon_v\omega_{2,v}kA_{2,c}-\frac{1}{4}\epsilon_v\alpha_{2,v}^2A_{2,c}$$
$$+\frac{1}{2}\epsilon_vk\alpha_{2,v}A_{2,c}]-2.25\epsilon_vUk^2A_{2,c}-0.5\epsilon_vk\alpha_{2,v}A_{2,c}+0.25\epsilon_vk\alpha_{1,v}\}$$
$$/[a_3\{(\omega_{1,v}-\omega_{2,v})^2-(\alpha_{1,v}+\alpha_{2,v})^2\}-b_3-2c_3(\alpha_{1,v}+\alpha_{2,v})] \tag{C.29}$$
$$D_{3,c,v}=\{-\rho[-\frac{3}{8}\epsilon_v^3\omega_{1,v}k\alpha_{1,v}+\frac{1}{2}\epsilon_v\omega_{1,v}^2D_{2,c}+\frac{1}{2}\epsilon_v\alpha_{1,v}^2G_{2,c}-\frac{1}{16}\epsilon_v^3\alpha_{1,v}^2k-\frac{5}{8}\epsilon_v\alpha_{1,v}^2D_{2,c}$$
$$-\frac{1}{8}\epsilon_v\omega_{1,v}^2G_{2,c}-\frac{1}{8}\epsilon_v\alpha_{1,v}UkG_{2,c}-\frac{1}{8}\epsilon_v\omega_{1,v}UkG_{2,c}-\frac{3}{8}\epsilon_v\omega_{1,v}UkD_{2,c}$$
$$-\frac{1}{16}\epsilon_v^3\alpha_{1,v}k^2U+\frac{1}{2}\epsilon_v\alpha_{1,v}UkD_{2,c}-\frac{1}{4}\epsilon_v^3\alpha_{1,v}^2k+\frac{1}{16}\epsilon_v^3\omega_{1,v}^2k]$$
$$+\frac{0.25}{\cosh(k)^3\sinh(k)}[-\frac{1}{4}\epsilon_v^3\alpha_{1,v}^2k+\frac{1}{4}\epsilon_v^3\omega_{1,v}\alpha_{1,v}k-\frac{1}{8}\epsilon_v^3\omega_{1,v}k$$
$$-\epsilon_v^3k^2\alpha_{1,v}^2+\frac{3}{8}\epsilon_vk\omega_{1,v}D_{2,c}+\frac{5}{8}\epsilon_vk\alpha_{1,v}G_{2,c}+\frac{1}{2}\epsilon_vk\omega_{1,v}G_{2,c}]$$

$$+\frac{1}{8}\epsilon_v^3\alpha_{1,v}k^2 - 2.25\epsilon_v k\alpha_{1,v}D_{2,c} - \frac{1}{4}\epsilon_v^3k^3U\}/[a_3(9\omega_{1,v}^2 - \alpha_{1,v}^2) - b_3 - 6c_3\alpha_{1,v}] \tag{C.30}$$

$$E_{3,c,v} = \{-\rho[-\frac{1}{16}\epsilon_v^3\omega_{1,v}k\alpha_{1,v} - \frac{1}{2}\epsilon_v\omega_{1,v}^2E_{2,c} + \frac{1}{8}\epsilon_v^3\alpha_{1,v}^2k - \frac{5}{8}\epsilon_v\alpha_{1,v}^2E_{2,c}$$
$$-\frac{1}{8}\epsilon_v\omega_{1,v}^2G_{2,c} + \frac{3}{8}\epsilon_v\alpha_{1,v}UkG_{2,c} - \frac{1}{8}\epsilon_v\omega_{1,v}UkG_{2,c} - \frac{3}{8}\epsilon_v\omega_{1,v}UkE_{2,c}$$
$$+\frac{1}{8}\epsilon_v^3\alpha_{1,v}k^2U + \frac{3}{8}\epsilon_v\alpha_{1,v}UkE_{2,c} - \frac{1}{4}\epsilon_v^3\alpha_{1,v}^2k + \frac{1}{8}\epsilon_v^3\omega_{1,v}^2k]$$
$$+\frac{0.25}{\cosh(k)^3\sinh(k)}[\frac{1}{16}\epsilon_v^3\alpha_{1,v}^2k + \frac{1}{4}\epsilon_v^3\omega_{1,v}\alpha_{1,v}k - \frac{1}{8}\epsilon_v^3\omega_{1,v}k$$
$$-\epsilon_v^3k^2\alpha_{1,v}^2 + \frac{3}{8}\epsilon_v k\omega_{1,v}E_{2,c} + \frac{1}{4}\epsilon_v k\omega_{1,v}G_{2,c}] - \frac{3}{8}\epsilon_v^3\alpha_{1,v}k^2 - 2.5\epsilon_v k\alpha_{1,v}E_{2,c} + \frac{1}{4}\epsilon_v^3k^3U\}$$
$$/[a_3(9\omega_{1,v}^2 - \alpha_{1,v}^2) - b_3 - 6c_3\alpha_{1,v}] \tag{C.31}$$

$$F_{3,c,v} = \{-\rho[\frac{1}{2}\epsilon_v\omega_{1,v}^2G_{2,c} + \frac{1}{4}\epsilon_v\alpha_{1,v}^2D_{2,c} + \frac{1}{8}\epsilon_v^3\alpha_{1,v}^2k + \frac{1}{16}\epsilon_v^3\alpha_{1,v}k^2U - \frac{1}{2}\epsilon_v\alpha_{1,v}UkG_{2,c}$$
$$-\epsilon_v\alpha_{1,v}UkD_{2,c} + \frac{3}{8}\epsilon_v^2\alpha_{1,v}k^2U + \epsilon_v\alpha_{1,v}^2D_{2,c} - \frac{1}{16}\epsilon_v^3\alpha_{1,v}^2k + \epsilon_v\alpha_{1,v}^2D_{2,c}$$
$$-\frac{3}{4}\epsilon_v^3\omega_{1,v}k\alpha_{1,v} + \frac{1}{16}\epsilon_v^3\omega_{1,v}^2k + \frac{3}{4}\epsilon_v\omega_{1,v}^2D_{2,c}]$$
$$+\frac{0.25}{\cosh(k)^3\sinh(k)}[-\frac{1}{4}\epsilon_v^3\alpha_{1,v}^2k + \frac{1}{4}\epsilon_v^3\omega_{1,v}\alpha_{1,v}k + \frac{1}{8}\epsilon_v^3\omega_{1,v}k + \epsilon_v^3\omega_{1,v}^2 - \epsilon_v^3k^2\alpha_{1,v}^2]$$
$$-\frac{1}{8}\epsilon_v^3k^2\alpha_{1,v} - 2.25\epsilon_v k\alpha_{1,v}D_{2,c} + \frac{1}{4}\epsilon_v Uk^2G_{2,c} - \frac{1}{16}\epsilon_v^3k^3U - 2.25\epsilon_v Uk^2G_{2,c}$$
$$-\frac{3}{8}\epsilon_v k\alpha_{1,v}G_{2,c} - \frac{1}{4}\epsilon_v Uk^2G_{2,c} + \frac{3}{8}\epsilon_v k\alpha_{1,v}G_{2,c}\}$$
$$/[a_3(\omega_{1,v}^2 - 9\alpha_{1,v}^2) - b_3 - 6c_3\alpha_{1,v}] \tag{C.32}$$

$$G_{3,c,v} = \{-\rho[\frac{1}{4}\epsilon_v\omega_{1,v}^2G_{2,c} + \frac{3}{8}\epsilon_v\alpha_{1,v}^2D_{2,c} - \frac{1}{4}\epsilon_v^3\alpha_{1,v}^2k - \frac{1}{8}\epsilon_v^3\alpha_{1,v}k^2U - \frac{1}{4}\epsilon_v\alpha_{1,v}UkH_{2,c}$$
$$-\epsilon_v\alpha_{1,v}UkD_{2,c} + \frac{5}{8}\epsilon_v^2\alpha_{1,v}k^2U + \frac{1}{4}\epsilon_v\alpha_{1,v}^2D_{2,c} + \frac{1}{8}\epsilon_v^3\alpha_{1,v}^2k$$
$$-\frac{1}{8}\epsilon_v\alpha_{1,v}^2D_{2,c} + \frac{3}{4}\epsilon_v^3\omega_{1,v}k\alpha_{1,v} - \frac{1}{8}\epsilon_v^3\omega_{1,v}^2k + \frac{3}{8}\epsilon_v\omega_{1,v}^2D_{2,c}] + \frac{0.25}{\cosh(k)^3\sinh(k)}$$
$$\times[-\frac{1}{4}\epsilon_v^3\alpha_{1,v}^2k + \frac{1}{16}\epsilon_v^3\omega_{1,v}\alpha_{1,v}k + \frac{3}{8}\epsilon_v^3\omega_{1,v}k - \frac{3}{8}\epsilon_v^3\omega_{1,v}^2 + \frac{1}{4}\epsilon_v^3k^2\alpha_{1,v}^2] - \frac{1}{8}\epsilon_v^3k^2\alpha_{1,v}$$
$$-2.5\epsilon_v k\alpha_{1,v}D_{2,c} + \frac{1}{16}\epsilon_v Uk^2E_{2,c} + \frac{1}{16}\epsilon_v^3k^3U - 2.25\epsilon_s Uk^2E_{2,c} - \frac{3}{8}\epsilon_v k\alpha_{1,v}E_{2,c}$$
$$-\frac{1}{4}\epsilon_v Uk^2E_{2,c} + 0.25\epsilon_v k\alpha_{1,v}E_{2,c}\}/[a_3(\omega_{1,v}^2 - 9\alpha_{1,v}^2) - b_3 - 6c_3\alpha_{1,v}] \tag{C.33}$$

$$H_{3,c,v} = \{-\rho[\frac{5}{8}\epsilon_v^2\epsilon_s\alpha_{1,s}Uk^2 - \frac{5}{8}\epsilon_v^2\epsilon_s\alpha_{1,v}Uk^2 - \epsilon_v^2\epsilon_s\omega_{1,v}\alpha_{1,s}k + \frac{1}{8}\epsilon_v^2\epsilon_s\omega_{1,v}\alpha_{1,v}^2$$
$$-\frac{1}{8}\epsilon_v\omega_{1,v}^2B_{2,c} + \frac{1}{2}\epsilon_v\omega_{1,s}\omega_{1,v}B_{2,c} - \frac{1}{2}\epsilon_v\omega_{1,s}\omega_{1,v}D_{2,c} + \frac{1}{8}\epsilon_v^2\epsilon_sk\omega_{1,s}\omega_{1,v} - \frac{1}{16}\epsilon_v^2\epsilon_s\alpha_{1,s}\alpha_{1,v}k$$
$$-\frac{1}{4}\epsilon_v\alpha_{1,s}\alpha_{1,v}B_{2,c} - \frac{3}{8}\epsilon_v\alpha_{1,s}UkB_{2,c} + \frac{1}{4}\epsilon_v\alpha_{1,v}^2B_{2,c} + \frac{1}{16}\epsilon_v^2\epsilon_s\omega_{1,s}^2k]$$
$$+\frac{0.25}{\cosh(k)^3\sinh(k)}[-\frac{1}{4}\epsilon_v^2\epsilon_s\alpha_{1,v}^2k + \frac{3}{8}\epsilon_s^2\epsilon_v\omega_{1,v}^2k + \epsilon_v^2\epsilon_s\alpha_{1,s}\alpha_{1,v}k$$
$$+\frac{1}{4}\epsilon_v^2\epsilon_s\omega_{1,s}\omega_{1,v}k - \frac{1}{4}\epsilon_v^2\epsilon_s\alpha_{1,s}\omega_{1,v}k + \frac{1}{4}\epsilon_v^2\epsilon_s\alpha_{1,v}^2k\cosh(k)^4]$$
$$-0.25\epsilon_v\omega_{1,s}\omega_{1,v}B_{2,c} - 0.25\epsilon_v\alpha_{1,s}\alpha_{1,v}B_{2,c} - 0.25\epsilon_v\omega_{1,v}^2B_{2,c} + 0.25\epsilon_vUk\alpha_{1,v}B_{2,c}$$
$$-0.8625\epsilon_v^2\epsilon_s\alpha_{1,v}k^2 + \frac{1}{8}\epsilon_v^2\epsilon_s\alpha_{1,v}k^2 + 0.25\epsilon_v^2\epsilon_sk^3U\}$$
$$/[a_3\{(2\omega_{1,v}^2 + \omega_{1,s})\}^2 - (2\alpha_{1,v} + \alpha_{1,s})^2 - b_3 - 2c_3(2\alpha_{1,v} + \alpha_{1,s})] \tag{C.34}$$

$$I_{3,c,v} = \{-\rho[-\frac{3}{8}\epsilon_v^2\epsilon_s\alpha_{1,s}Uk^2 - \frac{1}{4}\epsilon_v^2\epsilon_s\omega_{1,s}\alpha_{1,s}^2 - \frac{3}{4}\epsilon_v\omega_{1,s}\omega_{1,v}C_{2,c}$$
$$+\frac{1}{8}\epsilon_v^2\epsilon_s\omega_{1,s}\omega_{1,v}k + \frac{1}{4}\epsilon_v\omega_{1,s}\omega_{1,v}G_{2,c} + \frac{1}{2}\epsilon_v\omega_{1,v}^2C_{2,c} + \frac{1}{8}\epsilon_v\alpha_{1,v}UkC_{2,c} + \frac{3}{4}\epsilon_v^2\epsilon_s\alpha_{1,s}\alpha_{1,v}k$$
$$-\frac{1}{8}\epsilon_v^2\epsilon_s\alpha_{1,v}^2k + \frac{1}{4}\epsilon_v\alpha_{1,s}\alpha_{1,v}C_{2,c} - \frac{1}{8}\epsilon_v\alpha_{1,v}^2C_{2,c} + \frac{1}{8}\epsilon_v\alpha_{1,s}UkC_{2,c}$$
$$+\frac{1}{16}\epsilon_v\alpha_{1,s}^2C_{2,c} + \frac{3}{16}\epsilon_v^2\epsilon_s\omega_{1,s}\omega_{1,v}k - \frac{1}{4}\epsilon_v^2\epsilon_sk]$$
$$+\frac{0.25}{\cosh(k)^3\sinh(k)}[-\frac{1}{2}\epsilon_v^2\epsilon_s\alpha_{1,s}^2k + \frac{1}{4}\epsilon_v^2\epsilon_s\omega_{1,s}^2k + \frac{3}{8}\epsilon_v^2\epsilon_s\omega_{1,s}\omega_{1,v}k - \epsilon_v\alpha_{1,v}kC_{2,c}$$
$$-\frac{3}{8}\epsilon_v\omega_{1,v}kC_{2,c}] + 0.5\epsilon_v^2\epsilon_s\alpha_{1,v}k^2 - \frac{1}{4}\epsilon_v\alpha_{1,s}kC_{2,c} - \frac{5}{8}\epsilon_v^2\epsilon_s\alpha_{1,s}k^2 - 0.75\epsilon_v\alpha_{1,v}C_{2,c}$$
$$-\frac{1}{4}\epsilon_vUk^2C_{2,c} - \frac{3}{4}\epsilon_v^2\epsilon_sk^3U\}$$
$$/[a_3\{(2\omega_{1,v}^2 - \omega_{1,s})\}^2 - (2\alpha_{1,v} + \alpha_{1,s})^2 - b_3 - 2c_3(2\alpha_{1,v} + \alpha_{1,s})] \tag{C.35}$$

$$A_{3,c,v} = -[B_{3,c,v} + C_{3,c,v} + D_{3,c,v} + E_{3,c,v} + F_{3,c,v} + G_{3,c,v} + H_{3,c,v} + I_{3,c,v}] \tag{C.36}$$

Appendix D

Coefficients in the MEP formulation

$$
\begin{aligned}
\gamma &= \frac{\Lambda_2}{2\Lambda_3} \\
\delta &= (\bar{D}^3\Lambda_3)^{1/2} \\
\Omega &= f_0 \exp\left[-\Lambda_3 B\bar{D}^2 - \left(\Lambda_1 - \frac{\Lambda_2^2}{4\Lambda_3}\right)\bar{D}^3\right] \\
Q &= \mathrm{erf}(X_{max}) - \mathrm{erf}(X_{min}) \\
Q_0 &= \exp(-X_{max}^2) - \exp(-X_{min}^2) \\
Q_1 &= \bar{U}_{max}\exp(-X_{max}^2) - \bar{U}_{min}\exp(-X_{min}^2) \\
Q_2 &= \bar{U}_{max}^2\exp(-X_{max}^2) - \bar{U}_{min}^2\exp(-X_{min}^2) \\
Q_3 &= \bar{U}_{max}^3\exp(-X_{max}^2) - \bar{U}_{min}^3\exp(-X_{min}^2) \qquad \text{(D.1)} \\
f_1 &= \frac{\sqrt{\pi}}{2}\frac{\Omega Q}{\delta} \qquad \text{(D.2)} \\
B_0 &= \int_{\bar{D}_{min}}^{\bar{D}_{max}} f_1 d\bar{D} - 1 \qquad \text{(D.3)} \\
B_1 &= \int_{\bar{D}_{min}}^{\bar{D}_{max}} f_1\bar{D}^3 d\bar{D} - (1+\bar{S}_m) \qquad \text{(D.4)} \\
B_2 &= -\int_{\bar{D}_{min}}^{\bar{D}_{max}} \frac{1}{2}\frac{\Omega}{\Lambda_3} Q_0 d\bar{D} - \int_{\bar{D}_{min}}^{\bar{D}_{max}} \gamma f_1\bar{D}^3 d\bar{D} - (1+\bar{S}_{mv}) \qquad \text{(D.5)} \\
B_3 &= \int_{\bar{D}_{min}}^{\bar{D}_{max}} B f_1\bar{D}^2 d\bar{D} - \int_{\bar{D}_{min}}^{\bar{D}_{max}} \frac{1}{2}\frac{\Omega}{\Lambda_3} Q_1 d\bar{D}
\end{aligned}
$$

$$+\int_{\bar{D}_{min}}^{\bar{D}_{max}} \gamma\frac{1}{2}\frac{\Omega}{\Lambda_3}Q_0 d\bar{D} + \int_{\bar{D}_{min}}^{\bar{D}_{max}} \frac{1}{2\Lambda_3} f_1 d\bar{D}$$
$$+\int_{\bar{D}_{min}}^{\bar{D}_{max}} \gamma^2 f_1 \bar{D}^3 d\bar{D} - (1+\bar{S}_e) \tag{D.6}$$

$$I_0 = \int_{\bar{D}_{min}}^{\bar{D}_{max}} f_1 d\bar{D} \tag{D.7}$$

$$I_1 = \int_{\bar{D}_{min}}^{\bar{D}_{max}} f_1 \bar{D}^3 d\bar{D} \tag{D.8}$$

$$I_2 = \int_{\bar{D}_{min}}^{\bar{D}_{max}} \frac{1}{2}\frac{\Omega}{\Lambda_3}Q_0 d\bar{D} \tag{D.9}$$

$$I_3 = \int_{\bar{D}_{min}}^{\bar{D}_{max}} \frac{1}{2}\frac{\Omega}{\Lambda_3}Q_1 d\bar{D} \tag{D.10}$$

$$I_4 = \int_{\bar{D}_{min}}^{\bar{D}_{max}} \bar{D}^2 f_1 d\bar{D} \tag{D.11}$$

$$I_5 = \int_{\bar{D}_{min}}^{\bar{D}_{max}} \bar{D}^6 f_1 d\bar{D} \tag{D.12}$$

$$I_6 = \int_{\bar{D}_{min}}^{\bar{D}_{max}} \frac{1}{2}\frac{\bar{D}^3\Omega}{\Lambda_3}Q_0 d\bar{D} \tag{D.13}$$

$$I_7 = \int_{\bar{D}_{min}}^{\bar{D}_{max}} \frac{1}{2}\frac{\bar{D}^3\Omega}{\Lambda_3}Q_1 d\bar{D} \tag{D.14}$$

$$I_8 = \int_{\bar{D}_{min}}^{\bar{D}_{max}} \bar{D}^5 f_1 d\bar{D} \tag{D.15}$$

$$I_9 = \int_{\bar{D}_{min}}^{\bar{D}_{max}} \frac{1}{2}\frac{\bar{D}^3\Omega}{\Lambda_3}Q_2 d\bar{D} \tag{D.16}$$

$$I_{10} = \int_{\bar{D}_{min}}^{\bar{D}_{max}} \frac{1}{2}\frac{\bar{D}^2\Omega}{\Lambda_3}Q_0 d\bar{D} \tag{D.17}$$

$$I_{11} = \int_{\bar{D}_{min}}^{\bar{D}_{max}} \frac{1}{2}\frac{\bar{D}^3\Omega}{\Lambda_3}Q_3 d\bar{D} \tag{D.18}$$

$$I_{12} = \int_{\bar{D}_{min}}^{\bar{D}_{max}} \frac{1}{2}\frac{\bar{D}^2\Omega}{\Lambda_3}Q_1 d\bar{D} \tag{D.19}$$

$$I_{13} = \int_{\bar{D}_{min}}^{\bar{D}_{max}} f_1 \bar{D}^4 d\bar{D} \tag{D.20}$$

$$a_{0,0} = -1 \tag{D.21}$$

$$a_{0,1} = -I_1/I_0 \tag{D.22}$$

$$a_{0,2} = I_2/I_0 - \gamma a_{0,1} \tag{D.23}$$

$$a_{0,3} = I_3/I_0 - BI_4/I_0 - \gamma a_{0,2} - \frac{1}{2\Lambda_3} \tag{D.24}$$

$$a_{1,1} = -I_5/I_0 \tag{D.25}$$

$$a_{1,2} = I_6/I_0 - \gamma a_{1,1} \tag{D.26}$$

$$a_{1,3} = I_7/I_0 - BI_8/I_0 - \gamma a_{1,2} + \frac{a_{4,1}}{2\Lambda_3} \tag{D.27}$$

$$a_{2,2} = BI_8/I_0 + a_{1,3} \tag{D.28}$$

$$a_{2,3} = I_9/I_0 + BI_{10}/I_0 + \frac{a_{0,2}}{\Lambda_3} - \gamma a_{1,3} \tag{D.29}$$

$$\begin{aligned} a_{3,3} = \frac{1}{I_0}\big[\big(& -B^2 I_{13} - 2B^2\gamma^2 I_8 - B\gamma I_{10} + BI_{12} \\ & + I_{11} - \gamma I_9 - \gamma^4 I_5 - \gamma^3 I_6 + \gamma^2 I_7\big) \\ & - \frac{1}{\Lambda_3}\big(BI_4 + \frac{3}{2}I_3 + \frac{5}{2}\gamma I_2 + 3\gamma^2 I_1 + \frac{3}{4}\frac{I_0}{\Lambda_3}\big)\big] \end{aligned} \tag{D.30}$$

Appendix E

Aerometrics PDPA system

Table E.1: Aerometrics PDPA system optical parameters used in the experiment.

	Planar Nozzle	PWC Nozzle
Laser		
Coherent Inova 90 water-cooled argon ion laser	300 mW	300 mW
Transmitting Optics		
Beam expanding telescope ratio	0.5:1	1:1
Beam separation	10 mm	20 mm
Transmitting lens focal length	500 mm	250 mm
Receiving Optics		
Receiving lens focal length	300 mm	300 mm
Lens diameter	72 mm (f/4.2)	72 mm (f/4.2)
Spatial filter slit width	500 μm	150 μm
Collimating lens focal length	250 mm	250 mm
Magnification	0.833	0.833
Orientation	30°	30°

Table E.2: Aerometrics PDPA system settings

Parameter	Description	Range	Typical Value	
			Planar Nozzle	PWC nozzle
Hight Voltage	Photo-multiplier voltage.	$188 - 900\ V$	$375 - 400\ V$	$500 - 600\ V$
Frequency Shift	Frequency shift applied to beams.	$40\ MHz$ or OFF	$40\ MHz$	$40\ MHz$
DC Offset	DC bias in raw signal.	-75 to $+75\ mV$	$\approx 57\ mV$	$\approx 69\ mV$
Mixer Frequency	Frequency subtracted from observed Doppler frequency.	$30 - 45\ MHz$	$39 - 42\ MHz$	$39 - 41\ MHz$
Low Pass	Low pass filter setting applied to down-mixed signal.	$0.5 - 80\ MHz$	$5.0\ MHz$	$20\ MHz$
Burst Filter	Filter applied to raw signal.	$40\ MHZ$ B.P. $10\ MHZ$ or $50\ MHZ$ L.P.	$50\ MHZ$	$50\ MHZ$
Threshold	Minimum RMS trigger voltage required to trigger system.	$0 - 500\ mV$	$22 - 40\ mV$	$30 - 47\ mV$
Envelope Filter	Minimum time that threshold must be exceeded to trigger.	$0 - 3\ \mu s$	$3\ \mu s$	$3\ \mu s$
% After Peak	Selects % of processed signal that occurs after peak detection (50 % corresponds to signal peak).	0 – 100 %	50 %	50 %
$N^{\underline{o}}$ of Samples	Selects number of bits that A/D converter uses to digitize signal.	64	256	256
Sampling Rate	Rate at which signal is sampled.	$75\ kHz - 160\ MHz$	$40\ MHz$	$40\ MHz$
Min S/N Ratio	Minimum acceptable signal to noise ratio.	0.01 – 9.99	0.3	0.3

References

[1] J. Shen and X. Li. Instability of an annular viscous liquid jet. *Acta Mechanica*, 114:167–183, 1996.

[2] J. Shen and X. Li. Breakup of annular viscous liquid jets in two gas streams. *AIAA J. Prop. Power*, 12(4):752–759, 1996.

[3] A. H. Lefebvre. *Gas Turbine Combustion*. Hemisphere, New York, 1983.

[4] A. H. Lefebvre. *Atomization and Sprays*. Hemisphere, New York, 1989.

[5] J. L. York, H.E. Stubbs, and M.R. Tek. The mechanism of disintegration of liquid sheets. *Trans. ASME*, 75:1279–1286, 1937.

[6] H. B. Squire. Investigation of the instability of a moving film. *Br. J. Appl. Phys.*, 4:167–169, 1953.

[7] W. W. Hagerty and J. F. Shea. A study of the stability of plane liquid sheets. *J. Appl. Mech.*, 22:509–514, 1955.

[8] N. Dombrowski and W.R. Johns. The aerodynamic instability and disintegration of viscous liquid sheets. *Chem. Eng. Sci.*, 18:203–214, 1963.

[9] S. P. Lin. Stability of viscous liquid curtain. *J. Fluid Mech.*, 104:111–118, 1981.

[10] X. Li and R. S. Tankin. On the temporal instability of a two-dimensional viscous liquid sheet. *J. Fluid Mech.*, 226:425–443, 1991.

[11] X. Li. On the instability of plane liquid sheets in two gas streams of unequal velocities. *Acta Mechanica*, 106:137–156, 1994.

[12] J. Cao and X. Li. Stability of plane liquid sheets in compressible gas stream. *AIAA J. Prop. Power*, 16(4):623–627, 2000.

[13] X. Li. Spatial instability of plane liquid sheet. *Chem. Eng. Sci.*, 48:2973–2981, 1993.

[14] X. Li. *Mixed-Flow Hydrodynamics*, pages 145–166. Advances in Eng. Fluid Mechanics. Gulf Publishing Co., 1996.

[15] M. Gaster. A note on the relation between temporally-increasing and spatially-increasing disturbances in hydrodynamic stability. *J. Fluid Mech.*, 14:222–224, 1964.

[16] S. P. Lin, Z. W. Lian, and B. J. Creighton. Absolute and convective instability of a liquid sheet. *J. Fluid Mech.*, 220:673–689, 1990.

[17] N. Dombrowski, D. Hasson, and D. E. Ward. Some aspects of liquid flow through fan sprays. *Chemical Eng. Sci.*, 12:35–50, 1960.

[18] D. Weihs. Stability of thin radially moving liquid sheets. *J. Fluid Mech.*, 87:289–298, 1978.

[19] G.D. Crapper, N. Dombrowski, and G.A.D. Pyott. Kelvin-Helmholtz waves on thin liquid sheets. *Proc. Royal Soc. London*, 342:209–224, 1975.

[20] A. Mansour and N. Chigier. Disintegration of liquid sheets. *Phys. Fluids*, 2:706–719, 1990.

[21] H. Hashimoto and T. Suzuki. Experimental and theoretical study of fine interfacial waves on thin liquid sheet. *JSME Int J*, 34:277–283, 1991.

[22] C. J. Clark and N. Dombrowski. Aerodynamic instability and disintegration of inviscid liquid sheets. *Proc. Royal Soc. London*, 329:467–478, 1972.

[23] R. H. Rangel and W. A. Sirignano. Nonlinear growth of Kelvin-Helmholtz instability: Effect of surface tension and density ratio. *Phys. Fluids*, 31:1845–1855, 1988.

[24] R. H. Rangel and W. A. Sirignano. The linear and nonlinear shear instability of a fluid sheet. *Phys. Fluids*, 3:2392–2400, 1991.

[25] S. A. Jazayeri and X. Li. Nonlinear breakup of plane liquid sheets. *J. Fluid Mech.*, 206:281–308, 2000.

[26] D. B. Bogy. Drop formation in a circular liquid jet. *Ann. Rev. Fluid Mech.*, 11:207–228, 1979.

[27] K. Matsuuchi. Modulational instability of nonlinear capillary waves on thin liquid sheet. *J. Phys. Soc. Japan*, 37:1680–1687, 1974.

[28] K. Matsuuchi. Instability of thin liquid sheet and its break-up. *J. Phys. Soc. Japan*, 41:1410–1416, 1976.

[29] C. Mehring and W. A. Sirignano. Nonlinear capillary wave distortion and disintegration of thin planar liquid sheets. *J. Fluid Mech.*, 388:69–113, 1999.

[30] A. Mansour and N. Chigier. Dynamic behavior of liquid sheets. *Phys. Fluids*, 3:2971–2980, 1991.

[31] A. Lozano, C.J. Call, C. Dopazo, and A. García-Olivares. Experimental and numerical study of the atomization of a planar liquid sheet. *Atomization Sprays*, 6(1):77–87, 1996.

[32] A. Lozano, A. García-Olivares, and C. Dopazo. The instability growth leading to a liquid sheet breakup. *Phys. Fluids*, 10(9):2188–2197, 1998.

[33] I. Kim and W. A. Sirignano. Three-dimensional wave distortion and disintegration of thin planar liquid sheets. *J. Fluid Mech.*, 410:147–183, 2000.

[34] W. A. Sirignano and C. Mehring. Review of theory of distortion and disintegration of liquid streams. *Prog. Energy Comb. Sc.*, 26:609–655, 2000.

[35] P. Rosin and E. Rammler. The laws governing the fineness of powdered coal. *J. Inst. Fuel*, 31:389–393, 1933.

[36] S. Nukiyama and Y. Tanasawa. On the droplet-size distribution in an atomized jet. *Trans. Soc. Mech. Eng. Jpn.*, 5:62–67, 1939.

[37] R. Mugele and H. D. Evans. Droplet size distribution in sprays. *Ind. Eng. Chem.*, 43:1317–1324, 1951.

[38] S. D. Sovani, P. E. Sojka, and Y. R. Sivathanu. Prediction of drop size distributions from first principle: The influence of fluctuations in relative velocity and liquid physical properties. *Atomization Sprays*, 9(1):113–152, 1999.

[39] E. T. Jaynes. Information theory and statistical mechanics. *Phys. Rev.*, 106:620–630, 1957.

[40] C. E. Shannon. A mathematical theory of communications. *Bell System Tech. J.*, pages 379–623, 1948.

[41] R. W. Sellens and T. A. Brzustowski. A prediction of the drop size and velocity distribution in a spray from first principles. *Atomization Spray Technol.*, 1:195–201, 1985.

[42] R. W. Sellens and T. A. Brzustowski. A simplified prediction of droplet velocity distributions in a spray. *Combustion Flame*, 65:273–279, 1986.

[43] R. W. Sellens. Prediction of the drop size and velocity distribution in a spray based on the maximum entropy formalism. *Part. Part. Syst. Charact.*, 6:17–27, 1989.

[44] M. Ahmadi and R. W. Sellens. A simplified maximum-entropy-based drop size distribution. *Atomization Sprays*, 3(2):291–310, 1993.

[45] X. Li. and R. S. Tankin. Droplet size distribution: A derivation of a Nukiyama-Tanasawa type distribution function. *Combustion Sci. Technol.*, 56:65–76, 1988.

[46] X. Li and R.S. Tankin. Derivation of droplet size distribution in sprays by using information theory. *Combustion Sci. Technol.*, 60:345–357, 1988.

[47] X. Li, R. S. Tankin, and M. Renksizbulut. Calculated characteristics of droplet size and velocity distributions in liquid sprays. *Part. Part. Syst. Charact.*, 7:54–59, 1990.

[48] X. Li, L. P. Chin, R. S. Tankin, T. Jackson, J. Stutrud, and G. Switzer. Comparison between experiments and predictions based on maximum entropy for sprays from a pressure atomizer. *Combustion Flame*, 86:73–89, 1991.

[49] X. Li and R. S. Tankin. On the prediction of droplet size and velocity distributions in sprays through maximum entropy. *Part. Part. Syst. Charact.*, 9:195–201, 1992.

[50] L. P. Chin, P. C. Hsing, R. S. Tankin, and T. Jackson. Comparisons between experiments and predictions based on maximum entropy for the breakup of a cylindrical liquid jets. *Atomization Sprays*, 5(5):603–620, 1995.

[51] C. W. M. van der Geld and H. Vermeer. Prediction of drop size distributions in sprays using the maximum entropy formalism: The effect of satellite formation. *Int. J. Multiphase Flow*, 20(2):363–381, 1994.

[52] J. Cousin, S. J. Yoon, and C. Dumouchel. Coupling of classical linear theory and maximum entropy formalism for prediction of drop size distributions in sprays: Application to pressure-swirl atomizers. *Atomization Sprays*, 6(5):601–622, 1996.

[53] J. N. Kapur. Twenty-five years of maximum entropy principle. *J. Math. Phys. Sci.*, 17:103–156, 1983.

[54] C. Dumouchel and S. Boyaval. Use of the maximum entropy formalism to determine drop size distribution characteristics. *Part. Part. Syst. Charact.*, 16:177–184, 1999.

[55] C. Dumouchel and H. Malot. Development of a three-parameter volume-based spray drop size distribution through the application of the maximum entropy formalism. *Part. Part. Syst. Charact.*, 16:220–228, 1999.

[56] S. K. Mitra and X. Li. A predictive model for droplet size distribution in sprays. *Atomization Sprays*, 9(1):29–50, 1999.

[57] M. M. Sidahmed. A model for predicting the droplet size from liquid sheets in airstreams. *Trans. ASAE*, 39(5):1651–1655, 1996.

[58] H. S. Couto, J. A. Carvalho Jr., and D. Bastos-Netto. Theoretical formulation for Sauter mean diameter of pressure-swirl atomizers. *AIAA J. Prop. Power*, 13(5):691–696, 1997.

[59] H.R. Asare, R.K. Takahashi, and M.A. Hoffman. Liquid sheet jet experiments: comparison with linear theory. *J. Fluids Eng.*, 103:595–604, 1981.

[60] G.D. Crapper and N. Dombrowski. A note on the effect of forced disturbances on the stability of thin liquid sheets and on the resulting drop size. *Int. J. Multiphase Flow*, 10(6):731–736, 1984.

[61] J. L. Dressler. Atomization of liquid cylinders, cones, and sheets by acoustically-driven, amplitude-dependent instabilities. In *Proc. Int. Conf. Liquid Atomization Spray Systems*, pages 397–405, July 1991. Gaithersburg, M.D., USA.

[62] I-P. Chung, C. Presser, and J. L. Dressler. Effect of piezoelectric transducer modulation on liquid sheet disintegration. *Atomization Sprays*, 8(4):479–502, 1998.

[63] S. A. Jazayeri and X. Li. Structure of liquid-sheet sprays. *Part. Part. Syst. Charact.*, 17:56–65, 2000.

[64] G. Lavergne, P. Trichet, P. Hebrard, and Y. Biscos. Liquid sheet disintegration and atomization process on a simplified airblast atomizer. *J. Engng. Gas Turbines Power*, 115:461–466, 1993.

[65] P. Berthoumieu, H. Carentz, and A. Muller. Video techniques applied to the characteristics of liquid sheet breakup. In *Proc.* 9^{th} *Int. Symp. Flow Visualization*, pages 28–1–28–7, 2000. Edinburgh, U.K.

[66] L. D. Luca and M. Costa. Stationary waves on plane liquid sheets falling vertically. *Eur. J. Mech.*, 16(1):75–88, 1997.

[67] L. D. Luca. Experimental investigation of the global instability of plane sheet flows. *J. Fluid Mech.*, 399:355–376, 1999.

[68] K. Ramamurthi and T. J. Tharakan. Flow transition in swirled liquid sheets. *AIAA J.*, 36(3):420–427, 1998.

[69] B. E. Stapper, W. A. Sowa, and G. S. Samuelsen. An experimental study of the effects of liquid properties on the breakup of a two-dimensional liquid sheet. *J. Engng. Gas Turbines Power*, 114:39–45, 1992.

[70] J. M. Hespel, Y. Brunet, and A. Dyment. Liquid sheet and film atomization: A comparative experimental study. *Expt. Fluids*, 19:388–396, 1995.

[71] W. D. Bachalo and M. J. Houser. Phase Doppler spray analyzer for simultaneous measurements of drop size and velocity distributions. *Optical Eng.*, 23:583–590, 1984.

[72] Y. Yeh and H. Z. Cummins. Localized fluid flow measurements with an He-Ne laser spectrometer. *Appl. Phys. Lett.*, 4(10):176–178, 1964.

[73] H. van de Hulst. *Light scattering by small particles.* Wiley, New York, 1957.

[74] W. D. Bachalo and S. V. Sankar. *Phase Doppler particle analyzer*, chapter 37, pages 37–1—37–19. The handbook of fluid dynamics. CRC Press LLC, 1998.

[75] P. A. Strakey, D. G. Talley, S. V. Sankar, and W. D. Bachalo. Phase-Doppler interferometry with probe-to-droplet size ratios less than unity. I. Trajectory errors. *Appl. Optics*, 39(22):3875–3886, 2000.

[76] P. A. Strakey, D. G. Talley, S. V. Sankar, and W. D. Bachalo. Phase-Doppler interferometry with probe-to-droplet size ratios less than unity. II. Application of the technique. *Appl. Optics*, 39(22):3887–3893, 2000.

[77] J. A. Friedman and M. Renksizbulut. A method for increasing the sensitivity of phase Doppler interferometry to seed particles in liquid spray flows. *Part. Part. Syst. Charact.*, 12:225–231, 1995.

[78] P. D. Noymer. The use of single-point measurements to characterize dynamic behavior in sprays. *Expt. Fluids*, 29:228–237, 2000.

[79] N. K. Rizk. Airblast atomization: Studies on drop-size distribution. *J. Energy*, 6(5):323–327, 1982.

[80] M. P. Moses, S. H. Collicott, and S. D. Heister. Detection of aerodynamic effects in liquid jet breakup and droplet formation. *Atomization Sprays*, 9(2):331–342, 1999.

[81] H. E. Snyder and R. D. Reitz. Direct droplet production from a liquid film: A new gas-assisted atomization mechanism. *J. Fluid Mech.*, 375:363–381, 1998.

[82] R. W. Tate. Some problems associated with the accurate representation of droplet size distributions. In *Proc. Int. Conf. Liquid Atomization Spray Systems*, pages 341–351, July 1982. Madison, USA.

[83] A. H. lefebvre. Twin-fluid atomization: Factors influencing mean drop size. In *Proc. Int. Conf. Liquid Atomization Spray Systems*, pages 49–64, July 1991. Gaithersburg, M.D., USA.

[84] C. H. Teng, S. P. Lin, and J. N. Chen. Absolute and convective instability of a viscous liquid curtain in a viscous gas. *J. Fluid Mech.*, 332:105–120, 1997.

[85] F. M. White. *Viscous fluid flow.* McGraw-Hill Inc., New York, 1991.

[86] M. C. Yuen. Nonlinear capillary instability of a liquid jet. *J. Fluid Mech.*, 33:151–163, 1968.

[87] S. K. Mitra, X. Li, and M. Renksizbulut. Prediction of liquid sheet breakup from dual-mode linearized theory. In *Proc. 8th Int. Conf. Liquid Atomization Spray Systems*, pages 113–120, July 2000. Pasadena, CA, USA.

[88] S. K. Mitra, X. Li, and M. Renksizbulut. On the breakup of viscous liquid sheets by dual-mode linear analysis. *AIAA J. Prop. Power*, 17(3):728–735, 2001.

[89] S. Kullback and R. A. Leibler. On information and sufficiency. *Ann. Math. Stat.*, 22:79–86, 1951.

[90] M. Tribus. Information theory as the basis for thermostatics and thermodynamics. *J. Appl. Math.*, 28:1–8, 1961.

[91] R. D. Levine and M. Tribus, editors. *The maximum entropy formalism.* The MIT Press, Massachusetts, 1978.

[92] S. P. Lin and Z. W. Lian. Mechanism of the breakup of liquid jets. *AIAA J.*, 28:120–126, 1990.

[93] N. Dombrowski and P. C. Hooper. The effect of ambient density on drop formation in sprays. *Chemical Eng. Sci.*, 17:291–305, 1962.

[94] H. Schlichting. *Boundary-Layer Theory.* McGraw-Hill Book Co., New York, 1979.

[95] S. K. Mitra. A comprehensive model on spray formation and droplet size distribution. Master's thesis, University of Victoria, 1997.

[96] Lord Rayleigh. On the instability of jets. *Proc. Lond. Math. Soc.*, 10:4–13, 1879.

[97] R. Clift, J. R. Grace, and M. E. Weber. *Bubbles, Drops, and Particles.* Academic Press, New York, 1978.

[98] J. A. Friedman. *Investigating the interaction of an annular air jet with a spray flame using phase Doppler interferometry and laser-induced fluorescence.* PhD thesis, University of Waterloo, 1997.

[99] C. P. Salvador. Effect of turbulence on droplet evaporation and drag. Master's thesis, University of Waterloo, 2000.

[100] P. Berthoumieu. Personal communication. ONERA-CERT, France.

[101] J. Park. Personal communication. PostTech, South Korea.

[102] X. Li and J. Shen. Experimental study of sprays from annular liquid jet breakup. *AIAA J. Prop. Power*, 15(1):103–110, 1999.